AFOSR-TR- 2 0403

(2)

F49620-88-C-0022
ME-TSPC-TR-92-10

FINAL REPORT
CONTRACT F49620-88-C-0022

RESEARCH ON AERO-THERMODYNAMIC DISTORTION INDUCED STRUCTURAL DYNAMIC RESPONSE OF MULTISTAGE COMPRESSOR BLADING

Sanford Fleeter
March 1992

Thermal Sciences and Propulsion Center
School of Mechanical Engineering
Purdue University
West Lafayette, Indiana 47907

92 5 14 087

Prepared for

Directorate of Aerospace Sciences
Air Force Office of Scientific Research

REPORT DOCUMENTATION PAGE

Form Approved
OMB No. 0704-0188

1. AGENCY USE ONLY (Leave blank)	2. REPORT DATE	3. REPORT TYPE AND DATES COVERED
	March 1992	Final, 11-87 to 5-91

4. TITLE AND SUBTITLE
Research On Aero-Thermodynamic Distortion Induced Structural Dynamic Response of Multistage Compressor Blading

5. FUNDING NUMBERS
2307/DS
PE: 61102F

6. AUTHOR(S)
Sanford Fleeter

7. PERFORMING ORGANIZATION NAME(S) AND ADDRESS(ES)
School of Mechanical Engineering
Purdue University
West Lafayette, Indiana 47907

8. PERFORMING ORGANIZATION REPORT NUMBER
TSPC-TR-92-10

9. SPONSORING/MONITORING AGENCY NAME(S) AND ADDRESS(ES)
Directorate of Aerospace Sciences
Air Force Office of Scientific Research (N/A)
Building 410
Department of the Air Force (AFSC)
Bolling Air Force Base, DC 20332-6448

NA

10. SPONSORING/MONITORING AGENCY REPORT NUMBER
F49620-88-C-0022

11. SUPPLEMENTARY NOTES

12a. DISTRIBUTION/AVAILABILITY STATEMENT
Unlimited

12b. DISTRIBUTION CODE

13. ABSTRACT (Maximum 200 words)

ABSTRACT

This report summarizes the results obtained on Contract F49620-88-C-0022. The overall objective of this basic research program was the quantitative investigation of the fundamental phenomena relevant to aero-thermodynamic distortion induced structural dynamic blade responses in multistage gas turbine engines. The technical approach involved unique benchmark experiments and also analyses. In particular, the flow physics of multistage blade row interactions were investigated, with unique unsteady aerodynamic data obtained and analyses developed to understand, quantify, and discriminate the fundamental flow phenomena as well as to direct the modeling of advanced analyses. Data obtained define the flow interactions and the effects on both the aerodynamic forcing function and the resulting unsteady aerodynamics of compressor rotor blades and stator vanes in a multistage environment over a wide range of realistic reduced frequency values for the first time.

14. SUBJECT TERMS
Unsteady Aerodynamic,
Flow Induced Vibrations
Forced Response

15. NUMBER OF PAGES
143

16. PRICE CODE

17. SECURITY CLASSIFICATION OF REPORT	18. SECURITY CLASSIFICATION OF THIS PAGE	19. SECURITY CLASSIFICATION OF ABSTRACT	20. LIMITATION OF ABSTRACT
U	U	U	

F49620-88-C-0022
ME-TSPC-TR-92-10

FINAL REPORT
CONTRACT F49620-88-C-0022

RESEARCH ON AERO-THERMODYNAMIC DISTORTION INDUCED STRUCTURAL DYNAMIC RESPONSE OF MULTISTAGE COMPRESSOR BLADING

Sanford Fleeter
March 1992

Thermal Sciences and Propulsion Center
School of Mechanical Engineering
Purdue University
West Lafayette, Indiana 47907

Prepared for

Directorate of Aerospace Sciences
Air Force Office of Scientific Research

ABSTRACT

This report summarizes the results obtained on Contract F49620-88-C-0022. The overall objective of this basic research program was the quantitative investigation of the fundamental phenomena relevant to aero-thermodynamic distortion induced structural dynamic blade responses in multistage gas turbine engines. The technical approach involved unique benchmark experiments and also analyses. In particular, the flow physics of multistage blade row interactions were investigated, with unique unsteady aerodynamic data obtained and analyses developed to understand, quantify, and discriminate the fundamental flow phenomena as well as to direct the modeling of advanced analyses. Data obtained define the flow interactions and the effects on both the aerodynamic forcing function and the resulting unsteady aerodynamics of compressor rotor blades and stator vanes in a multistage environment over a wide range of realistic reduced frequency values for the first time.

TABLE OF CONTENTS

I. INTRODUCTION

The structural dynamic response of turbomachinery blading to aero-thermodynamic distortion induced excitations is an item of rapidly increasing concern to designers and manufacturers of gas turbine engines for advanced technology applications. Namely, the increasing variety of modern aircraft and missions has resulted in expanded variations of engine designs and requirements. These have a direct and significant effect on the blading components, i.e., fans, compressors, and turbines, and thus on the structural dynamic characteristics of these components.

Turbomachinery blading forced response is a universal problem, with every new gas turbine engine having had at least one blade row or stage with turbomachinery blading forced response problems and each engine company having at least one such problem. The primary mechanism of blade failure is fatigue caused by vibrations at levels exceeding material endurance limits. These vibrations occur when a periodic forcing function, with frequency equal to a natural blade resonant frequency, acts upon a blade row. Because a blade may have as many critical points of high stress as it has natural modes, the designer must determine which particular modes have the greatest potential for aerodynamic excitation.

With the resonant airfoil frequencies able to be accurately predicted with finite element structural models, the Campbell diagram is the key design tool in a 0^{th} order bladed disk forced response design system These display the natural frequency of each blade mode versus rotor speed and, on the same plot, the aerodynamic forcing function frequency versus rotor speed, Figure 1.

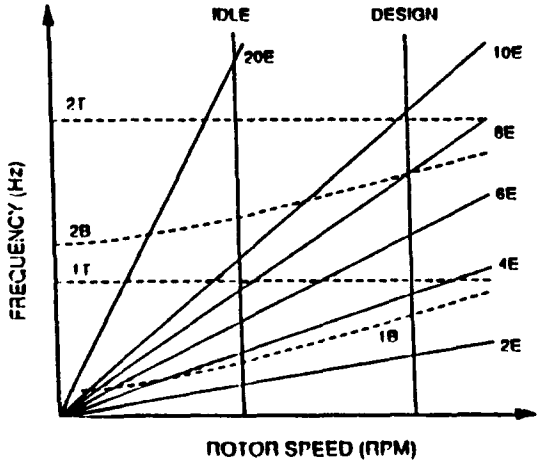

Figure 1. Campbell Diagram Schematic

At each intersection point, an aerodynamically induced vibration problem is possible. Thus, these intersection points, termed resonant speeds, indicate a potentially significant increase in vibratory blade response. However, as Campbell diagrams do not consider either the detailed aerodynamic forcing function or the resulting airfoil row unsteady aerodynamics, they provide no measure of the amplitude of the resulting stress at the various resonant speeds.

I.1 Unsteady Aerodynamic Modeling

A 1st order forced response design system is defined as one which predicts the amplitude of the resulting stress at the resonant speeds utilizing a linearized unsteady aerodynamic model, i.e., with the unsteady flow considered to be a small perturbation superimposed on the steady flow. Thus, 1st order design system unsteady aerodynamic modeling is performed in the frequency domain, requiring a definition of the unsteady aerodynamic forcing function in terms of its harmonics. The unsteady aerodynamic response of the airfoil row to each forcing function harmonic is then assumed to be comprised of: (1) the disturbance being swept past the nonresponding airfoils, termed the gust unsteady aerodynamics, and (2) the airfoil vibratory response to this disturbance, referred to as the motion-induced unsteady aerodynamics or the aerodynamic damping. Finally, an aeroelastic or structural dynamics model is utilized to predict the blade row response, typically accomplished by a classical Newton's second law approach with the unsteady aerodynamics combined with a lumped parameter airfoil model.

1st order design system unsteady flow models can be broadly categorized in terms of the hierarchy of steady flow and gust models, Figure 2.

* **Flat Plate Cascade at zero incidence**

$$\vec{Q}(\vec{x},t) = U_\infty + \nabla\phi(\vec{x})e^{i\omega t}$$

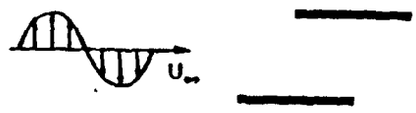

* **Cambered Airfoil Cascade - Irrotational flow (Linearized Potential Flow)**

$$\vec{Q}(\vec{x},t) = \nabla\Phi_o(\vec{x}) + \nabla\phi(\vec{x})e^{i\omega t}$$

* **Cambered Airfoil Cascade - Rotational flow (Linearized Euler Flow)**

$$\vec{Q}(\vec{x},t) = Q_o(\vec{x}) + q(\vec{x})e^{i\omega t}$$

Figure 2. 1st order design system unsteady flow model hierarchy

* For a uniform steady flow, both the steady and unsteady flow fields are independent, with a flat plate airfoil cascade at zero incidence considered.

$$\vec{Q}(\vec{x},t) = U_\infty + \nabla\phi(\vec{x})e^{i\omega t}$$

where $\vec{Q}(\vec{x},t)$ is the total flow field, U_∞ is the steady uniform flow, $\nabla\phi(\vec{x})$ is the linearized unsteady potential flow and w is the gust frequency.

* Linearizing about a steady potential flow, the classical models were extended to predict aerodynamic damping and gust loading including blade profile effects.

$$\vec{Q}(\vec{x},t) = \nabla\Phi_o(\vec{x}) + \nabla\phi(\vec{x})e^{i\omega t}$$

where Φ_o is the steady potential mean flow and although the steady field is still independent of the unsteady flow, the unsteady flow is coupled to the steady flow through the boundary conditions.

* Linearizing about a steady rotational flow modeled by the Euler equations, the gust modeling is being further extended.

$$\vec{Q}(\vec{x},t) = Q_o(\vec{x}) + q(\vec{x})e^{i\omega t}$$

where Q_o is the steady Euler mean flow.

I.2 Forcing Functions

There are many analytical and physical assumptions inherent in the various mathematical models. This is demonstrated in the following discussion of state-of-the art linear theory forcing function modeling.

The source of the aerodynamic forcing function is generally a distortion in the inlet or exit flow field of an airfoil row. To analyze the resulting airfoil row forced response, the forcing function is assumed to be specified. In a 1st order design system, this forcing function is then Fourier decomposed into harmonics, with the response to each harmonic then determined. Note that although forcing functions can be generated by a wide variety of sources, the resulting forced response to each harmonic is assumed to be the same if the particular forcing function harmonic is the same, i.e., if the harmonic frequency and

amplitude of two forcing functions generated by different flow phenomena are the same, then the resulting forced response will be the same.

Wakes from upstream airfoil rows are one of the most common unsteady aerodynamic forcing functions. Thus, consider a wake from an upstream rotor blade row. In classical linear theory, the wake flow field is considered to be composed of a uniform mean flow and a superimposed harmonic vortical gust $\vec{w}$ propagating according to the wave-number vector $\vec{k}$. The corresponding turbomachine blade-row flow field schematic is presented in Figure 3. For convenience, the rotor wake periodic shape has been Fourier decomposed and the fundamental harmonic depicted. The downstream relative velocity decreases from the mean in the rotor wake and increases from the mean in the free stream by the amplitude of the vortical gust w^+. It is this harmonic velocity which is the unsteady aerodynamic forcing function to the downstream airfoil rows.

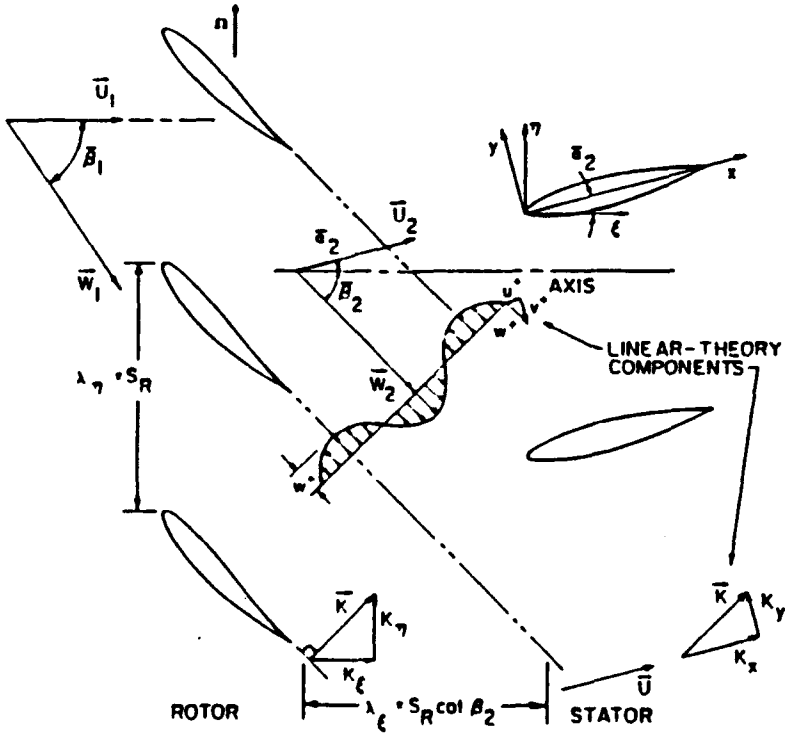

Figure 3. Turbomachine blade-row flow field schematic

In the downstream airfoil row stationary reference frame, the propagation of the harmonic vortical gust is defined by considering periodicity requirements in the axial-circumferential coordinate system. As a consequence of this periodicity, the downstream mean-relative flow $\vec{W}_2$ and the gust propagation vector $\vec{k}$ must be perpendicular.

The stator row flow field is modeled as being compressible and isentropic. For a uniform steady flow, the linearized continuity and momentum equations describing the perturbation velocity and pressure are

$$\frac{1}{\rho_o c_o^2}\frac{D_o p}{Dt} + \nabla \cdot \vec{u} = 0 \tag{1}$$

$$\frac{D_o \vec{u}}{Dt} = \frac{1}{\rho_o}\nabla p \tag{2}$$

where $\frac{D_o}{Dt} = \frac{\partial}{\partial t} + \overline{U}\frac{\partial}{\partial x}$.

This inviscid flow is analyzed by superpositioning rotational and irrotational flow fields. Thus the unsteady velocity perturbation $\vec{u}$ is considered to consist of a rotational velocity component $\vec{w}$ and an irrotational component, with these components satisfying continuity independently. The airfoil surface boundary condition introduces the effect of the forcing function rotational flow or gust into the unsteady pressure field. This requires the specification of the rotational flow field generated by the gust $\vec{w}$.

The propagation of the gust is described by

$$\vec{w} = \vec{w}^{+} e^{i(\vec{k}\cdot\vec{x} - k_x t)} = 0 \tag{3}$$

where the gust component amplitude vector is $\vec{w}^{+} = u^{+}\hat{i} + v^{+}\hat{j}$, the gust propagation vector is $\vec{k} = k_x\hat{i} + k_y\hat{j}$ and $\vec{x} = x\hat{i} + y\hat{j}$.

To satisfy continuity, the rotational gust velocity perturbation and propagation vector must be perpendicular for all time and space, $\vec{W}\cdot\vec{k} = 0$. Thus, continuity considerations result in two constraints on the rotational gust forcing function flow field.

* The primary constraint is the requirement that the phase angle between the streamwise and transverse gust component harmonics ϕ_w be equal to either 0° or 180°, i.e., the gust-component phase angle $\phi_w = 0°$ or 180°. When this primary constraint is satisfied, the gust amplitude simplifies to $w^{+} = \sqrt{u^{+2} + v^{+2}}$, with the

periodic velocity vectors parallel over the gust periodic cycle. If the primary constraint is not satisfied, the gust amplitude is not a simple function of the gust-component amplitudes and the velocity vector direction is a function of time and space.

* The secondary constraint stipulates that the gust-component amplitude vector must be parallel to the downstream mean-relative flow $\vec{w}^+ \,||\, \vec{W}_2$ if the primary constraint is satisfied.

I.3 Significance

As demonstrated in the above, there are many analytical and physical assumptions inherent in the various mathematical models. However, minimal attention has been given to either the aerodynamic forcing function or to the blade row interactions, i.e., only isolated airfoil rows are considered with viscous effects not analyzed. Experimentally only very limited appropriate fundamental unsteady aerodynamic data exist to verify existing models, with these data generally not suitable to discriminate and quantify the fundamental flow phenomena and direct the development of advanced mathematical models. Also, all of the existing data have been obtained in isolated blade rows or in single stages. Thus, the important effects associated with multistaging, including the blade row potential and viscous flow interactions, have not been investigated.

II. PROGRAM OBJECTIVES & TECHNICAL APPROACH

The overall objective of this research program was the quantitative investigation of the fundamental phenomena relevant to aero-thermodynamic distortion induced structural dynamic blade responses in multistage gas turbine engine components. In particular, the flow physics of multistage blade row interactions were experimentally investigated, with unique unsteady aerodynamic data obtained to understand, quantify, and discriminate the fundamental flow phenomena as well as to direct the flow modeling in advanced analyses. Data obtained investigate the flow interactions and their effect on both the aerodynamic forcing function and the resulting unsteady aerodynamics of both compressor rotor blades and stator vanes in a multistage environment at realistic reduced frequency values for the first time. Namely, the effects of various aerodynamic forcing functions on rotor blade row unsteady aerodynamic response over a range of operating conditions in a multistage compressor environment were to be investigated.

The technical approach to achieving these experimental objectives included the acquisition and analysis of unique unsteady aerodynamic data to quantify the aerodynamic forcing function and the resulting unsteady aerodynamics on each rotor blade row of the Purdue Three-Stage Axial Flow Research Compressor. Also, analytically, unsteady viscous flow analyses were developed which model the unsteady cascade aerodynamics generated by both a convected gust and harmonic airfoil oscillations.

III. RESULTS

The experimental and analytical research results obtained are contained in both the publications and the graduate student theses. The publications describing these results are summarized in the following, with the detailed results and publications presented in the appendices.

These results are categorized in the following as: (1) Data Analysis, (2) Experimental Gust Generated Unsteady Aerodynamics which is further divided into Blade Row Response and Forcing Function Significance, and (3) Mathematical Modeling.

III.1 Data Analysis

The acquisition and analysis of time-variant data by ensemble averaging discards information describing significant unsteady flow phenomena.

Figure 4 presents samples of the instantaneous cross hot-wire probe signal which make up the ensemble averaged rotor blade exit flow field together with the exit flow field averaged 200 times. In the free stream region, the instantaneous signals are analogous to one another and to the ensemble averaged free stream results as expected. However, the instantaneous signals in the rotor blade wake region are somewhat surprising. Namely, some of these instantaneous signals are analogous to one another and to the characteristics of the ensemble averaged wake, but others differ significantly from the expected wake profile.

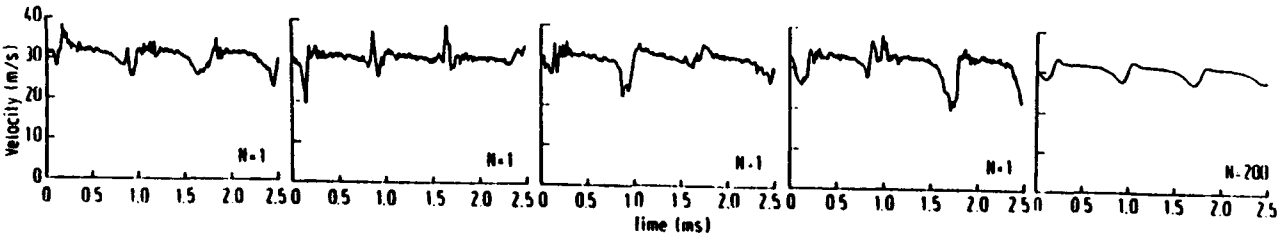

Figure 4. Rotor blade exit instantaneous and averaged flow field

The unsteady flow phenomena resulting in the differences in the instantaneous rotor blade wake data have been investigated and these data interpreted. This was accomplished by developing a mathematical model of the rotor blade exit flow field, with a vortex street structure for the blade wake. Predictions from this model were then utilized to interpret the instantaneous rotor blade exit flow field data and demonstrate the existence of a vortex street structure in the rotor blade wake. This wake vortex street structure is analogous to the unsteady flow field behind bluff bodies due to classical von Karman vortex shedding.

III.2 Experimental Gust Generated Unsteady Aerodynamics

Experiments to investigate the fundamental flow physics and quantify the blade row unsteady aerodynamic response to gusts generated by inlet flow distortions and blade wakes have been performed in an extensively instrumented research three stage axial flow compressor for both low and high reduced frequency values, with steady loading as a parameter. These unique data were then correlated with state of the art linearized gust response predictions.

The significant results of these experiments, including their implications to advanced mathematical model requirements, include the following.

Blade Row Response

* The steady aerodynamic loading level, not the incidence angle, is the key parameter to obtain good correlation with linearized cascade gust model predictions.

* The aerodynamic forcing function chordwise gust affects both the dynamic pressure coefficient magnitude and phase whereas the transverse gust primarily affects the magnitudes. These effects cannot be predicted with harmonic gust models because these data have been Fourier decomposed, with the predictions thus identical for all forcing function wave forms.

* The chordwise gust is not small compared to either the absolute velocity or the transverse gust. Thus to provide accurate predictions, unsteady aerodynamic models must consider this gust component.

* There are large and significant differences between high and very high reduced frequency gust generated unsteady aerodynamic response of the rotor blade row, with

current state-of-the art math models not able to predict these responses, Figure 5. As blade row forced response problems are significant over the complete range of reduced frequency values, i.e. low, high and very high reduced frequency values, advanced math models must be developed.

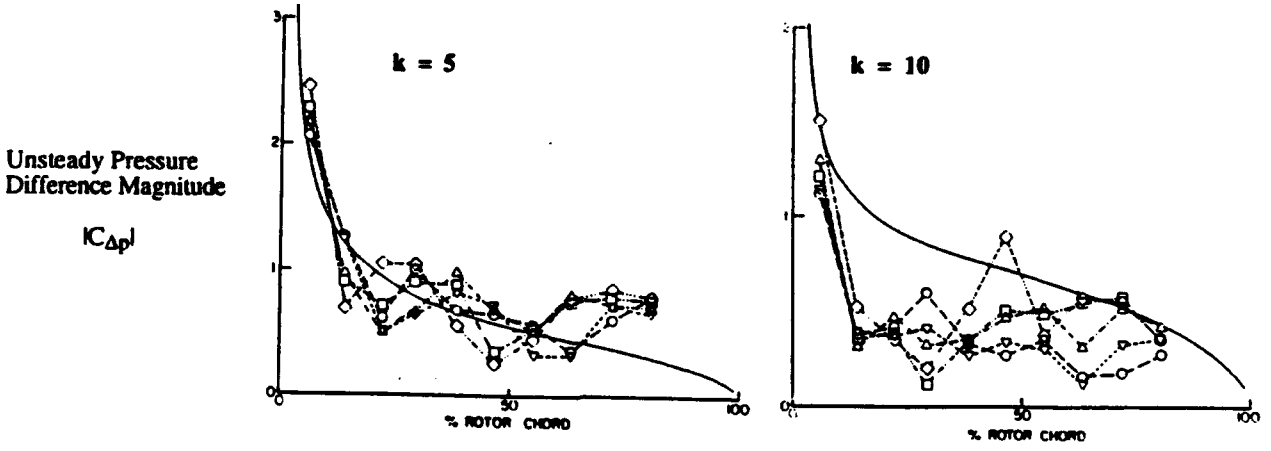

Figure 5. High and very high reduced frequency rotor blade gust response

* For closely spaced stages, downstream airfoils rows are potential aerodynamic excitation sources which affect the unsteady loading in the trailing edge region of the upstream airfoils. Since the trailing edge is thin, it would be highly susceptible to fatigue failure.

* Steady flow separation has a significant influence on the unsteady aerodynamics of the separation point and also in the trailing edge region. As most forced response problems are at off-design conditions, additional research is needed to understand steady flow separation effects on the resulting gust generated unsteady aerodynamic blade row response.

* The unsteady pressure response on the blade pressure surface, i.e., the low camber surface is primarily affected by the level of steady loading as characterized by the mean flow incidence angle except in the accelerating mean flow field of the front chord region at negative incidence angle.

* The unsteady pressure response on the high camber blade suction surface is affected by the level of steady loading, i.e., the accelerating mean flow field in the front half of the surface and the large viscous regions in the aft half of the surface. Thus, for turbines with highly cambered high turning airfoils and accelerating flow fields, the level of steady loading and the interaction between the steady and unsteady flow fields must be considered. Unfortunately, no fundamental turbine blade row gust response unsteady aerodynamic data has been obtained to date. In view of the high degree of susceptibility of turbine blade rows to flow induced vibration problems, this area of research needs attention, both with regard to flow induced vibrations and unsteady heat transfer.

Forcing Function Significance

Two different two per rev aerodynamic forcing functions were considered: (1) the velocity deficit from two 90° circumferential inlet flow distortions and (2) the wakes from two upstream obstructions, Figure 6. These aerodynamic forcing functions to the first stage rotor blade row were equivalent in terms of state-of-the-art linearized unsteady flow models, including the reduced frequency, interblade phase angle and ratio of the streamwise-to-normal gust component amplitude ratio.

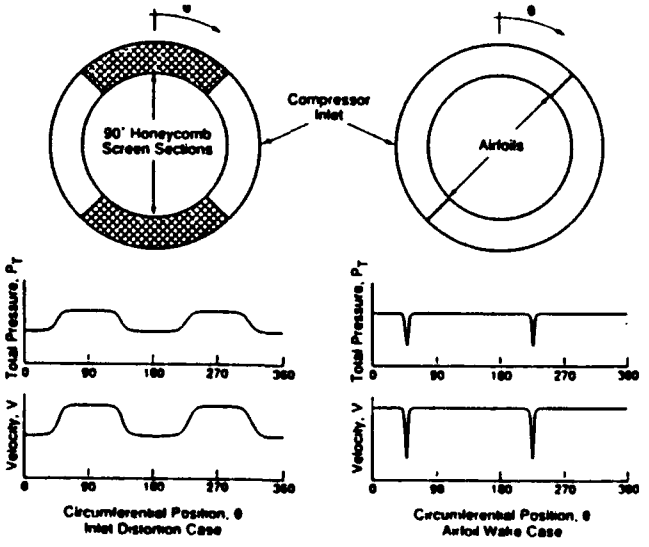

Figure 6. Fundamentally equivalent inlet distortion and wake forcing functions

* The rotor steady aerodynamic performance was found to be independent of the aerodynamic forcing function.

* The wake generated rotor row unsteady first harmonic response is much greater than that generated by the inlet distortion, with the difference decreasing with increased steady loading, Figure 7. Also, these results can not be predicted with state-of-the-art linearized gust response models as the fundamental parameters for the two forcing functions are equivalent. Note that these are the first quantitative results clearly showing that the forcing function fluid dynamics is significant with regard to flow induced vibration modeling and is not considered in current state-of-the-art gust response models.

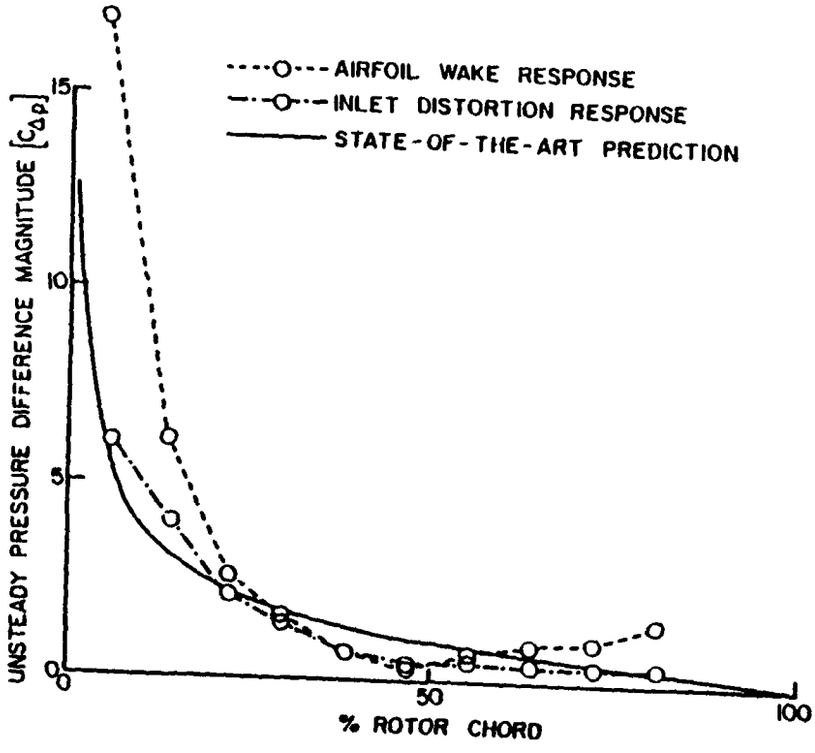

Figure 7. Inlet distortion and wake generated rotor row unsteady 1st harmonic response

III.3 Mathematical Modeling

The resonant conditions at which significant flow induced vibrations may occur can be predicted with Campbell diagrams, although Campbell diagrams give no information concerning the amplitude of the response. However, many of the resonant conditions indicated on the Campbell diagram correspond to off-design operating conditions where viscous effects may be significant. Thus, although considerable progress has been made in the prediction of the unsteady aerodynamics of oscillating airfoils, these analyses are not applicable to these off-design conditions. This is because these small perturbation analyses are typically limited to inviscid potential flows.

To begin to address these important off-design flow conditions, two mathematical models have been developed.

(1) The first analysis models the unsteady aerodynamics of an harmonically oscillating flat plate airfoil, including the effects of mean flow incidence angle, in an incompressible laminar flow at moderate values of the Reynolds number. The unsteady viscous flow is assumed to be a small perturbation to the steady viscous flow field. The nonuniform and nonlinear steady flow is described by the Navier-Stokes equations and is independent of the unsteady flow. The small perturbation unsteady viscous flow is described by a system of linear partial differential equations that are coupled to the steady flow field, thereby modeling the strong dependence of the unsteady aerodynamics on the steady flow.

(2) The second analysis predicts the effect of flow separation on the unsteady aerodynamic lift and moment acting on a two dimensional flat plate cascade which is harmonically oscillating in a subsonic flow field. The unsteady flow is considered to be a small perturbation to the uniform steady flow, with the steady flow assumed to separate at a specified fixed position on the airfoil suction surface. This formulation does not require the difference in the upwash velocity across the airfoil in the separated flow region to be determined before calculating the unsteady pressure difference in the upwash velocity across the airfoil in the separated flow region to be determined before calculating the unsteady pressure difference across the chordline of the airfoils, thereby eliminating the assumption that the upwash difference is zero at the trailing edge when the steady flow is separated. Results obtained demonstrate that although flow separation decreases bending mode stability, it does not result in bending mode flutter.

However, flow separation can result in torsion mode flutter, with this instability being a function of the location of both the separation point and the elastic axis.

In addition, a model has been develop which predicts the turbulence generated single degree-of-freedom bending and torsion mode vibration response of a turbomachine blade row operating in a subsonic compressible flow field. The turbulence is assumed to be random in the neighborhood of the blade natural frequency of interest and to generate a large number of constant amplitude harmonic unsteady aerodynamic lift forces and moments on the blading with equally distributed frequencies. The resulting random airfoils vibrations thus occur at the blade natural frequency. The unsteady aerodynamics generated by the blade response i.e., the aerodynamic damping, as well as the effect of blade aerodynamic coupling are also considered.

IV. PUBLICATIONS

Experimental Results

APPENDIX I. Capece, V.R., and Fleeter, S., "Measurement and Analysis of Unsteady Flow Structures in Rotor Blade Wakes," *Experiments in Fluids*, Vol. 7, No. 1, 1989, pp. 61-67.

APPENDIX II. Capece, V.R., and Fleeter, S., "Experimental Investigation of Multistage Interaction Gust Aerodynamics," *ASME Journal of Turbomachinery*, Volume 111, No.4, October 1989, pp 409-417.

APPENDIX III. Manwaring, S.R. and Fleeter, S., "Inlet Distortion Generated Periodic Aerodynamic Rotor Response," *ASME Journal of Turbomachinery*, Vol. 112, No. 2, April 1990, pp. 298-307.

APPENDIX IV. Manwaring, S.R. and Fleeter, S., "Periodic Unsteady Rotor Blade Aerodynamics Including Loading Effects," *AIAA Journal of Propulsion and Power*, September-October 1990, pp. 590-597.

APPENDIX V. Fleeter, S., Capece, V.R., and Chiang, H.D., "Unsteady Aerodynamic Gust Response Including Steady Flow Separation," *AIAA Journal*, Vol. 28, No. 6, June 1990, pp. 1024-1032.

APPENDIX VI. Manwaring, S.R. and Fleeter, S., "Forcing Function Effects on Rotor Periodic Aerodynamic Response," *ASME Journal of Turbomachinery*, Vol. 113, No. 2, April 1991, pp. 312-319.

APPENDIX VII. Manwaring, S.R., and Fleeter, S., "Rotor Blade Unsteady Aerodynamic Gust Response to Inlet Guide Vane Wakes," *ASME Paper 91-GT-129*, June 1991, *ASME Journal of Turbomachinery*, in press

Analytical Results

APPENDIX VIII. Schroeder, L.M., and Fleeter, S., "Viscous Aerodynamic Analysis of an Oscillating Flat Plate Airfoil with a Locally Analytical Solution, *AIAA Journal*, Volume 27, No. 8, August 1989, pp. 1021-1023.

APPENDIX IX. Schroeder, L.M., Wolff, J.M., and Fleeter, S., "Locally Analytical Prediction of the Viscous Aerodynamics of an Oscillating Flat Plate," *International Journal of Mathematical and Computer Modeling*, Vol. 12, No. 6, 1989, pp. 707-719.

APPENDIX X. Booth, T.E. and Fleeter, S., "Prediction of Turbulence Generated Random Vibrational Response of Turbomachinery Blading," *International Journal of Turbo and Jet Engines*, Vol. 6, No. 3 and 4, 1989, pp. 247-256.

APPENDIX XI. Wolff, J.M. and Fleeter, S., "Viscous Oscillating Cascade Aerodynamics and Flutter by a Locally Analytical Method," *AIAA Paper 90-0579*, January 1990.

APPENDIX XII. Eley, J.A. and Fleeter, S., "Oscillating Cascade Unsteady Aerodynamics Including Separated Flow Effects," *Computational Mechanics*, Vol. 8, No. 6, pp. 383-398, 1991.

APPENDIX I

Measurement and Analysis of Unsteady Flow Structures in Rotor Blade Wakes

Experiments in Fluids

Experiments in Fluids 7, 61 - 67 (1989)

Experiments in Fluids

Measurement and analysis of unsteady flow structures in rotor blade wakes

V. R. Capece and S. Fleeter

Thermal Sciences and Propulsion Center, School of Mechanical Engineering, Purdue University, West Lafayette, IN 47907, USA

Abstract. Time-variant data are obtained to investigate the exit flow field from a rotor in a research compressor. In the free-stream region, the instantaneous data are analogous to one another and to the ensemble averaged free-stream results. However, in the wake region, some of the instantaneous signals are similar to one another and to the ensemble averaged wake, but others differ significantly. These variations in the instantaneous data are interpreted and shown to be due to a vortex street structure in the wake. This is accomplished by: (1) developing a mathematical model of the rotor blade exit flow field based on a wake vortex street structure analogous to the unsteady flow field behind bluff bodies due to classical von Karman vortex shedding; and (2) correlating predictions of both the ensemble averaged and instantaneous rotor blade exit flow fields as well as the velocity probability density distributions from this vortex wake flow field model with the corresponding data. The correlation of the ensemble averaged rotor blade exit flow fields is very good and the flow angle distribution correlation excellent. The predicted instantaneous rotor blade exit flow field exhibits many of the flow features found in the data. Also, the probability density distributions for the data and the vortex wake flow field model are analogous to one another.

List of symbols

N	number of rotor revolutions
S_w	rotor blade wake width
S_x	vortex core horizontal spacing
S_y	vortex core vertical spacing
u	velocity component parallel to vortex street motion
v	velocity component normal to vortex street motion
W	instantaneous relative velocity
W_i	velocity induced by vortex street
W_∞	free-stream relative velocity
W_s	velocity of vortex street
x	coordinate parallel to vortex street motion
y	coordinate normal to vortex street motion
β_∞	free-stream relative flow angle
β_{inst}	instantaneous relative flow angle
Γ	vortex strength

Subscripts

lower	lower row of vortices
upper	upper row of vortices

Superscripts

'	reference frame moving with vortices with origin at vortex street centerline
"	reference frame moving with vortices with origin at center of vortex rows

1 Introduction

The basic unsteady flow phenomena inherent in turbomachine blade rows are, at present, generally detrimental to both aerodynamic efficiency and durability (Mikolajczak 1976). To eliminate these detrimental effects in advanced high performance component designs, fundamental time-variant flow data are required. The acquisition and analysis of such data has only recently become possible with the development and availability of high-response transducers and computer controlled digital data acquisition and analysis systems.

The time-variant data of interest in turbomachines are typically periodic, being generated at rotor blade passing frequency. Hence, a digital ensemble averaging technique based on the signal enhancement concept of Gostelow (1977) is used for data acquisition and analysis (e.g., Rothrock et al. 1982, Capece et al. 1986, Shaw et al. 1986). The key to this technique is the ability to sample data with the same data initiation reference over a time interval greater than the periodic signal characteristic time. The periodic component of the time-variant signal is determined by averaging a series of corresponding digitized signals with the same data initiation reference, thereby eliminating any random signal components.

To demonstrate this ensemble averaging of time-variant transducer signals, the rotor blade exit flow field is measured in the Purdue University low speed research compressor with a cross hot-wire probe positioned axially midway between the rotor and stator rows at mid-stator circumferential spacing, as schematically depicted in Fig. 1. The signal from this probe is digitized and averaged over 25, 50, 75, 100 and 200 rotor revolutions to determine the rotor blade exit flow field as defined by the velocity distribution (Fig. 2). The ensemble averaging significantly reduces the random fluctuations superimposed on the periodic signal, with the time-

variant signals essentially unchanged when averaged over 75 or more rotor revolutions. It is this ensemble averaged rotor blade exit flow field which is predicted by state-of-the-art viscous flow models.

However, the acquisition and analysis of time-variant data by ensemble averaging techniques discards information describing significant unsteady flow phenomena. Figure 3 presents samples of the instantaneous cross hot-wire probe signals, which make up the ensemble averaged rotor blade exit flow field, together with the exit flow field averaged 200 times. In the free-stream region, the instantaneous signals are analogous to one another and to the ensemble averaged free-stream results, as expected. However, the instantaneous signals in the rotor blade wake region are somewhat surprising. Namely, some of these instantaneous signals are analogous to one another and to the characteristics of the ensemble averaged wake, but others differ significantly from the expected wake profile.

These differences in the instantaneous rotor blade wake region data are a result of fundamental unsteady flow phenomena which are also a source of total pressure loss, flow unsteadiness, and acoustic excitation. These unsteady flow phenomena, as well as the resulting instantaneous rotor blade wake region data, cannot be predicted by three-dimensional inviscid flow field models and are not compatible with analyses which impose steady flow boundary conditions. In addition, current flow models cannot predict the viscous flow features within blade wakes. Thus, it is important to interpret these instantaneous blade wake region data and to understand these unsteady flow phenomena.

In this paper, the unsteady flow phenomena resulting in the differences in the instantaneous rotor blade wake data are investigated and these data interpreted. This is accomplished by developing a mathematical model of the rotor blade exit flow field, with a vortex street structure for the blade wake. Predictions from this mathematical model are then utilized to interpret the instantaneous rotor blade exit flow field data and demonstrate the existence of a vortex street structure in the rotor blade wake. This wake vortex street flow structure is analogous to the unsteady flow field

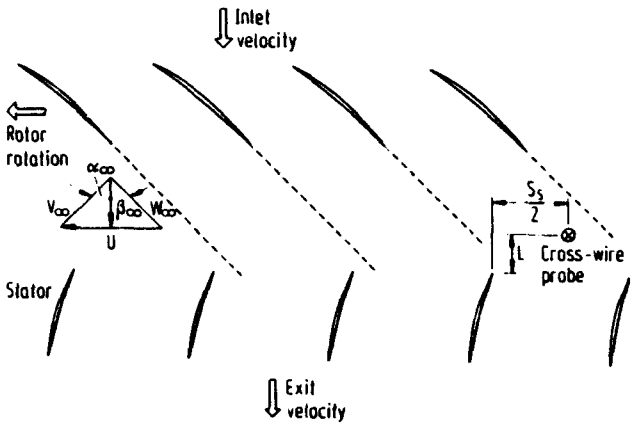

Fig. 1. Schematic of flow field

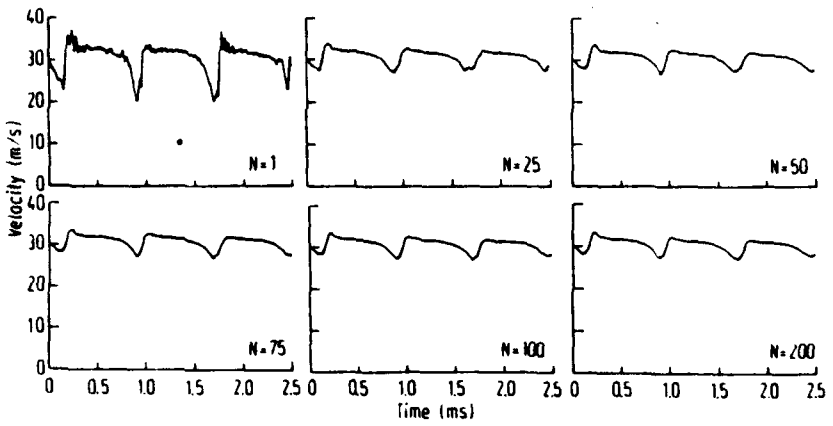

Fig. 2. Ensemble averaging of rotor exit flow field

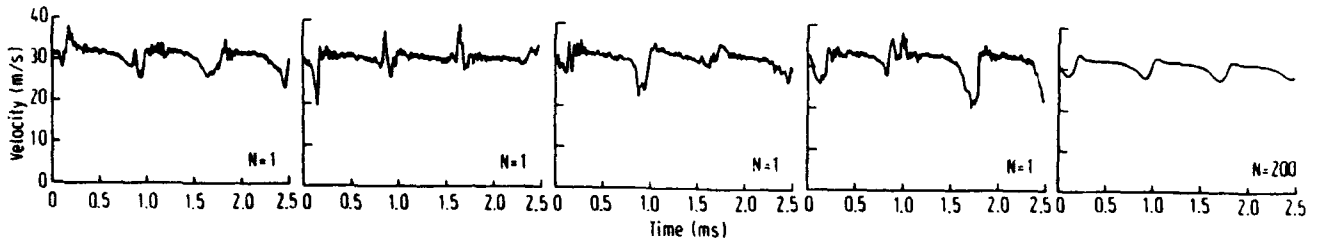

Fig. 3. Instantaneous and ensemble averaged rotor exit flow field

behind bluff bodies due to classical von Karman vortex shedding. Vortex streets have been identified in the wakes behind bluff bodies, flat plates, airfoils, and rotor blades, with the vortex shedding from airfoils with sharp trailing edges somewhat ambiguous (Hathaway et al. 1986, Heinemann and Butefish 1977, Hobbs et al. 1982, Binder et al.

2 Rotor blade wake model

2.1 Model of vortex street

To understand the basic unsteady flow features illustrated in Figs. 2 and 3, an investigation was undertaken using the rotor blade wake model proposed by Hathaway et al. (1986). Thus, only a brief description of the model is presented herein.

Figure 4 presents the two-dimensional model of the rotor blade exit flow field in the relative frame, i.e., the frame of reference fixed to the rotor blade. The free-stream region is assumed to be uniform, with the wake modeled by two rows of opposite sense vortices convected downstream with the uniform free-stream flow. These vortices are positioned such that the vortices in one row are mid-way between the vortices in the opposite row. The spacing between adjacent vortex cores is denoted by S_x, the distance between the vortex cores of the two opposing rows is S_y, with the width of the rotor blade wake denoted by S_w.

Three coordinate systems are defined in Fig. 4. The (x, y) system is fixed to the trailing edge of the rotor blade. The (x', y') coordinate system is located on the centerline between the two vortex rows and moves with the vortex cores. The (x'', y'') coordinate system also moves with the vortex cores but is fixed to the cores of the moving vortices in either row. The velocity components in these coordinate systems are denoted by (u, v), (u', v'), and (u'', v''), respectively.

The velocity components of the vortex cores have been determined by Lamb (1945) in the (x'', y'') coordinate system which moves with the vortex cores, Eq. (1).

$$u'' = \frac{-\Gamma}{2S_x} \frac{\sinh\left(2\pi\frac{y''}{S_x}\right)}{\cosh\left(2\pi\frac{y''}{S_x}\right)-\cos\left(2\pi\frac{x''}{S_x}\right)} \tag{1a}$$

$$v'' = \frac{\Gamma}{2S_x} \frac{\sin\left(2\pi\frac{x''}{S_x}\right)}{\cosh\left(2\pi\frac{y''}{S_x}\right)-\cos\left(2\pi\frac{x''}{S_x}\right)} \tag{1b}$$

where Γ is the vortex strength.

The vortices are assumed to have continuous velocity distributions. Thus, the singularity at the vortex center must be removed. This is accomplished by assuming a forced vortex motion, subtracting the contribution of an isolated free vortex, and adding the contribution of an isolated forced vortex. Thus, the velocities in the (x'', y'') reference frame are determined by summing the contributions from the upper $(\Gamma<0)$ and the lower $(\Gamma>0)$ rows of vortices, taking into account the singularity at the center of the vortex.

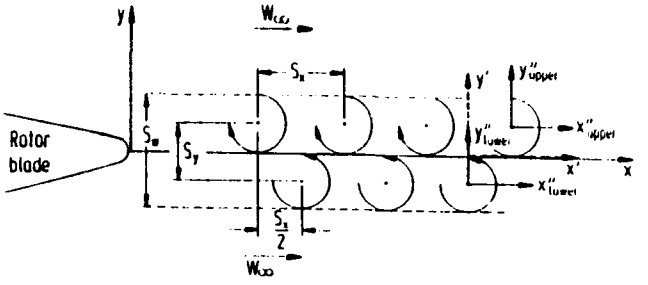

Fig. 4. Geometry of rotor blade exit flow field vortex model

2.2 Vortex street relative to rotor

Equation (1) defines the vortex street in a coordinate system moving with the vortex cores in (x'', y'') coordinates. It is necessary to transform this vortex street to the (x', y') coordinate system which is located on the centerline between the two vortex rows and moves with the vortex cores.

The induced velocity of the vortex system which is comprised of the two opposing rows of vortices, with strengths $+\Gamma$ and $-\Gamma$ for the lower and upper rows, respectively, in the (x', y') coordinate system moving with the vortex cores, is given in Eq. (2).

$$W_i = \frac{-\Gamma}{2S_x} \tanh\left(\pi\frac{S_y}{S_x}\right) \tag{2}$$

In the relative frame of reference of the rotor blades, the (x, y) coordinate system, the vortex street moves with velocity W_x.

$$W_x = W_i + W_{x_\infty} \tag{3}$$

where W_{x_∞} is the free-stream velocity in the relative frame of reference.

Thus, the coordinate transformation from the (x'', y'') coordinates to the (x', y') system is determined by adding the induced velocity given in Eq. (2) to the u'' velocity component in the (x'', y'') system.

2.3 Transformation to rotor reference frame

To interpret the unsteady flow phenomena which generate the differences in the instantaneous rotor blade wake data, the trajectory of the cross hot-wire probe through the moving vortex street is considered, i.e., the instantaneous position of the cross hot-wire probe as it traverses the vortex street is determined. This is accomplished by transforming the probe from the absolute frame of reference to the (x, y) rotor relative coordinate system and accounting for the convection of the vortices and the wheel speed of the rotor blades.

The (x', y') coordinate system is convecting at a velocity W_x relative to the rotor blades, with the time to convect one vortex core spaning proportional to the vortex spacing divided by this convection velocity. Because the starting position of the vortices is unknown, a random value of x'/S_x between 0.0 and 1.0 is utilized to initiate the prediction of the instantaneous position of the vortices. From the initial x'/S_x value, all subsequent positions are determined through use of the convection time and a time increment. The initial y'/S_x position is taken as one-half the wake width, $-S_y/S_x$, with all subsequent positions determined from the trajectory of the probe position in the relative frame.

2.4 *Solution procedure*

With the initial x'/S_x and y'/S_x positions specified, the coordinate transformations in the (x'', y'') reference frame are resolved. These velocities are then transformed to the (x', y') reference frame and then to the rotor relative reference frame. Finally the instantaneous relative velocity and flow angle are calculated.

$$W = \sqrt{u^2 + v^2} \tag{4a}$$

$$\beta_{\text{inst}} = \tan^{-1}\left[\frac{v}{u}\right]$$

2.5 *Rotor exit flow field in absolute coordinates*

The instantaneous rotor exit relative velocities are transformed to the absolute frame of reference by considering the velocity triangles depicted in Fig. 1. Using the relative velocity and flow angle, Eq. (15), together with the free-stream averaged relative exit flow angle, β_{2_∞}, the instantaneous relative exit flow angle is determined, Eq. (5). This is used to transform the velocities and flow angles from the relative to the absolute reference frame.

$$\beta = \beta_{2_\infty} + \beta_{\text{inst}} \tag{5}$$

This rotor blade wake model is quite general. To utilize this model to interpret the instantaneous rotor blade exit flow field data, the vortex geometry and strength must be specified. The geometric parameters are the vortex core radius ratio, r_0/S_y, the vortex spacing ratio, S_y/S_x, and the width of the wake, S_w, with the vortex strength given by $\Gamma/2\pi S_x W_{x_2}$.

2.6 *Vortex geometry for research compressor*

To apply this vortex street wake model to the rotor blade exit flow field data obtained in the Purdue University Research Compressor, the vortex geometry and strength are specified as follows. The vortex vertical spacing, S_y, is taken to be one-half the wake width, S_w. The vortex vertical spacing is adjusted such that the predicted ensemble averaged rotor blade wake has the same width as the measured wake. The vortex strength, $\Gamma/2\pi S_x W_{x_2}$, and the vortex spacing ratio, S_y/S_x, are determined by the deficit of the ensemble averaged rotor blade wake and the probability density distributions.

Table 1. Rotor blade vortex street parameters

Spacing ratio (S_y/S_x)	0.70
Core-radius ratio (r_0/S_y)	0.50
Vortex strength $\left(\frac{\Gamma}{2\pi S_x W_{x_2}}\right)$	0.06
Induced velocity ratio $\left(\frac{W_i}{W_{x_2}}\right)$	0.18
Wake width ratio (S_w/S_x)	1.40

A study of these key parameters revealed that increasing S_y/S_x decreases the width of the probability density distributions and increases the number of velocity measurements, while increasing the vortex strength increases the width of the probability density distributions and decreases the number of velocity measurements per bin. For this investigation, the vortex strength is taken to be 0.06 and the spacing ratio 0.70. The parameters for the vortex model are summarized in Table 1.

3 Results

The instantaneous rotor blade exit flow field data previously presented in Fig. 3, are now interpreted with this rotor blade vortex wake model. This is accomplished by correlating predictions of both the ensemble averaged and instantaneous rotor blade exit flow fields as well as the velocity probability density distributions from this vortex wake flow field model with the corresponding data.

The instantaneous data are acquired by sampling and digitizing the time-variant hot-wire signals with the same data initiation reference. This sampling and digitizing measurement technique is simulated in the vortex model through the use of a random number generator to establish the instantaneous position of the vortices at the start of each sampling. For both the data and the mathematical model, a series of corresponding digitized signals is generated by repeating this signal sampling process, with the ensemble averaged rotor blade exit flow field then determined by averaging this series of digital data samples.

Figure 5 presents both the predicted and the measured rotor blade exit flow field after 200 averages. The correlation of the velocity field is very good. The predicted velocity distribution is symmetric while the data are not due to the steady loading on the rotor blades, with the predicted velocity deficit somewhat less than that measured. The flow angle distribution correlation is excellent.

Samples of the instantaneous rotor blade exit flow field predicted by the vortex wake model are presented in Fig. 6. The predictions exhibit many of the instantaneous flow features previously noted in the data presented in Fig. 3. In the

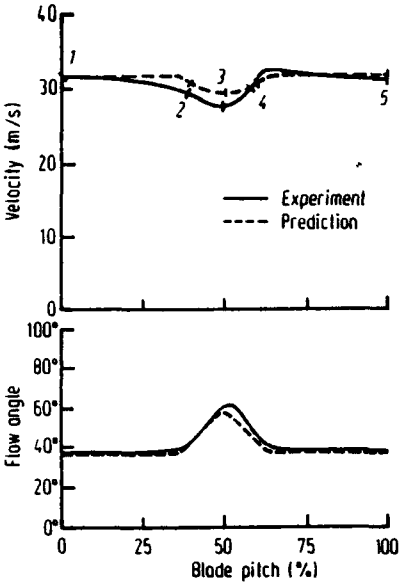

Fig. 5. Correlation of predicted and measured ensemble averaged rotor exit flow field

free-stream region, the instantaneous data are similar to one another and to the ensemble averaged free-stream results. However, in the wake region, some of the instantaneous signals are similar to one another and to the ensemble averaged wake, but others differ significantly. Thus, these variations in the data, as well as in the predictions, are a result of the vortex street structure of the rotor blade wake.

The velocity probability density distributions for the ensemble averaged measured and predicted rotor blade exit flow fields are investigated at five exit flow field positions. As indicated schematically in Fig. 5, positions 1 and 5 are on opposite sides of the wake in the free-stream region, positions 2 and 4 are on the two wake edges, and position 3 is at the center of the wake. The velocity probability density distributions are constructed with 0.5 m/s bins, and are presented in Figs. 7–9, with the center velocity of each bin as the ordinate and the number of velocity measurements which occur within a velocity bin as the abscissa.

The probability density distributions determined from the data in the free-stream, on the wake edges, and on the centerline of the wake are presented in Figs. 7–9, respectively. In the free-stream region outside of the wake, these distri-

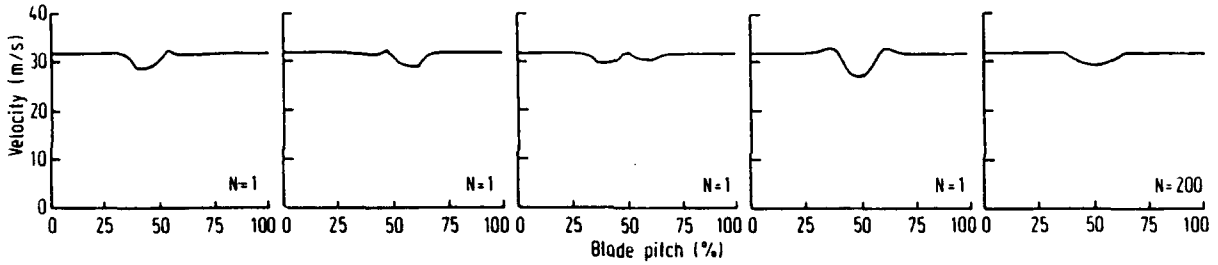

Fig. 6. Predicted instantaneous and ensemble averaged rotor exit flow field velocities

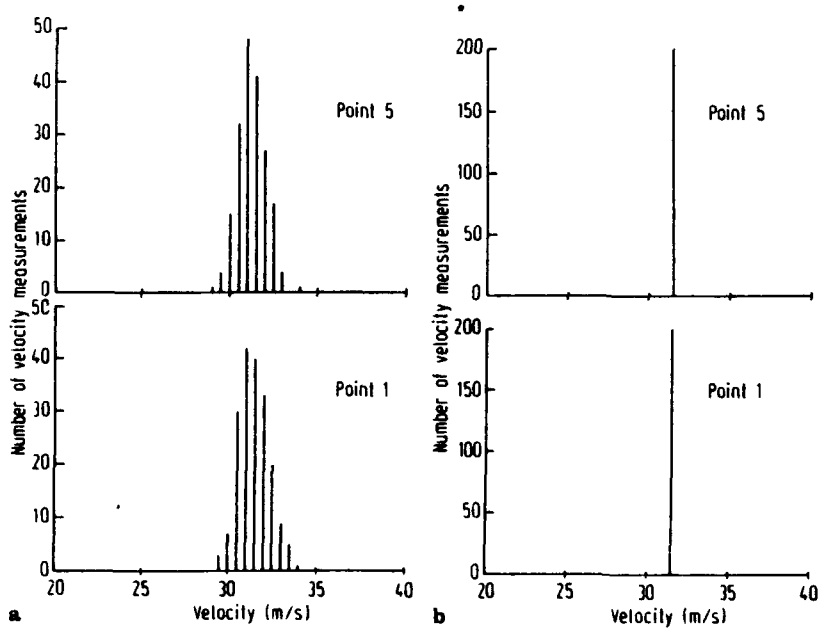

Fig. 7 a and b. Free stream region a measured and b predicted velocity probability density distributions

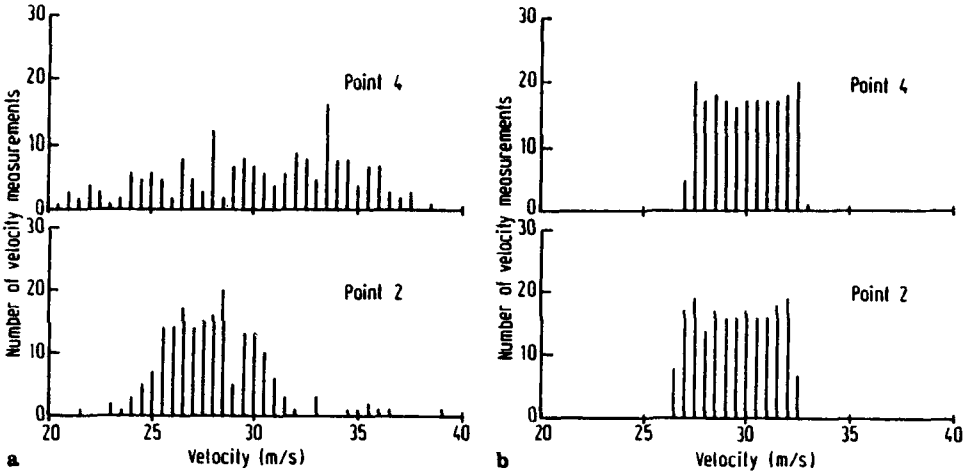

Fig. 8a and b. Wake edge region **a** measured and **b** predicted velocity probability density distributions

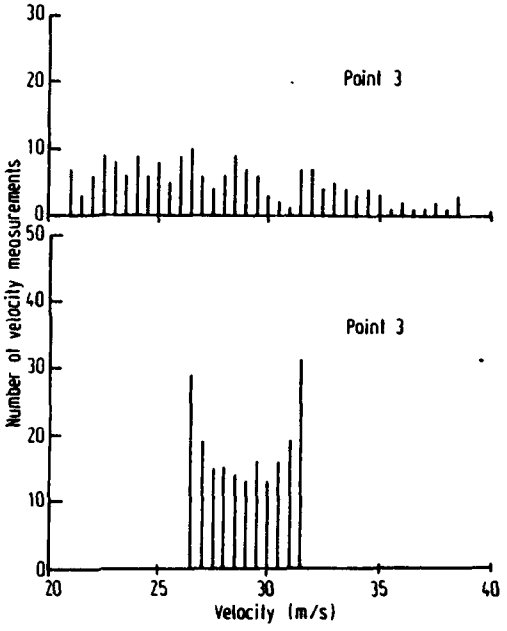

Fig. 9a and b. Wake centerline **a** measured and **b** predicted velocity probability density distributions

butions are single valued, with the most probable velocity occurring in the bin centered at 31 m/s. On the edges of the wakes, the probability density distributions exhibit a broad range of velocities with the two most probable velocities indicated. At the wake centerline, a still broader range of velocities are found, although the most probable velocities are not clearly apparent.

The analogous wake vortex model predicted free-stream, wake edge, and wake centerline probability density distributions are also presented in Figs. 7–9. These distributions exhibit the same trends as those determined from the data. In particular, the free-stream distributions are single valued and the wake edge and centerline distributions broader, with the two most probable velocities indicated not only on the wake edges but also on the centerline of the wake.

4 Summary and conclusions

Unsteady flow phenomena which are a source of total pressure loss, flow unsteadiness, and acoustic excitation, result in significant differences in the instantaneous rotor blade wake region data. These differences have been investigated and the data interpreted. This was accomplished by: (1) developing a mathematical model of the rotor blade exit flow field based on a vortex street structure for the wake which is analogous to the unsteady flow field behind bluff bodies due to classical von Karman vortex shedding; and (2) correlating predictions of both the ensemble averaged and instantaneous rotor blade exit flow fields as well as the velocity probability density distributions from this vortex flow field model with the corresponding data.

Correlation of the ensemble averaged predicted and measured rotor blade exit flow fields was very good and the flow angle distribution correlation excellent. The instantaneous rotor blade exit flow field predicted by the vortex wake model was shown to exhibit many of the instantaneous flow features previously noted in the data. Namely, some of these instantaneous results were analogous to one another and to the characteristics of the ensemble averaged wake, but others differed significantly from the averaged wake profile.

Probability density distributions from both the data and the vortex wake flow field model were also investigated in the free-stream, on the wake edges, and on the centerline of the wake. The vortex wake model distributions exhibit the same trends as those determined from the data. In the free-stream region outside of the wake, these distributions are single valued. On the edges of the wakes, the probability density distributions exhibit a broad range of velocities with the two most probable velocities indicated. At the wake

centerline a still broader range of velocities is found, with the model distributions indicating a dual peak but the probable velocities from the data are not clearly apparent.

Thus, it is concluded that the variations in the instantaneous data in the wake region are a result of the vortex street structure of the rotor blade wake.

Acknowledgements

Support of this experimental research program by the Air Force Office of Scientific Research, Dr. J. Wilson program manager, is gratefully acknowledged.

References

1. Binder, A.; Forster, W.; Mach, K.; Rogge, H. 1986: Unsteady flow interaction caused by stator secondary vortices in a turbine rotor. ASME pap. 86-GT-302
2. Capece, V. R.; Manwaring, S. R.; Fleeter, S. 1986: Unsteady blade row interactions in a multi-stage compressor. AIAA J. Propulsion Power 2, 168–174
3. Gostelow, J. P. 1977: A new approach to the experimental study of turbomachinery flow phenomena. ASMA J. Eng. Power 99, 97–105
4. Hathaway, M. D.; Gertz, J.; Epstein, A.; Strazisar, A. J. 1986: Rotor wake characteristics of a transonic axial flow fan. AIAA J. 24, 1802–1810
5. Heinemann, H. J.; Butefisch, K. A. 1977: Determination of the vortex shedding frequency of cascades with different trailing edge thicknesses. AGARD CP-277, pp. 35-1 to 35-10
6. Hobbs, D. E.; Wagner, J. H.; Dannenhoffer, J. F.; Al Dring, R. P. 1982: Experimental investigation of compressor cascade wakes. ASME pap. 82-GT-299
7. Lamb, H. L. 1945: Hydrodynamics, pp. 224–229. New York: Dover
8. Mikolajczak, A. A. 1976: The practical importance of unsteady flow. AGARD-CP-177
9. Rothrock, M. D.; Jay, R. L.; Riffel, R. E. 1982: Time-variant aerodynamics of high turning blade elements. ASME J. Eng. Power 104, 412–419
10. Shaw, L. M.; Boldman, D. R.; Buggele, A. E.; Buffum, D. H. 1986: Unsteady pressure measurements on a biconvex airfoil in a transonic oscillating cascade. ASME J. Eng. Gas Turbines Power 108, 53–59

Received March 1, 1988

APPENDIX II

Experimental Investigation of Multistage Interaction Gust Aerodynamics

ASME Journal of Turbomachinery

Experimental Investigation of Multistage Interaction Gust Aerodynamics

V. R. Capece[1]

S. Fleeter

Thermal Sciences and Propulsion Center,
School of Mechanical Engineering,
Purdue University,
West Lafayette, IN 47907

The fundamental flow physics of multistage blade row interactions are experimentally investigated at realistic reduced frequency values. Unique data are obtained that describe the fundamental unsteady aerodynamic interaction phenomena on the stator vanes of a three-stage axial flow research compressor. In these experiments, the effect on vane row unsteady aerodynamics of the following are investigated and quantified: (1) steady vane aerodynamic loading; (2) aerodynamic forcing function waveform, including both the chordwise and transverse gust components; (3) solidity; (4) potential interactions; and (5) isolated airfoil steady flow separation.

Introduction

Airfoil rows of advanced gas turbine engines are susceptible to destructive aerodynamically induced vibrational responses, with upstream blade and vane wakes the most common excitation source. For example, in the single-stage compressor flow field schematically depicted in Fig. 1, the rotor wake velocity deficits appear as a temporally varying excitation source to a coordinate system fixed to the downstream stator vanes, i.e., the rotor blade wakes are the forcing function to the downstream stator vanes. Also as shown, the reduction of the rotor relative velocity causes a decrease in the absolute velocity and increases the incidence to the stator vanes. This produces a fluctuating aerodynamic lift and moment on the vanes, which can result in high vibratory stress and high cycle fatigue failure.

First-principle forced response predictive techniques require a definition of the unsteady forcing function in terms of harmonics. The total response of the airfoil to each harmonic is then assumed to be comprised of two parts. One is due to the disturbance being swept past nonresponding airfoils. The second arises when the airfoils respond to the forcing function. A gust analysis predicts the unsteady aerodynamics of the nonresponding airfoils, with a harmonically oscillating airfoil analysis used to predict the additional motion-induced unsteady aerodynamics.

Both gust and harmonically oscillating unsteady aerodynamic models are being developed (e.g., Fleeter, 1973; Verdon and Caspar, 1981; Englert, 1982; Atassi, 1984; Chiang and Fleeter, 1988). Within these models are many numerical, analytical, and physical assumptions. Unfortunately, there is only a limited quantity of high reduced frequency data appropriate for model verification and direction.

Carta and St. Hilaire (1979) and Carta (1982) measured the surface chordwise unsteady pressure distribution on an harmonically oscillating cascade in a linear wind tunnel. This work was extended by Hardin et al. (1987) to an isolated rotor with oscillating blades. In addition, inlet distortion generated gust response unsteady aerodynamics were also studied. Although the interblade phase angles in these experiments were within the range found in turbomachines, the reduced frequencies, less than 0.4, were low for forced response unsteady aerodyanmics found in the mid and aft stages of multistage turbomachines where the reduced frequency is typically greater than 2.0. Fleeter et al. (1978, 1980, 1981) investigated the effects of airfoil profile and rotor-stator axial

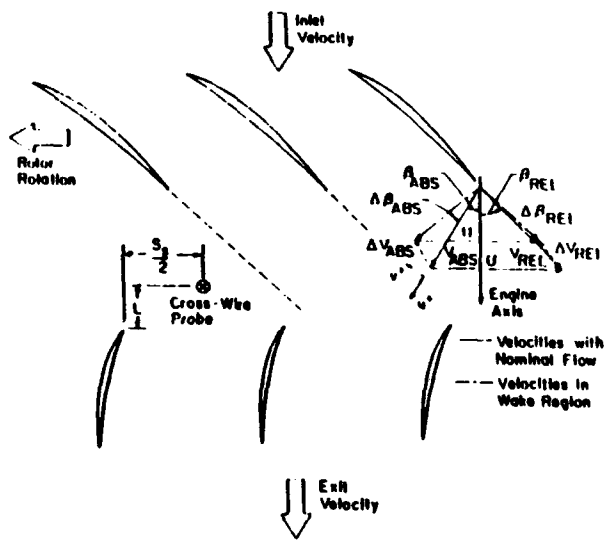

Fig. 1 Single-stage compressor flow field

[1] Currently at Pratt & Whitney Engineering Division South.

Contributed by the International Gas Turbine Institute and presented at the 33rd International Gas Turbine and Aeroengine Congress and Exhibition, Amsterdam, The Netherlands, June 5-9, 1988. Manuscript received at ASME Headquarters February 11, 1988. Paper No. 88-GT-56.

Table 1 Overall compressor and airfoil characteristics

	ROTOR	STATOR
Airfoil Type	C4	C4
Number of Airfoils	43	41
Chord, C (mm)	30	30
Solidity, C/S	1.14	1.09
Camber, θ	27.95	27.70
Stagger Angle, λ	38	-38.1
Aspect Ratio	2.0	2.0
Thickness/Chord (%)	10	10
Axial Gap (cm)	1.27	
Flow Rate (kg/s)	2.68	
Design Axial Velocity (m/s)	32.0	
Rotational Speed (RPM)	3000	
Number of Stages	3	
Stage Pressure Ratio	1.003	
Inlet Tip Diameter (mm)	420	
Hub/Tip Radius Ratio	0.714	
Stage Efficiency (%)	85	

spacing on the transverse gust unsteady aerodynamic response in a single-stage, low-speed research compressor at realistic values of the reduced frequency, with these data also showing the influence of the forcing function waveform.

These previous experimental investigations were performed in linear cascades, isolated rotor rows, and single-stage compressors. They did not consider the multistage and potential interaction effects that exist in the mid and aft stages of turbomachines. For multistage compressors, the unsteady aerodynamics on the first two vane rows of a three-stage low-speed research compressor were studied for the first time by Capece et al. (1986). The transverse gust forcing function and the chordwise distributions of the harmonic pressure difference coefficients on the first two vane rows were determined for a variety of geometric and compressor operating conditions. These results indicated that the unsteady aerodynamic loading of an airfoil row was related to the aerodynamic forcing function, which itself is significantly influenced by the multistage blade row interactions. This work was extended by Capece and Fleeter (1987) to include all three vane rows, with the effects of both the transverse and chordwise gust components quantified.

In this paper, the fundamental flow physics of multistage blade row interactions are experimentally investigated at realistic reduced frequency values, with unique data obtained to describe the fundamental unsteady aerodynamic phenomena on the stator vanes of a three-stage research compressor. In particular, a series of experiments are performed to investigate and quantify the effect of the following on vane row unsteady aerodynamics: (1) steady loading; (2) forcing function waveform, including both the chordwise and transverse gust components; (3) solidity; (4) potential interactions, and (5) steady flow separation.

Research Compressor and Instrumentation

The Purdue University Three-Stage Axial Flow Research Compressor is driven by a 15 hp d-c electric motor over a speed range of 300 to 3000 rpm. The three identical compressor stages consist of 43 rotor blades and 41 stator vanes, with the first-stage rotor inlet flow field controlled by variable setting angle inlet guide vanes. The free-vortex design airfoils have a British C4 section profile, a chord of 30 mm, an aspect ratio of 2, and a maximum thickness-to-chord ratio of 0.10. The overall airfoil and compressor characteristics are presented in Table 1.

The aerodynamic forcing functions to the stator rows are the upstream airfoil wakes. The first-stage vane row forcing function is varied by changing the setting angle of the inlet guide vanes, thereby altering the inlet flow to the first stage rotor (Fig. 2). This results in a change in the rotor blade exit flow field, in particular, the chordwise and transverse gust components. The second and third-stage vane row forcing function variations are accomplished by independently circumferentially indexing the upstream vane rows relative to one another, as also depicted.

The stator vane forcing function is quantified by measuring the stator inlet time-variant velocity and flow angle with a cross-wire probe located midway between rotor and stator at midstator circumferential spacing (Fig. 1). The rotor mean absolute exit flow angle is determined by rotating the probe until a zero voltage difference is obtained between the two hot-wire channels. This mean angle is then used as a reference for calculating the instantaneous absolute and relative flow angles and defines the vane steady incidence angle. From the instantaneous velocity triangles, the individual fluctuating velocity components parallel and normal to the mean flow, the aerodynamic gust components, are calculated. The accuracy of the velocity magnitude and angle are ±4 percent and ±2 deg, respectively.

The steady and unsteady aerodynamic loading on the vane surfaces are measured with chordwise distributions of midspan surface pressure taps and tranducers. Flow visualization along this streamline shows the flow to be two dimensional for the operating conditions of this investigation. A

Nomenclature

C = vane chord

$\hat{C}_l$ = steady lift coefficient $= \int_0^C (\hat{p}_p - \hat{p}_s)dx \Big/ \frac{1}{2}\rho U_t^2 C$

C_p = first harmonic dynamic pressure coefficient $= \Delta\hat{p}/\rho V_x \hat{v}^+$

$\hat{C}_p$ = static pressure coefficient $= (\hat{p} - \hat{p}_{exit}) \Big/ \frac{1}{2}\rho U_t^2$

i = incidence angle

k = reduced frequency $= \omega C/2V_x$

$\hat{p}$ = stator surface static pressure

$\hat{p}_{exit}$ = stator exit static pressure

$\Delta\hat{p}$ = first harmonic dynamic pressure difference

u^+ = instantaneous chordwise gust component

$\hat{u}^+$ = first harmonic chordwise gust

U_t = blade tip speed

v^+ = instantaneous transverse gust component

$\hat{v}^+$ = first harmonic transverse gust

V_x = absolute axial velocity

δ = solidity

ω = blade passing frequency

reverse transducer mounting technique is utilized to minimize disturbances, with the transducer connected to the measurement surface by a pressure tap. Static and dynamic calibrations of the embedded transducers demonstrate no hysteresis, with the mounting method not affecting the frequency response. The accuracy of the unsteady pressure measurements is ±3.5 percent.

Data Acquisition and Analysis

The steady-state data define the steady aerodynamic loading on the vane surfaces and the compressor operating point. A root-mean-square error analysis is performed, with the steady data defined as the mean of 30 samples and their 95 percent confidence intervals determined. The detailed steady loading on the vanes is defined by the chordwise distribution of the vane surface steady static pressure coefficient $\bar{C}_p$, with the overall loading level specified by the incidence angle i and the steady lift coefficient $\bar{C}_l$.

The time-variant data quantify the aerodynamic forcing function and the resulting unsteady pressure difference on the stator vanes, and are analyzed by means of a data-averaging or signal enhancement concept, as proposed by Gostelow (1977). The key to this technique is the sampling of data at a preset time, which is accomplished with a shaft-mounted optical encoder. At a steady-state operating point, an averaged time-variant data set consisting of the two hot-wire and the vane-mounted transducer signals, digitized at a rate of 200 kHz and averaged over 200 rotor revolutions, is obtained. Each is Fourier decomposed into harmonics by means of a Fast Fourier Transform algorithm, with the magnitude and phase angle of the first harmonic referenced to the data initiation pulse determined. Analyzing the data in this form was found to be equivalent to averaging the Fourier transforms for each rotor revolution. Also, ensemble averaging and then Fourier decomposing of the signal is used because it significantly reduces the data storage requirements.

The rotor and stator spacing, the axial spacing between the vane leading edge plane and the probe, and the absolute and relative flow angles are known. To time relate the hot wire and vane surface unsteady pressure signals, the rotor exit velocity triangles are examined and the following asumptions made: (1) The wakes are identical at the hot wire and stator leading edge planes, and (2) the wakes are fixed in the relative frame. The wakes are located relative to the hot wires and the leading edges of the instrumented vanes and the times at which the wakes are present at various locations determined. The incremented times between occurrences at the hot wire and the vane leading edge planes are then related to phase differences between unsteady velocities and the vane surfaces. These assumptions are necessary in order to correlate the data with a gust analysis, which fixes the gust at the airfoil leading edge. The hot wire was located approximately midway between the rotor and stator and was less than 25 percent of the stator chord upstream of its leading edge.

In final form, the detailed waveform of the aerodynamic forcing function is specified by the first harmonics of the chordwise and transverse gust components, $\hat{u}^+$ and $\hat{v}^+$, respectively. The unsteady pressure data describe the chordwise variation of the first harmonic pressure difference across a stator vane, presented as a dynamic pressure difference coefficient magnitude and phase. As a reference, these data are correlated with predictions from Fleeter (1973). This gust analysis assumes the flow to be inviscid, irrotational, two dimensional, and compressible. Small unsteady transverse velocity perturbations, v^+, are assumed to be convected with the uniform flow past a cascade of flat plate airfoils. The parameters modeled include the cascade solidity, stagger angle, inlet Mach number, reduced frequency, and the interblade phase angle. The analysis does not consider flow separation or chordwise gust perturbations u^+.

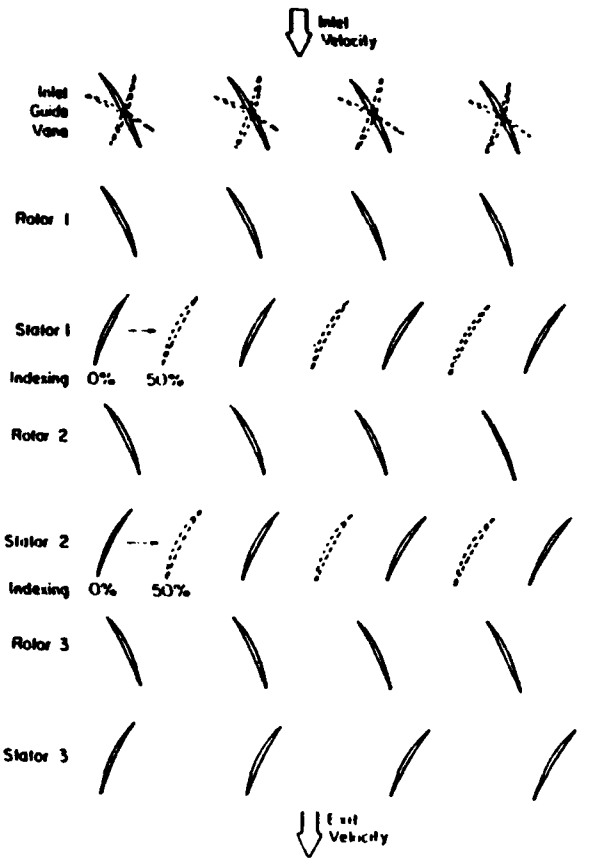

Fig. 2 Compressor geometry variations to alter forcing function

Results

Three stator vane solidities are investigated: the design value of 1.09; a reduced value of 0.545; and 0.10, which results in a spacing between vanes large enough so that the influence of neighboring vanes is negligible; i.e., each vane is an isolated airfoil. The results are presented for each solidity for variations in one of the key parameters. All design solidity data, except for the potential interaction effects, are presented for the first stator vane row. The data sets for the other solidities are presented for the third stator vane row. Since there are no airfoil rows downstream of the third stage vane row, there are no potential interaction effects on the trailing edge region of these vanes. Data from Capece and Fleeter (1987) have been added for the design solidity in order to have a complete presentation of the results and to indicate the significant effects that solidity has on the unsteady aerodynamic response of the stator vanes. Also, the error in the static pressure coefficient data is represented by the symbol size.

Vane Steady Loading

Steady aerodynamic loading effects are considered for the design and reduced solidities of 1.09 and 0.545. The first harmonics of the forcing function are maintained nearly constant (Fig. 3). Note that relative to the absolute velocity, the instantaneous gust components are not small. For example, the instantaneous transverse and chordwise gust components are approximately 40 and 25 percent of the absolute velocity at −5.9 deg of incidence. However, in terms of the first harmonics these gust components are approximately 11 and 6 percent of the absolute velocity.

Fig. 3 Aerodynamic forcing functions for steady loading study

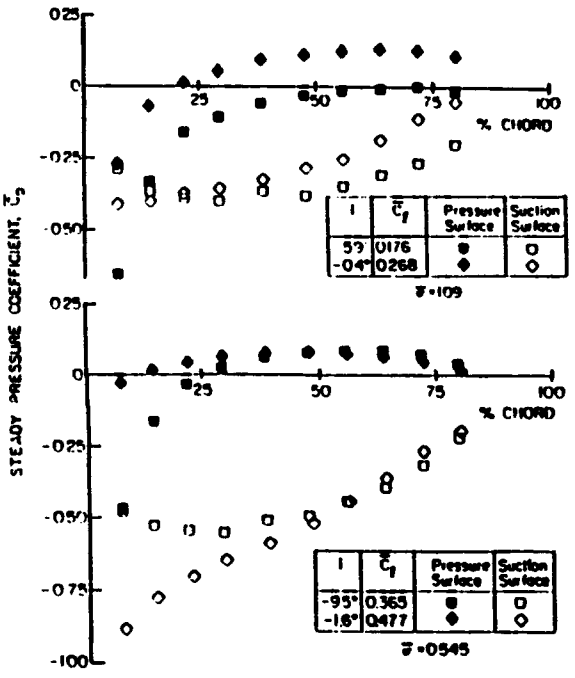

Fig. 4 Vane static pressure distributions for steady loading study

For each solidity, the vane surface steady pressure distributions are smooth and show no indication of flow separation (Fig. 4). At the design solidity, the surface static pressures for the lift coefficient of 0.268 are greater than those for the lift coefficient of 0.176, a result of the inlet guide vane indexing altering the compressor operating point. Also, the reduced solidity has much higher pressure differences and steady lift coefficients due to the decreased number of vanes.

The resulting chordwise distributions of the dynamic pressure difference coefficient and the predictions are shown in Fig. 5. At the design solidity, good correlation exists between the magnitude data and the prediction for the lift coefficient of 0.176, with an increase in lift to 0.268 resulting in poorer correlation. The higher loading data are decreased in amplitude relative to both the prediction and the lower loading data over the front 25 percent of the vane. Aft of 25 percent chord, the data correlate well with each other and the prediction until 63 percent chord, with both data sets then increasing to a larger value than the prediction.

The phase data exhibit a somewhat different chordwise

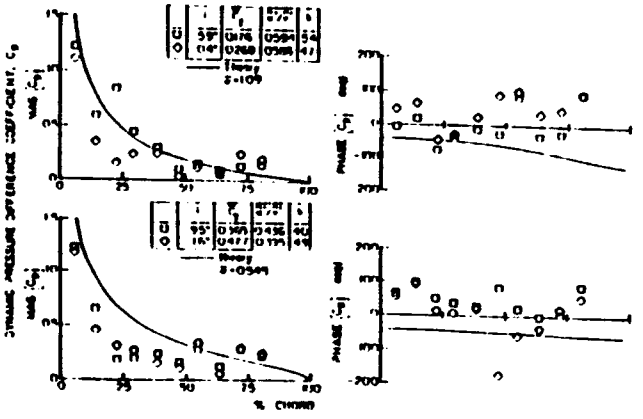

Fig. 5 Effect of steady loading on the complex unsteady pressure coefficient

distribution than the prediction. In particular, the phase data are increased relative to the prediction over the first 14 percent of vane chord. The data then decrease to the level of the prediction and then increase to values greater than the prediction with increasing chordwise position. The phase data for both loading levels exhibit the same trends, with the higher loading data increased relative to both the prediction and the lower loading data over most of the chord. The differences between the phase data and the prediction are attributed to the vane camber and the detailed steady loading distributions on the vane surfaces.

The magnitude data for the reduced solidity are also decreased relative to the prediction over the front 50 percent of the vane, with the higher loading data having, in general, a decreased amplitude relative to the lower loading data. The decrease in amplitude relative to the prediction is due to the high levels of steady aerodynamic loading. Aft of 50 percent chord, the magnitude data increase to the level of the prediction and show better correlation. The phase data increase to a level larger than the prediction over the front 14 percent of the vane, then decrease toward the prediction, and from approximately 25 to 50 percent chord, the phase data are almost constant. Aft of 50 percent chord this trend changes, with the higher loading data decreased relative to both the lower loading data and the prediction, and then increasing as the chordwise position increases. Thus, from these results it is evident that steady loading primarily affects the magnitude of the dynamic pressure difference coefficient.

The best correlation of the dynamic pressure difference coefficient data and the prediction is obtained at the low level of steady loading at the design solidity, as expected, since this most closely approximates the unloaded flat plate cascade model. Also, the steady loading level and distribution have a significant effect on the unsteady aerodynamics of the vane row. In general, different airfoil designs will produce different steady surface pressure distributions and steady lift for the same incidence angle. Therefore, the level of steady aerodynamic loading, not the incidence angle, is the key parameter in obtaining good correlation with mathematical models.

Aerodynamic Forcing Function

The influence of each gust component on the complex dynamic pressure coefficient, with the steady aerodynamic loading held constant, is considered.

Transverse Gust. The surface static pressure distributions for each solidity are smooth, with no evidence of separation and only small variations apparent near the leading edge, which result in the slight variations in the steady lift coeffi-

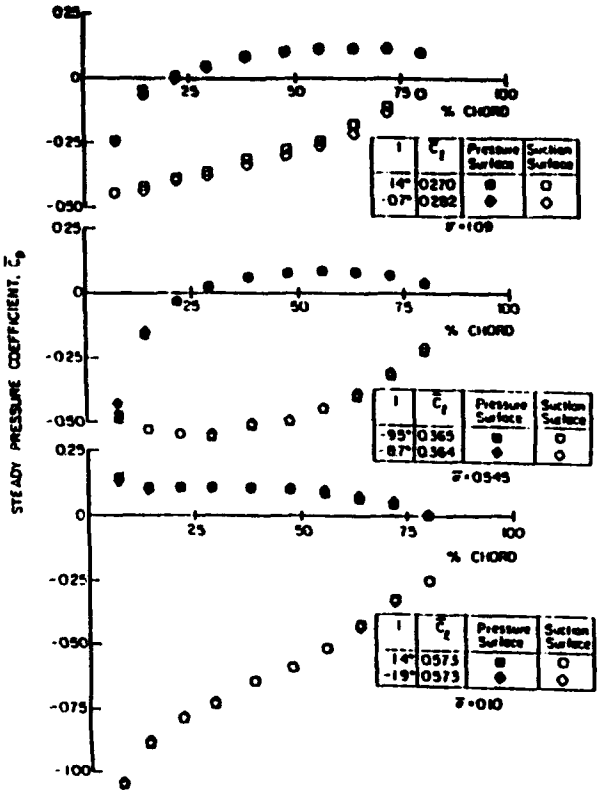

Fig. 6 Surface static pressure distributions for transverse gust study

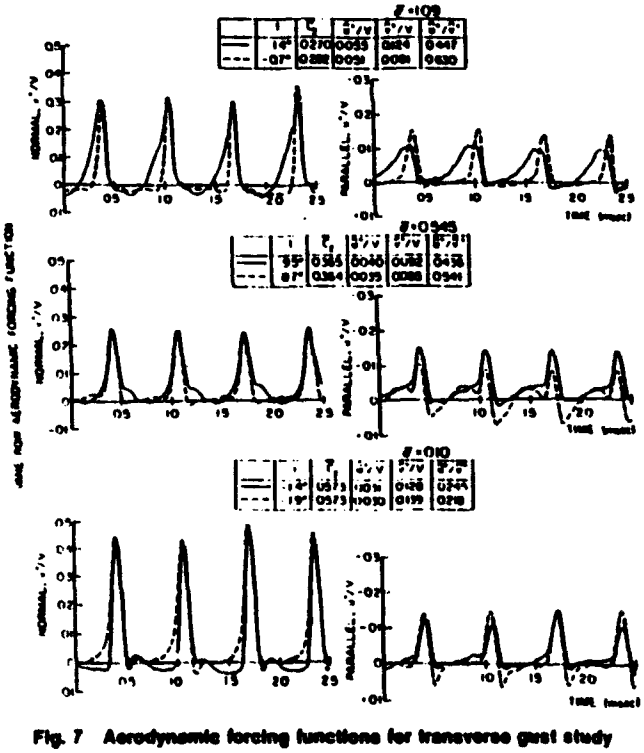

Fig. 7 Aerodynamic forcing functions for transverse gust study

cients (Fig. 6). As the solidity is decreased, there is an increase in the level of steady surface pressures and a corresponding increase in the steady lift coefficient. The chordwise gust $\hat{u}^+$ is held approximately constant while the transverse gust $\hat{v}^+$ is varied (Fig. 7), with the difference between the configurations specified by the first harmonic gust ratio $\hat{u}^+/\hat{v}^+$.

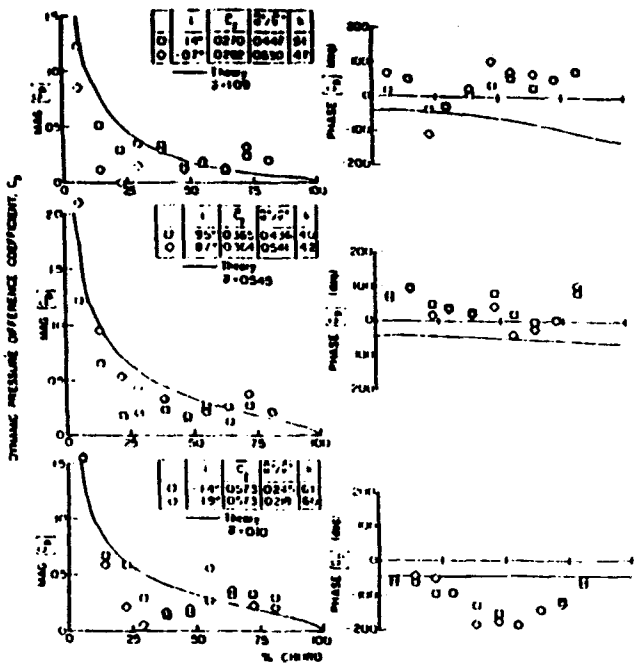

Fig. 8 Effect of transverse gust on the complex unsteady pressure coefficient

The effect of the transverse gust on the chordwise distributions of the dynamic pressure difference coefficient data is presented in Fig. 8. At the design solidity, both configurations show the magnitude data to be decreased relative to the prediction over the leading 30 percent of the vane, with the ($\hat{u}^+/\hat{v}^+$) data of 0.630 having a decreased amplitude relative to the 0.447 data. However, in the midchord region, the data for these two configurations correlate well with each other and with the prediction. As in the previous cases, aft of 70 percent chord the data increase relative to the prediction. This is a result of both the potential interaction from the downstream second-stage rotor row and the parallel gust component $\hat{u}^+$, as the design solidity data are acquired on the first stage. This phenomenon will be discussed in greater detail in the section on Potential Flow Interactions.

The reduced solidity and the isolated airfoil data show a different trend with the ratio of ($\hat{u}^+/\hat{v}^+$) than that of the design solidity, with the data for the larger values of ($\hat{u}^+/\hat{v}^+$) increased in value relative to the lower values. This is opposite to the trend noted at the design solidity. However, examination of the magnitudes of the first harmonics of the chordwise gust component $\hat{u}^+$ indicates that the magnitudes of the chordwise gust are lower in value than the design case. This indicates that the chordwise pressure distributions are not governed simply by the ratio of the two gust components but also by their magnitudes.

For each of the reduced solidity values, 0.545 and 0.10, the magnitude data are generally decreased relative to the prediction over the leading 50 percent of the vane, with the lower ($\hat{u}^+/\hat{v}^+$) data having a decreased amplitude relative to the higher ($\hat{u}^+/\hat{v}^+$) data. In the trailing edge portion of the vane, the magnitude data correlate well with each other but are increased in level relative to the prediction. This is a result of the chordwise gust, which is not considered by the model.

The design solidity phase data are increased relative to the prediction over the front 14 percent of the vane, decrease to the level of the prediction at 22 percent chord, and then increase to values greater than the prediction with increasing chordwise position, becoming nearly constant aft of 40 percent chord. At the reduced solidity, the phase data are in-

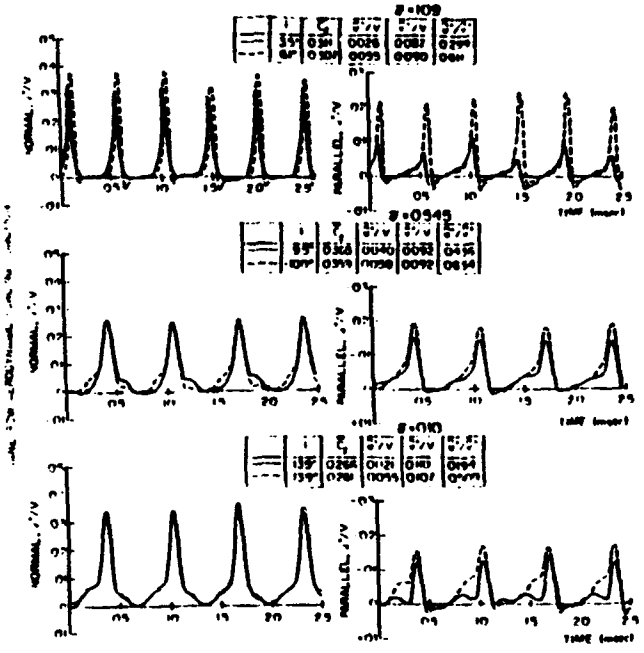

Fig. 9 Aerodynamic forcing function for chordwise gust study

creased relative to the prediction over the entire vane chord, being nearly constant in the 22 to 38 percent chord region. For the isolated airfoil, the phase data show good trendwise correlation with the prediction over the leading 29 percent of the vane, with the $(\hat{u}'/\hat{v}')$ data of 0.245 decreasing relative to both the prediction and the $(\hat{u}'/\hat{v}')$ 0.218 data. Aft of 29 percent chord, where the vane does most of its turning, the phase data decrease until 54 percent chord and then increase with increasing chordwise position.

These results show that the transverse gust primarily influences the magnitude of the dynamic pressure difference coefficient. Also, the unsteady data variations with forcing function waveform cannot be predicted by harmonic gust models. This is because the forcing function waveforms and the resulting unsteady pressure distributions have been Fourier decomposed, with the first harmonic of the unsteady data presented. Thus, all of these first harmonic data are correlated with the same prediction curve; i.e., the predictions from these harmonic gust models are identical for all of the forcing function waveforms.

Chordwise Gust. The effect of the forcing function chordwise gust component $\hat{u}'$ on the vane row unsteady aerodynamics for each solidity is considered. This is accomplished by establishing compressor configurations such that the transverse gust and the steady aerodynamic loading are nearly identical; see Figs. 9 and 10, respectively.

The resulting chordwise distributions of the dynamic pressure coefficient data and the predictions are presented in Fig. 11. In general, the magnitude data exhibit analogous trends for each solidity, decreasing over the front of the vane and increasing over the aft part. The magnitude data increase over the prediction at the design solidity, whereas they increase up to the prediction for the other two solidity values. This is again the result of the design solidity data being acquired on the first stage, with the data for the other solidities being acquired on the third stage. Also, the higher $(\hat{u}'/\hat{v}')$ data are decreased relative to both the prediction and the lower $(\hat{u}'/\hat{v})$ data for each solidity. This is particularly apparent at the design and reduced solidity.

The design solidity phase data at a $(\hat{u}'/\hat{v}')$ of 0.611 show good trendwise correlation with the prediction over the aft 50

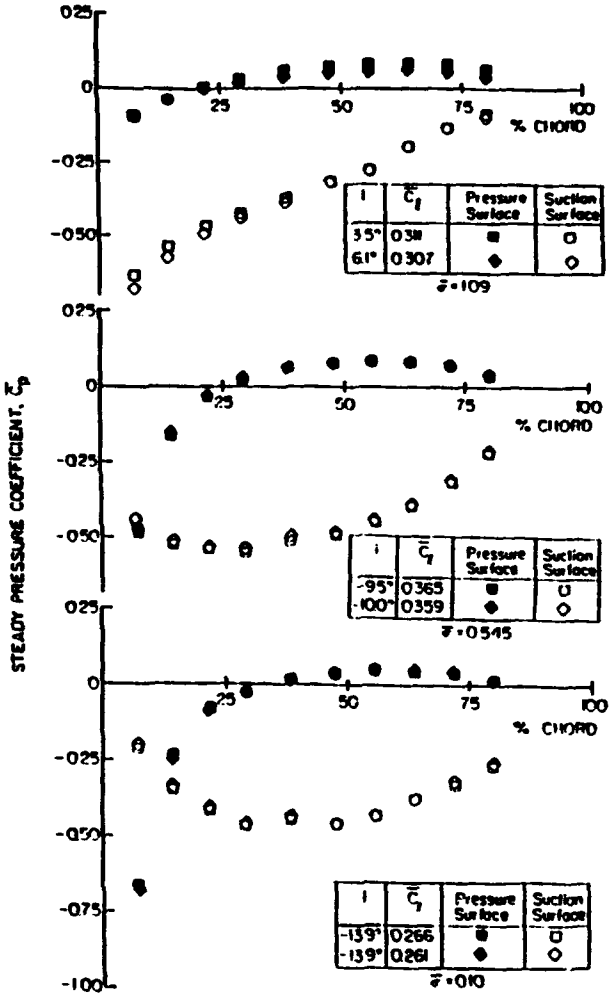

Fig. 10 Steady vane loading distributions for chordwise gust study

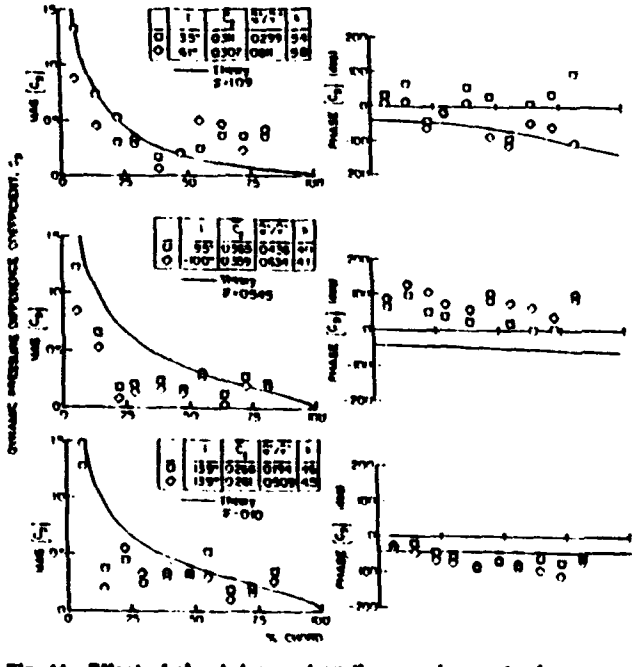

Fig. 11 Effect of chordwise gust on the complex unsteady pressure coefficient

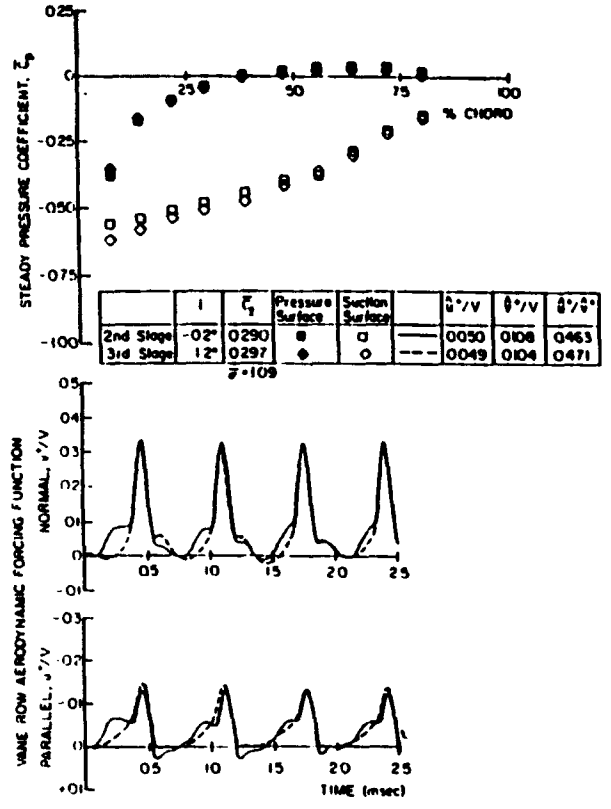

Fig. 12 Steady loading and forcing functions for potential flow interaction study

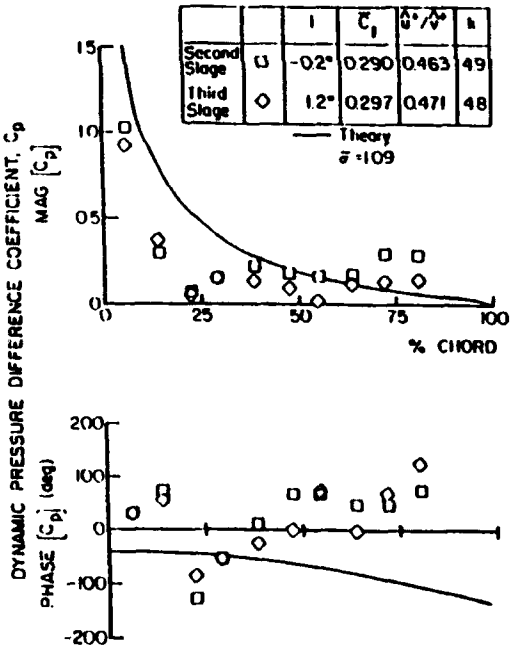

Fig. 13 Potential flow interaction effect on the complex unsteady pressure coefficient

percent of the vane while the lower ($\hat{u}^*/\hat{v}^*$) data are increased relative to the prediction, as seen in previous cases. Over the front 50 percent of the vane, the data correlate trendwise with each other but are increased compared to the prediction. The reduced solidity phase data are increased relative to the prediction and remain relatively constant over the entire vane chord, with the ($\hat{u}^*/\hat{v}^*$) phase data of 0.634 consistently increased over the ($\hat{u}^*/\hat{v}^*$) 0.436 data.

A somewhat different trend is evident in the phase data for the isolated airfoil than previous isolated airfoil cases and the other solidity values. In this case, the data are seen to correlate trendwise with the prediction over the front of the vane, then decrease slightly lower than the prediction and remain almost constant for the remainder of the vane. In addition, the phase data for these two configurations correlate quite well with one another over almost the entire vane. Comparing these results to the phase data of Fig. 8 for a ($\hat{u}^*/\hat{v}^*$) of 0.218 indicates that loading has a dramatic effect on the phase as well as the magnitude data: Both the phase and the magnitude data show the maximum deviations from the analysis in the 25 to 50 percent chord locations. Aft of this point the magnitude and phase increase to the prediction.

The differences apparent in the dynamic pressure difference coefficient phase data for the three different solidity values are a result of the details of the steady static pressure distributions and the spacing between the airfoils. As the airfoil spacing increases for low levels of aerodynamic loading, the correlation of the phase data with the predictions gets increasingly better. This indicates that the influence of adjacent airfoils is much greater than predicted by the zero incidence flat plate analysis.

Thus, both the transverse and chordwise gust components affect the magnitude data, with the chordwise gust having a larger influence on the phase, particularly at the design solidity. In addition, the magnitude of the chordwise gust is not small as compared to either the absolute velocity or the transverse gust.

Potential Flow Interactions

Data in the vane trailing edge region are consistently increased relative to the prediction. Part of this increase is attributable to the chordwise gust that is not modeled by the prediction. However, first-stage magnitude data exhibit larger deviations in the trailing edge region than third-stage data with similar steady lift coefficients. To investigate this phenomenon, unsteady data are acquired on the second and third stages at the design solidity for operating conditions where the steady loading and the forcing function are nearly identical (Fig. 12). Thus the only difference between these two configurations is the presence of the third stage downstream of the second-stage stator row.

The resulting dynamic pressure difference coefficient data and corresponding prediction are presented in Fig. 13. The magnitude data are decreased relative to the prediction over the leading 30 percent of the vane due to the steady loading level, with the deviations in the amplitude attributed to the differences in the steady surface pressure distributions in the leading edge region. Aft of 30 percent chord, the data increase to the level of the prediction, with the second-stage data higher in amplitude than the third-stage data, particularly in the trailing edge region. Since the steady pressure distributions and the forcing function are nearly identical, this deviation of the second-stage data is attributed to a potential interaction effect caused by the downstream third stage. The increase of the third-stage data above the prediction in this region is a result of the chordwise gust since there are no downstream airfoil rows, with the further increase in the second-stage data due to the potential interaction.

The phase data also show different trends in the trailing edge region due to potential interactions. Over the front part of the vane, the data are increased with respect to the prediction, but then decrease in relation to the prediction at 22 percent chord. The data then increase until 50 percent chord, with the data up to this point exhibiting good trendwise correlation. Aft of 50 percent chord the second-stage data are nearly constant with increasing chordwise position, whereas the third-

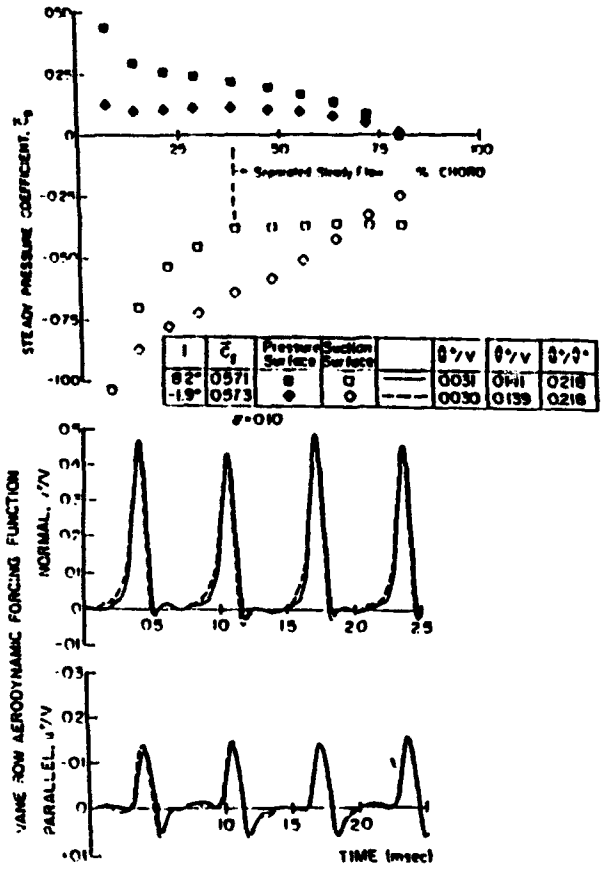

Fig. 14 Steady loading and forcing functions for isolated airfoil separated flow investigation

stage data show another decrease in phase and then increase with increasing chordwise position.

Thus, potential interaction effects influence both the magnitude and phase, with the larger effect being upon the magnitude of the dynamic pressure difference coefficient. Hence, the downstream airfoil row is another aerodynamic excitation source to the upstream blade or vane row and would act on the trailing edge region.

Isolated Airfoil Separation

The effect of separated flow on the stator vane unsteady aerodynamics for a solidity of 0.10, i.e., an isolated airfoil, is now investigated. The separated flow is generated by restaggering the stator vanes such that a mean flow incidence angle of 8.2 deg is established. At this incidence angle, the flow separates from the vane suction surface as indicated by the region of constant static pressure, which originates at 38 percent chord (Fig. 14). The separated flow data are compared with data for a configuration where the steady lift coefficient and both the chordwise and transverse gust componets are nearly identical, but the flow is not separated.

The resulting dynamic pressure difference coefficient data and the attached flow flat plate prediction are shown in Fig. 15. The attached and separated flow data show somewhat different trends in the leading and trailing edge regions. The separated flow magnitude data are nearly constant over the front 14 percent of the vane, whereas the attached flow data and prediction indicate a decrease in amplitude with increasing chordwise position. Aft of 14 percent chord the data show analogous trends, with both separated and attached flow data decreasing with increasing chordwise position and attaining a minimum amplitude value at 20 percent chord, similar to previous isolated airfoil results. The magnitude data for both

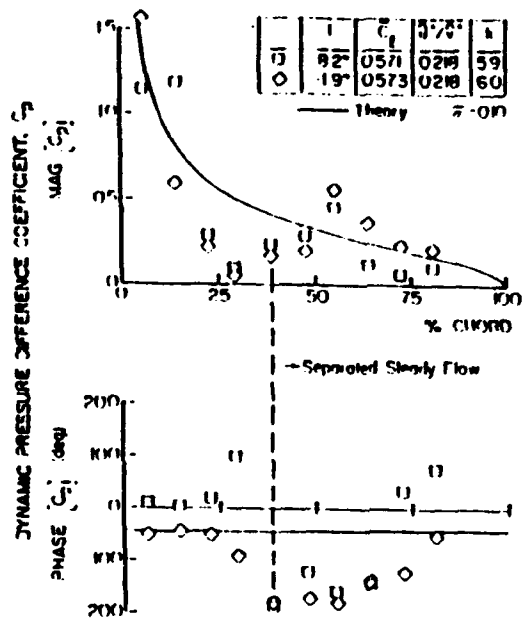

Fig. 15 Steady suction surface separation effect on the complex unsteady pressure coefficient

cases then gradually increase to values that are greater than the prediction at 54 percent chord, with the attached flow data being lower in magnitude up to this point. Both data sets then decrease with further chordwise position, with the separated data decreased in amplitude relative to both the prediction and the attached flow data. This is a result of the increased steady loading in this region of the airfoil due to the separation zone.

The attached and separated flow phase data have different trends near the separation point and in the trailing edge region. Over the front 22 percent of the vane, the data and the prediction show analogous trends, being nearly constant. The separated data are increased relative to the prediction, with the attached flow data exhibiting excellent correlation with the prediction. Aft of 22 percent chord the separated data increase, whereas the attached flow data decrease relative to the prediction. In the separated flow region, both the separated and attached flow data exhibit similar trends. However, at 70 percent chord the separated data indicate a jump to values larger than the prediction and increase with further chordwise position. On the other hand, the attached flow phase data show a gradual increase. Thus, separation affects both the magnitude and phase of the dynamic pressure difference coefficient.

Summary and Conclusions

A series of experiments were performed to investigate the wake-generated gust aerodynamics on each vane row of a three-stage axial flow research compressor at high reduced frequency values, including multistage interactions. In these experiments, the effects, on vane row unsteady aerodynamics of the following were investigated and quantified: (1) steady vane aerodynamic loading; (2) aerodynamic forcing function waveform, including both the chordwise and transverse gust components; (3) solidity; (4) potential interactions; and (5) isolated airfoil steady flow separation. The analysis of these unique vane row unsteady aerodynamic data determined the following.

- The steady aerodynamic loading level, not the incidence angle, is the key parameter to obtain good correlation with flat plate cascade gust models.
- The steady loading level and chordwise loading distribution have a significant effect on vane row unsteady

aerodynamics, having a larger influence on the magnitude than on the phase.

- The aerodynamic forcing function chordwise gust affects both the dynamic pressure coefficient magnitude and phase, whereas the transverse gust primarily affects the magnitude. These effects cannot be predicted with harmonic gust models because these data have been Fourier decomposed, with the predictions thus identical for all forcing function waveforms.
- The chordwise gust is not small compared to either the absolute velocity or the transverse gust. Thus, to provide accurate predictions, unsteady aerodynamic models must consider this gust component.
- For closely spaced stages (the compressor rotor-stator axial spacing herein is 0.432 chord), downstream airfoil rows are potential aerodynamic excitation sources, which affect the unsteady loading in the trailing edge region of the upstream airfoils. Since the trailing edge is thin, it would be highly susceptible to fatigue failure.
- Flow separation of the low solidity vane row affects the unsteady surface pressures upstream of the separation point, with the phase affected in the trailing edge region.

Acknowledgments

Support of this research program by the Air Force Office of Scientific Research, Dr. James Wilson, program manager, is most gratefully acknowledged.

References

Atassi, H. M., 1984, "The Sears Problem for a Lifting Airfoil Revisited—New Results," *Journal of Fluid Mechanics*, Vol. 141, pp. 109-122.

Capece, V. R., Manwaring, S. R., and Fleeter, S., 1986, "Unsteady Blade Row Interactions in a Multi-stage Compressor," *AIAA Journal of Propulsion*, Vol. 2, No. 2, pp. 168-174.

Capece, V. R., and Fleeter, S., 1987, "Unsteady Aerodynamic Interactions in a Multi-stage Compressor," ASME JOURNAL OF TURBOMACHINERY, Vol. 109, No. 3, pp. 420-428.

Carta, F. O., and St. Hilaire, A. O., 1979, "Effect of Interblade Phase Angle and Incidence Angle on Cascade Pitching Stability," ASME Paper No. 79-GT-153.

Carta, F. O., 1982, "An Experimental Investigation of Gapwise Periodicity and Unsteady Aerodynamic Response in an Oscillating Cascade, Part I: Experimental and Theoretical Results," NASA CR 3513.

Chiang, H. D., and Fleeter, S., 1988, "Prediction of Loaded Airfoil Unsteady Aerodynamic Gust Response by a Locally Analytical Method," *International Journal of Mathematical Modeling*, in press.

Englert, G. W., 1982, "Interaction of Upstream Flow Distortions With High Mach Number Cascades," ASME Paper No. 82-GT-137.

Fleeter, S., 1973, "Fluctuating Lift and Moment Coefficients for Cascaded Airfoils in Nonuniform Compressible Flow," *AIAA Journal of Aircraft*, Vol. 10, pp. 93-98.

Fleeter, S., Jay, R. L., and Bennett, W. A., 1978, "Rotor Wake Generated Unsteady Aerodynamic Response of a Compressor Stator," ASME *Journal of Engineering for Power*, Vol. 100, pp. 664-675.

Fleeter, S., Bennett, W. A., and Jay, R. L., 1980, "The Time Variant Aerodynamic Response of a Stator Row Including the Effects of Airfoil Camber," ASME *Journal of Engineering for Power*, Vol. 102, pp. 334-343.

Fleeter, S., Jay, R. L., and Bennett, W. A., 1981, "Wake Induced Time Variant Aerodynamics Including Rotor-Stator Axial Spacing Effects," ASME *Journal of Fluids Engineering*, Vol. 103, No. 1, pp. 59-66.

Gostelow, J. P., 1977, "A New Approach to the Experimental Study of Turbomachinery Flow Phenomena," ASME *Journal of Engineering for Power*, Vol. 99, pp. 97-105.

Hardin, L. W., Carta, F. O., and Verdon, J. M., 1987, "Unsteady Aerodynamic Measurements on a Rotating Compressor Blade Row at Low Mach Number," ASME JOURNAL OF TURBOMACHINERY, Vol. 109, No. 4, pp. 499-507.

Verdon, J. M., and Caspar, J. R., 1981, "Development of an Unsteady Aerodynamic Analysis for Finite Deflection Subsonic Cascades," NASA CR 3455.

APPENDIX III

Inlet Distortion Generated Periodic Aerodynamic Rotor Response

ASME Paper 89-GT-299

THE AMERICAN SOCIETY OF MECHANICAL ENGINEERS
345 E. 47 St., New York, N.Y. 10017

89-GT-299

Inlet Distortion Generated Periodic Aerodynamic Rotor Response

STEVEN R. MANWARING and SANFORD FLEETER
Thermal Sciences and Propulsion Center
School of Mechanical Engineering
Purdue University
West Lafayette, Indiana

ABSTRACT

Fundamental inlet distortion generated rotor blade row unsteady aerodynamics, including the effects of both the detailed aerodynamic forcing function for the first time and steady loading are experimentally investigated in an extensively instrumented axial flow research compressor. A two-per-rev forcing function with three gust amplitude ratios is generated. On the rotor blade pressure surface, the unsteady pressure nondimensionalization compresses the magnitude data with mean flow incidence angle. This is not the case on the higher camber suction surface. Also, these pressure surface unsteady data are primarily affected by the steady loading level whereas the suction surface unsteady data are a function of the steady loading level and distribution as well as the gust amplitude ratio. In addition, a design inlet distortion blade surface unsteady pressure correlation is considered.

NOMENCLATURE

b	Rotor blade semichord
$\bar{C}_l$	Rotor blade steady loading = $\int_0^c (\bar{C}_{p,\text{pressure}} - \bar{C}_{p,\text{suction}})\, dx$
$\bar{C}_p$	Rotor blade steady pressure coefficient
C_p	Rotor blade unsteady pressure coefficient
$C_{\Delta p}$	Rotor blade unsteady pressure difference coefficient
$\bar{i}$	Rotor blade mean incidence angle
k	Reduced frequency = $\omega b/\bar{V}_x$
p	Digitized ensembled averaged unsteady pressure
$\bar{P}_s$	Rotor blade surface steady pressure
$\hat{p}_+$	First harmonic complex unsteady pressure
$\hat{u}^+$	Streamwise gust first harmonic component
$\hat{v}^+$	Transverse gust first harmonic component
$\bar{V}_x$	Mean axial velocity
ΔW	Total unsteady velocity
$\Delta \hat{W}$	Total first harmonic gust vector
$\bar{\beta}$	Relative mean flow angle
ω	Two-per-rev forcing function frequency, radians

INTRODUCTION

Inlet flow distortions are generated by a variety of sources, including engine inlet designs and aircraft maneuvers. In addition to the performance degradation associated with inlet flow distortions, they can also result in detrimental aeromechanical effects. Namely, as schematically depicted in Figures 1 and 2, inlet flow distortions represent unsteady aerodynamic forcing functions to downstream rotor blade rows due to rotor blade relative velocity and incidence angle fluctuations, thereby resulting in the possibility of significant aerodynamically induced blade vibrations. In fact, distortions are one of the most common excitation sources for aerodynamically forced response of blade rows. Distortions also affect the stability margin of rotor blade rows as the resulting flow degradation from distortion can cause incidence angle migration that experience has shown to generally be destabilizing (Cardinale, Bankhead and McKay, 1980).

Of particular interest in this paper are distortion generated unsteady aerodynamic blade response phenomena. In the high speed regime, Datko and O'Hara (1987) measured the forced vibratory response of an advanced transonic compressor first stage integrally bladed disk (a blisk) generated by seven different inlet total pressure distortion screens. The blisk was found to be susceptible to excessive resonant stresses generated by the inlet distortions, with complex inlet distortions exciting the lower natural frequencies at a number of engine orders. Also, the harmonic content of the distortion was not always discernible from the inlet total pressure profiles. In addition, these results demonstrated that the uniform inlet flow rotor forced response characteristics may not be representative of the response when a distortion is present. They concluded that unless vibratory responses to inlet distortion can be accurately predicted, rotors, particularly blisks, should be tested to assess the resonant stresses in the presence of inlet distortions.

The accurate prediction of distortion generated blade response requires the development of a first principles based design system. On a first principles basis, inlet flow distortions represent high energy aerodynamic excitations characterised by low to moderate values of the reduced frequency, with the distortion generated blade row response analyzed by first defining the unsteady aerodynamic forcing function in terms of harmonics. The periodic vibratory response of the airfoil row to each harmonic of the forcing function is then assumed to be comprised of two components. One is due to the streamwise and transverse components of the harmonic forcing function, $\hat{u}^+$ and $\hat{v}^+$ respectively, being swept past the nonresponding airfoil row, termed the streamwise and transverse gust responses. The second, the self-induced unsteady aerodynamics, arises when the aerodynamic forcing function generates a vibrational response of the airfoil row.

Unfortunately, current state-of-the-art analyses do not model the unsteady aerodynamic forcing function. Also, the gust and motion-induced unsteady aerodynamic models involve many physical and numerical assumptions, (AGARD Manual, 1987). Therefore experimental modeling of the fundamental inlet distortion generated blade row periodic unsteady aerodynamic response, including both the forcing function and the blade row unsteady aerodynamics, is needed for the development, validation and enhancement of theoretical and numerical models.

Presented at the Gas Turbine and Aeroengine Congress and Exposition—June 4-8, 1989—Toronto, Ontario, Canada
This paper has been accepted for publication in the Transactions of the ASME
Discussion of it will be accepted at ASME Headquarters until September 30, 1989

Unsteady aerodynamic gust experiments of direct interest to turbomachines have been performed in low speed research compressors. With regard to inlet flow distortions, O'Brien, Cousins and Sexton (1980) used six dynamic pressure transducers embedded on each rotor blade surface to measure unsteady aerodynamic response. However, the periodic rotor blade row inlet flow field was not measured and, thus, the unsteady aerodynamic gust forcing function was not quantified. Also, Hardin, Carta and Verdon [1987] measured low reduced frequency oscillating airfoil aerodynamics on a rotor of a single stage compressor and also stated that they had performed similar distortion experiments although they did not present these results.

In this paper, the fundamental flow physics of distortion generated periodic rotor blade row unsteady aerodynamics, including the effects of both the detailed unsteady aerodynamic forcing function for the first time and steady loading, are experimentally investigated. This is accomplished by performing a series of experiments in an extensively instrumented axial flow research compressor. In particular, the effects of the detailed forcing function, defined in terms of the ratio of the forcing function streamwise-to-transverse first harmonic gust components, $\hat{u}^+ / \hat{v}^+$, as well as the steady aerodynamic loading level, characterized by the mean incidence angle, on the gust generated unsteady aerodynamic response of a first stage rotor blade are quantified.

In these experiments, the two-per-rev unsteady aerodynamic forcing function is generated by two 90 degree circumferential inlet flow distortions, Figure 1. This distortion, measured with a rotating cross hot wire probe, is then analyzed and decomposed into streamwise and transverse components, Figure 2. The resulting unsteady aerodynamic gust generated rotor blade surface unsteady pressure chordwise distributions are measured with embedded ultra-miniature high response dynamic pressure transducers.

RESEARCH COMPRESSOR

The Purdue Axial Flow Research Compressor experimentally models the fundamental turbomachinery unsteady aerodynamic multistage interaction phenomena including the incidence angle, the velocity, and pressure variations, the aerodynamic forcing function, the reduced frequency, and the unsteady blade row interactions. The compressor is driven by a 15 HP DC electric motor and is operated at a speed of 2,250 RPM. Each identical stage of the baseline compressor contains 43 rotor blades and 31 stator vanes having a British C4 profile, with the first stage rotor inlet flow field established by a row of 36 variable setting inlet guide vanes. The overall airfoil and compressor characteristics are presented in Table 1. For these experiments, the first stage rotor blade row was extensively instrumented. To eliminate any potential flow effects on the instrumented first stage rotor blades, the first stage stators and second stage rotors were removed, as schematically depicted in Figure 3.

INSTRUMENTATION

Both steady and unsteady first stage rotor blade row data are required. The steady data quantify the rotor mean inlet flow field and midspan steady loading distribution. The unsteady data define the periodic aerodynamic forcing function and the resulting midspan blade surface periodic pressure distributions.

The inlet flow field, both steady and unsteady, is measured with a rotating cross hot-wire probe mounted 30% of blade chord upstream of the rotor row. The cross hot-wire probe was calibrated and linearized for velocities from 18.3 m/sec to 53.4 m/sec and +/- 35 degrees angular variation, with the accuracy of the velocity magnitude and flow angle determined to be 4% and +/- 1.0 degree, respectively. Centrifugal loading effects on the rotating hot-wire sensor resistances and, thus, the responses, were found to be negligible.

The detailed steady aerodynamic loading on the rotor blade surfaces is measured with a chordwise distribution of 20 midspan static pressure taps, 10 on each surface. The static pressure at the rotor exit plane, measured with a rotor drum static tap, is used as the blade surface static pressure reference. These static pressure measurements are made using a rotor based 48 port constant speed drive Scanivalve system located in the rotor drum.

The measurement of the midspan rotor blade surface unsteady pressures is accomplished with 20 ultra-miniature, high response transducers embedded in the rotor blades at the same chordwise locations as the static pressure taps. To minimize the possibility of flow disturbances associated with the inability of the transducer diaphragm to exactly maintain the surface curvature of the blade, a reverse mounting technique is utilized. The pressure surface of one blade and the suction surface of the adjacent blade are instrumented, with transducers embedded in the nonmeasurement surface and connected to the measurement surface by a static tap. The embedded dynamic transducers were both statically and dynamically calibrated. The static calibrations showed good linearity and no discernible hysteresis. The dynamic calibrations demonstrated that the frequency response, in terms of gain attenuation and phase shift, were not affected by the reverse mounting technique. The accuracy of the unsteady pressure measurements, determined from the calibrations, is +/- 4%.

The rotor-based static pressure Scanivalve transducer, rotating cross hot-wire probe and 20 blade surface dynamic pressure transducers are interfaced to the stationary frame-of-reference through a 40 channel slip ring assembly. On-board signal conditioning of the transducer output signals is performed to maintain a good signal-to-noise ratio through the slip ring. The remaining 17 channels of the slip-ring assembly are used to provide excitation to the transducers and on/off switching to the Scanivalve DC motor.

DATA ACQUISITION AND ANALYSIS

Steady Data

The rotor blade surface static pressure data, measured with the rotor-based Scanivalve system, are defined by a root-mean-square error analysis of 20 samples with a 95% confidence interval. The reference for these midspan blade pressure measurements is the static pressure at the exit of the rotor measured on the rotor drum. Thus, the blade surface and the reference static pressures are measured at different radii. Hence, a correction for the resulting difference in the radial acceleration is applied in calculating the blade surface static pressure coefficient defined in Equation 1.

$$\bar{C}_p = \frac{\bar{P}_s - \bar{P}_{exit}}{\frac{1}{2}\rho U_t^2} \qquad (1)$$

where U_t is the rotor blade tip speed.

Periodic Data

The periodic data of interest are the harmonic components of the aerodynamic forcing function to the first stage rotor blade row together with the resulting rotor blade surface unsteady pressures and unsteady pressure differences. These are determined by defining a digitized ensemble averaged periodic unsteady aerodynamic data set consisting of the rotating cross hot-wire probe and blade surface dynamic pressure transducer signals at each steady operating

point. In particular, these time-variant signals are digitized with a high speed A-D system at a rate of 20 kHz and then ensemble averaged.

The key to this averaging technique is the ability to sample data at a preset time, accomplished by an optical encoder mounted on the rotor shaft. The microsecond range step voltage signal from the encoder is the data initiation time reference and triggers the high speed A-D multiplexer system. To significantly reduce the random fluctuations superimposed on the periodic signals of interest, 200 averages are used. A Fast Fourier Transform (FFT) algorithm is then applied to these ensemble averaged signals to determine the harmonic components of the unsteady aerodynamic forcing function and the resulting rotor blade surface harmonic unsteady pressures and pressure difference.

The unsteady inlet flow field to the rotor row is measured with the rotating cross hot-wire probe which quantifies the relative velocity and flow angle. The velocity triangle relations depicted in Figure 2 are then used to determine the unsteady inlet flow field to the rotor, in particular, the streamwise and transverse velocity components, u^+ and v^+, respectively. These are then Fourier decomposed to determine the first harmonic of the streamwise and transverse velocity components, termed the streamwise and transverse gust components, $\hat{u}^+$ and $\hat{v}^+$.

The various unsteady aerodynamic gust mathematical models reference the gust generated airfoil aerodynamic response to a transverse gust at the leading edge of the airfoil. However, in the experiments described herein, the time-variant data are referenced to the initiation of the data acquisition shaft trigger pulse. Thus, for consistency with the models, the periodic data are further analyzed and referenced to a transverse gust at the leading edge of the first stage rotor blade. This is accomplished by assuming that: (1) the aerodynamic forcing function remains fixed in the stationary reference frame; and (2) the forcing function does not decay from the rotating hot-wire probe axial location to the rotor row leading edge plane.

The rotor blade surface unsteady pressure data, measured with the embedded high response pressure transducers, are analyzed to determine the harmonics of the chordwise distribution of the unsteady pressure coefficient, C_p, and the unsteady pressure difference coefficient, $C_{\Delta p}$. These are defined in Equation 2 and are specified from the Fourier coefficients of the digitized ensemble averaged dynamic pressure transducer signals.

$$C_p = \frac{\hat{p}}{\rho \bar{V}_x^2 \left(\frac{\hat{v}^+}{\bar{V}_x}\right)\bar{\beta}} \qquad (2a)$$

$$C_{\Delta p} = C_{p,\text{pressure}} - C_{p,\text{suction}} \qquad (2b)$$

where $\hat{v}^+$ is the first harmonic transverse gust component, $\bar{V}_x$ is the mean axial velocity, and $\bar{\beta}$ is the relative mean flow angle.

The final form of the gust generated rotor blade row unsteady aerodynamics is the chordwise distribution of the harmonic complex unsteady pressure and pressure difference coefficients. Also included as a reference where appropriate are predictions from the transverse gust analysis of Smith (1971). This model analyzes the unsteady aerodynamics generated on a flat plate airfoil cascade at zero incidence by a transverse gust convected with an inviscid, subsonic, compressible flow.

RESULTS

A series of experiments are performed to investigate and quantify the effects of the detailed inlet distortion aerodynamic forcing function, defined by the ratio of the amplitudes of the first harmonic streamwise-to-transverse gust components, $|\hat{u}^+ / \hat{v}^+|$, and the level of steady aerodynamic loading, characterized by the mean incidence angle, on the periodic gust unsteady aerodynamics of the first stage rotor blade row. The variation in the rotor blade steady loading was obtained by holding the rotor speed constant and varying the mass flow rate and, thus, the mean flow incidence angle to the rotor blade row.

PERIODIC AERODYNAMIC FORCING FUNCTION

Three distinct two-per-revolution aerodynamic forcing functions to the first stage rotor blade row are generated by varying the orientation of the two honeycomb sections mounted in the inlet. These are characterized by nominal first harmonic streamwise-to-transverse gust amplitude ratios of 0.4, 0.7, and 0.9. The Fourier decomposition of these inlet distortion aerodynamic forcing functions to the first stage rotor row in terms of the streamwise and transverse gust components for these three gust amplitude ratios are presented in Figures 4, 5, and 6. The inlet distortion results in a dominant two-per-rev excitation fundamental harmonic with much smaller higher harmonics. Also, as the gust amplitude ratio increases, many of the higher harmonics of both gust velocity components increase in amplitude, although they do not approach that of the two-per-rev fundamental.

BLADE SURFACE STATIC PRESSURES

The effect of steady aerodynamic loading, characterized by the mean incidence angle, on the rotor blade surface static pressure coefficient with the inlet distortion is shown in Figure 7. The level of steady loading only affects the static pressure distribution on the pressure surface over the front 40% of the chord. On the suction surface, the steady loading variation has a large effect on the static pressure distribution over the entire suction surface. Also, these data give no indication of suction surface flow separation. It should be noted that these surface static pressure distributions are not affected by the characteristics of the periodic unsteady aerodynamic forcing function.

ROTOR PERIODIC AERODYNAMIC RESPONSE

The periodic aerodynamic response of the first stage rotor blade row to the inlet distortion forcing function, including the effect of steady aerodynamic loading, are presented in Figures 8 through 16. In particular, these figures present the chordwise distributions of the complex unsteady pressure coefficient on the individual rotor blade surfaces as well as the corresponding complex unsteady pressure difference coefficients generated by the two-per-rev inlet distortion forcing function.

Pressure Surface Unsteady Pressures

The effect of steady aerodynamic loading level on the distortion generated first harmonic complex unsteady pressure distribution on the rotor blade pressure surface is shown in Figures 8, 9, and 10 for nominal streamwise-to-transverse gust amplitude ratios of 0.4, 0.7, and 0.9, respectively.

The unsteady pressure magnitude data decrease monotonically with increasing chord location, with a sharp decrease in the front region of the pressure surface and then a gradual decrease over the remainder of the chord for all steady loading levels and gust amplitude ratios. For each nominal value of the gust amplitude ratio, this form of the dimensionless unsteady pressure coefficient, Equation 2a,

results in the compression of these magnitude data for all mean flow incidence angle values. Also, as the gust amplitude ratio increases, these magnitude data exhibit a small decrease in value. This is due to the gust vector becoming more parallel to the mean flow and, thus, less normal to the blade pressure surface. Thus, the magnitude of the unsteady pressure response on the blade pressure surface, i.e., the low camber airfoil surface, is primarily due to the level of steady loading as characterized by the mean flow incidence angle.

The unsteady pressure phase data increase monotonically with chord over the front half of the blade, becoming nearly constant over the aft half for all steady loading levels and gust amplitude ratios. Also, the steady aerodynamic loading and the gust amplitude ratio have only a very small effect on these phase data. Thus, the phase of the unsteady pressure response on the low camber blade pressure surface is nearly independent of the steady loading level and the gust amplitude ratio.

Suction Surface Unsteady Pressures

The effect of steady aerodynamic loading on the distortion generated first harmonic complex unsteady pressure on the rotor blade suction surface is shown in Figures 11, 12 and 13 for the three gust amplitude ratios.

The unsteady pressure magnitude data decrease over the front 25% of the chord for all steady loading levels and gust amplitude ratios. On this part of the suction surface, the magitude data decrease in value as the gust takes on larger streamwise components. In contrast to the pressure surface, this form of the dimensionless unsteady pressure coefficient, Equation 2a, does not compress these magnitude data with mean flow incidence angle, the exception being between 13% and 20% of the chord. Also, as the gust amplitude ratio increases, these magnitude data exhibit a relatively large decrease in value over the front half of the chord. This is due to the gust vector becoming more parallel to the mean flow and, thus, less normal to the blade pressure surface. Thus, the magnitude of the unsteady pressure response on the blade suction surface, i.e., the higher camber airfoil surface, is due to both the level of steady loading as characterized by the mean flow incidence angle and the streamwise-to-chordwise gust amplitude ratio.

The unsteady pressure phase data generally decrease monotonically with increasing chord for all gust amplitude ratios and steady loading levels. As the gust amplitude ratio increases, i.e., as the gust takes on a larger streamwise component, the phase data generally decrease in value, with the chordwise phase data variation decreasing more rapidly over the front half of the blade and more slowly over the aft half. With regard to the steady loading level, the phase data are nearly independent of the steady loading level in the neighborhood of the quarter chord. Forward and aft of the quarter chord, steady loading has different effects. In particular, aft of the quarter chord, the phase data decrease as the mean incidence angle is increased. In contrast, near the leading edge, the phase data increase with increasing mean incidence angle.

Unsteady Pressure Differences

The effect of steady loading on the first harmonic complex unsteady pressure differences across the rotor blade camberline is shown in Figures 14, 15 and 16 for streamwise-to-transverse gust amplitude ratios of 0.4, 0.7, and 0.9, respectively. Also presented as a reference are the flat plate cascade inviscid transverse gust predictions.

The unsteady pressure difference magnitude data generally decrease with increasing chord, attaining a near minimum value in the midchord region of the airfoil. As the gust amplitude ratio increases, i.e., as the gust takes on a larger streamwise component, the chordwise position of this minimum magnitude moves forward. Aft of this minimum magnitude position, the magnitude data are a function of the steady loading level. In the front chord region, increased steady loading results in an increase in the magnitude data. In the mid to aft chord region of the blade, the unsteady pressure differences are greatly decreased in magnitude, but still increase with increased mean incidence with this increase greater for higher values of the gust amplitude ratio. Also, the lowest gust amplitude ratio value and lowest mean incidence angle data most closely approximate the transverse gust flat plate cascade model and exhibit the best correlation with the prediction.

An inviscid, incompressible flow cascade model that accounts for airfoil profile effects was used to determine the effect of variations in the mean flow incidence angle on the airfoil surface steady pressure difference distribution. Figure 17 demonstrates that the pressure difference in the front chord region increases with increasing mean flow incidence angle. Thus, for a quasisteady harmonic gust disturbance, i.e. a low reduced frequency inlet distortion, the unsteady pressure difference magnitude will increase in the front chord region as the mean flow incidence angle is increased, for example Figures 14, 15 and 16.

The unsteady pressure difference phase data are nearly constant over the front part of the blade for all three gusts. There is a sharp increase in the phase in the quarter to mid-chord region of the blade. The chordwise location of the onset of this rapid increase is a function of the steady loading and the gust amplitude ratio. Aft of the chordwise location of this rapid phase increase, the phase data increase with increased steady loading.

SUMMARY AND CONCLUSIONS

The fundamental flow physics of distortion generated periodic rotor blade row unsteady aerodynamics, including the effects of both the detailed unsteady aerodynamic forcing function for the first time and steady loading, were experimentally investigated. This was accomplished through a series of experiments performed in an extensively instrumented axial flow research compressor. A two-per-rev aerodynamic forcing function was generated by mounting two 90 degree honeycomb sections 180 degrees apart circumferentially in the compressor inlet. In terms of the gust amplitude ratio, three distinct two-per-revolution aerodynamic forcing functions were considered.

The rotor blade surface steady loading distributions were quantified with surface static pressure taps and a rotor-based Scanivalve system. The aerodynamic forcing function to the rotor blade row was determined with a rotating cross hot-wire probe, with the aerodynamic gust generated rotor blade surface unsteady pressure chordwise distributions measured with embedded ultraminiature high response dynamic pressure transducers.

The detailed distortion gust generated unsteady aerodynamic results of these experiments are summarized in the following.

Forcing Function:

* The inlet distortion forcing function shows a dominant two-per-rev, with much small higher harmonic content.

* As the gust streamwise-to-chordwise gust amplitude ratio increases, many of the higher harmonic amplitudes increase, although they do not approach that of the two-per-rev.

Pressure Surface:

* The unsteady pressure phase data are nearly independent of the steady loading level and the gust amplitude ratio.

* The unsteady pressure magnitude data decrease monotonically with increasing chord, with a sharp decrease in the front region.

* The selected nondimensionalization compresses the unsteady pressure magnitude data with regard to mean flow incidence angles for each gust amplitude ratio.

* Increasing gust amplitude ratio results in a small decrease in the magnitude data in the front chord region due to the gust vector becoming more parallel to the mean flow.

* The magnitude of the unsteady pressure response on the blade pressure surface, i.e., the low camber surface, is thus primarily affected by the level of steady loading as characterized by the mean flow incidence angle.

Suction Surface:

* The unsteady pressure phase data generally decrease as the gust amplitude ratio increases. As the incidence angle is increased, the phase data increase and then, aft of 25% chord, decrease.

* The unsteady pressure magnitude data decrease over the front 25% of the chord for all steady loading levels and gust amplitude ratios.

* The selected nondimensionalization does not compress these unsteady pressure magnitude data with regard to mean flow incidence angle, the exception being between 13% and 20% of the chord.

* Increasing gust amplitude ratio results in a large decrease in the magnitude data in the front chord region due to the gust vector becoming more parallel to the mean flow.

* The magnitude of the unsteady pressure response on the blade suction surface, i.e., the high camber surface, is thus affected by both the level of steady loading and the gust amplitude ratio.

Unsteady Pressure Difference:

* The magnitude data increase in the front chord region as the steady loading is increased. In the mid to aft chord region, the increase in these data with loading is a function of the gust amplitude ratio.

* The phase data exhibit a sharp increase in the quarter to mid-chord region of the blade, with this location a function of the steady loading and the gust amplitude ratio. Aft of this chordwise location, the phase data increase with increased steady loading.

ACKNOWLEDGEMENTS

Research sponsored by the Air Force Office of Scientific Research (AFSC) under Contract F49620-88-C-0022. The United States Government is authorized to reproduce and distribute reprints for governmental purposes notwithstanding any copyright notation hereon.

REFERENCES

1. AGARD Manual on Aeroelasticity in Axial Flow Turbomachines, Volume 1: Unsteady Turbomachinery Aerodynamics, *AGARDograph No. 298*, 1987.

2. Cardinale, V., Bankhead, H., and McKay, R., "Experimental Verification of Turboblading Aeromechanics," *Paper No. 23, 56th Symposium of the AGARD Propulsion and Energetics Panel*, 1980.

3. Datko Jr., J.T. and O'Hara, J.A., "The Aeromechanical Response of an Advanced Transonic Compressor to Inlet Distortion," *ASME Paper 87-GT-189*, 1987.

4. Hardin, L.W., Carta, F.O., and Verdon, J.M., "Unsteady Aerodynamic Measurements on a Rotating Compressor Blade Row at Low Mach Number," *ASME Journal of Turbomachinery*, Vol. 109, No. 4, October 1987, pp. 499-507.

5. O'Brien, W.F., Cousins, W.T., and Sexton, M.R., "Unsteady Pressure Measurements and Data Analysis Techniques in Axial Flow Compressors," *Measurement Methods in Rotating Components of Turbomachinery, ASME*, 1980, pp. 195-201.

6. Smith, S.N., "Discrete Frequency Sound Generation in Axial Flow Turbomachines," *ARC R&M 3709*, 1971.

APPENDIX

As noted, when the transverse gust is utilized in the nondimensionalization of the unsteady pressure, Equation 2a, the magnitude data on both the pressure and suction surfaces decrease with increasing value of the streamwise-to-chordwise gust amplitude ratio. To provide a more advanced design tool which accounts for this effect, semi-empirical analysis of these unsteady pressure data was considered.

The blade surface unsteady pressure response is generated by the velocity fluctuations normal to the blade surfaces. Therefore, an unsteady pressure nondimensionalization which considers the gust component normal to each blade surface was considered, accomplished with the following modified complex unsteady pressure coefficient.

$$C'_p = \frac{\hat{P}}{\rho \bar{V}_x^2 \left(\frac{a_n \Delta \hat{W}}{\bar{V}_x}\right) \bar{\beta}} \qquad \text{(A1)}$$

$$\Delta \hat{W} = \sqrt{(\hat{v}^+)^2 + (\hat{u}^+)^2} \qquad \text{(A2)}$$

where a_n is the magnitude ratio of the gust component normal to the chordline and the total gust.

Figure A1 schematically depicts the blade pressure surface flow field with zero mean flow incidence. The blade surfaces are approximated by the chordline, with the normal gust component calculated from the data. On the pressure surface, the low camber airfoil surface which is well approximated by the chordline, this semiempirical correlation is valid, with the magnitude data for the various streamwise-to-chordwise gust amplitude ratios collapsing to a single curve, Figure A2. However on the high camber suction surface, although this semiempirical correlation does decrease the differences in the magnitude data for the three streamwise-to-chordwise gust amplitude ratios, there are still large differences, Figure A3. This is most likely associated with the strong interactions between the steady and unsteady flow fields in the leading edge region and aft of midchord region. Also, the chordline is a poor approximation to this high camber airfoil surface. It should be noted that incorporating only the total gust vector, $\Delta \hat{W}$, i.e. setting a_n to unity in Equation A1, was also considered. However, rather than a collapsing of the magnitude data with increasing streamwise-to-chordwise gust amplitude ratio, this resulted in an amplification of this effect.

Table 1. Overall airfoil and compressor characteristics

	ROTOR	STATOR	IGV
Airfoil Type	C4	C4	C4
Number of Airfoils	43	31	36
Chord, C (mm)	30	30	30
Solidity, C/S	1.14	1.08	0.96
Camber, θ	27.95	27.70	36.9
Stagger Angle, λ	36	-36.1	18.5
Aspect Ratio	2.0	2.0	2.0
Thickness/Chord (%)	10	10	10
Design Flow Rate (kg/s)		2.03	
Design Axial Velocity (m/s)		24.4	
Rotational Speed (RPM)		2250	
Number of Stages		2	
Stage Pressure Ratio		1.003	
Inlet Tip Diameter (mm)		420	
Hub/Tip Radius Ratio		0.714	
Stage Efficiency (%)		85	

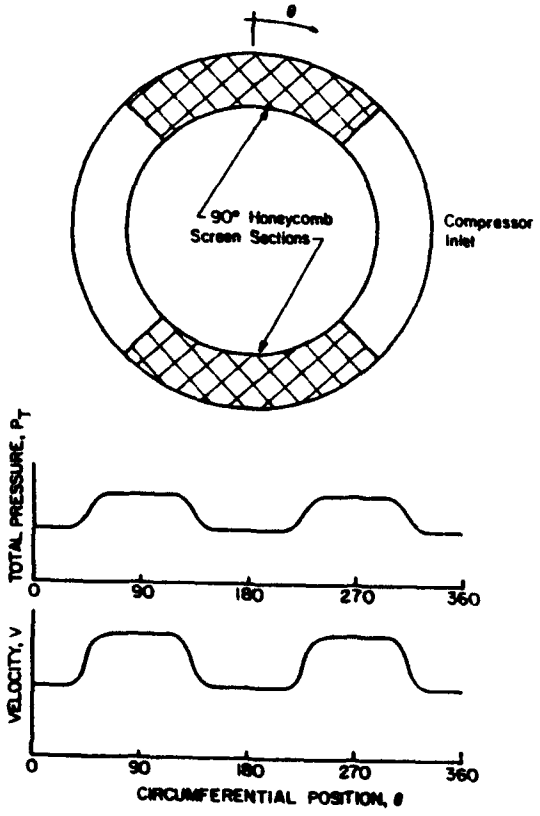

Figure 1. Two-per-rev distortion aerodynamic forcing functions

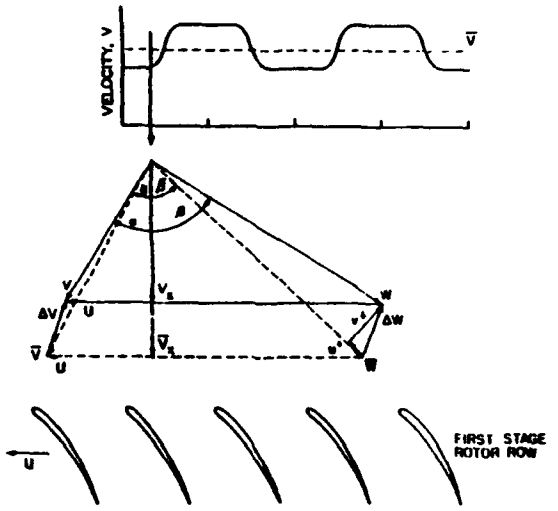

Figure 2. Decomposition of distortion forcing function

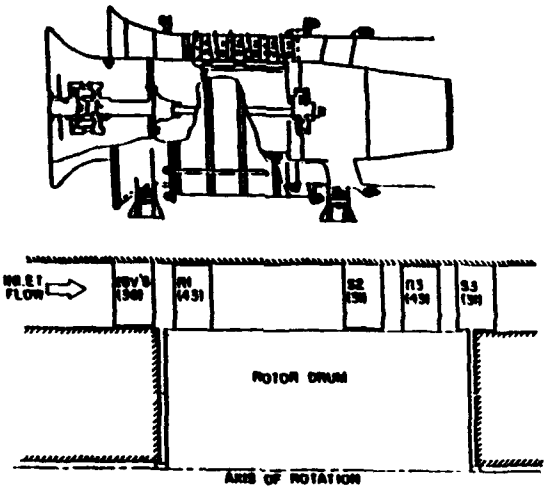

Figure 3. Research compressor schematic

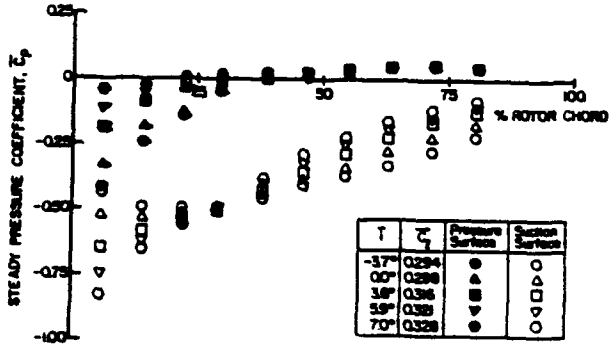

Figure 4. Fourier decomposition of forcing function, $|\hat{u}^+ / \hat{v}^+| = 0.4$

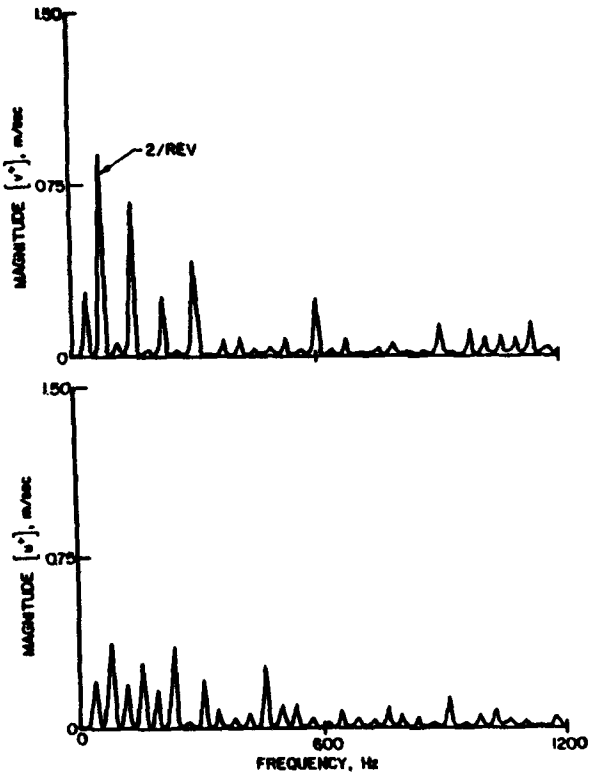

Figure 5. Fourier decomposition of forcing function, $|\hat{u}^+ / \hat{v}^+| = 0.7$

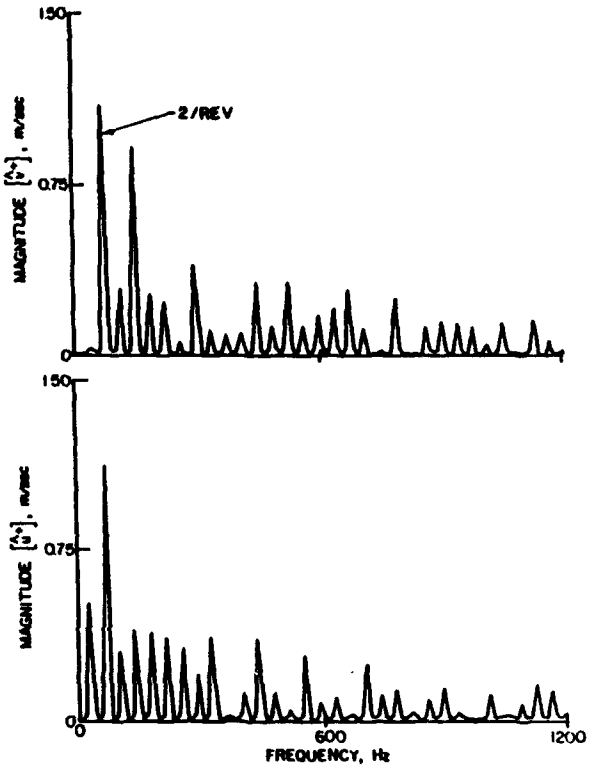

Figure 7. Steady loading effect on surface static pressure coefficient with inlet flow distortion

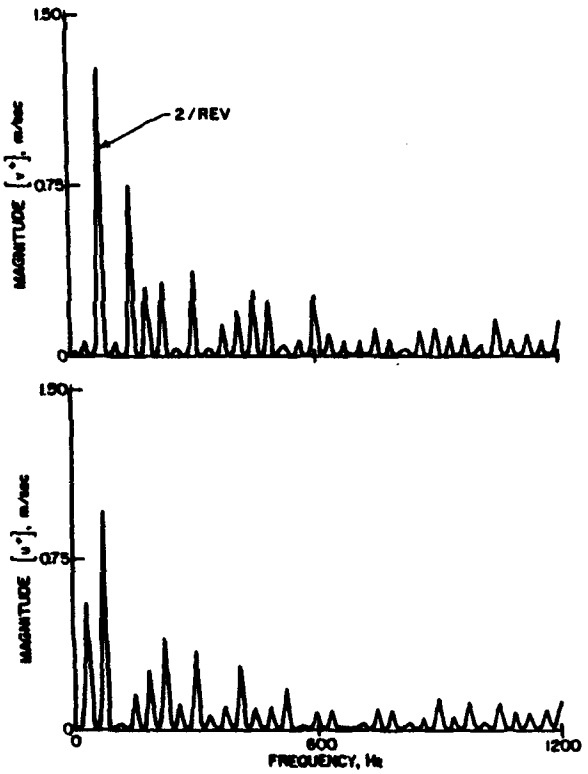

Figure 6. Fourier decomposition of forcing function, $|\hat{u}^+ / \hat{v}^+| = 0.9$

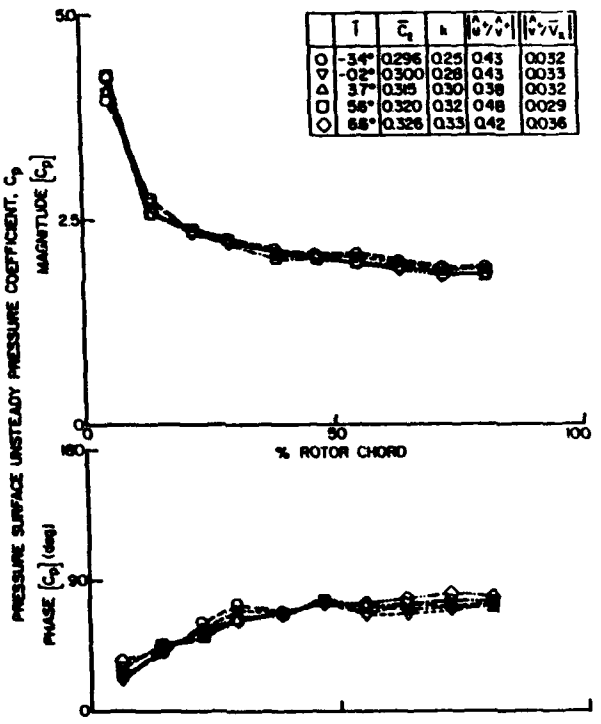

Figure 8. Pressure surface steady loading effect on unsteady pressure, $|\hat{u}^+ / \hat{v}^+| = 0.4$

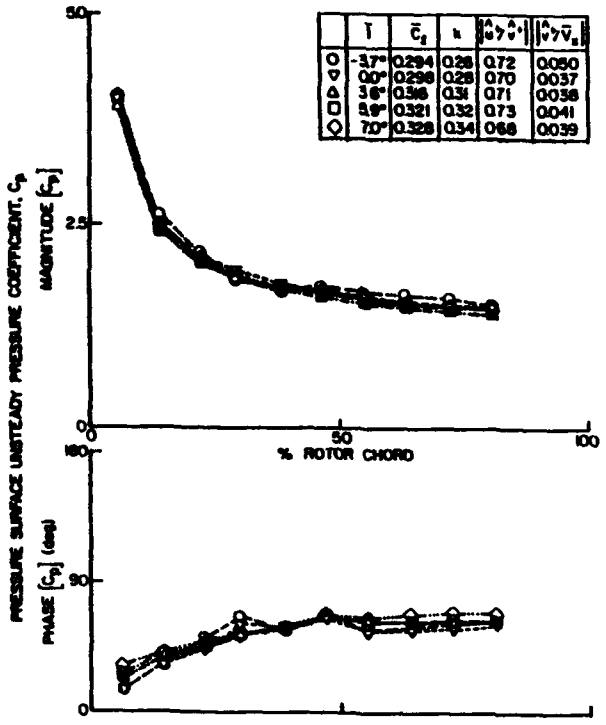

Figure 9. Pressure surface steady loading effect on unsteady pressure, $|\hat{u}^+ / \hat{v}^+| = 0.7$

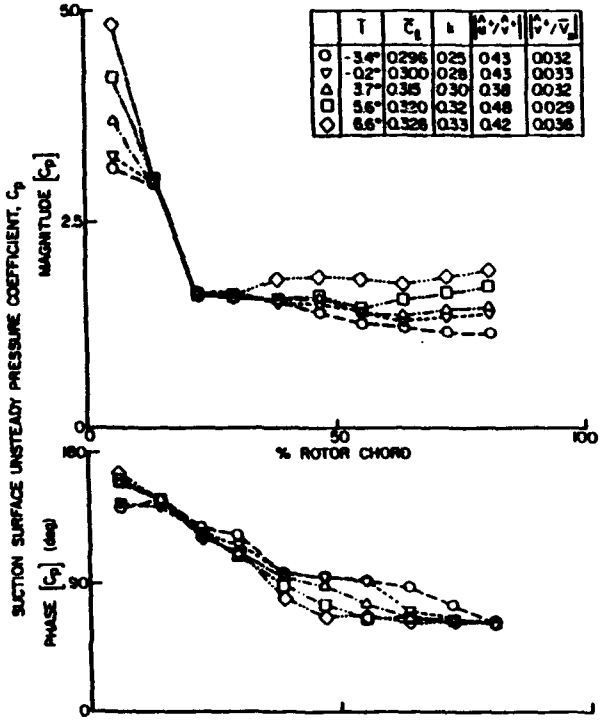

Figure 11. Suction surface steady loading effect on unsteady pressure, $|\hat{u}^+ / \hat{v}^+| = 0.4$

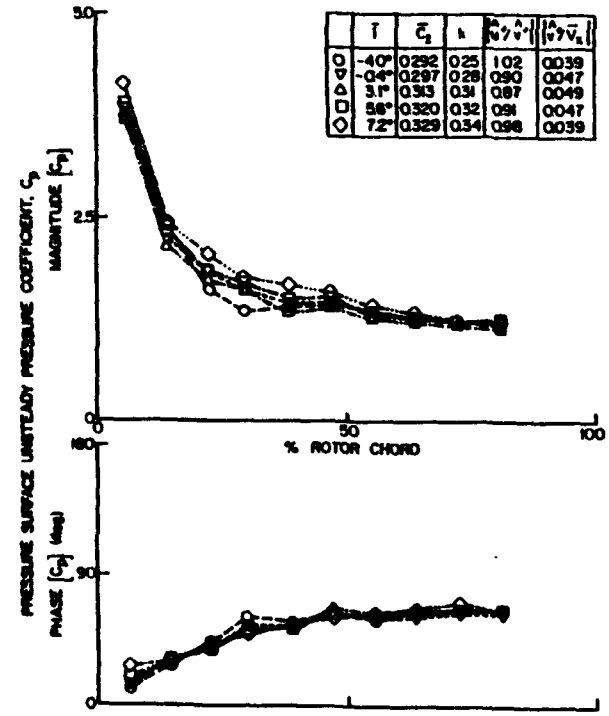

Figure 10. Pressure surface steady loading effect on unsteady pressure, $|\hat{u}^+ / \hat{v}^+| = 0.9$

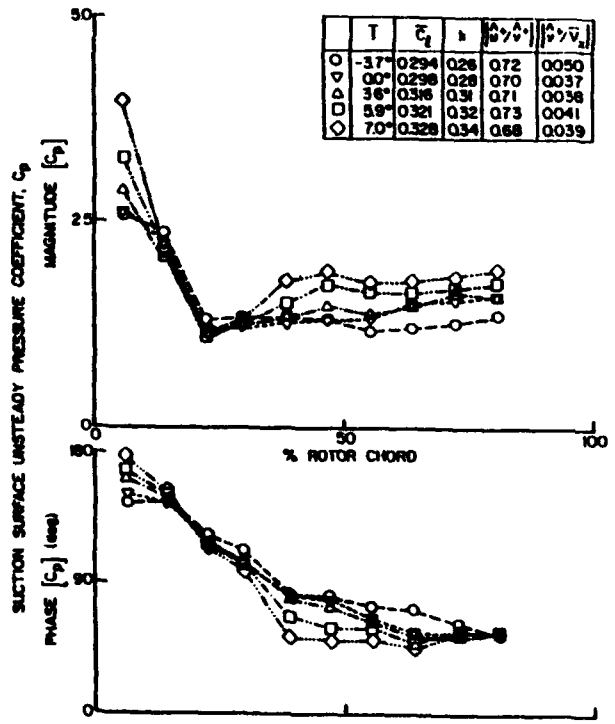

Figure 12. Suction surface steady loading effect on unsteady pressure, $|\hat{u}^+ / \hat{v}^+| = 0.7$

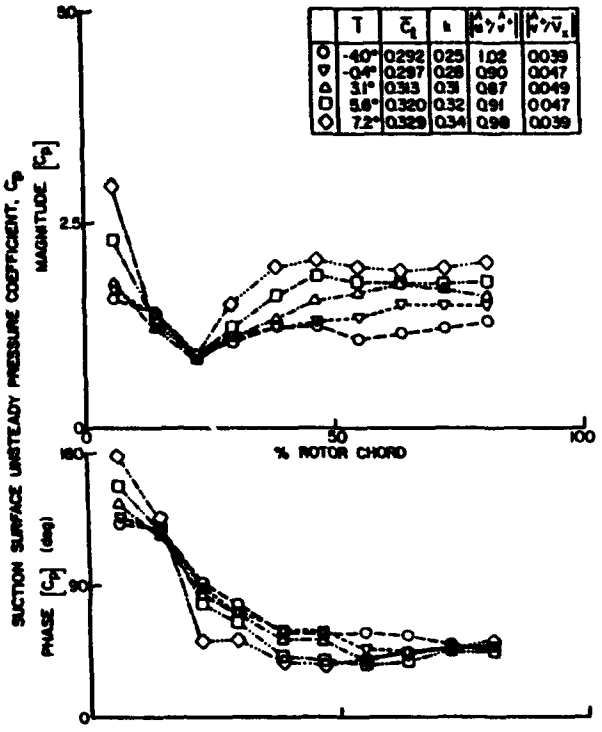

Figure 13. Suction surface steady loading effect on unsteady pressure, $|\hat{u}^+ / \hat{v}^+| = 0.9$

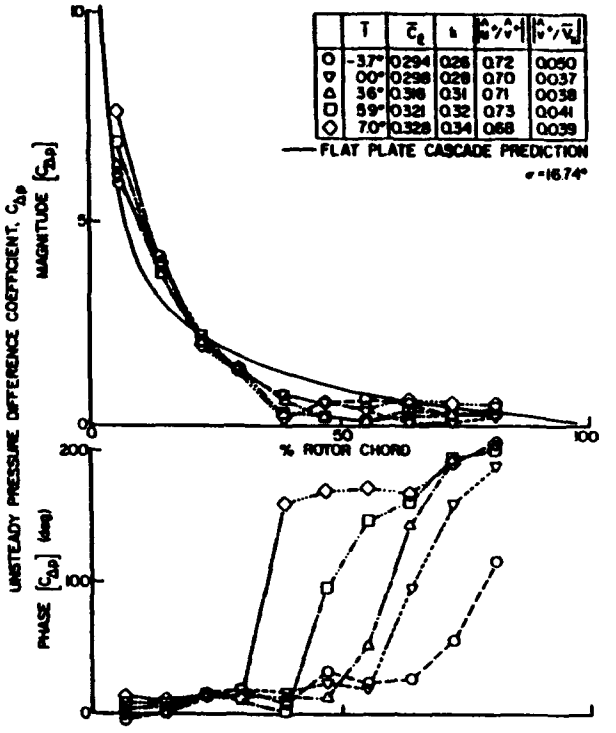

Figure 15. Steady loading effect on unsteady pressure difference, $|\hat{u}^+ / \hat{v}^+| = 0.7$

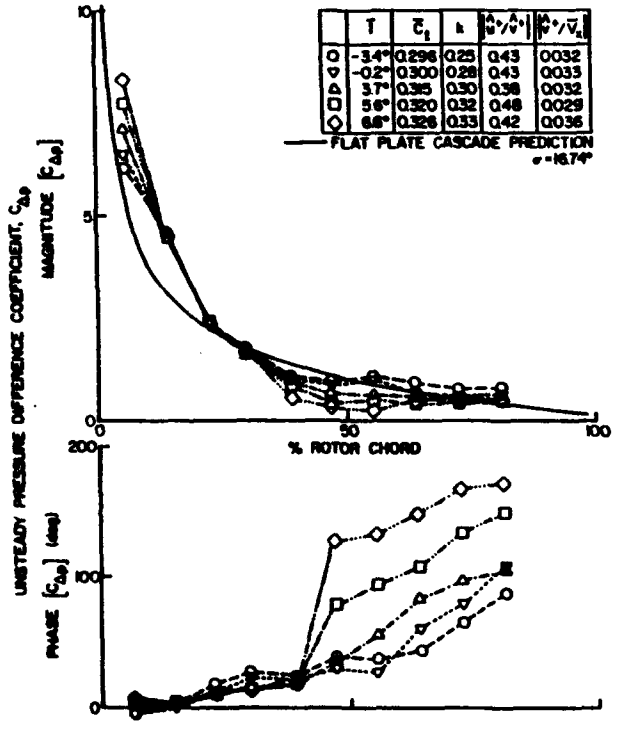

Figure 14. Steady loading effect on unsteady pressure difference, $|\hat{u}^+ / \hat{v}^+| = 0.4$

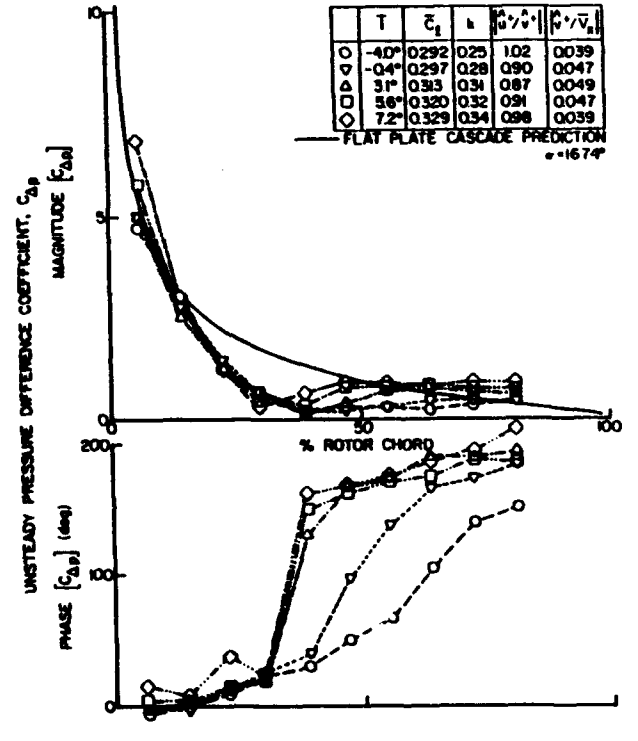

Figure 16. Steady loading effect on unsteady pressure difference, $|\hat{u}^+ / \hat{v}^+| = 0.9$

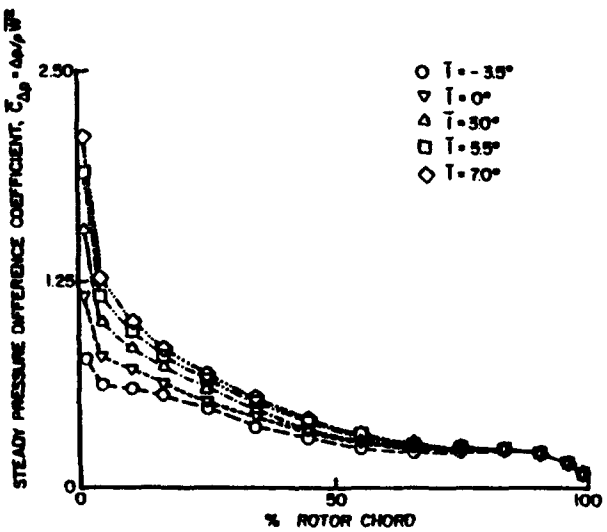

Figure 17. Steady loading effect on prediction steady pressure difference

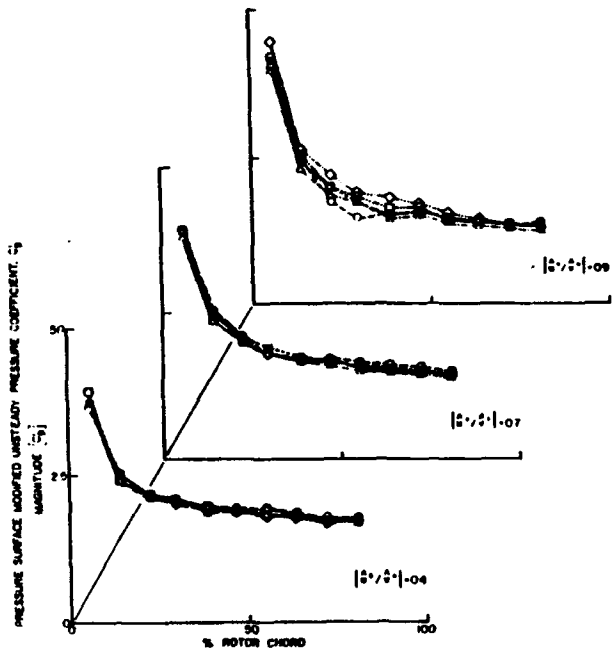

Figure A2. Pressure surface semiempirical correlation

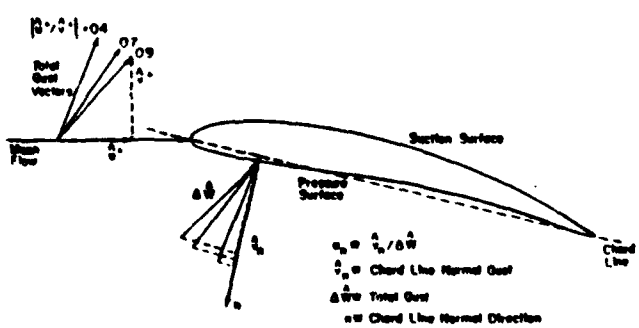

Figure A1. Blade pressure surface gust vector orientation

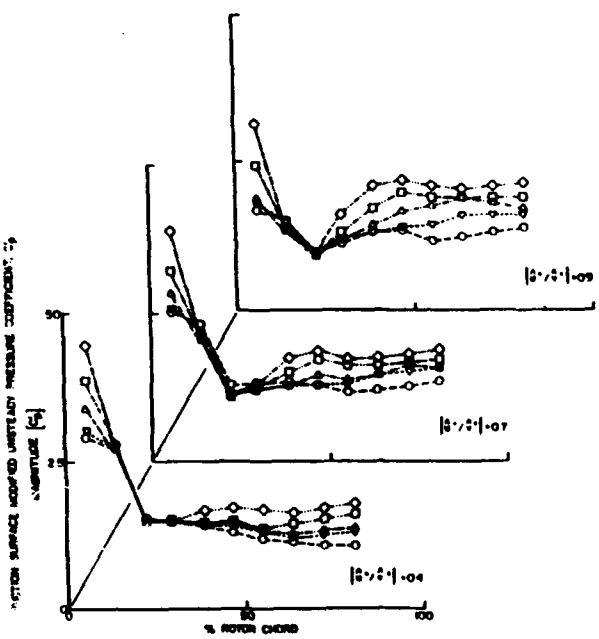

Figure A3. Suction surface semiempirical correlation

APPENDIX IV

Periodic Unsteady Rotor Blade Aerodynamics Including Loading Effects

AIAA Journal of Propulsion and Power

Periodic Rotor-Blade Aerodynamics Including Loading Effects

Steven R. Manwaring* and Sanford Fleeter†
Purdue University, West Lafayette, Indiana 47907

A series of experiments are performed to investigate and quantify the effects of steady aerodynamic loading on the unsteady gust aerodynamics of a first-stage rotor blade at realistic values of the reduced frequency. These are accomplished in an extensively instrumented axial flow research compressor with the high-reduced frequency gusts generated by the wakes from the inlet guide vanes. The unsteady pressure response on the low-camber blade pressure surface is primarily affected by mean flow incidence angle except in the accelerating mean flowfield of the front chord region at negative incidence. However, the unsteady pressure response on the high-camber suction surface is affected by steady loading over the entire surface, i.e., gust interactions with the accelerating mean flowfield in the front half and the large viscous regions in the aft half. The multistage effects associated with compressor rotor-stator blade-row operation in the super-resonant flow regime, wherein acoustic waves propagate, are also considered. The unsteady pressure difference and thus, the unsteady lift, due to acoustic waves generated by the downstream super-resonant, rotor-stator interaction, is nearly zero, even though the individual surface unsteady pressures are of relatively large amplitude.

Nomenclature

C = rotor chord
$\bar{C}_l$ = steady lift coefficient, $\int_0^C (\bar{p}_p - \bar{p}_s)\, dx/\frac{1}{2}\rho U_t^2 C$
C_p = first harmonic unsteady pressure coefficient
$\bar{C}_p$ = static pressure coefficient
$C_{\Delta p}$ = first harmonic unsteady pressure difference
$\bar{i}$ = mean incidence angle
k = reduced frequency, $\omega C/2\bar{V}_x$
$\bar{p}$ = rotor-surface static pressure
$\bar{p}_{exit}$ = rotor-exit static pressure
$\hat{p}$ = first harmonic complex unsteady pressure
u^+ = first harmonic streamwise gust component
U_t = blade tip speed
v^+ = first harmonic transverse gust component
$\bar{V}_x$ = mean axial velocity
$\bar{\beta}$ = rotor relative mean flow angle
σ = interblade phase angle
ω = inlet guide vane (IGV) passing frequency

Introduction

PERIODIC aerodynamic excitations generate unsteady aerodynamic forces and moments on turbomachinery blading. When the aerodynamic excitation frequency corresponds to a blade natural frequency, catastrophic vibrational responses may occur. The operating conditions at which these resonance conditions are found can be predicted with Campbell diagrams. However, accurate predictions of the amplitude of the resonant blade vibration cannot currently be made due to the inability of mathematical models to accurately analyze the aerodynamic forcing function and the resulting unsteady aerodynamics acting on the blading.

Wakes shed by upstream airfoil rows are the most common aerodynamic excitation source (see Fig. 1). On a first principles basis, the resulting high-reduced frequency forced response problems are analyzed by first defining the unsteady aerodynamic forcing function in terms of its harmonics. The periodic response of the airfoil row to each harmonic is then assumed to include two components. The first is due to the parallel and normal components of the harmonic forcing function being swept past the nonresponding airfoil row, termed the streamwise (parallel) and transverse (normal) gust responses, respectively. The second, the self-induced, unsteady aerodynamics, arises when the aerodynamic forcing function generates a vibrational response of the airfoils.

Mathematical models to predict the unsteady aerodynamic response of an airfoil row to a gust are being developed. Small perturbation thin airfoil analyses were considered initially with integral solutions obtained for the unsteady lift on a flat plate airfoil cascade at zero incidence in an inviscid, irrotational flowfield, for example, Refs. 1–4. Models that consider the profile of the airfoil as well as finite incidence angles have subsequently been developed. Goldstein and Atassi[5] and Atassi[6] analyzed the inviscid, incompressible flow past an isolated airfoil of arbitrary shape at finite angle of attack subject to an interacting gust. Chiang and Fleeter[7] utilized the complete first-order model and a locally analytical solution technique to predict the unsteady loading on a cascade of thick, cambered airfoils at nonzero incidence angles in an incompressible flow due to a convected gust.

Unsteady aerodynamic gust experiments of direct interest to turbomachines have been performed in low-speed research compressors at both high and low values of the reduced frequency. The effects of airfoil camber, rotor-stator axial spacing, and the waveform of the aerodynamic forcing function have been investigated on the stationary vane rows of both single and multistage compressors.[8-11] The aerodynamic forcing function in these experiments was made up of the high-reduced frequency wakes shed by the upstream rotor blades. Hardin et al.[12] measured low-reduced frequency oscillating airfoil aerodynamics on a rotor of a single-stage, low-speed compressor and also stated that they had performed distortion gust response experiments, although they did not present these results.

In this paper, the fundamental flow physics of rotor-blade row unsteady gust aerodynamics are experimentally investigated at realistic high values of the reduced frequency for the

Received Aug. 22, 1988; revision received July 24, 1989.

*AFRAPT Trainee, Thermal Sciences and Propulsion Center, School of Mechanical Engineering.
†Professor and Director, Thermal Sciences and Propulsion Center, School of Mechanical Engineering.

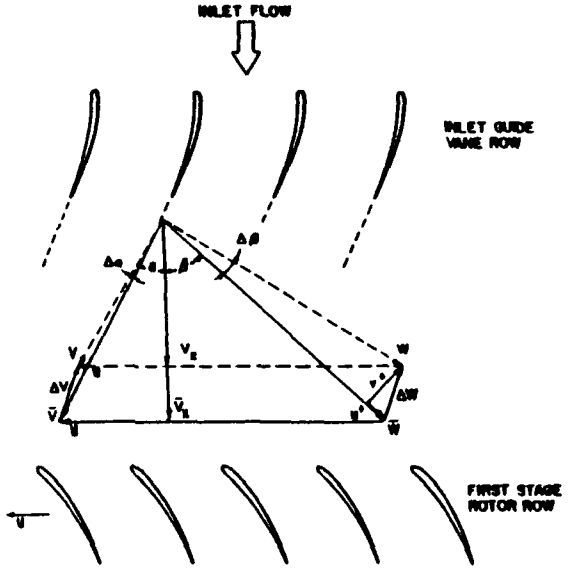

Fig. 1 Rotor-blade row inlet flowfield.

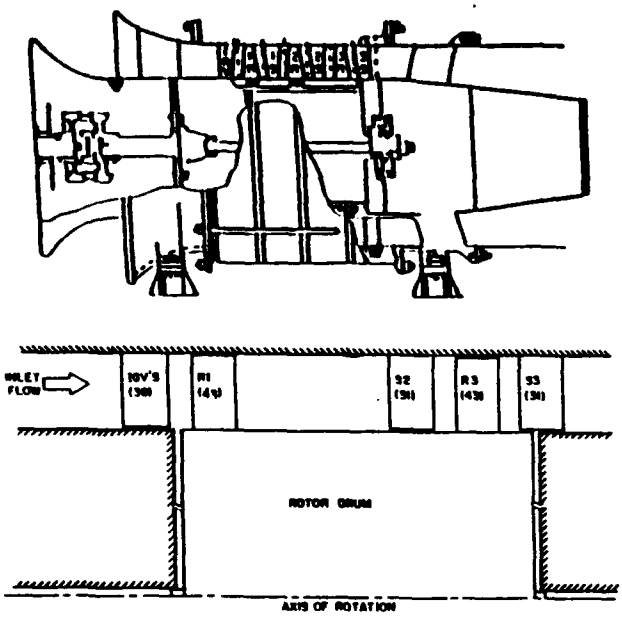

Fig. 2 Baseline compressor configuration.

Table 1 Overall airfoil and compressor characteristics

	Rotor	Stator	IGV
Airfoil type	C4	C4	C4
Number of airfoils	43	31	36
Chord, C, mm	30	30	30
Solidity, C/S	1.14	1.09	0.96
Camber, θ	28.0	27.7	36.9
Stagger angle, γ	36.0	−36.0	21.0
Aspect ratio	2.0	2.0	2.0
Thickness/chord, %	10.0	10.0	10.0
Flow rate, kg/s		2.03	
Design axial velocity, m/s		24.4	
Design rotational speed, RPM	2250		
Number of stages		3	
Design stage pressure ratio		1.0	
Inlet tip diameter, mm		420	
Hub/tip radius ratio		0.714	
Stage efficiency, %		85	

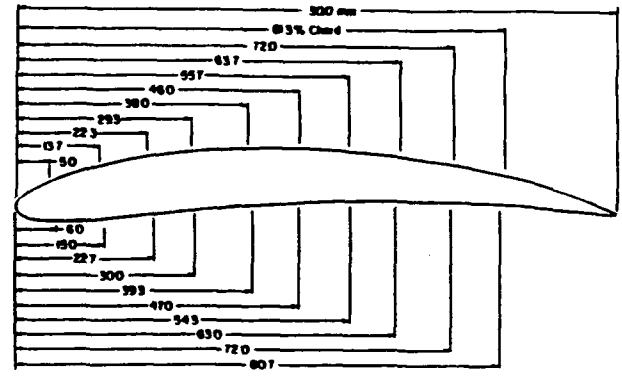

Fig. 3 Rotor-blade profile and instrumentation locations.

first time. In particular, a series of experiments are performed in an extensively instrumented axial flow research compressor to investigate the effects of steady aerodynamic loading on the unsteady gust aerodynamics of a first-stage rotor blade with the high-reduced frequency gusts generated by the wakes from the inlet guide vanes (IGV). The multistage effects associated with operation in the super-resonant flow regime wherein acoustic waves propagate are also considered.

Research Compressor

The Purdue Axial Flow Research Compressor experimentally models the fundamental aerodynamic phenomena inherent in turbomachinery airfoil rows including the airfoil incidence angles, the velocity and pressure variations, the aerodynamic forcing function, the reduced frequency, and the unsteady blade and vane row interactions. The three-stage compressor is driven by a 15-HP dc electric motor and is operated at a speed of 2250 rpm. Each identical stage of the baseline compressor contains 43 rotor-blades and 31 stator vanes having a British C4 profile with the first-stage rotor inlet flowfield established by a row of 36 variable setting IGVs. The overall airfoil and compressor characteristics are presented in Table 1. For these experiments, the first-stage rotor-blade row is extensively instrumented. Because of the large axial gap between the IGV row and the first-stage rotor row, approximately 74% of vane chord, the potential flow effects from the IGV row are negligible and the rotor-row periodic disturbances are due only to the vane viscous wakes. To eliminate potential flow effects from the downstream stator vane row on the instrumented first-stage rotor-blades, the first-stage stators and second-stage rotors are removed, as schematically depicted in Fig. 2.

Instrumentation

Both steady and unsteady data are required. The steady data define the chordwise distribution of the rotor-blade surface static pressure. The unsteady data quantify both the unsteady aerodynamic forcing function to the first-stage rotor and the resulting chordwise distribution of the unsteady pressure on the rotor-blade surfaces.

The detailed steady aerodynamic loading on the rotor-blade surfaces is measured with a chordwise distribution of 20 midspan static pressure taps, 10 on each surface (see Fig. 3). The static pressure at the rotor-exit plane, measured with a rotor-drum static tap, is used as the blade surface static pressure reference. These static pressure measurements are made using a rotor-based, 48-port, constant-speed-drive Scanivalve system located in the rotor drum.

The unsteady aerodynamic forcing function to the instrumented first-stage rotor-blade row, i.e., the exit flowfield of

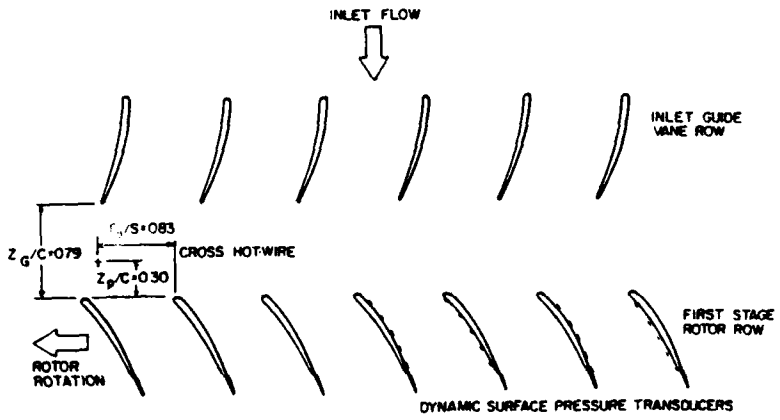

Fig. 4 Schematic of rotating time-variant instrumentation.

the IGVs is measured with a cross hot-wire probe mounted in the rotor frame of reference. The probe is circumferentially located 2.83 blade spacings from the instrumented rotor-blades and 30% of blade chord upstream of the rotor-leading-edge plane as schematically shown in Fig. 4. It is angularly aligned to obtain rotor-relative velocity and flow angle data. The hot wires are calibrated for velocities from 9.1 m/s to 53.4 m/s and ± 35 deg angular variation with the accuracy of the velocity magnitude and angle being 4% and ± 1 deg, respectively.

The measurement of the midspan rotor-blade surface unsteady pressures is accomplished with 20 ultraminiature, high-response transducers embedded in the rotor-blade surfaces at the same chordwise locations as the static pressure taps. Because of blade space limitations, only five transducers are fitted per blade surface and, thus, four instrumented blades, mounted in the rotor row as shown in Fig. 4, are utilized to obtain the 20 unsteady pressure measurements. To minimize the possibility of flow disturbances associated with the inability of the transducer diaphragm to exactly maintain the surface curvature of the blade, a reverse mounting technique is utilized. The pressure surface of one blade and the suction surface of the adjacent blade are instrumented, with transducers embedded in the nonmeasurement surface and connected to the measurement surface by a static tap. The embedded dynamic transducers were both statically and dynamically calibrated. The static calibrations showed good linearity and no discernible hysteresis. The dynamic calibrations demonstrated that the frequency response, in terms of gain attenuation and phase shift, was not affected by the reverse mounting technique. The accuracy of the unsteady pressure measurements, determined from the calibrations, is ± 4%.

The rotating frame-of-reference data signals, i.e., the signals from: 1) the rotor-based Scanivalve static pressure transducer, 2) the 20 rotor-blade surface dynamic pressure transducers, and 3) the cross hot-wire probe are transferred to the stationary reference frame by means of a 40-channel slip ring assembly. Onboard signal conditioning is performed to maintain a good signal-to-noise ratio through the slip rings. The remaining 17 channels of the slip-ring assembly are used to provide excitation to the transducers and excitations and on/off switching to the rotor-based Scanivalve dc motor.

Data Acquisition and Analysis

The rotor-blade surface static pressure data, measured with the rotor-based Scanivalve system, are defined by a root-mean-square error analysis of 20 signal samples with a 95% confidence interval. The reference for these midspan blade pressure measurements is the static pressure at the exit of the rotor, measured on the rotor drum. Thus, the blade surface and the reference static pressures are measured at different

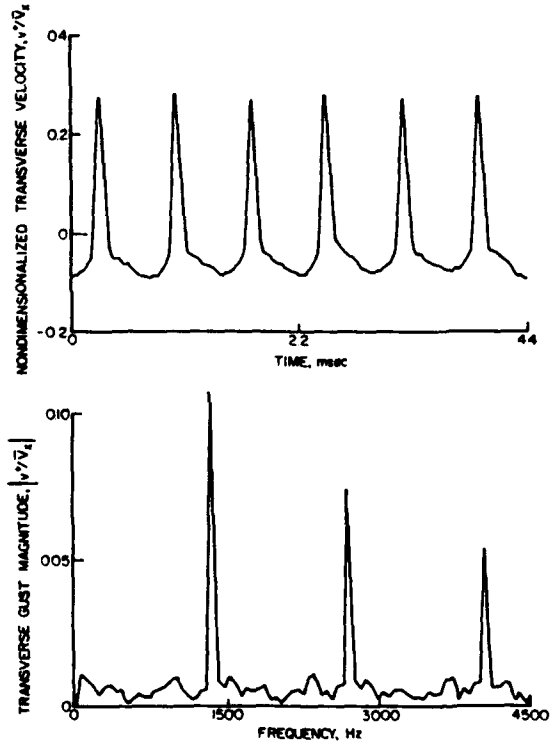

Fig. 5 Periodic transverse velocity and gust entering rotor row.

radii. To account for the resulting difference in the centrifugal forces acting on the air in the static pressure tubing, a correction is applied in calculating the values of the airfoil surface static pressure coefficient defined in Eq. (1)

$$\bar{C}_p = \frac{\bar{p} - \bar{p}_{exit}}{\frac{1}{2}\rho U_t^2} \tag{1}$$

where U_t is the rotor-blade tip speed.

The unsteady data of primary interest are the first harmonic component of the aerodynamic forcing function, i.e., the unsteady rotor inlet flowfield together with the resulting rotor-blade surface first harmonic unsteady pressures and pressure differences. These are determined by defining a digitized ensemble-averaged unsteady aerodynamic data set consisting of the rotating hot-wire and surface pressure transducer signals at each steady operating point. In particular, these time-variant signals are digitized with a high-speed analog-digital (A/D) system and then ensemble averaged. The key to this

averaging technique is the ability to sample data at a preset time, accomplished by an optical encoder mounted on the rotor shaft. The microsecond range step voltage signal from the encoder is the data initiation time reference and triggers the high-speed A/D multiplexer system. To reduce significantly the random fluctuations superimposed on the periodic signals of interest, 200 averages are used. A Fast Fourier Transform (FFT) algorithm is then applied to these ensemble-averaged signals, and the first harmonic component of the unsteady aerodynamic forcing function, the gust, and the resulting rotor-blade surface, unsteady pressures are determined.

The unsteady inlet flow to the rotor row is measured with the rotating cross hot-wire probe, which quantifies the relative velocity and flow angle. The velocity triangle relations depicted in Fig. 1 are then used to determine the inlet flowfield to the rotor, in particular, the first harmonics of the streamwise and transverse gust components u^+ and v^+, respectively. To account for the development of the IGV wakes from the rotating hot-wire measurement location upstream of the rotor-blade row to the rotor-leading-edge plane, the wake similarity and decay model of Lakshminarayana and Davino[13] is utilized.

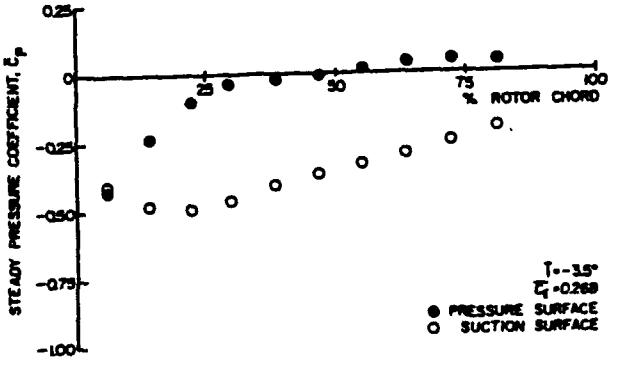

Fig. 6 Blade surface static pressure at low steady loading.

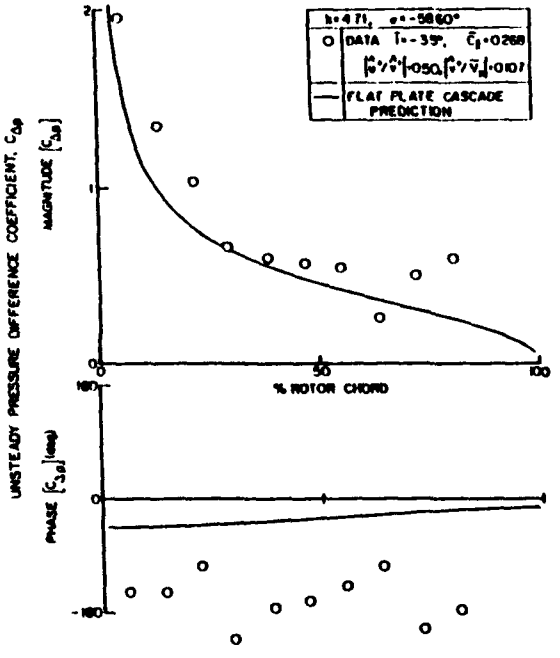

Fig. 7 Baseline blade unsteady pressure difference.

The rotor-blade surface unsteady pressure data, measured with the embedded high-response pressure transducers, are analyzed to determine the first harmonics of the chordwise distribution of the unsteady pressure coefficient C_p and the unsteady pressure difference coefficient, $C_{\Delta p}$. These are defined in Eqs. 2 and are specified from the Fourier coefficients of the digitized blade surface unsteady pressure signals

$$C_p = \frac{\hat{p}}{\rho \bar{V}_x^2 \left(\frac{v^+}{\bar{V}_x}\right)\hat{\beta}} \tag{2a}$$

$$C_{\Delta p} = (C_p)_{\text{pressure}} - (C_p)_{\text{suction}} \tag{2b}$$

where $\hat{p}$ is the first harmonic complex unsteady pressure, $\hat{v}^+$ is the first harmonic complex transverse gust component, $\bar{V}_x$ is the mass-averaged axial velocity, and $\hat{\beta}$ is the relative mean flow angle.

The gust generated rotor-blade row unsteady aerodynamics are presented in the form of chordwise distributions of the first harmonic, complex harmonic pressure and pressure difference coefficients. Also included as a reference where appropriate are predictions from the transverse gust analysis of Smith.[4] This model analyzes the unsteady aerodynamics generated on a flat plate airfoil cascade at zero incidence by a harmonic transverse gust convected with an inviscid, irrotational, subsonic compressible flow.

Results

To investigate and quantify the effects of steady aerodynamic loading on the unsteady gust aerodynamics of a first-stage rotor blade at realistic values of the reduced frequency, a series of experiments are performed. The high-reduced frequency aerodynamic forcing function to the rotor blades is made up of the wakes from the IGVs. Figure 5 presents a sample of the transverse periodic unsteady velocity generated by the IGV wakes and obtained from the rotating cross hot-wire measurement digitized at a rate of 100 kHz. The frequency content of this signal is also demonstrated by the Fourier components, determined by means of a FFT algorithm. The multistage effects associated with operating in the super-resonant flow regime wherein acoustic waves propagate are also considered.

Baseline

The baseline steady and gust-generated, time-variant data for the investigation of the effect of steady loading on rotating blade-row unsteady aerodynamics are obtained at a compressor operating condition corresponding to a low level of steady rotor-blade aerodynamic loading. This also most closely corresponds to the reference transverse gust model, which considers a flat plate airfoil cascade and, thus, no steady loading. For this compressor configuration, this lowest loading condition is defined by a first-stage rotor-blade row mean incidence angle of -3.5 deg. The chordwise distribution of the blade surface static pressure coefficient is presented in Fig. 6.

The first harmonic, gust-generated, unsteady pressure difference coefficient data, with the transverse gust flat plate cascade prediction as a reference, are presented in Fig. 7. Overall, the magnitude data exhibit fair correlation with the prediction with the data increased in value relative to the prediction over the front and midchord regions of the blade. Also, the aft three chordwise data points increase in a somewhat linear fashion, contrary to the trend of the prediction. The correlation of the phase data with the prediction is relatively poor, with the differences being on the order of 90 deg over the entire chord. These differences between the complex unsteady pressure difference data and the flat plate predictions are associated with the airfoil profile and nonzero mean incidence, i.e., the steady loading, as will be discussed in the next section.

Steady Loading Effects

The effect of steady aerodynamic loading, characterized by the mean incidence angle, on the rotor-blade surface static pressure coefficient is shown in Fig. 8. The level of steady loading only affects the static pressure distribution on the rotor-blade pressure surface over the front 40% of the chord. On the suction surface, the variation in the steady loading has a large effect on the static pressure distribution over the entire chord. Also, these data exhibit no indication of steady flow separation.

The effect of steady aerodynamic loading level on the first harmonic, complex, unsteady pressure coefficient on the rotor-blade pressure surface is shown in Fig. 9. The form of the dimensionless unsteady pressure coefficient specified in Eq. (2a) results in a compression of the unsteady pressure magnitude data over the entire pressure surface for all but the two lowest steady loading levels. For these two loading cases, large variations are found in the magnitude data in the neighborhood of the quarter chord. This corresponds to the previously noted effects of steady loading on the rotor-blade surface static pressure wherein loading primarily influenced the front part of the pressure surface. In particular, the static pressure coefficient value for the hub static pressure coefficient upstream of the rotor row is approximately -0.24, thereby indicating that the mean flowfield accelerates around the pressure surface leading edge before decelerating (diffusing) for the two lowest mean incidence angles, i.e., the static pressure coefficient decreases and then increases. Similar to the magnitude data, the effects of steady loading on the pressure surface unsteady pressure phase collapse into approximately one curve with the exception being the lowest steady loading level in the front chord region.

In summary, for the chordwise region where the mean flowfield does not accelerate, i.e., the mid-to-aft chord region for all steady loading levels and the front chord region for the three high steady loading levels, the data compress for all gust amplitude ratios, which indicates that steady loading as characterized by the mean flow incidence is a key mechanism for the low-camber pressure surface unsteady aerodynamic wake response. However, in an accelerating mean flowfield, i.e., the front chord region for the two low steady loading levels, mean flowfield interactions with the unsteady gust are also important.

The entire suction surface unsteady pressure chordwise distribution, both magnitude and phase, is affected by the level of the steady aerodynamic loading (see Fig. 10). Again, this corresponds to the previously presented suction surface static pressure data variation with mean incidence angle. In particular, the front-to-mid-chord region data show a decreasing-increasing magnitude trend with chord with the minimum magnitude chordwise location moving forward with increasing steady loading. This minimum corresponds to the minimum in the static pressure chordwise distribution (see Fig. 8), wherein the chordwise location of the change from accelerating to decelerating mean flow moves forward with increasing mean incidence. Thus, similar to the pressure surface unsteady response in the front chord region at negative mean incidence flow, the unsteady gust interacts with the accelerating mean flowfield around the suction surface in the front chord region. In the mid-to-aft chord, a second decreased magnitude region occurs, with the minimum moving forward with increased mean incidence. In the suction surface aft chord region, where the boundary layer and other viscous effects are at their greatest due to the severe adverse pressure gradient, the gust interaction with this mean flowfield most likely causes the decreasing-increasing magnitude trend shown. As the mean flow incidence angle is increased, i.e., steady loading increases, the aft

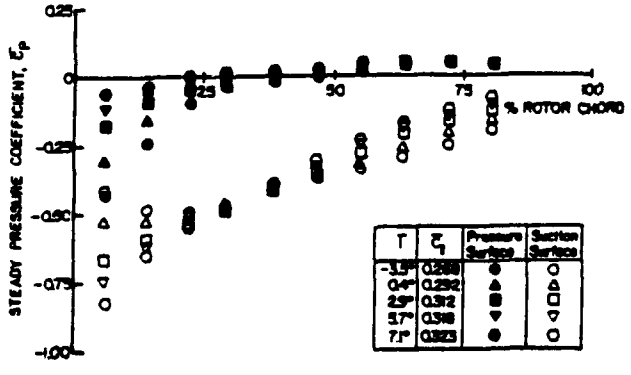

Fig. 8 Steady loading effect on blade surface static pressure.

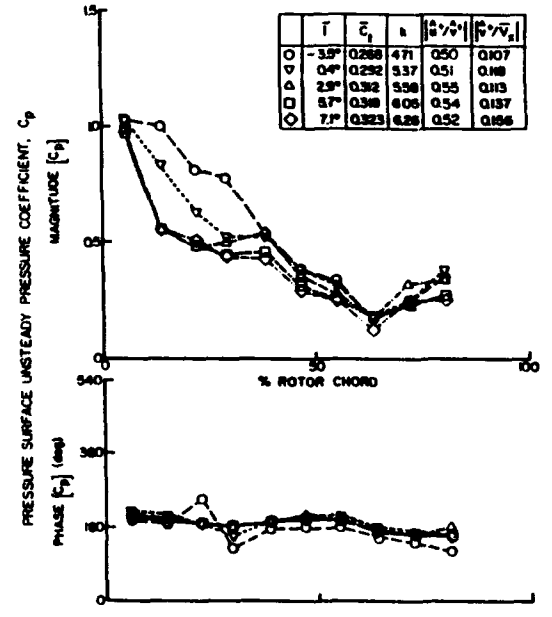

Fig. 9 Loading effect on rotor-blade pressure, surface unsteady pressure.

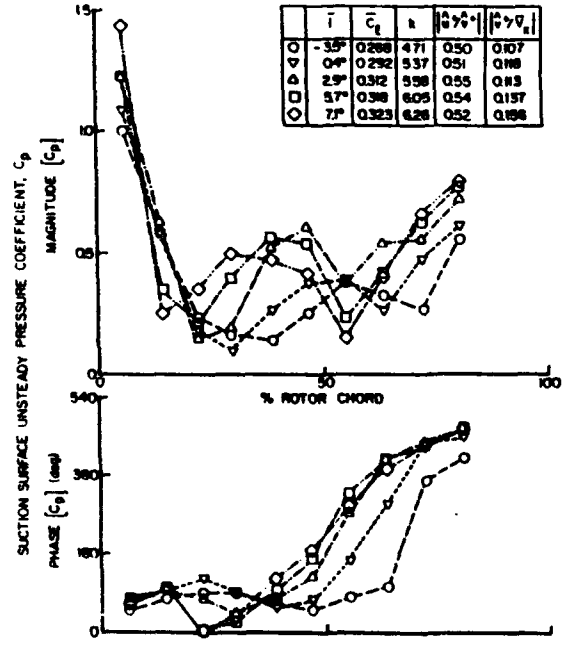

Fig. 10 Loading effect on rotor-blade suction surface unsteady pressure.

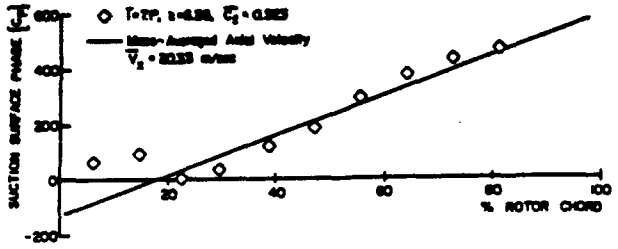

Fig. 11 Chordwise distribution of suction surface phase data at high loading.

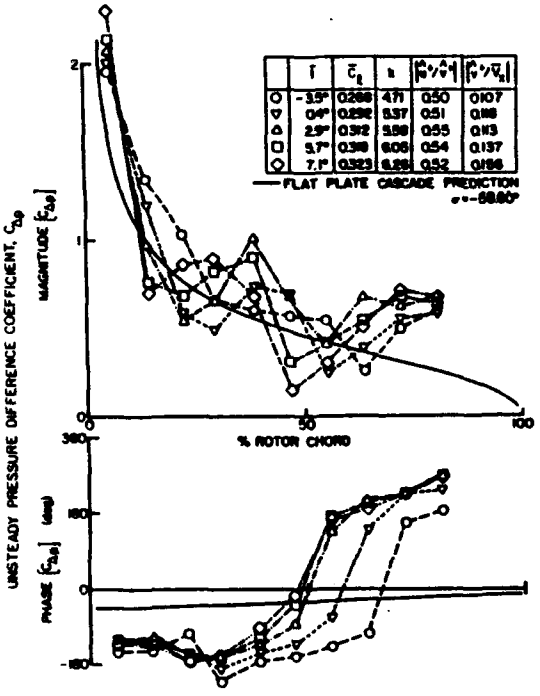

Fig. 12 Loading effect on blade unsteady pressure difference.

suction surface diffusion rate increases and, thus, the large viscous effects move forward, similar to the magnitude minimum trends discussed above. However, verification of this hypothesis cannot be made, with this requiring substantially increased unsteady flow instrumentation to obtain detailed boundary layer and completed unsteady flowfield data.

The steady loading level primarily affects the phase data on the aft three quarters of the rotor-blade suction surface. As the mean incidence angle is increased from the baseline low-loading condition, the chordwise variation of the phase data on the aft part of the suction surface becomes linear, with the extent of this linear distribution increasing with increasing mean incidence. This linear chordwise distribution of the phase data indicates the existence of a convected wave phenomena. This is more clearly demonstrated in Fig. 11, wherein the highest steady loading level suction surface phase data are replotted together with the linear phase curve corresponding to the mass-averaged axial velocity convection time lag. As seen, the wave on the suction surface is convected at approximately the mean axial velocity of the flow through the rotor-blade row. Other authors[8,14] have noted this linear phase distribution corresponding to the mean axial velocity. However, the physical explanation of this wave phenomenon could not be made. This wave phenomenon is related to the gust interacting with the large viscous effects along the suction surface mid-to-aft chord. However, once again, until detailed measurements are made, but this cannot be verified.

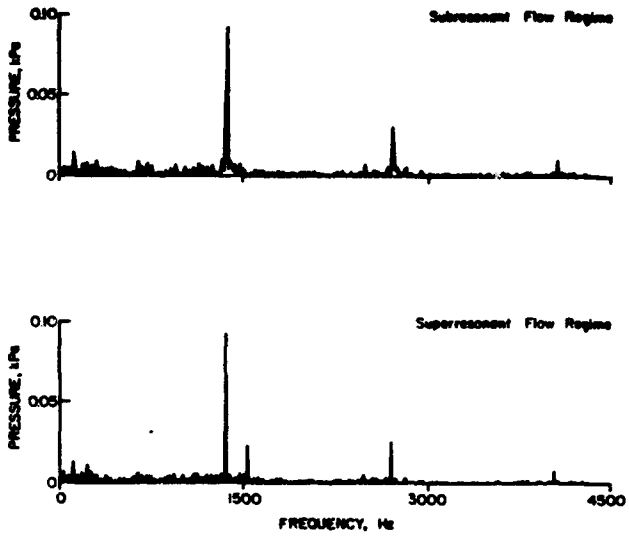

Fig. 13 Harmonic content variation with number of stators in downstream rows.

In summary, on this high-camber suction surface, the steady loading affects the interaction between the mean flowfield and the unsteady gust and, thus, the unsteady aerodynamic response over the entire blade surface. On the front half of the surface, an accelerating mean flowfield affects the unsteady pressure gust response, whereas on the aft half of the surface, large boundary-layer viscous effects affect the unsteady pressure gust response.

The variation of the complex, unsteady pressure difference coefficient data with steady loading level is shown in Fig. 12. The effects of loading on the previously presented individual pressure and suction surface magnitude and phase data are still apparent with the suction surface effects being dominant. For example, analogous to the loading trends on the suction surface, the unsteady difference magnitude data show two decreased magnitude regions, one in the front chord region and the other in the mid-to-aft chord region, with the chordwise location of the magnitude minimums moving forward with increased steady loading. Also, the extent of the increased difference magnitude data on the aft portion of the blade increases with increased steady loading. The difference phase data remain nearly constant over the front portion of the blade. The chordwise location where the rapid increase in the value of the phase data begins to occur moves forward with increasing steady loading. The increased steady loading causes the chordwise distribution of the difference magnitude and phase data to differ greatly from the prediction with the magnitude data not just decreasing with increasing chord and the phase data not remaining nearly constant with chord per the predictions. Thus, to accurately predict the gust generated unsteady loading, the physical unsteady flow effects discussed in the previous blade surface sections must be adequately modeled.

Super-Resonant Flow Regime

The physical description of an acoustic stator-rotor interaction given in Ref. 15 clearly explains the acoustic environment in which resonant conditions occur. The configurations for which subresonant and super-resonant conditions occur for these experiments are described below. The compressor configuration utilized for the above described steady loading experiments had 43 blades in both rotor rows and 31 vanes in each far downstream stator row (see Fig. 2). This corresponds to a subresonant condition wherein the acoustic waves generated by the downstream rotor-stator interactions do not propagate appreciably upstream and, thus, the first-stage rotor row is not affected by the downstream rotor-stator interactions. A

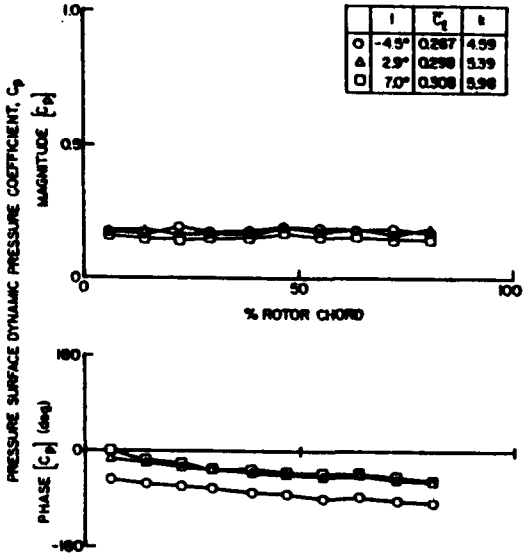

Fig. 14 Blade pressure surface unsteady data at acoustic wave frequency.

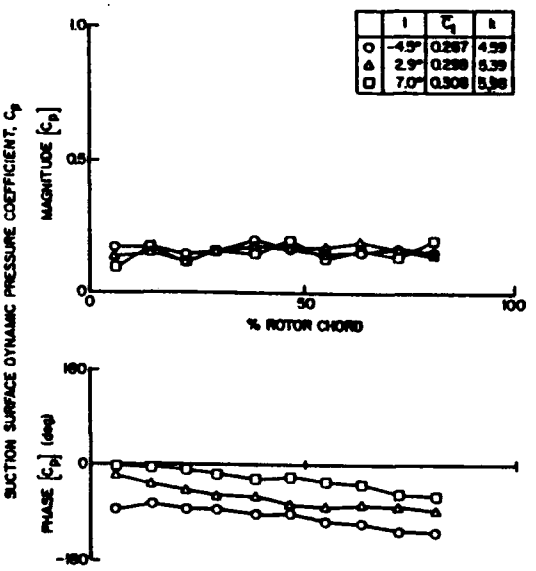

Fig. 15 Blade suction surface unsteady pressure data at acoustic wave frequency.

super-resonant condition was also established in the compressor, accomplished by altering the number of vanes in each stator row. In particular, the number of blades in each rotor row was held constant at 43 with the number of stator vanes changed to 41 vanes per stator row. In this configuration, acoustic waves generated by the downstream rotor-stator interactions propagate upstream to the instrumented first-stage rotor-blade row.

With the compressor operating in a downstream rotor-stator interaction super-resonant flow regime generated with 41 vanes per stator row and 43 blades per rotor row, the upstream propagating acoustic wave could not be detected by the rotating cross hot wire located upstream of the first-stage rotor row. Therefore, to demonstrate the relative amplitude of the downstream generated acoustic wave, Fig. 13 shows the Fourier decomposition of the signal from the first-stage rotor-blade suction surface pressure transducer located nearest the leading edge for both the subresonant condition and the super-resonant conditions. Clearly seen is the relatively large amplitude acoustic wave generated by the downstream rotor-stator interactions. In particular, in the super-resonant condition with 41 vanes per stator row, the transducer signal contains a component at a frequency of 1537.5 Hz that 1) is not seen in the baseline subresonant data obtained with 31 vanes per stator row and 2) has approximately one-fourth the amplitude of that at the IGV wake passing frequency.

The resulting first harmonic, complex, unsteady pressure data on the pressure and suction surfaces of the first-stage rotor-blade row generated by the propagating acoustic wave at three steady loading levels are shown in Figs. 14 and 15. The steady loading has minimal effect on the unsteady pressure magnitude data on either blade surface with both surfaces showing nearly identical constant magnitude vs chord distribution for all three steady loading levels. The phase data chordwise trends are also unaffected by steady loading, but the data increase in level slightly with increased loading. A wave speed of approximately 320 m/s on each surface of the rotor blade is calculated from the linear, constant slope, chordwise distributions of these phase data. This corresponds to the speed of propagation of an upstream traveling acoustic wave, i.e., the speed of sound minus the axial velocity. Since the unsteady pressure magnitude and phase chordwise distributions are nearly identical for both the pressure surface and suction surface, the unsteady pressure difference distribution across the blade is nearly zero. Therefore, the unsteady lift due to acoustic waves is also nearly zero.

Summary and Conclusions

The effects of steady aerodynamic loading on the first harmonic unsteady gust aerodynamics of a first-stage rotor blade at realistic high values of the reduced frequency were investigated and quantified. This was accomplished by means of a series of experiments performed in an extensively instrumented axial flow research compressor with the high-reduced frequency gusts generated by the wakes from the IGV. The analysis of these rotor-blade surface steady and unsteady data determined the following.

1) Steady loading affects the rotor-blade, static pressure distributions on the front portion of the pressure surface and over the entire suction surface with no steady flow separation indicated.

2) The unsteady pressure response on the blade pressure surface, i.e., the low-camber surface, is primarily affected by the level of steady loading as characterized by the mean flow incidence angle except in the accelerating mean flowfield of the front chord region at negative mean flow incidence.

3) The unsteady pressure response on the high-camber blade suction surface is affected by the level of steady loading, i.e., the accelerating mean flowfield in the front half of the surface and the large viscous regions in the aft half of the surface.

4) The unsteady pressure difference data reflect the effects of loading on the pressure and suction surface unsteady data with the suction surface effects being dominant.

5) These steady loading effects cause the chordwise distribution of the magnitude and phase data to differ greatly from the flat plate cascade predictions. A super-resonant condition was also established in the compressor, accomplished by altering the number of vanes in each downstream stator row. This resulted in a relatively large amplitude upstream propagating acoustic wave generated by the downstream rotor-stator row interactions.

6) In the leading-edge region of the first-stage, rotor-blade row suction surface, the acoustic wave has an amplitude approximately one-fourth that of the first harmonic of the IGV wakes.

7) Loading has minimal effect on the resulting rotor-blade surface acoustic wave generated unsteady pressure data with the only effect being a slight phase increase with increased steady loading.

8) Since the unsteady pressure chordwise magnitude and phase distributions are nearly identical for both the pressure

and suction surfaces, the unsteady pressure difference across the blade and, thus, unsteady lift, due to acoustic waves is nearly zero.

Acknowledgments

Research was sponsored by the Air Force Office of Scientific Research under Contract F49620-88-C-0022.

References

[1]Sears, W. R., "Some Aspects of Non-Stationary Airfoil Theory and its Practical Application," *Journal of Aeronautical Sciences*, Vol. 8, No. 3, 1941, pp. 104–108.

[2]Whitehead, D. C., "Force and Moment Coefficients for Vibrating Airfoils in Cascade," British Aeronautical Research Council, London, ARC R&M 3254, Feb. 1960.

[3]Fleeter, S., "Fluctuating Lift and Moment Coefficients for Cascaded Airfoils in Nonuniform Compressible Flow," *Journal of Aircraft*, Vol. 10, No. 2, Feb. 1973, pp. 93–98.

[4]Smith, S. N., "Discrete Frequency Sound Generation in Axial Flow Turbomachines," British Aeronautical Research Council, London, ARC R&M 3709, 1971.

[5]Goldstein, M. E., and Atassi, H., "A Complete Second-Order Theory for the Unsteady Flow about an Airfoil due to a Periodic Gust," *Journal of Fluid Mechanics*, Vol. 74, 1976, pp. 741–766.

[6]Atassi, H. M., "The Sears Problem for a Lifting Airfoil Revisited-New Results," *Journal of Fluid Mechanics*, Vol. 141, 1984, pp. 109–122.

[7]Chiang, H. D., and Fleeter, S., "Prediction of Loaded Airfoil Unsteady Aerodynamic Gust Response by a Locally Analytical Method," *International Journal of Mathematical Modeling*, Vol. 10, No. 3, 1988, pp. 193–206.

[8]Fleeter, S., Jay, R. L., and Bennett, W. A., "Rotor Wake Generated Unsteady Aerodynamic Response of a Compressor Stator," *ASME Journal of Engineering for Power*, Vol. 100, Oct. 1978, pp. 664–675.

[9]Fleeter, S., Jay, R. L., and Bennett, W. A., "Wake Induced Time Variant Aerodynamics Including Rotor-Stator Axial Spacing Effects," *ASME Journal of Fluids Engineering*, Vol. 103, No. 1, March 1981, pp. 59–66.

[10]Capece, V. R., Manwaring, S. R., and Fleeter, S., "Unsteady Blade Row Interactions in a Multi-Stage Compressor," *Journal of Propulsion and Power*, Vol. 2, No. 2, 1986, pp. 168–174.

[11]Capece, V. R., and Fleeter, S., "Unsteady Aerodynamic Interactions in a Multi-Stage Compressor," *ASME Journal of Turbomachinery*, Volume 109, No. 3, July 1987, pp. 420–428.

[12]Hardin, L. W., Carta, F. O., and Verdon, J. M., "Unsteady Aerodynamic Measurements on a Rotating Compressor Blade Row at Low Mach number," *ASME Journal of Turbomachinery*, Vol. 109, No. 4, Oct. 1987, pp. 499–507.

[13]Lakshminarayana, B., and Davino, R., "Mean Velocity and Decay Characteristics of the Guidevane and Stator Blade Wake of an Axial Flow Compressor," American Society of Mechanical Engineers, New York, ASME Paper 79-GT-9, April 1979.

[14]Hodson, H. P., "Measurement of the Wake-Generated Unsteadiness in the Rotor Passages of Axial-Flow Turbines," American Society of Mechanical Engineers, New York, ASME Paper 84-GT-189, June 1984.

[15]Carta, F. O., "Aeroelasticity and Unsteady Aerodynamics," *The Aerothermodynamics of Aircraft Gas Turbine Engines*, edited by G. Oates, Air Force AeroPropulsion Lab, AFAPL-TR-78-52, July 1978, pp. 22-1–22-54.

APPENDIX V

Unsteady Aerodynamic Gust Response Including Steady Flow Separation

AIAA Journal

Unsteady Aerodynamic Gust Response Including Steady Flow Separation

Sanford Fleeter,* Vincent R. Capece,† and Hsiao-Wei D. Chiang‡
Purdue University, West Lafayette, Indiana

A series of experiments are performed to investigate and quantify the unsteady aerodynamic response of an airfoil to a high reduced frequency gust including the effects of the gust forcing function waveform, airfoil loading, and steady flow separation. This is accomplished by using an axial flow research compressor to experimentally model the high reduced frequency gust forcing function and replacing the last stage stator row with isolated instrumented airfoils. Appropriate data are correlated with predictions from flat plate and cambered airfoil convected gust models. The airfoil surface steady loading is shown to have a large effect on the unsteady aerodynamic response. Also, the steady flow separation has a significant influence on the gust response, particularly upstream of the separation point and in the airfoil trailing-edge region.

Nomenclature

C = airfoil chord
$\bar{C}_l$ = steady lift coefficient $\int_0^C (\bar{p}_p - \bar{p}_s)\,dx/\frac{1}{2}\rho U_t^2 C$
$\hat{C}_p$ = first harmonic unsteady pressure coefficient $\Delta\hat{p}/\rho V_x \hat{v}^+$
$\bar{C}_p$ = static pressure coefficient $(\bar{p} - \bar{p}_{exit})/\frac{1}{2}\rho U_t^2$
$\mathcal{K}$ = gust propagation direction vector
k_1 = reduced frequency, $\omega C/2V_x$
k_2 = transverse gust wave number
$\bar{p}$ = airfoil surface static pressure
$\bar{p}_{exit}$ = exit static pressure
$\Delta\hat{p}$ = first harmonic unsteady pressure difference
$\hat{u}^+$ = first harmonic chordwise gust
U_t = rotor blade tip speed
$\hat{v}^+$ = first harmonic transverse gust
V_x = absolute axial velocity
α_0 = angle of attack
ρ = inlet air density

Introduction

THE unsteady flow past a stationary airfoil is of primary concern in many important applications. For example, the unsteady interaction of an airfoil with gusts and similar vortical disturbances plays a significant role in the aerodynamics, dynamic loading, aeroelasticity, and acoustics of modern aircraft, missiles, helicopter rotors, advanced turboprops, and turbomachines. As a result, the interest in unsteady flow theory initiated by Theodorsen,[1] Kussner,[2] and Sears[3] has continued to the present.

Theoretical gust models have typically been restricted to thin-airfoil theory, with the unsteady gust disturbance assumed to be small as compared to the mean steady potential flowfield. However, in most applications, airfoils with arbitrary shape, large camber, and finite angles of attack are required. In an attempt to meet this need, Horlock[4] and Naumann and Yeh[5] developed heuristic second-order analyses that take into account some second-order terms. These analyses showed that the unsteady aerodynamic forces acting on an airfoil were affected by both the small incidence angle and the small airfoil camber. However, these models neglect some second-order terms and also assume a small angle of attack. Thus, these results are only approximate and cannot be extended to finite-incidence angles or large airfoil camber.

It is apparent that the thin airfoil approach is not adequate for many applications of interest. In this regard, Goldstein and Atassi[6] and Atassi[7] developed a theory for the inviscid incompressible flow past an airfoil that fully accounts for the distortion of the impinging gust by the mean flow. The theory assumes that the fluctuating flow velocity is small compared to the mean velocity, with the unsteady flow linearized about the full potential steady flow, and accounts for the effects of both airfoil profile and angle of attack.

Experimental investigations have typically been restricted to low-reduced-frequency aerodynamic gusts. In part, this is due to the difficulties associated with generating a periodic unsteady gust, with low reduced frequency gust tunnels having been developed by Holmes,[8] Satyanarayana, Gostelow, and Henderson,[9] and Ostdiek,[10] for example. Also contributing is the difficulty in obtaining and analyzing the fundamental high-frequency unsteady data that define both the aerodynamic forcing function and the resulting airfoil surface pressure distributions. The acquisition and analysis of such high-frequency data have only recently become possible with the development and availability of miniature high-response pressure transducers, digital instrumentation, and computers for both control of instrumentation and digital data acquisition and analysis.

The above noted experiments and analyses are all concerned with attached steady flow. Separated flow oscillating airfoil phenomena, including stall flutter and dynamic stall, also have been addressed. Thus, oscillating airfoil models and experiments have considered the effects of steady loading and flow separation, for example, Refs. 11–17. In this regard it should be noted that only minimal attention has been directed toward the effect of steady loading and flow separation on the unsteady aerodynamic response of an airfoil to a periodic gust.

In this paper the effects of the gust waveform, as characterized by the chordwise (parallel) and transverse (normal) gust

Received May 9, 1988; revision received Oct. 10, 1988.

*Professor, School of Mechanical Engineering and Director, Thermal Sciences and Propulsion Center. Associate Fellow AIAA.
†Air Force Research in Aero Propulsion Technology (AFRAPT) Trainee, Thermal Sciences and Propulsion Center, School of Mechanical Engineering.
‡Graduate Research Assistant, Thermal Sciences and Propulsion Center, School of Mechanical Engineering.

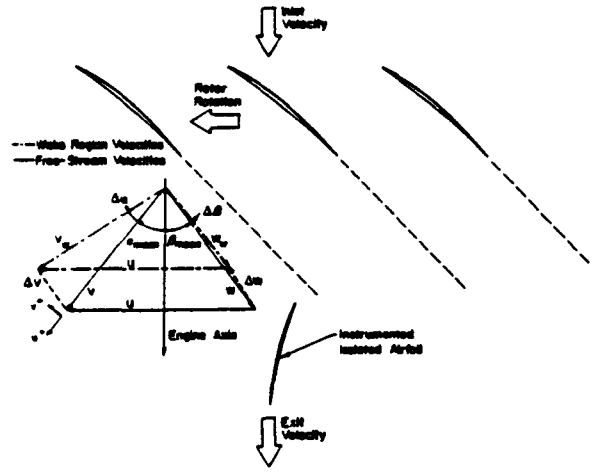

Fig. 1 Schematic of flowfield.

components u^+ and v^+ depicted in Fig. 1, airfoil loading, and steady flow separation on the unsteady aerodynamic response of an airfoil are experimentally investigated at high reduced frequency values for the first time. This is accomplished by 1) using an axial flow research compressor to experimentally model the high reduced frequency aerodynamic gust forcing function, 2) replacing the last stage stator row with instrumented isolated airfoils, and 3) developing and using computer-based time-variant digital data acquisition and analysis techniques, including ensemble averaging and Fast Fourier Transforms (FFT), for the analysis of the periodic data. In particular, high reduced frequency aerodynamic gusts are generated by the upstream rotor blade wakes, with the unsteady aerodynamic gust response determined by replacing the downstream stator row with static and dynamically instrumented isolated airfoils. Thus, there is complete experimental modeling of the basic unsteady aerodynamic phenomena inherent in this high reduced frequency unsteady interaction including angle-of-attack effects, the velocity and pressure variations, and the waveform of the aerodynamic forcing function.

Research Compressor

The Purdue axial flow research compressor with the last stage stator row replaced by an isolated airfoil is used for these experiments. It is driven by a 15 hP dc electric motor over a speed range of 300–3000 rpm. The wakes from the upstream rotor blades are the source of the unsteady surface pressures on the downstream isolated airfoil, i.e., the rotor wakes define the aerodynamic forcing function to the airfoil as depicted schematically in Fig. 1. The 43 rotor blades and the isolated airfoil are free vortex design airfoils with a British C4 section profile, a chord of 30 mm, and a maximum thickness-to-chord ratio of 0.10.

The variations in the airfoil steady loading are accomplished by compressor throttling and adjusting the setting angles of the instrumented airfoils, thereby altering the airfoil angle of attack. The detailed steady aerodynamic loading of the instrumented airfoils is specified by the chordwise distribution of the airfoil surface steady static pressure coefficient with the overall loading level given by the angle of attack and the steady lift coefficient.

The waveform of the aerodynamic forcing function is defined by the first harmonic chordwise and transverse gust components $\hat{u}^+$ and $\hat{v}^+$, respectively. The forcing function waveform variations to the instrumented last stage airfoils are accomplished by independently circumferentially indexing the upstream compressor vane rows relative to one another while maintaining a constant instrumented airfoil steady loading distribution.

Instrumentation

Both steady and unsteady data are required. The steady data define the detailed airfoil surface aerodynamic loading. The unsteady data quantify the time-variant aerodynamic forcing function to the isolated airfoil, i.e., the airfoil unsteady inlet flowfield and the resulting chordwise distribution of the time-variant pressures on the surfaces of the downstream airfoil. Flow visualization studies showed the flow to be two-dimensional on the midspan streamline. Thus, midspan chordwise distributions of airfoil surface static and dynamic instrumentation are used.

The unsteady aerodynamic forcing function to the airfoil, the time-variant inlet flowfield, is measured with a cross hot-wire probe. The airfoil mean absolute inlet flow angle is determined by rotating the cross-wire probe until a zero voltage difference is obtained between the two hot-wire signals. This mean angle is subsequently used as a reference to calculate the airfoil angle of attack and the instantaneous absolute and relative flow angles.

The airfoil surface time-variant pressure measurements are accomplished with flush-mounted ultraminiature high-response transducers. To minimize potential flow disturbances due to the transducer mounting or the inability of the transducer diaphragm to exactly maintain the surface curvature of the airfoil, a reverse mounting technique is used. The pressure surface of one airfoil and the suction surface of a second are instrumented, with the transducers embedded in the nonmeasurement surface and connected to the measurement surface by a static tap.

To assure the accuracy of the experiments and to minimize the number of stator row reconfigurations needed to obtain the isolated airfoil steady and unsteady data of interest, the complete last stage compressor stator row was replaced with a stator row comprised of only two airfoils, these being either the statically instrumented airfoils or the dynamically instrumented airfoils. This corresponds to a vane row with a solidity (chord/spacing) of less than 0.10, which results in a spacing between the instrumented vanes large enough so that the influence of the neighboring vanes is negligible, i.e., each vane is essentially an isolated airfoil. For example, the complex unsteady lift predicted by inviscid, incompressible transverse gust flat plate models at a reduced frequency of 5.0 are $(-0.0812, -0.1596)$ for an isolated airfoil and $(-0.0809, -0.1575)$ for a cascade with solidity of 0.1.

Data Acquisition and Analysis

The steady-state pressure data are acquired with a 48-channel Scanivalve system. Under computer control, the Scanivalve is calibrated each time data are acquired, with compensation automatically made for variations in the zero and span output. As part of the steady-state data acquisition and analysis process, a root mean square error analysis is performed. The steady data are defined as the mean of 30 samples, with the 95% confidence intervals determined.

The time-variant data from the hot-wire probe and the dynamic pressure transducers are obtained under computer control by first conditioning their signals and then digitizing them with a high-speed A-D system. This eight-channel system is able to digitize signals simultaneously at rates to 5 MHz per channel, storing 2048 points per channel. In addition, after conditioning the time-variant hot-wire and pressure transducer signals are monitored by a dynamic signal processor that can digitize, average, and Fourier decompose unsteady analog signals.

The time-variant data of interest are periodic, being generated at rotor blade passing frequency, with a digital ensemble averaging technique used for data analysis. As will be discussed, the key to this technique is the ability to sample data at a preset time. This is accomplished by means of an optical encoder mounted on the rotor shaft. The microsecond-range square wave voltage signal from the encoder is the time or data initiation reference that triggers the high-speed A-D

system. The time-variant signal is sampled and digitized over a time frame that is greater than the periodic signal component characteristic time. With the same initiation reference, i.e., the signal from the rotor-shaft-mounted optical encoder, a series of corresponding digitized signals is generated by repeating this signal sampling and digitization process. The time-variant signal ensemble average is then determined by averaging this series of digital data samples.

At each steady-state operating point, an averaged time-variant data set is obtained that consists of the hot-wire and the airfoil-mounted transducer signals digitized at a rate of 200 kHz and ensemble-averaged over 200 rotor revolutions. This sample rate allows approximately 91 points between each rotor blade at the design compressor rotational speed. These rotor revolutions are not consecutive due to the finite time required for the A-D multiplexer system to sample the data and the computer to then read the digitized data. Each of these digitized signals is Fourier decomposed into harmonics by means of a Fast Fourier Transform algorithm.

The first harmonic magnitude and phase angle referenced to the data initiation pulse are determined from the Fourier analysis of the data. To then relate the rotor-wake-generated velocity profiles with the first harmonic surface dynamic pressures on the instrumented downstream airfoil, the rotor exit velocity triangles are examined. The change in the rotor relative exit velocity that occurs as a result of the wake from a rotor blade is seen in Fig. 1. This velocity deficit creates a change in the absolute velocity vector, which is measured with the cross-wire probe. From this instantaneous absolute flow angle and velocity, the rotor exit relative flow angle and velocity and the amplitude and phase of the perturbation quantities are determined. The normal v^+ and parallel u^+ perturbation velocities are determined from the following relationships:

$$u^+ = V_{mean} - V_w \cos(\alpha - \alpha_{mean}), \quad v^+ = V_w \sin(\alpha - \alpha_{mean}) \tag{1}$$

where V_{mean} is the mean flow velocity, V_w the wake velocity, α the wake absolute flow angle, and α_{mean} the mean absolute flow angle.

The hot-wire probe is positioned upstream of the leading edge of the instrumented airfoil. To relate time-based events as measured by this hot-wire probe to the unsteady pressures on the airfoil surfaces, the following assumptions are made: 1) the wakes are identical at the hot-wire and the instrumented airfoil leading-edge plane, and 2) the wakes are fixed in the relative frame. At a steady operating point, the hot-wire data are analyzed to determine the absolute flow angle and the rotor exit relative flow angle. Using the above two assumptions, the wake is located relative to the hot-wire and the leading edges of the instrumented airfoil suction and pressure surfaces. From this, the times at which the wakes are present at various locations are determined. The incremental times between occurrences at the hot-wire and the instrumented airfoil leading-edge plane are then related to phase differences between perturbation velocities and the airfoil surface.

The final form of the unsteady pressure data defines the chordwise variation of the first harmonic pressure difference across the chord-line of a stator vane and is presented as a nondimensional complex unsteady pressure difference across the airfoil chord in the format of the magnitude and the phase lag referenced to a transverse gust at the airfoil leading edge.

Predicted Gust Response

An unsteady aerodynamic gust response model that considers steady aerodynamic loading is needed to provide a baseline for accurate interpretation of the unsteady data. This is accomplished using the complete first-order model, i.e., the thin airfoil approximation is not used, and locally analytical solution developed by Chiang and Fleeter.[18] This model considers the flow of a two-dimensional unsteady aerodynamic gust convected with the mean flow past a thick, cambered airfoil at finite angle of attack α_0 as schematically depicted in Fig. 2. The periodic gust amplitude and harmonic frequency are denoted by A and ω, respectively. The two-dimensional gust propagates in the direction $\mathscr{K} = k_1\hat{i} + k_2\hat{j}$, where k_1 is the reduced frequency, and k_2 is the transverse gust wave number, i.e., the transverse component of the gust propagation direction vector.

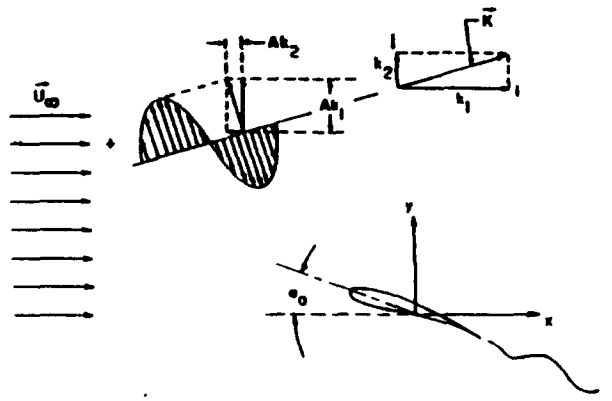

Fig. 2 Flow of a two-dimensional airfoil past a cambered airfoil.

The unsteady flowfield is considered to be rotational and is linearized about the full steady potential flow past the airfoil. Thus, the effects of airfoil thickness and camber as well as mean flow angle of attack are completely accounted for through the mean potential flowfield. The steady potential flowfield is independent of the unsteady flowfield. However, the strong dependence of the unsteady aerodynamics on the steady effects of airfoil geometry and angle of attack are manifested in the coupling of the unsteady and steady flowfields through the unsteady boundary conditions.

A locally analytical solution is then developed. In this method, the discrete algebraic equations that represent the flowfield equations are obtained from analytical solutions in individual grid elements. A body-fitted computational grid is used. General analytical solutions to the transformed Laplace equation are developed by applying these solutions to individual grid elements, i.e., the integration and separation constants are determined from the boundary conditions in each grid element. The complete flowfield is then obtained by assembling these locally analytical solutions.

Results

Nonseparated Flow

A low steady aerodynamic loading condition is established by setting the airfoil at an angle of attack of 0.1 deg. The data defining the airfoil surface static pressure distributions are presented in Fig. 3. There is a smooth chordwise pressure variation on each airfoil surface, with no indication of flow separation. Also, there is generally good correlation between the data and the inviscid Chiang-Fleeter cambered airfoil steady flow prediction, with the exception of the airfoil leading-edge region.

The aerodynamic gust waveform is characterized by the ratio of the first harmonic chordwise-to-normal gust components ($\hat{u}^+/\hat{v}^+$). The effect of the gust waveform on the unsteady aerodynamic response of the airfoil is considered by establishing compressor configurations such that the airfoil angle of attack and steady surface static pressure distributions are maintained per Fig. 3, but with the gust component ratio taking on values of 0.19, 0.35, and 0.53 (Fig. 4).

The effect of the aerodynamic gust waveform on the resulting unsteady pressure difference data is shown in Fig. 5. The

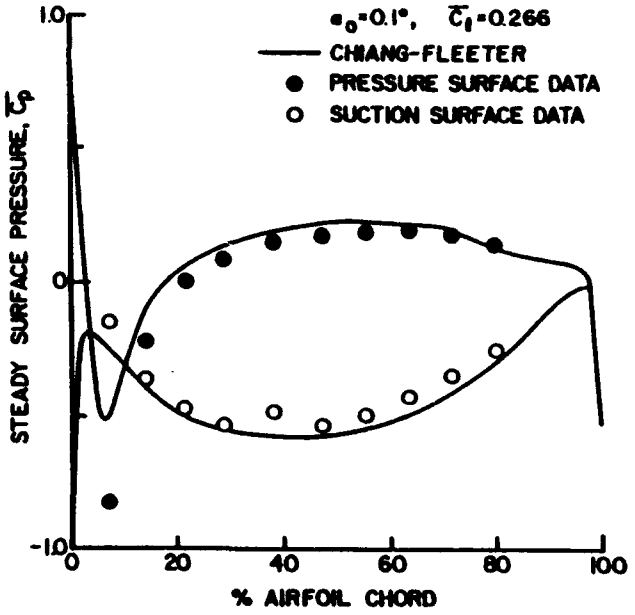

Fig. 3 Steady airfoil surface static pressure at low loading.

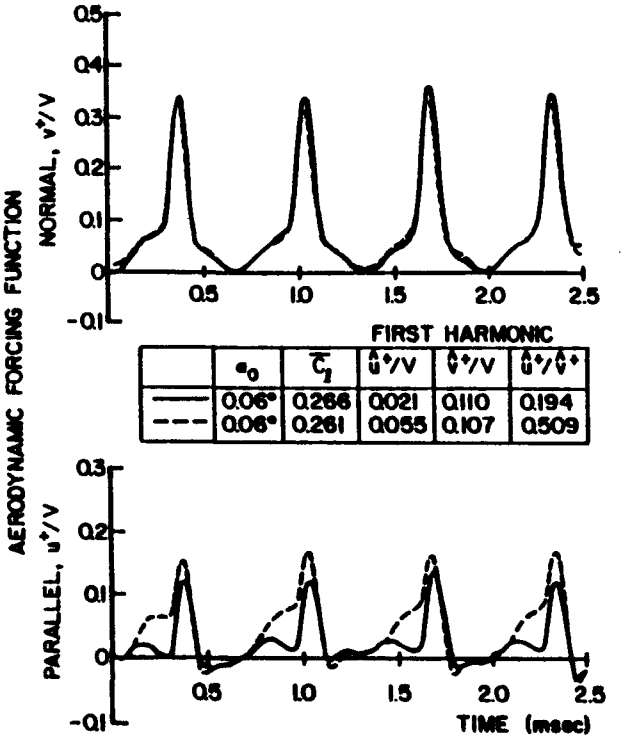

FIRST HARMONIC

	α_0	$\bar{C}_l$	$\hat{u}/V$	$\hat{v}/V$	$\hat{u}/\hat{v}$
——	0.06°	0.266	0.021	0.110	0.194
- - -	0.06°	0.261	0.055	0.107	0.509

Fig. 4 Gust aerodynamic forcing functions at low loading.

profile of the airfoil and, thus, the surface steady loading distribution have a significant effect on the unsteady aerodynamic gust response. In particular, the chordwise variation of both the magnitude and the phase of the unsteady pressure difference generally exhibit much better correlation with the cambered airfoil predictions than with those from the flat plate model. The magnitude data exhibit good trendwise agreement with the cambered airfoil prediction, with this model typically overpredicting the magnitude of the pressure difference on the front 30% of the airfoil chord. This is due to the strong coupling of the unsteady prediction on an accurate representation of the steady flowfield. As previously noted, the steady flow prediction did not exhibit good correlation with the steady airfoil surface static pressure data over the front part of the airfoil. Hence, the poor unsteady data-prediction correlation in this region. Also, the ratio of the first harmonic gust components ($\hat{u}^+/\hat{v}^+$) has an effect on both the magnitude and phase of the unsteady pressure difference, although the general chordwise variation of these data is not affected.

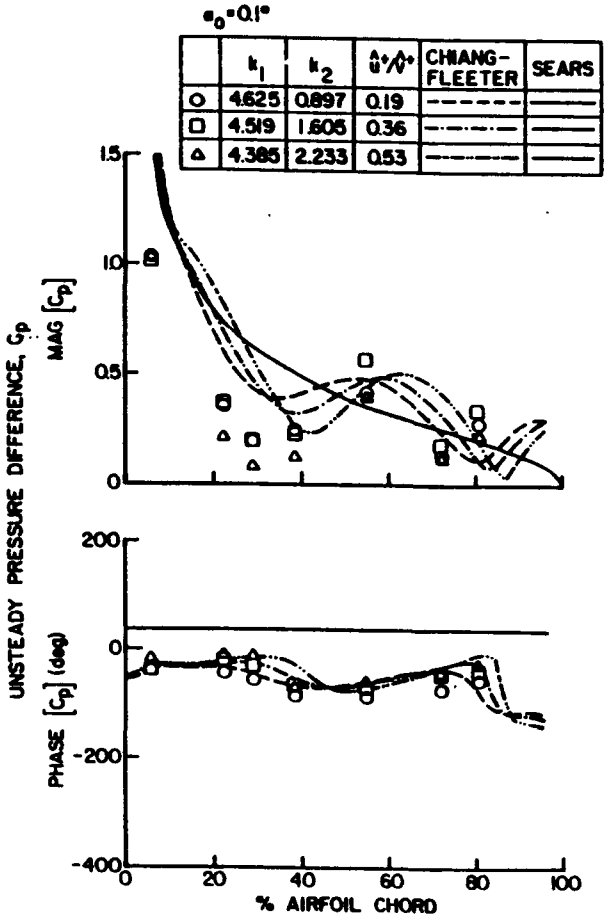

	k_1	k_2	$\hat{u}^+/\hat{v}^+$	CHIANG-FLEETER	SEARS
○	4.625	0.897	0.19	-------	——
□	4.519	1.605	0.36	-·-·-·-	——
△	4.385	2.233	0.53	-··-··-	——

Fig. 5 Effect of gust waveform on unsteady airfoil surface pressure difference at low loading.

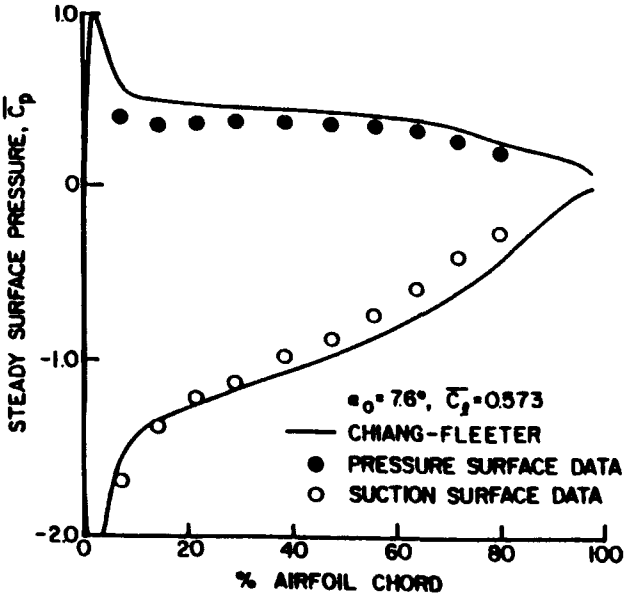

Fig. 6 Steady airfoil surface static pressure at intermediate loading.

To investigate the effect of steady airfoil loading on the aerodynamic gust response, the airfoil angle of attack was increased to 7.6 deg. The static pressure distributions on the airfoil suction and pressure surfaces together with the steady Chiang-Fleeter predictions are shown in Fig. 6. Relatively good correlation is obtained, although not quite as good as at the lower angle of attack. Again, the correlation between the data and the predictions is not very good in the leading-edge region of the airfoil.

The resulting unsteady aerodynamic gust response of the airfoil together with the flat plate and cambered airfoil predictions for a gust first-harmonic-component ratio of 0.22 are shown in Fig. 7. It should be noted that the reduced frequency k_1 for these intermediate angle-of-attack data is increased as compared to the previously presented low-angle-of-attack data. This is associated with the use of a low-speed research compressor to generate the aerodynamic gust forcing function. Again, the correlation of these complex unsteady pressure data with the cambered airfoil predictions is much better than with the flat plate model. In particular, the chordwise variations of both the magnitude and phase of the unsteady pressure-difference data exhibit good trendwise agreement with the cambered airfoil predictions. However, the phase correlation is not quite as good as at the lower loading level, with the magnitude data now overpredicted on the front half of the airfoil. This is again associated with the poor correlation between the steady surface pressure data and the model over the front part of the airfoil and the dependence of the unsteady predictions on the steady flow-field.

Figure 8 shows the correlation between the unsteady pressure-difference data and the corresponding predictions for 1) the Sears flat plate airfoil convected gust analysis, 2) the cambered airfoil convected gust model developed by Chiang and Fleeter, and 3) the cambered airfoil interaction gust model of Atassi. The magnitude data exhibit relatively good

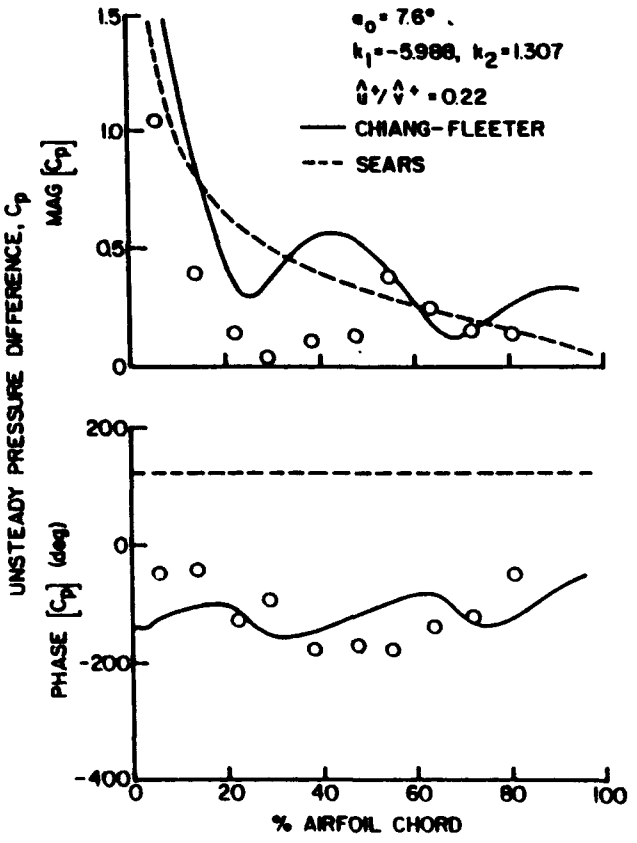

Fig. 7 Unsteady airfoil surface pressure differences at intermediate loading.

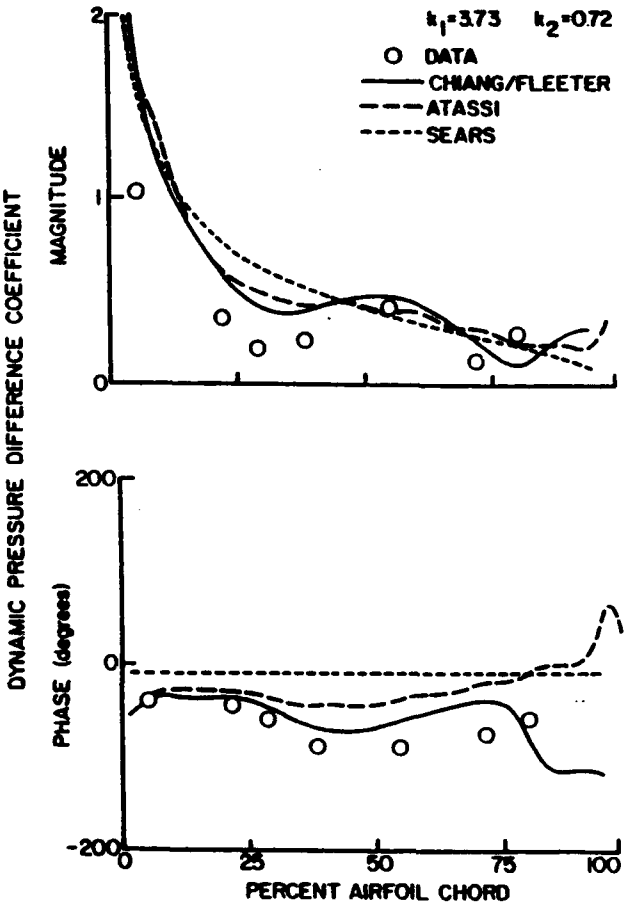

Fig. 8 Unsteady pressure difference correlation.

correlation with all three predictions, with consideration of the airfoil profile and steady loading resulting in the best correlation regardless of whether the gust is considered to be convected with the mean flow or not. The phase data correlate well with the cambered airfoil predictions and not the flat plate one, with the best correlation obtained with the convected gust cambered airfoil prediction. This is due to the coupling between the unsteady airfoil aerodynamics and the steady flowfield.

Separated Flow

Steady flow separation at approximately 35% of the airfoil suction surface was established by increasing the angle of attack to 14 deg. (Fig. 9). The effects of this flow separation on the unsteady aerodynamic gust response are investigated by comparing the resulting separated flow gust data with corresponding data obtained at the previous intermediate airfoil angle of attack of 7.6 deg. where the steady lift coefficient is nearly the same, but the steady flow is not separated. Also, both the parallel and normal gust components are maintained to be nearly identical for these two configurations (Fig. 10) with the ratio of the first-harmonic gust components being 0.218.

The resulting first-harmonic unsteady pressure difference data are presented in Fig. 11. Also shown is the nonseparated flat plate prediction of Sears. The cambered airfoil prediction is not presented because of the strong dependence of the cambered airfoil predictions on the steady flowfield and the inappropriateness of the inviscid steady model for separated flow. The magnitude data for the separated flow case show somewhat different trends than that for the nonseparated flow in the leading- and trailing-edge regions of the airfoil. For the separated flow configuration, the magnitude data are nearly

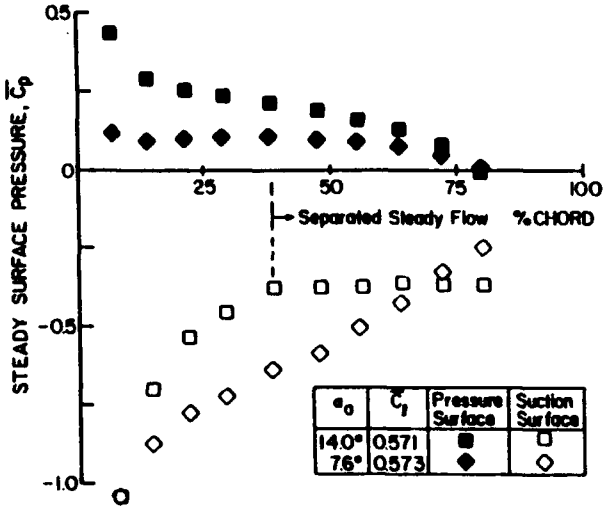

Fig. 9 Effect of suction surface flow separation on steady surface static pressure.

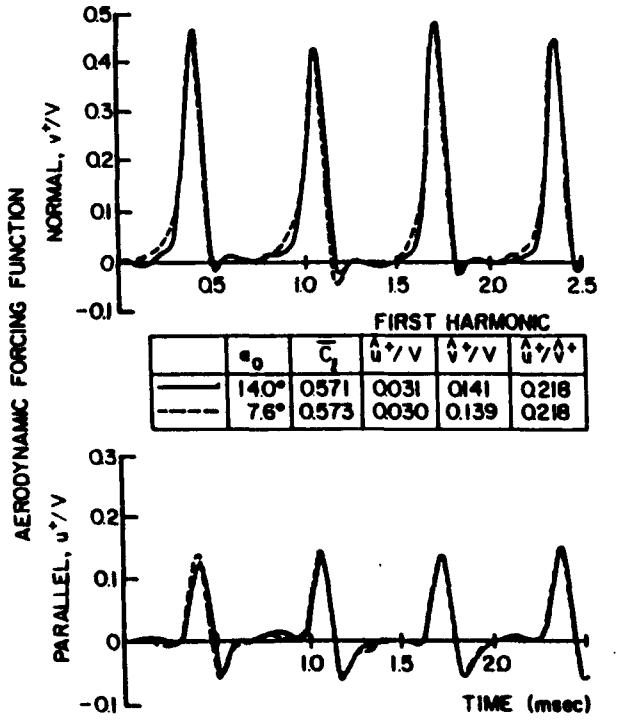

Fig. 10 Gust forcing functions for attached and separated flows.

constant over the front 15% of the airfoil, whereas the nonseparated data and the prediction indicate a decreasing amplitude. Aft of 15% chord, the magnitude data show analogous trends, with both the separated and nonseparated data decreasing with increasing chordwise position and attaining a minimum pressure amplitude value at 30% chord, similar to the previous results. The magnitude data for both cases then gradually increase to values that are greater than the prediction near midchord, with the nonseparated data being lower in amplitude up to this point due to the larger steady surface pressure differences between the suction and pressure surfaces. Both data sets then decrease with increasing chordwise position, with the separated data decreased in amplitude relative to the prediction and the nonseparated data. This is a result of the increased steady loading due to the separation in this region.

The phase data for the separated flow configuration have different trends than the nonseparated data and the flat plate prediction near the separation point and in the airfoil trailing-edge region. Over the front 20% of the airfoil, the data and the prediction show analogous trends of being nearly constant, with the separated data increased relative to the prediction and the nonseparated data. Aft of 20% chord, the separated phase data increase, whereas the nonseparated data decrease relative to the prediction. In the separated flow region, both the separated and nonseparated data show similar trends. However, at 70% chord the separated phase data jump to values larger than the prediction and increase with further chordwise position. On the other hand, the phase data for the nonseparated case show a gradual increase. Thus, separation affects both the magnitude and phase of the dynamic pressure difference data, with the primary effect being on the phase.

To further investigate these separation effects, individual suction surface time-variant pressure signals and their Fourier decompositions are considered. Figure 12 presents a typical unsteady pressure signal upstream of the separation point and the unsteady pressure signal at the same chordwise location for a configuration where the flow is not separated. It is clear that the downstream separation point affects both the amplitude and waveform of the unsteady pressure. This becomes more apparent in the spectrums of these nonseparated and separated unsteady pressures. The separated flow unsteady pressure has a much broader spectrum than the nonseparated one. This pressure field distortion is most probably due to the oscillation of the separation point generated by the periodic aerodynamic gusts. This would occur at the same frequency as the forcing function but would be out of phase with it.

A completely different trend is found within the separated flow region. Figure 13 presents the unsteady pressure signals for the separated and nonseparated flow cases for the same chordwise position and their resulting Fourier decomposition. There is little difference between the separated and nonseparated unsteady pressures. However, the nonseparated unsteady pressure has slightly more distortion, which results in

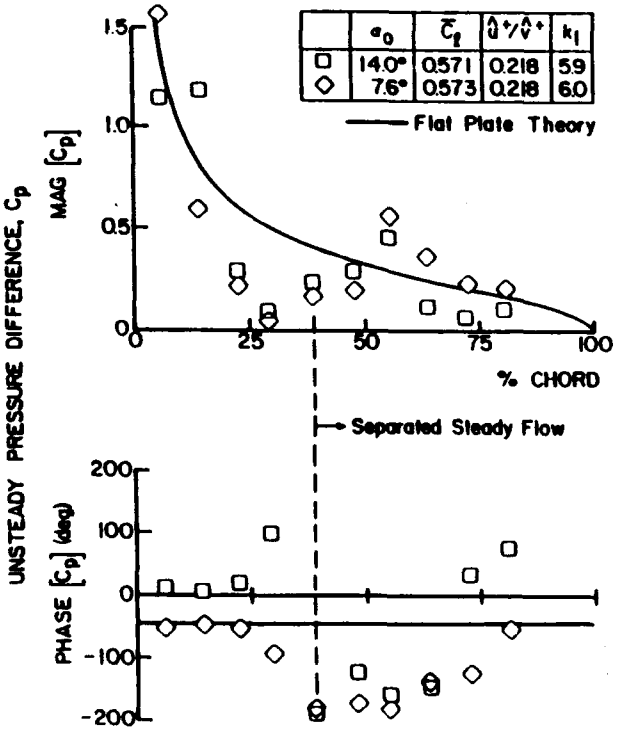

Fig. 11 Effect of suction surface flow separation on unsteady surface pressure.

the higher-order harmonics of the Fourier spectrum. This distortion is due to the steady flow turning and the aerodynamic loading of the airfoil. Within the separation zone where there is a constant steady static surface pressure, the pressure fluctuations generated by the separation-point oscillation are negligible, in contrast to the effect upstream of the separation point. Such a phenomenon also was noted by Maybey.[19] The effect of the separation-point oscillation is probably damped out by the mass of recirculating fluid within the separated flow region. Thus, the unsteady pressure within the separation zone is primarily responding to the aerodynamic forcing function.

The influence of the aerodynamic gust forcing function on the airfoil unsteady aerodynamics when the steady flow is separated is considered by establishing an additional airfoil configuration where the steady loading is nearly the same, having an angle of attack on the order of 14.0 deg., but the ratios of the gust components are different. The airfoil steady surface static pressure distributions for these two configurations are shown in Fig. 14. The airfoil pressure and suction surfaces have nearly identical distributions, with a fully separated flow starting at approximately 35% of the chord. Fig. 15 shows the aeodynamic forcing function to the airfoil. The

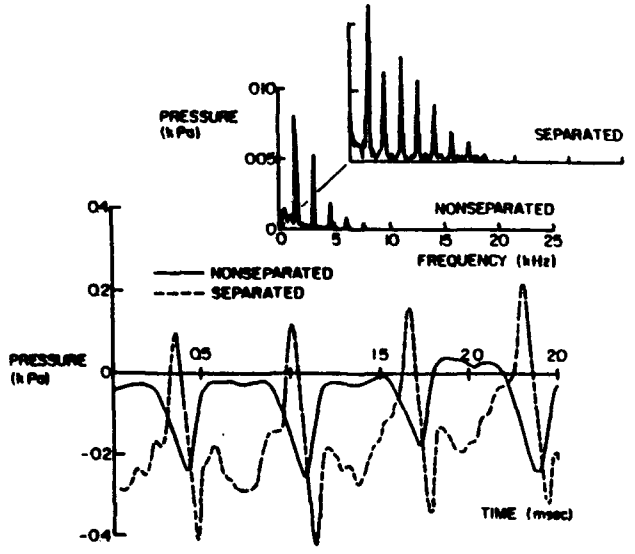

Fig. 12 Unsteady separated and attached flow pressure signals upstream of separation point.

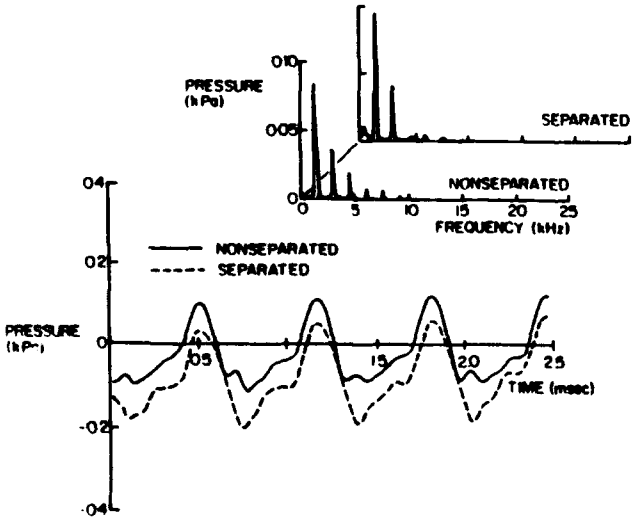

Fig. 13 Unsteady separated and attached flow pressure signals downstream of separation point.

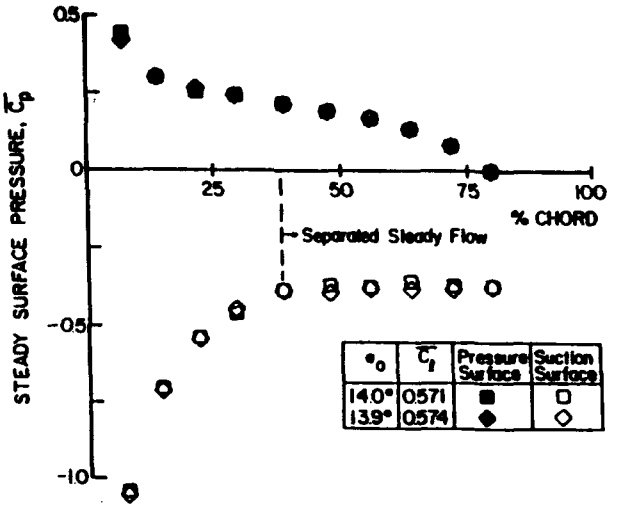

Fig. 14 Effect of gust waveform on airfoil surface steady static pressure.

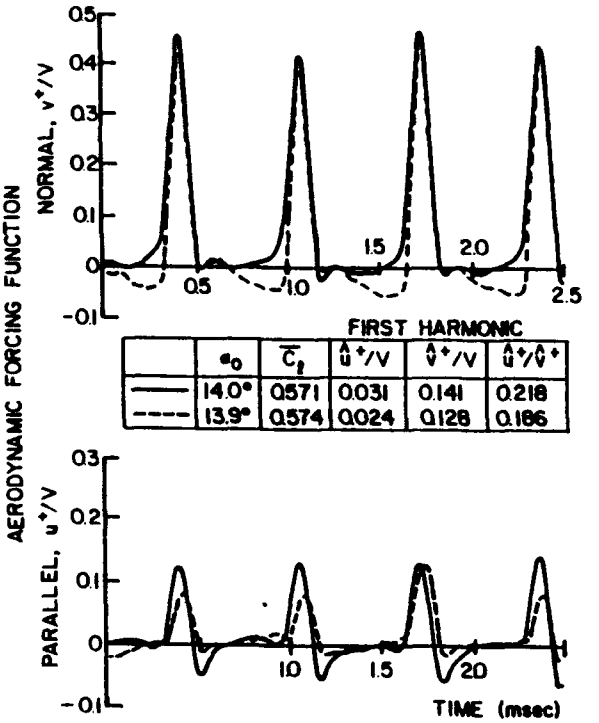

	α_0	$\bar{C}_l$	$\hat{u}^+/V$	$\hat{v}^+/V$	$\hat{u}^+/\hat{v}^+$
———	14.0°	0.571	0.031	0.141	0.218
- - - -	13.9°	0.574	0.024	0.128	0.186

Fig. 15 Gust forcing function with suction surface flow separation.

first-harmonic ratios of the gust components ($\hat{u}^+/\hat{v}^+$) are 0.218 and 0.186, with both the normal $\hat{v}^+$ and the parallel $\hat{u}^+$ gust components having different values.

The first-harmonic unsteady pressure difference data for these two configurations, with the nonseparated flat plate prediction as a reference, are presented in Fig. 16. The magnitude data indicate analogous trends over the entire airfoil chord, with the 0.186 ($\hat{u}^+/\hat{v}^+$) data being decreased in value relative to both the prediction and the 0.218 ($\hat{u}^+/\hat{v}^+$) data. In the trailing-edge region, the data correlate well with each other and are decreased relative to the prediction due to the high steady loading in this region. The phase data show different trends than the previous high-loading cases and with each other near the separation point and the trailing edge. Over the front 25% of the chord, the phase data show the same trends, with the 0.186 ($\hat{u}^+/\hat{v}^+$) data being in closer agreement with the prediction. At 30% chord, the 0.218

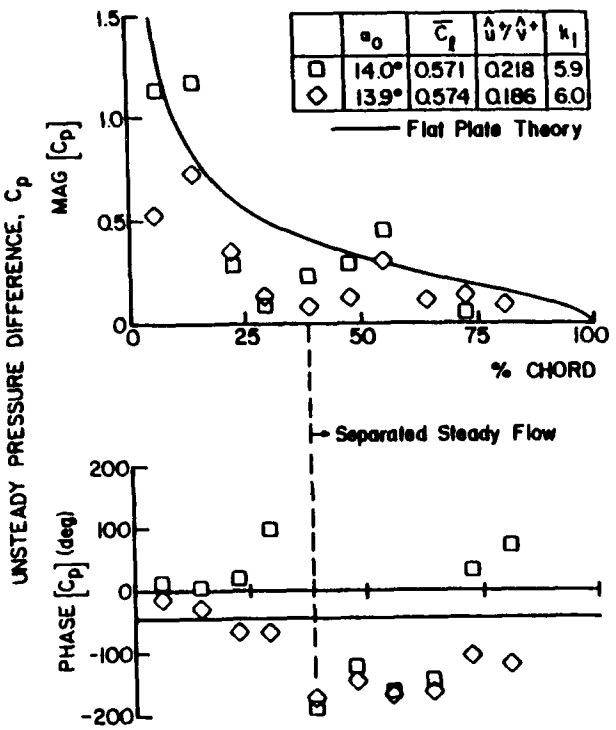

Fig. 16 Effect of gust waveform on unsteady pressure differences with separated steady flow.

$(\hat{u}^+/\hat{v}^+)$ data increase in phase, whereas the 0.186 $(\hat{u}^+/\hat{v}^+)$ data continue to show good trendwise correlation with the prediction. From 40% to 60% chord, the phase data correlate with each other but are decreased in value with respect to the prediction. Aft of 60% chord, the 0.218 $(\hat{u}^+/\hat{v}^+)$ phase data are increased relative to the prediction and increase with increasing chord. However, the phase data for 0.186 $(\hat{u}^+/\hat{v}^+)$ first increase in phase and then indicate a slight decrease with increasing chordwise position.

Summary and Conclusions

A series of experiments have been performed to investigate and quantify the unsteady aerodynamic response of an airfoil to a high reduced frequency gust, including the effects of the gust-forcing-function waveform, airfoil steady loading, and steady flow separation. This was accomplished by using an axial flow research compressor to experimentally model the high reduced frequency gust-forcing function, with the last stage stator vane row replaced with isolated instrumented airfoils. Appropriate data were correlated with predictions from flat plate and cambered airfoil gust models.

At low and intermediate airfoil angles of attack with the steady flow not separated, the profile of the airfoil and, thus, the surface steady loading distribution were shown to have a significant effect on the unsteady aerodynamic gust response of the airfoil. Also, the ratio of the first harmonic gust components affects both the magnitude and phase of the unsteady pressure difference, although the general chordwise variation of these data was not affected. In addition, the magnitude data exhibit relatively good correlation with all three predictions, with consideration of the airfoil profile and steady loading resulting in the best correlation regardless of whether the gust is considered to be convected with the mean flow or not. The phase data correlate well with the cambered airfoil predictions and not the flat plate one, with the best correlation obtained with the convected gust cambered airfoil prediction. This is due to the coupling between the unsteady airfoil aerodynamics and the steady flowfield.

The steady flow separation was shown to have a significant influence on the unsteady aerodynamics on the airfoil surface upstream of the separation point and also in the trailing-edge region. Also, the separation affects both the magnitude and the phase of the unsteady pressure difference data, with the primary effect being on the phase. Consideration of the individual suction surface unsteady pressure signals revealed that 1) separation affects the magnitude, waveform, and spectrum of the unsteady pressure upstream of the separation point, possibly a result of an oscillation of the separation point due to the harmonic gust, 2) the pressure signals in the separated flow region and the corresponding signals with the flow not separated exhibit only small differences, and 3) there is a constant steady static surface pressure in the separated flow region.

Acknowledgment

Support of this experimental research program by the Air Force Office of Scientific Research, James Wilson, program manager, is gratefully acknowledged.

References

[1]Theodorsen, T., "General Theory of Aerodynamic Instability and the Mechanism of Flutter," NACA TR 496, 1935.

[2]Kussner, H. G., "Das Zweidimensionale Problem der Beliebig Bewgegten Tragflache unter Berucksichtigung von Patialbewegungen der Flussigkeit, *luftfahrtorsch*, Vol. 17, No. 355, 1940.

[3]Sears, W. R., "Some Aspects of Non-Stationary Airfoil Theory and its Practical Application," *Journal of the Aeronautical Sciences*, Vol. 104, No. 8, Jan. 1941, pp. 104–108.

[4]Horlock, J. H., "Fluctuating Lift Forces on Airfoils Moving Through Transverse and Chordwise Gusts," *ASME Journal of Basic Engineering*, Vol. 90, No. 4, Dec. 1968, pp. 494–500.

[5]Naumann, H., and Yeh, H., "Lift and Pressure Fluctuations of a Cambered Airfoil Under Periodic Gusts and Applications to Turbomachinery," *ASME Journal of Engineering for Power*, Vol. 95, No. 1, Jan. 1973, pp. 1–10.

[6]Goldstein, M. E., and Atassi, H., "A Complete Second-Order Theory for Unsteady Flow about an Airfoil due to a Periodic Gust," *Journal of Fluid Mechanics*, Vol. 74, 1976, pp. 741–765.

[7]Atassi, H. M., "The Sears Problem for a Lifting Airfoil Revisted-New Results," *Journal of Fluid Mechanics*, Vol. 141, 1984, pp. 109–122.

[8]Holmes, D. W., "Lift Measurements on an Airfoil in Unsteady Flow," American Society of Mechanical Engineers, New York, Paper 73-GT-41, 1973.

[9]Satyanarayana, B., Gostelow, J. P., and Henderson, R. E., "A Comparison Between Experimental and Theoretical Fluctuating Lift on Cascades at Low Frequency Parameters", American Society of Mechanical Engineers, New York, Paper 74-GT-78, 1974.

[10]Ostdiek, F. R., "A Cascade in Unsteady Flow," Air Force Aeropropulsion Lab. TR-76-115, Wright-Patterson AFB, Dec. 1976.

[11]Woods, L. C., "Aerodynamic Forces on an Oscillating Airfoil Fitted with a Spoiler," *Proceedings of the Royal Society of London*, Ser. A, No. 239, 1957, pp. 328–337.

[12]Yashima, S., and Tanaka, H., "Torsional Flutter in Stalled Cascade," American Society of Mechanical Engineers, New York, Paper 77-GT-72, 1977.

[13]Sisto, F., and Perumal, P. V. K., "Lift and Moment Predictions for an Oscillating Airfoil with a Moving Separation Point," *ASME Journal of Engineering for Power*, Vol. 96, No. 4, Oct. 1974, pp. 372–378.

[14]Ericsson, L. E., and Reding, J. P., "Unsteady Airfoil Stall, Review and Extension," *AIAA Journal*, Vol. 19, Aug. 1981.

[15]Carstens, V., "Theoretical Investigations on a Two-Dimensional Cascade in Incompressible Flow," Symposium on Unsteady Aerodynamics of Turbomachines and Propellers, Cambridge University Engineering, England, Sept. 1984, pp. 277–300.

[16]Chi, R. M., "Separated Flow Unsteady Aerodynamic Theory," *Journal of Aircraft*, Vol. 22, No. 11, Nov. 1985, pp. 956–964.

[17]Lorber, P. F., and Carta, F. D., "Airfoil Dynamic Stall at Constant Pitch Rate and High Reynolds Number," AIAA Paper 87-1329, 1987.

[18]Chiang, H. D., and Fleeter, S., "Prediction of Loaded Airfoil Unsteady Aerodynamic Gust Response by a Locally Analytical Method," *International Journal of Mathematical Modeling* (to be published).

[19]Maybey, D. G., "Analysis and Correlation of Data on Pressure Fluctuations in Separated Flow," *Journal of Aircraft*, Vol. 9, No. 9, Dec. 1972, pp. 642–645.

APPENDIX VI

Forcing Function Effects on Rotor Periodic Aerodynamic Response

ASME Journal of Turbomachinery

Forcing Function Effects on Rotor Periodic Aerodynamic Response

S. R. Manwaring

S. Fleeter

Thermal Sciences and Propulsion Center,
School of Mechanical Engineering,
Purdue University,
West Lafayette, IN 47907

A series of experiments are performed in an extensively instrumented axial flow research compressor to investigate the effects of different low reduced frequency aerodynamic forcing functions and steady loading level on the gust-generated unsteady aerodynamics of a first-stage rotor blade row. Two different two-per-rev forcing functions are considered: (1) the velocity deficit from two 90 deg circumferential inlet flow distortions, and (2) the wakes from two upstream obstructions, which are characteristic of airfoil or probe excitations. The data show that the wake-generated rotor row first harmonic response is much greater than that generated by the inlet distortion, with the difference decreasing with increased steady loading.

Introduction

Periodic aerodynamic excitations generate unsteady aerodynamic forces and moments on turbomachinery blading. At the resonance conditions where the aerodynamic excitation frequency matches a blade natural frequency, catastrophic vibrational responses of the blading may occur. In the design process, Campbell diagrams are utilized to predict the occurrence of the resonant conditions in the operating range of the engine. Unfortunately, accurate predictions of the amplitude of the blade vibration at these resonances cannot currently be made due to the inability of mathematical models to predict the unsteady aerodynamics accurately, i.e., the aerodynamic forcing function to the blade row and the resulting unsteady aerodynamics acting on the blading. As a result, empirical correlations are currently used to indicate the blade row response to the various excitations with varying degrees of success. However, the applicability of these correlations to advanced blade designs has been in question for some time; see for example Mikolajczak et al. (1975).

Nonuniform inlet flow to a rotor represents the most common aerodynamic excitation source for aerodynamically forced vibrations. These nonuniformities are broadly categorized as wake excitations or inlet distortions, with two-per-rev schematic depictions of each shown in Fig. 1. They are generated by a variety of sources including support struts, inlet guide vanes, stator vanes, engine inlet designs, and aircraft maneuvers. In addition to the degradation in performance associated with the various nonuniform inlet flows, they can also result in detrimental aeromechanical effects. Namely, the distortion and wakes both represent unsteady aerodynamic forcing functions to downstream rotor blade rows, thereby resulting in the possibility of aerodynamically induced blade vibrations. This impacts the fatigue life of the blading and, thus, has an adverse effect on overall engine durability.

Distortions and wakes are both high energy aerodynamic forcing functions characterized by low to moderate values of the reduced frequency. On a first principles basis, they are analyzed by first defining the unsteady aerodynamic forcing function in terms of harmonics. The periodic response of an airfoil row to each harmonic is then assumed to be comprised of two components. One is due to the harmonic components of the unsteady aerodynamic forcing function being swept past the nonresponding airfoil row, termed the streamwise and transverse gust responses. The second, the self-induced unsteady aerodynamics, arises when a vibrational response of the airfoil row is generated.

Current state-of-the-art unsteady aerodynamic models for the prediction of forced response do not consider differences in the various types of aerodynamic forcing functions, i.e., distortion or wake-generated aerodynamic response. Also, the gust and motion-induced unsteady aerodynamic models involve many physical and numerical assumptions. Therefore, experimental modeling of the fundamental distortion and wake-generated blade row periodic unsteady aerodynamic response,

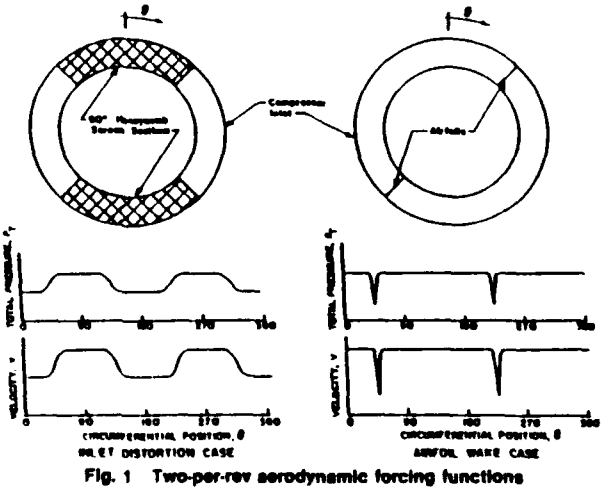

Fig. 1 Two-per-rev aerodynamic forcing functions

Contributed by the International Gas Turbine Institute and presented at the 35th International Gas Turbine and Aeroengine Congress and Exposition, Brussels, Belgium, June 11-14, 1990. Manuscript received by the International Gas Turbine Institute January 15, 1990. Paper No. 90-GT-109.

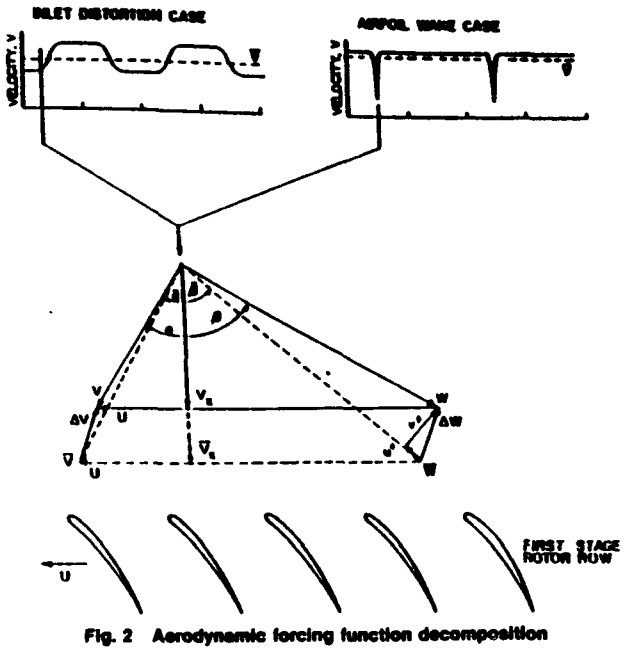

Fig. 2 Aerodynamic forcing function decomposition

Table 1 Overall airfoil and compressor characteristics

	ROTOR	STATOR	IGV
Airfoil type	C4	C4	C4
Number of Airfoils	43	31	36
Chord, C (mm)	30	30	30
Solidity, C/S	1.14	1.09	0.96
Camber, θ	28.0	27.7	36.9
Stagger Angle, γ	36.0	36.0	21.0
Aspect Ratio	2.0	2.0	2.0
Thickness/Chord (%)	10.0	10.0	10.0
Flow Rate (kg/s)		2.03	
Design Axial Velocity (m/s)		21.4	
Design Rotational Speed (RPM)		2250	
Number of Stages		3	
Design Stage Pressure Ratio		1.0	
Inlet Tip Diameter (mm)		420	
Hub/Tip Radius Ratio		0.714	
Stage Efficiency (%)		85	

including both the forcing function and the resulting blade row unsteady aerodynamics, is needed for validation and enhancement of theoretical and numerical models.

Unsteady aerodynamic gust experiments of direct interest to turbomachines have been performed in low-speed research compressors. Utilizing the stationary vane rows of both single and multistage compressors, with the aerodynamic forcing function being the high reduced frequency wakes shed by the upstream rotor blades, the effects of airfoil camber, rotor-stator axial spacing, and the waveform of the aerodynamic forcing function on the first harmonic vane row response have been investigated (Fleeter et al., 1978, 1980; Capece et al., 1986; Capece and Fleeter, 1987). Gallus et al. (1980) utilized five transducers embedded in each vane surface to quantify the unsteady lift coefficients corresponding to the first five harmonics of rotor blade passing frequency.

With regard to inlet flow distortions, O'Brien et al. (1980) used six dynamic pressure transducers embedded on each rotor blade surface to measure the unsteady aerodynamic response to a distorted inlet flow field. However, the periodic rotor blade row inlet flow field was not measured and, thus, the unsteady aerodynamic gust forcing function was not quantified. Manwaring and Fleeter (1990) investigated the effect of inlet distortion waveform shape on the unsteady pressure response of a first-stage rotor row in a multistage compressor. Hardin et al. (1987) measured low reduced frequency oscillating airfoil aerodynamics on a rotor of a single-stage compressor and also stated that they performed similar distortion experiments, although the results were not presented. In the high-speed flow regime, Datko and O'Hara (1987) measured the forced vibratory response of an advanced transonic compressor first-stage integrally bladed disk (a blisk) generated by seven different inlet total pressure distortion screens. These experiments found that the blisk was susceptible to excessive resonant stresses generated by the inlet distortions, with complex inlet distortions exciting the lower natural frequencies at a number of engine orders. Although the distorted inlet flow field was measured with a total pressure probe, the harmonic content of the distortion was not always discernible. Also, the detailed forcing function, i.e., the streamwise and transverse gusts, and the rotor blade surface unsteady pressure and pressure differences were not quantified.

In this paper, the fundamental flow physics of disturbance-generated periodic rotor blade row unsteady aerodynamics, including the effect of different unsteady aerodynamic forcing functions, are experimentally investigated for the first time. This is accomplished by means of a series of experiments performed in an extensively instrumented axial flow research compressor directed at the investigation of the effects of both the aerodynamic forcing function and steady aerodynamic loading level on the gust-generated unsteady aerodynamics of a first stage rotor blade.

As schematically depicted in Fig. 1, two different two-per-rev aerodynamic forcing functions are considered: (1) the velocity deficit from two 90 deg circumferential inlet flow distortions, and (2) the wakes from two upstream obstructions, which are characteristic of airfoil or probe excitations. These aerodynamic forcing functions to the first-stage rotor blade row are measured with a rotating cross hot wire probe, with these data then analyzed to determine the streamwise and trans-

Nomenclature

b = rotor blade semichord
$\bar{C}_l$ = rotor blade steady loading = $\int_0^1(\bar{C}_{p,\text{pressure}} - \bar{C}_{p,\text{suction}})dx$
$\bar{C}_p$ = rotor blade steady pressure coefficient
C_{pi} = rotor blade harmonic unsteady pressure coefficient
$C_{\Delta pi}$ = rotor blade harmonic unsteady pressure difference coefficient
$\bar{i}$ = rotor blade mean incidence angle
k = reduced frequency = $\omega b/\bar{V}_x$
p = rotor blade surface unsteady pressure
P_{exit} = rotor drum steady pressure
$\bar{P}_s$ = rotor blade surface steady pressure
$\hat{p}_i$ = harmonic unsteady pressure
U_t = rotor blade tip speed
u^+ = streamwise unsteady velocity component
$\hat{u}_i$ = streamwise gust harmonic component
v^+ = transverse unsteady velocity component
$\hat{v}_i^+$ = transverse gust harmonic component
$\bar{V}_x$ = mean axial velocity
ρ = density of air
σ = interblade phase angle
ω = two-per-rev forcing function frequency, rad

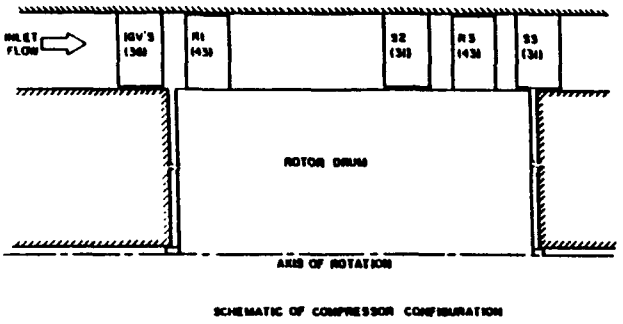

Fig. 3 Research compressor configuration

verse velocity components, u^+ and v^+, shown in Fig. 2. The resulting unsteady aerodynamic gust-generated rotor blade surface unsteady pressure chordwise distributions are measured with embedded ultraminiature high response dynamic pressure transducers.

Research Compressor

The Purdue Axial Flow Research Compressor experimentally models the fundamental turbomachinery unsteady aerodynamic multistage interaction phenomena including the incidence angle, the velocity and pressure variations, the aerodynamic forcing function, the reduced frequency, and the unsteady blade row interactions. The compressor is driven by a 15 hp d-c electric motor and is operated at a speed of 2250 rpm. Each identical stage of the baseline compressor contains 43 rotor blades and 31 stator vanes having a British C4 profile, with the first-stage rotor inlet flow field established by a row of 36 variable setting inlet guide vanes. The overall airfoil and compressor characteristics are presented in Table 1. For these experiments, the first-stage rotor blade row was extensively instrumented. Due to the large gap between the IGV row and the first-stage rotor row, approximately 75 percent vane chord, the potential flow effects are negligible compared to the viscous wakes. To eliminate any potential flow effects from the downstream stator row on the instrumented first-stage rotor blades, the first-stage stators and second-stage rotors were removed, as schematically depicted in Fig. 3.

Instrumentation

Both steady and unsteady first-stage rotor blade row data are required. The steady data quantify the rotor mean inlet flow field and midspan steady loading distribution. The unsteady data define the periodic aerodynamic forcing function and the resulting midspan blade surface periodic pressure distributions.

The inlet flow field, both steady and unsteady, is measured with a rotating cross hot-wire probe mounted 30 percent of blade chord upstream of the rotor row. The cross hot-wire probe is calibrated and linearized for velocities from 18.3 m/s to 53.4 m/s and $+/-35$ deg angular variation, with the accuracy of the velocity magnitude and flow angle determined to be 4 percent and $+/-1.0$ deg, respectively. Centrifugal loading effects on the rotating hot-wire sensor resistances and, thus, responses were found to be negligible.

The detailed steady aerodynamic loading on the rotor blade surfaces is measured with a chordwise distribution of 20 midspan static pressure taps, 10 on each surface. The static pressure at the rotor exit plane, measured with a rotor drum static tap, is used as the blade surface static pressure reference. These static pressure measurements are made using a rotor based 48 port constant speed drive Scanivalve system located in the rotor drum. To determine the accuracy of the steady pressure measurements, a 95 percent confidence internal, root-mean-square error analysis of 20 samples is performed.

The measurement of the midspan rotor blade surface unsteady pressures is accomplished with 20 ultraminiature, high response transducers embedded in the rotor blades at the same chordwise locations as the static pressure taps. To minimize the possibility of flow disturbances associated with the inability of the transducer diaphragm to maintain the surface curvature of the blade exactly, a reverse mounting technique is utilized. The pressure surface of one blade and the suction surface of the adjacent blade are instrumented, with transducers embedded in the nonmeasurement surface and connected to the measurement surface by a static tap. The embedded dynamic transducers were both statically and dynamically calibrated. The static calibrations showed good linearity and no discernible hysteresis. The dynamic calibrations demonstrated that the frequency response, in terms of gain attenuation and phase shift, were not affected by the reverse mounting technique. The accuracy of the unsteady pressure measurements, determined from the calibrations, is $+/-4$ percent.

The rotor-based static pressure Scanivalve transducer, rotating hot-wire probe, and 20 blade surface dynamic pressure transducers are interfaced to the stationary frame of reference through a 40 channel slip ring assembly. Onboard signal conditioning of the transducer output signals is performed to maintain a good signal-to-noise ratio through the slip ring. The remaining 17 channels of the slip-ring assembly are used to provide excitation to the transducers and on/off switching excitations to the Scanivalve DC Motor.

Data Acquisition and Analysis

Steady Data. The rotor blade surface static pressure data, measured with the rotor-based Scanivalve system, are defined by a root-mean-square error analysis of 20 samples with a 95 percent confidence interval. The reference for these midspan blade pressure measurements is the static pressure at the exit of the rotor measured on the rotor drum. Thus, the blade surface and the reference static pressures are measured at different radii. Hence, a correction for the resulting difference in the radial acceleration is derived and applied in calculating the blade surface static pressure coefficient defined in equation (1).

$$\bar{C}_p = \frac{\bar{P}_s - \bar{P}_{\text{exit}}}{1/2\rho U_t^2} \tag{1}$$

where U_t is the rotor blade tip speed.

Periodic Data. The periodic data of interest are the harmonic components of the aerodynamic forcing function to the first-stage rotor blade row together with the resulting rotor blade surface unsteady pressures and unsteady pressure differences. These are determined by defining a digitized ensemble averaged unsteady aerodynamic data set consisting of the rotating cross hot-wire probe and blade surface dynamic pressure transducer signals at each steady operating point. In particular, these time-variant signals are digitized with a high-speed A-D system at a rate of 20 kHz and then ensemble averaged. The key to this averaging technique is the ability to sample data at a preset time, accomplished by an optical encoder mounted on the rotor shaft. The microsecond range step voltage signal from the encoder is the data initiation time reference and triggers the high speed A-D multiplexer system. To significantly reduce the random fluctuations superimposed on the periodic signals of interest, 200 averages are used. A Fast Fourier Transform (FFT) algorithm is then applied to these ensemble-averaged signals to determine the harmonic components of the unsteady aerodynamic forcing function and the resulting rotor blade surface harmonic unsteady pressures and pressure differences.

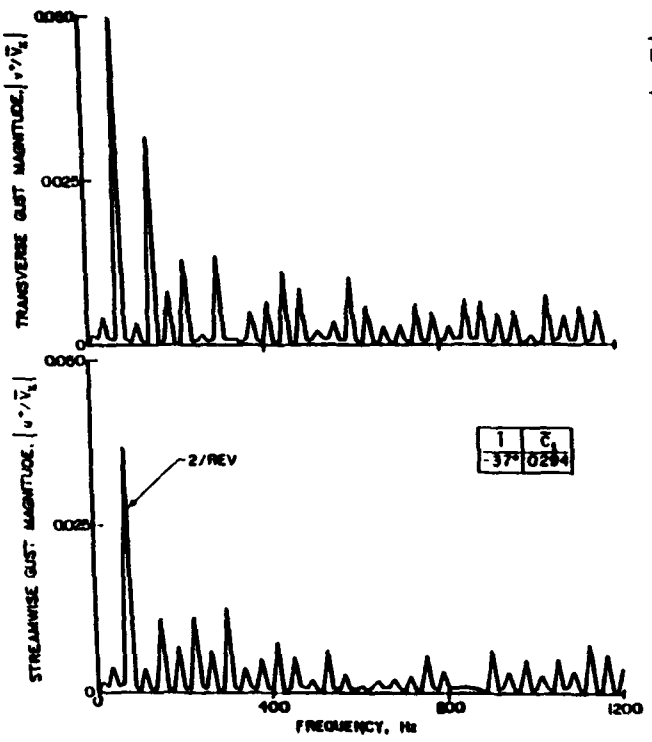

Fig. 4 Fourier decomposition of inlet distortion forcing function for low steady loading

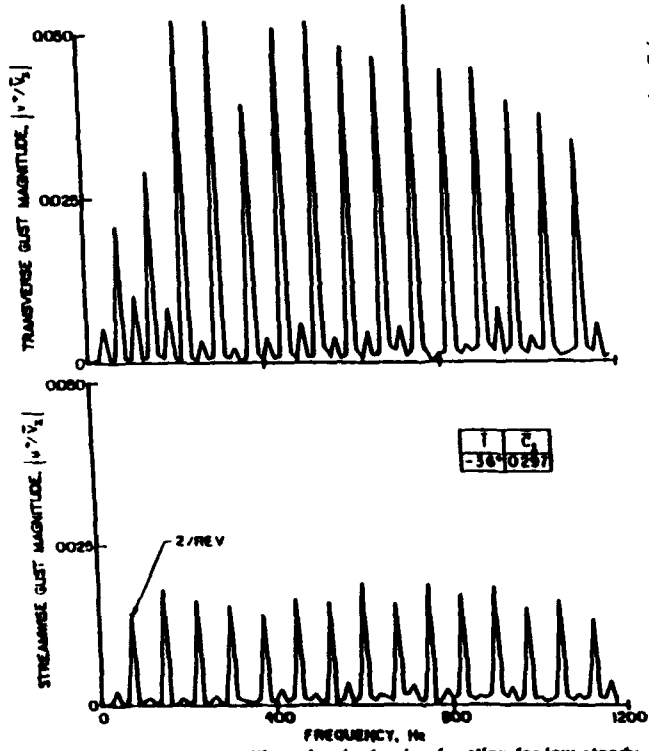

Fig. 5 Fourier decomposition of wake forcing function for low steady loading

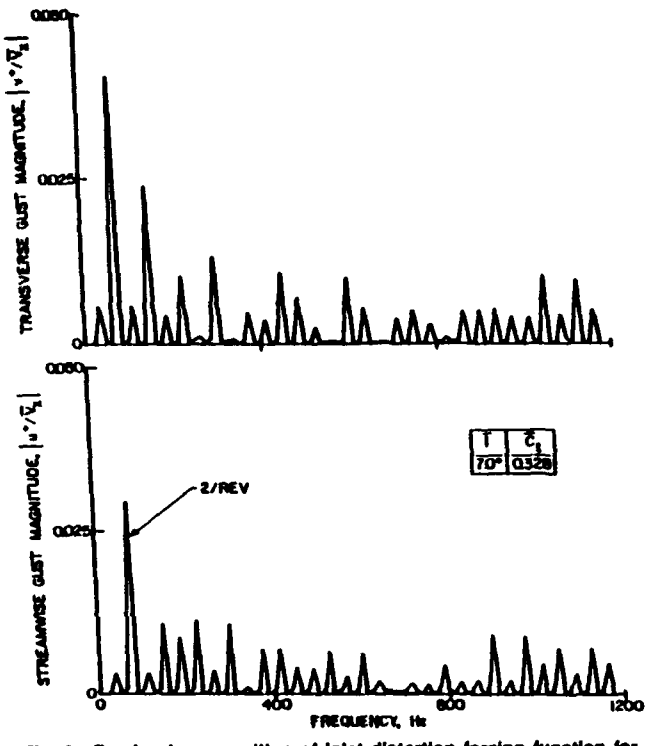

Fig. 6 Fourier decomposition of inlet distortion forcing function for high steady loading

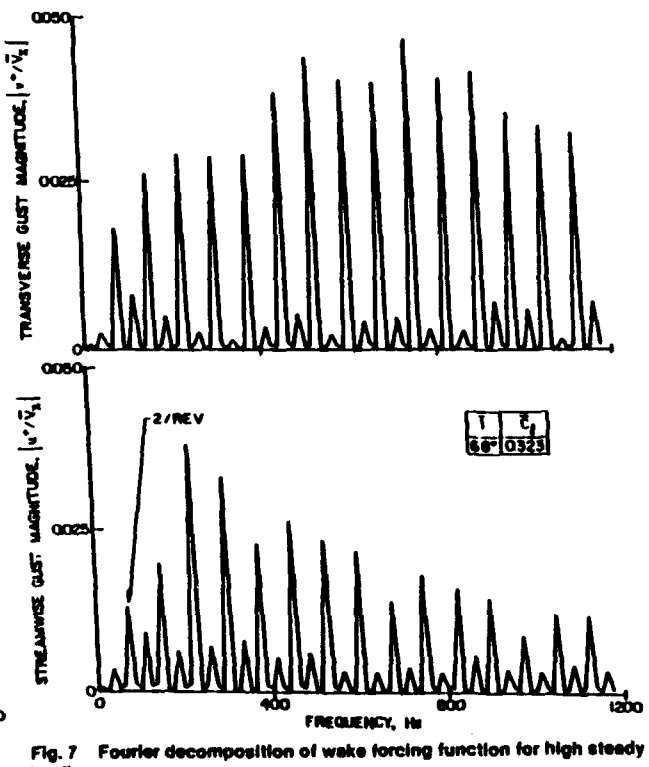

Fig. 7 Fourier decomposition of wake forcing function for high steady loading

The unsteady inlet flow field to the rotor row, measured with the rotating cross hot-wire probe, is quantified by the inlet relative velocity and flow angle. The velocity triangle relations depicted in Fig. 2 are then used to determine the detailed unsteady velocity into the rotor row, in particular, the streamwise and transverse velocity components, u^+ and v^+, respectively. These are then Fourier decomposed to determine their harmonic components, $\hat{u}_i^+$ and $\hat{v}_i^+$.

The various unsteady aerodynamic gust mathematical models reference the gust-generated airfoil aerodynamic response to a transverse gust at the leading edge of the airfoil. However, in the experiments described herein, the time-variant data are

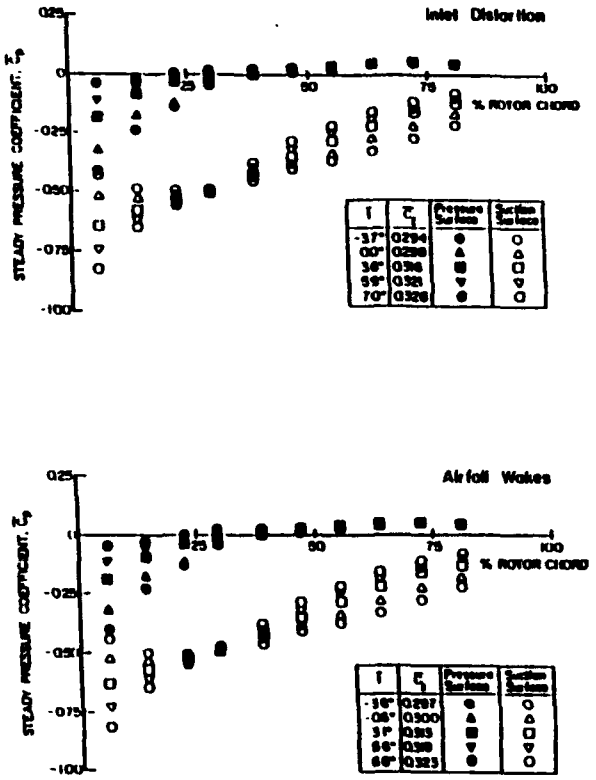

Fig. 8 Forcing function and steady loading effects on surface static pressure coefficient

referenced to the initiation of the data acquisition shaft trigger pulse. Thus, for consistency with the models, the periodic data are further analyzed and referenced to a transverse gust at the leading edge of the first stage rotor blade. This is accomplished by assuming that: (1) The aerodynamic forcing function remains fixed in the stationary reference frame; and (2) the forcing function does not change from the rotating hot-wire probe axial location to the rotor row leading edge plane.

The rotor blade surface unsteady pressure data, measured with the embedded high response pressure transducers, are analyzed to determine the harmonics of the chordwise distribution of the unsteady pressure coefficient, C_{pi}, and the unsteady pressure difference coefficient, $C_{\Delta pi}$. These are defined in equation (2) and are specified from the Fourier coefficients of the digitized unsteady pressure transducer signals. The nondimensionalization term, $\hat{\beta}$, is used in addition to the standard terms to collapse the steady loading effects associated with mean incidence angle as will be shown later.

$$C_{pi} = \frac{\hat{p}_i}{\rho \bar{V}_x^2 \left(\frac{\hat{v}_i^+}{\bar{V}_x}\right) \hat{\beta}} \tag{2a}$$

$$C_{\Delta pi} = C_{pi,\text{pressure}} - C_{pi,\text{suction}} \tag{2b}$$

where $\hat{v}_i^+$ is the harmonic transverse gust component, $\bar{V}_x$ is the mean axial velocity, and $\hat{\beta}$ is the relative mean flow angle.

The final form of the gust-generated rotor blade row unsteady aerodynamics is the chordwise distribution of the harmonic complex unsteady pressure and pressure difference coefficients. Also included as a reference where appropriate are predictions from the transverse gust analysis of Smith (1971). This model analyzes the unsteady aerodynamics generated on a flat plate airfoil cascade at zero incidenee by a transverse gust convected with an inviscid, subsonic, compressible flow.

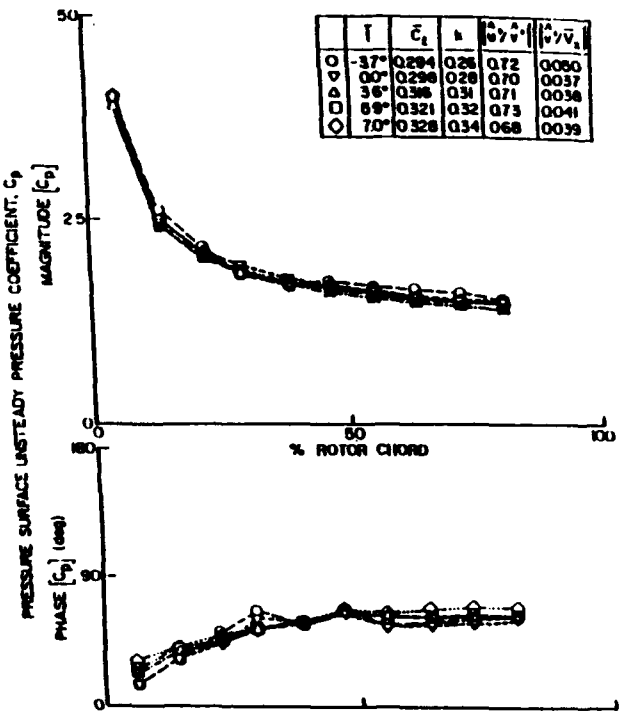

Fig. 9 Pressure surface steady loading effect on unsteady pressure with inlet distortion forcing function

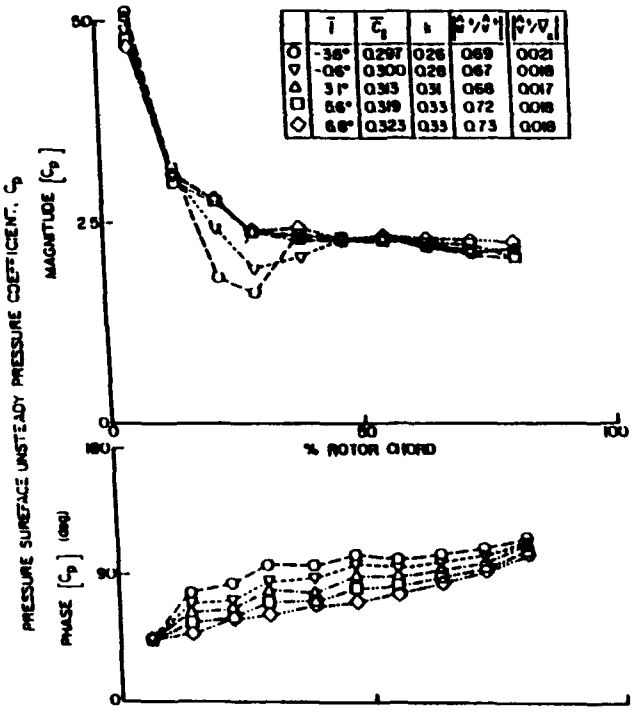

Fig. 10 Pressure surface steady loading effect on unsteady pressure with wake forcing function

Results

A series of experiments are performed to investigate and quantify the effects of different aerodynamic forcing functions and the level of steady aerodynamic loading on periodic gust unsteady aerodynamics of a first stage rotor blade. Two different types of two-per-rev forcing functions are considered:

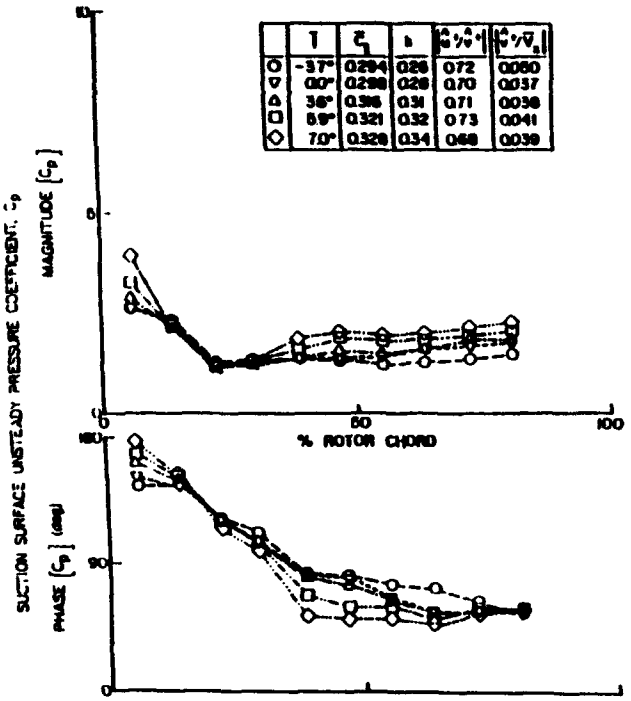

Fig. 11 Suction surface steady loading effect on unsteady pressure with inlet distortion forcing function

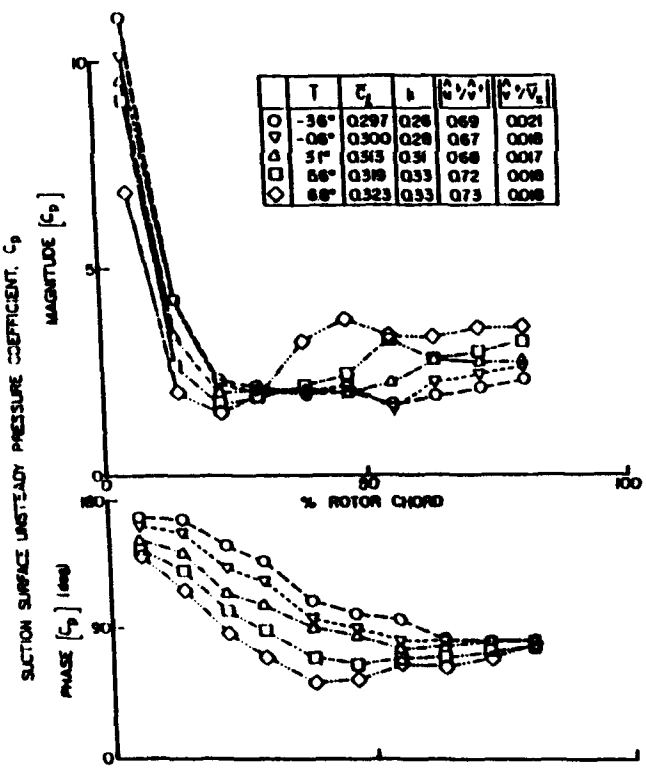

Fig. 12 Suction surface steady loading effect on unsteady pressure with wake forcing function

(1) a circumferential inlet flow distortion, and (2) upstream airfoil wakes. In these experiments, the two two-per-rev forcing functions are equivalent in terms of aerodynamically forced response as each has approximately the same nominal value for the first harmonic streamwise-to-transverse gust amplitude ratio, 0.72 for the inlet distortion and 0.70 for the wakes.

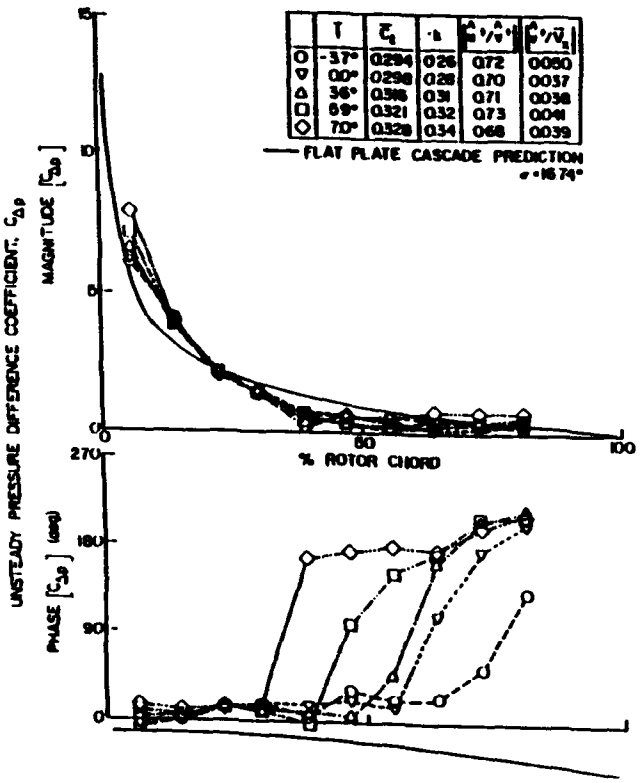

Fig. 13 Steady loading effect on unsteady pressure difference with inlet distortion forcing function

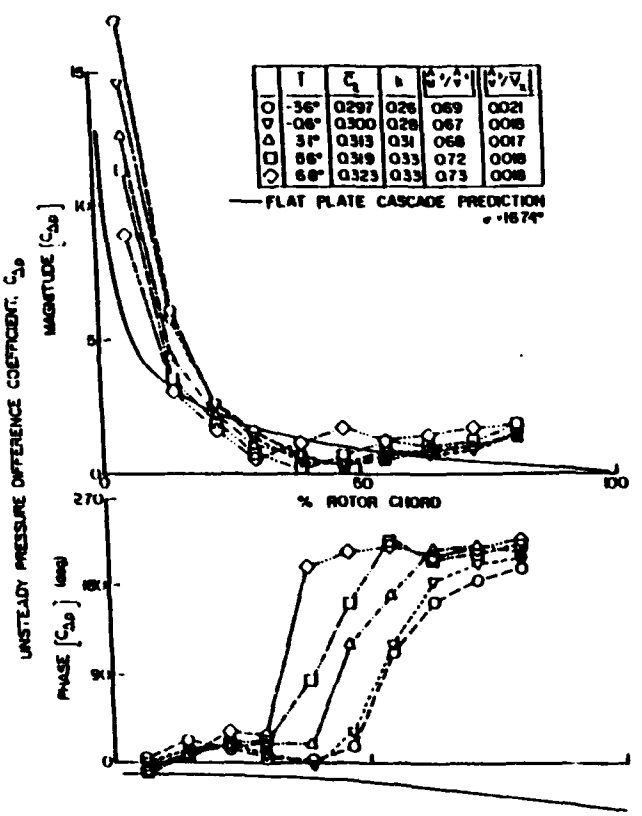

Fig. 14 Steady loading effect on unsteady pressure difference with wake forcing function

Periodic Aerodynamic Forcing Functions. The Fourier decompositions of the inlet distortion and wake aerodynamic forcing functions to the first-stage rotor in terms of the gust components are presented in Figs. 4 and 5 for the lowest steady loading level. The inlet distortion results in a dominant two-per-rev excitation with smaller higher harmonics. With the wake forcing function, a strong two-per-rev signal is again present. However, the higher harmonic amplitudes are approximately the same magnitude as the generating wake two-per-rev fundamental for the streamwise gust components and are larger for the transverse gust component.

The inlet distortion and wake aerodynamic forcing functions for the highest steady loading level are shown in Figs. 6 and 7. The effect of steady loading on the inlet distortion forcing function is minimal, with both the transverse and streamwise harmonic gust components having relatively the same magnitudes as the low steady loading level. However, for the wake forcing function, while the first harmonic streamwise and transverse gust amplitudes are relatively unchanged from the low steady loading level results, the higher harmonic gust component magnitudes differ considerably. For this higher steady loading level, the larger higher harmonics imply that the wake deficit and flow angle changes through the airfoil wake are increased.

Blade Surface Static Pressures. The effect of steady aerodynamic loading, characterized by the mean incidence angle, on the rotor blade surface static pressure coefficient for both the inlet distortion and the obstruction wake forcing function are shown in Fig. 8. The level of steady loading only affects the static pressure distribution on the pressure surface over the front 40 percent of the chord. On the suction surface, the steady loading variation has a large effect on the static pressure distribution over the entire suction surface. Also, these data exhibit no indication of flow separation. Of particular interest to the unsteady experiments, these data clearly show that these different aerodynamic forcing functions have no effect on the steady aerodynamic performance of the rotor, i.e., the airfoil steady surface static pressures are independent of the unsteady aerodynamic forcing function.

Rotor Periodic Aerodynamic Response. The unsteady aerodynamic response of the first-stage rotor blade row to the first harmonic of the inlet distortion and wake forcing functions, including the effect of steady aerodynamic loading, are presented in Figs. 9–14. In particular, these figures present the chordwise distributions of the complex unsteady pressure coefficient on the individual rotor blade surfaces as well as the corresponding complex unsteady pressure difference coefficients generated by these equivalent first harmonic two-per-rev aerodynamic forcing functions.

Pressure Surface Unsteady Pressures. The effect of steady aerodynamic loading level on the first harmonic of the complex unsteady pressure distribution on the rotor blade pressure surface for the inlet distortion and the wake forcing functions is shown in Figs. 9 and 10, respectively.

For the inlet distortion, the unsteady pressure magnitude decreases monotonically with increasing chord for all steady loading levels. This form of the dimensionless unsteady pressure coefficient, equation (2*a*), results in the compression of these magnitude data for all mean flow incidence angle values. Thus, the magnitude of the unsteady pressure response on the blade pressure surface, i.e., the low camber airfoil surface, is primarily due to the level of steady loading as characterized by the mean flow incidence angle.

With the wake forcing function, the unsteady pressure magnitude also decreases monotonically with increasing chord for the three highest steady loading levels, with the data collapsed for these loadings. For the lowest steady loading levels, the data are also collapsed in the aft half of the surface but exhibit a significant decreased magnitude region between 15 and 40 percent of the chord. This is attributed to the acceleration of the mean flow around the pressure surface leading edge region at these two negative mean incidence angles. As this effect was not seen in the inlet distortion case, this indicates that the first harmonic gust generated by the wake has a much larger interaction with the accelerated mean flow field than the corresponding inlet distortion-generated gust.

The effects of steady loading on the unsteady pressure phase data are also dependent on the specific forcing function. With the inlet distortion, these phase data are essentially independent of the steady loading level. However, with the wake forcing function, the phase of the unsteady pressure is a function of the level of steady loading, with the phase decreasing as the incidence angle increases. Another difference in the effect of the two forcing functions is that with the inlet distortion, the unsteady pressure phase increases over the front half of the surface and remains constant over the aft half, whereas the corresponding phase data increase in value along the entire pressure surface with the wake forcing function.

Suction Surface Unsteady Pressures. The effect of steady aerodynamic loading on the first harmonic complex unsteady pressure on the rotor blade suction surface is shown in Fig. 11 for the inlet distortion and in Fig. 12 for the wake forcing function.

In contrast to the pressure surface, the form of the dimensionless unsteady pressure coefficient, equation (2*a*), does not compress the suction surface magnitude data with mean flow incidence angle, the exception being between 13 and 20 percent of the chord for the inlet distortion. For both forcing functions, the unsteady pressure magnitude data decrease to a minimum and then increase as the chord is traversed. Also, the magnitude data exhibit the same steady loading trends aft of the minimum magnitude chordwise position for the two forcing functions, with the unsteady pressure magnitude increasing with increasing steady loading. In the front chord region, however, the unsteady pressure magnitudes generated by the wake decrease with increasing steady loading, whereas the corresponding inlet distortion-generated magnitudes increase with increasing steady loading. Another difference associated with the forcing functions is that the wake-generated unsteady pressure magnitude

Table 2 Summary of unsteady aerodynamic experimental results

PRESSURE SURFACE UNSTEADY PRESSURE

	DISTORTION	WAKE
MAGNITUDE	decreases monotonically with chord	decreases monotonically with chord for higher loadings
	compressed distributions with respect to mean incidence	decreased between 15% and 40% chord at lowest loadings
PHASE	increases from 0% to 50% chord	increases over entire chord
	independent of steady loading	dependent on steady loading, decreasing with increased loading

SUCTION SURFACE UNSTEADY PRESSURE

	DISTORTION	WAKE
MAGNITUDE	decreases to a minimum and then increases with chord	decreases to a minimum and then increases with chord
	dependent on steady loading, increasing with increased steady loading	dependent on steady loading, decreasing forward of 30% chord and increasing aft with increased loading
PHASE	decreases over chord	decreases over chord
	dependent on steady loading, with different trends forward and aft of 25% chord	dependent on steady loading

UNSTEADY PRESSURE DIFFERENCE

	DISTORTION	WAKE
MAGNITUDE	decreases with increasing chord	decreases with increasing chord
	increases with increased incidence	decreases forward of 40% chord and increases aft with increased incidence
PHASE	nearly constant and independent of loading forward of 40% chord	nearly constant and independent of loading forward of 40% chord
	sharp increase in midchord region, with the onset location moving forward with increasing incidence	sharp increase in midchord region, with the onset location moving forward with increasing incidence

data are significantly larger in value than the corresponding inlet distortion-generated magnitudes for all steady loading levels, particularly in the front chord region, with the differences decreasing with increasing steady loading.

The forcing function has a significant influence on the effect of steady loading level on the unsteady pressure phase data. For the inlet distortion at approximately 25 percent chord and for the wake forcing function over the entire suction surface, the phase data decrease as the incidence angle is increased. However, there is a much larger steady loading effect apparent with the wake forcing function, particularly over the front 75 percent of the chord. Other differences in the effects of the two forcing functions on the suction surface phase data are that with the inlet distortion: (1) The variation with steady loading in the leading edge region changes, increasing with the increasing incidence angle; and (2) these data are nearly independent of the loading level from approximately 15 to 25 percent chord, the vicinity of the minimum unsteady pressure magnitude data. Neither of these effects are found in the wake-generated phase data.

Unsteady Pressure Differences. The effects of steady loading on the first harmonic complex unsteady pressure difference across the rotor blade are shown for the inlet distortion and for the wake forcing functions in Figs. 13 and 14. Also presented in these figures as a reference are the flat plate cascade predictions.

The unsteady pressure difference magnitude data for both forcing functions generally decrease with increasing chord, in trendwise agreement with the predictions. The wake-generated magnitude data are of greater amplitude than the corresponding distortion data in the front chord region, with the distortion data increasing and the wake data decreasing with increasing steady loading. The unsteady pressure difference data generated by the two forcing functions are greatly decreased in magnitude and are in better agreement with one another in the mid to aft chord region, with both increasing slightly with increased loading. Thus, the unsteady lift response of the rotor blade is much greater for the wake forcing function than for the inlet distortion, with the differences decreasing with increasing steady loading.

The unsteady pressure difference phase data are nearly independent of the forcing function. Over the front part of the blade, the phase is nearly constant and is independent of the steady loading level. There is a sharp increase in the phase data in the midchord region, with the phase increasing to an aft chord value, which is slightly greater for the wake forcing function than for the inlet distortion for all steady loading levels. The chordwise location of the onset of this rapid phase increase moves forward with increasing steady loading level.

Summary and Conclusions

The fundamental flow physics of wake and distortion-generated periodic rotor blade row unsteady aerodynamics, including the effect of different unsteady aerodynamic forcing functions, were experimentally investigated. This was accomplished through a series of experiments performed in an extensively instrumented axial flow research compressor, which quantified the effects of the aerodynamic forcing function and the steady aerodynamic loading level on the wake and distortion-generated gust unsteady aerodynamics of a first-stage rotor blade. Two different two-per-rev forcing functions were considered: (1) the velocity deficit from two 90 deg circumferential inlet flow distortions, and (2) the wakes from two upstream obstructions, which are characteristics of airfoil or probe excitations. General experimental results are noted in the following with detailed unsteady aerodynamic results summarized in Table 2.

- The rotor steady aerodynamic performance is independent of the aerodynamic forcing function.
- The inlet distortion forcing function shows a dominant two-per-rev, with much small higher harmonic content. In contrast, the wake forcing function shows a strong two-per-rev with higher harmonics of larger amplitudes.
- On both the suction and pressure surfaces, the first harmonic complex unsteady pressure distributions are dependent on the particular forcing function.
- The unsteady pressure difference magnitude data generally decrease with increasing chordwise distance for both forcing functions, in trendwise agreement with the flat plate cascade predictions.
- The wake-generated rotor row unsteady first harmonic response is much greater than that generated by the inlet distortion, with the difference decreasing with increased steady loading.

Acknowledgments

This research was sponsored by the Air Force Office of Scientific Research (AFSC) under Contract No. F49620-88-C-0022. The United States Government is authorized to reproduce and distribute reprints for governmental purposes notwithstanding any copyright notation hereon.

References

Capece, V. R., Manwaring, S. R., and Fleeter, S., 1986, "Unsteady Blade Row Interactions in a Multi-stage Compressor," *AIAA Journal of Propulsion and Power*, Vol. 2, No. 2, pp. 168–174.

Capece, V. R., and Fleeter, S., 1987, "Unsteady Aerodynamic Interactions in a Multi-stage Compressor," ASME JOURNAL OF TURBOMACHINERY, Vol. 109, No. 3, pp. 420–428.

Datko, F. T., Jr., and O'Hara, J. A., 1987, "The Aeromechanical Response of an Advanced Transonic Compressor to Inlet Distortion," ASME Paper No. 87-GT-189.

Fleeter, S., Jay, R. L., and Bennett, W. A., 1978, "Rotor Wake Generated Unsteady Aerodynamic Response of a Compressor Stator," ASME *Journal of Engineering for Power*, Vol. 100, No. 4, pp. 664–675.

Fleeter, S., Bennett, W. A., and Jay, R. L., 1980, "The Time Variant Aerodynamic Response of a Stator Row Including the Effects of Airfoil Camber," ASME *Journal of Engineering for Power*, Vol. 102, No. 2, pp. 334–343.

Gallus, H. E., Lambertz, J., and Wallman, Th., 1980, "Blade-Row Interaction in an Axial-Flow Subsonic Compressor Stage," ASME *Journal of Engineering for Power*, Vol. 102, No. 1, pp. 169–177.

Hardin, L. W., Carta, F. O., and Verdon, J. M., 1987, "Unsteady Aerodynamic Measurements on a Rotating Compressor Blade Row at Low Mach Number," ASME JOURNAL OF TURBOMACHINERY, Vol. 109, No. 4, pp. 499–507.

Manwaring, S. R., and Fleeter, S. 1990, "Inlet Disortion Generated Periodic Aerodynamic Rotor Response," ASME JOURNAL OF TURBOMACHINERY, Vol. 112, pp. 298–307.

Mikolajczak, A., Arnoldi, R., Snyder, L., and Stargardter, H., 1975, "Advanced Fan and Compressor Blade Flutter Analysis Predictions," *AIAA Journal*, Vol. 12, No. 4, pp. 325–332.

O'Brien, W. F., Cousins, W. T., and Sexton, M. R., 1980, "Unsteady Pressure Measurements and Data Analysis Techniques in Axial-Flow Compressors," *ASME Measurement Methods in Rotating Components of Turbomachinery*, pp. 195–201.

Smith, S. N., 1971, "Discrete Frequency Sound Generation in Axial Flow Turbomachines," ARC R&M 3709.

APPENDIX VII

Rotor Blade Unsteady Aerodynamic Gust Response to Inlet Guide Vane Wakes

ASME Paper 91-GT-129

THE AMERICAN SOCIETY OF MECHANICAL ENGINEERS
345 E. 47 St., New York, N.Y. 10017

91-GT-129

Rotor Blade Unsteady Aerodynamic Gust Response to Inlet Guide Vane Wakes

STEVEN R. MANWARING[†] and SANFORD FLEETER
Thermal Sciences and Propulsion Center
School of Mechanical Engineering
Purdue University
West Lafayette, Indiana 47907

ABSTRACT

A series of experiments are performed in an extensively instrumented axial flow research compressor to investigate the fundamental flow physics of wake generated periodic rotor blade row unsteady aerodynamics at realistic values of the reduced frequency. Unique unsteady data are obtained which describe the fundamental unsteady aerodynamic gust interaction phenomena on the first stage rotor blades of a research axial flow compressor generated by the wakes from the Inlet Guide Vanes. In these experiments, the effects of steady blade aerodynamic loading and the aerodynamic forcing function, including both the transverse and chordwise gust components, and the amplitude of the gusts, are investigated and quantified.

NOMENCLATURE

b	Rotor blade semichord
$\bar{C}_l$	Rotor blade steady loading= $\int_0^c (\bar{C}_{p,pressure} - \bar{C}_{p,suction})\, dx$
$\bar{C}_p$	Rotor blade steady pressure coefficient
C_p	Rotor blade unsteady pressure coefficient
$C_{\Delta p}$	Rotor blade unsteady pressure difference coefficient
$\bar{i}$	Rotor blade mean incidence angle
k	Reduced frequency = $\omega b / \bar{V}_x$
p	Digitized ensembled averaged unsteady pressure
P_s	Rotor blade surface steady pressure
$\hat{p}$	First harmonic complex unsteady pressure
$\hat{u}^+$	Streamwise gust first harmonic component
$\hat{v}^+$	Transverse gust first harmonic component
$\bar{V}_x$	Mean axial velocity
ΔV	Absolute velocity vector difference from mean value
ΔW	Total unsteady velocity
$\bar{\beta}$	Relative mean flow angle
$\Delta\bar{\beta}$	Relative flow angle difference from mean value
ω	Forcing function frequency, radians

INTRODUCTION

Periodic aerodynamic excitations generate unsteady aerodynamic forces and moments on turbomachinery blading. At the resonance conditions where the aerodynamic excitation frequency matches a blade natural frequency, catastrophic vibrational responses of the blading may occur. In the design process, Campbell diagrams are utilized to predict the occurrence of the resonant conditions in the operating range of the blade row. Unfortunately, accurate predictions of the amplitude of the blade vibration at these resonances cannot currently be made due to the inability of mathematical models to accurately predict the unsteady aerodynamics, i.e., the aerodynamic forcing function to the blade row and the resulting unsteady aerodynamics acting on the blading. As a result, empirical correlations are currently used to indicate the blade row response to an excitation, with varying degrees of success.

On a first principles basis, forced response unsteady aerodynamics are analyzed by first defining the forcing

[†] Currently Engineer, Aerodynamics Research Laboratory, General Electric Aircraft Engines, Cincinnati, Ohio

Presented at the International Gas Turbine and Aeroengine Congress and Exposition
Orlando, FL June 3-6, 1991
This paper has been accepted for publication in the Transactions of the ASME
Discussion of it will be accepted at ASME Headquarters until September 30, 1991

function in terms of harmonics. The periodic response of an airfoil row to each harmonic is then assumed to be comprised of two components. One is due to the harmonic components of the unsteady aerodynamic forcing function being swept past the nonresponding airfoil row, termed the streamwise and transverse gust responses. The second, the self-induced unsteady aerodynamics, arises when a vibrational response of the airfoil row is generated.

The gust and motion-induced unsteady aerodynamic models involve many physical and numerical assumptions. Therefore, experimental modeling of the fundamental distortion and wake generated blade row periodic unsteady aerodynamic response, including both the forcing function and the resulting blade row unsteady aerodynamics, is needed for validation and enhancement of theoretical and numerical models.

Unsteady aerodynamic gust experiments of direct interest to turbomachines have been performed in low speed research compressors. Fleeter, Jay and Bennett (1978) and Fleeter, Bennett and Jay (1980) investigated the effects of airfoil camber and rotor-stator axial spacing on the unsteady aerodynamics of a stator vane row of a single stage low speed research compressor. Capece, Manwaring and Fleeter (1986) and Capece and Fleeter (1987) performed measurements in a three stage low speed research compressor to investigate the effect of steady airfoil loading and detailed aerodynamic forcing function waveshape on the unsteady aerodynamic response of a stator vane row. Gallus, Lambertz and Wallman (1980) performed measurements at the midspan of a low camber vane of a single stage axial flow compressor. The unsteady lift coefficients corresponding to the first five harmonics of rotor blade wake passing were measured with five transducers embedded in each vane surface.

Gust experiments performed in rotor blade rows include the following. With regard to inlet flow distortions, O'Brien, Cousins, and Sexton (1980) utilized six dynamic pressure transducers embedded on each rotor blade surface to measure the unsteady aerodynamic response to a distorted inlet flow field. However, the periodic rotor blade row inlet flow field was not measured and, thus, the unsteady aerodynamic gust forcing function was not quantified. Hardin, Carta, and Verdon (1987) measured low reduced frequency oscillating airfoil aerodynamics on the rotor of a single stage compressor and also stated that they performed similar distortion experiments although the results were not presented.

Manwaring and Fleeter (1989, 1990) experimentally investigated the unsteady aerodynamic rotor blade row gust response generated by low reduced frequency inlet distortions and wake type disturbances. The major advantage of rotor based unsteady gust experiments over stationary blade row experiments is that the unsteady aerodynamic forcing function is located in the stationary reference frame. This enables a wide range of forcing functions to be more easily generated and without large detrimental effects on compressor overall performance.

In this paper, the rotor blade row fundamental unsteady aerodynamic flow physics generated by periodic wakes are investigated at realistic values of the reduced frequency. In particular, the effects of the detailed unsteady aerodynamic forcing function, including both the transverse and chordwise gust components and the gust amplitude, as well as steady aerodynamic loading on the unsteady aerodynamic gust response of the first stage rotor blade row are investigated. This is accomplished by means of a series of experiments performed in an extensively instrumented axial flow research compressor. Unique unsteady aerodynamic data are obtained which describe both the detailed unsteady aerodynamic forcing function generated by the wakes from the IGV's and the resulting first stage rotor blade row unsteady aerodynamic gust response.

In these experiments, the primary data obtained define the midspan chordwise distributions of both the steady and unsteady pressure on the rotor blade surfaces, with the aerodynamic forcing function generated in the stationary reference frame. These forcing functions are measured with a rotating cross hot-wire probe, with these data then analyzed to determine the streamwise and transverse velocity components, u^+ and v^+ shown in Figure 1. The resulting unsteady aerodynamic gust generated rotor blade surface unsteady pressure chordwise distributions are measured with embedded ultra-miniature high response dynamic pressure transducers. The blade surface steady pressure chordwise distributions are measured with blade surface static taps ported to a rotor-based Scanivalve system.

RESEARCH COMPRESSOR

The Purdue Axial Flow Research Compressor models the fundamental turbomachinery unsteady aerodynamic multistage interaction phenomena which include the incidence angle, the velocity and pressure variations, the aerodynamic forcing function waveforms, the reduced frequency, and the unsteady blade row interactions. The compressor is driven by a 15 HP DC electric motor at a speed of 2,250 RPM. Each identical stage contains 43 rotor blades and 31 stator vanes having a British C4 airfoil profile, with the first stage rotor inlet flow field established by a variable setting inlet guide vane (IGV) row of 36 airfoils. The overall compressor and airfoil characteristics are defined in Table 1.

The compressor aerodynamic performance is determined utilizing a 48 port Scanivalve system, thermocouples, and a venturi orifice to measure the required pressures, temperatures and flow rate, respectively. The Scanivalve transducer is calibrated each time data are acquired, thus automatically compensating for zero and span shifts of the transducer output. A 95% confidence interval, root-mean-square error analysis of 20 samples is performed for each steady data measurement.

INSTRUMENTATION

Both steady and unsteady rotor blade row data are required. These are acquired with the rotor-based instrumentation system schematically depicted in Figure 2. The steady data quantify the rotor row mean inlet flowfield and the resulting rotor blade midspan steady loading distribution. The unsteady data define the periodic aerodynamic forcing function and the resulting midspan blade surface periodic unsteady pressure distributions.

The inlet flow field, both steady and unsteady, is measured with a rotating cross hot-wire probe. Disturbances in the stationary frame-of-reference, i.e., the IGV wakes, are the unsteady aerodynamic forcing functions to the first stage rotor row. The rotor periodic unsteady inlet flow field generated by these disturbances is measured with a cross hot-wire mounted in the rotor frame-of-reference. The probe is axially mounted 30% of rotor chord upstream of the rotor leading edge plane. A potential flow field analysis determined this axial location to be such that leading edge potential effects are negligible for all steady loading levels. The probe is angularly aligned to obtain rotor relative velocity and flow angle data. The cross hot-wire probe was calibrated and linearized for velocities from 18.3 m/sec to 53.4 m/sec and +/- 35 degrees angular variation, with the accuracy of the velocity magnitude and flow angle were determined to be 4% and +/- 1.0 degree, respectively. Centrifugal loading effects on the rotating hot-wire sensor resistances and, thus, the responses, were found to be negligible.

The detailed steady aerodynamic loading on the rotor blade surfaces is measured with a chordwise distribution of 20 midspan static pressure taps, 10 on each surface. The static pressure at the rotor exit plane, measured with a rotor drum static tap, is used as the blade surface static pressure reference. These static pressure measurements are made using a rotor based 48 port constant speed drive Scanivalve system located in the rotor drum.

The measurement of the midspan rotor blade surface unsteady pressures is accomplished with 20 ultra-miniature, high response transducers embedded in the rotor blades at the same chordwise locations as the static pressure taps. To minimize the possibility of flow disturbances associated with the inability of the transducer diaphragm to exactly maintain the surface curvature of the blade, a reverse mounting technique is utilized. The pressure surface of one blade and the suction surface of the adjacent blade are instrumented, with transducers embedded in the nonmeasurement surface and connected to the measurement surface by a static tap. The embedded dynamic transducers are both statically and dynamically calibrated. The static calibrations show good linearity and no discernible hysteresis. The dynamic calibrations demonstrate that the frequency response, in terms of gain attenuation and phase shift, are not affected by the reverse mounting technique. The accuracy of the unsteady pressure measurements, determined from the calibrations, is +/- 4%.

The rotor-based static pressure Scanivalve transducer, rotating cross hot-wire probe and 20 blade surface dynamic pressure transducers are interfaced to the stationary frame-of-reference through a 40 channel slip ring assembly. On-board signal conditioning of the transducer output signals is performed to maintain a good signal-to-noise ratio through the slip rings. The remaining 17 channels of the slip-ring assembly are used to provide excitation to the transducers and on/off switching to the Scanivalve DC motor.

DATA ACQUISITION AND ANALYSIS

Steady Data

The rotor blade surface static pressure data, measured with the rotor-based Scanivalve system, are defined by a root-mean-square error analysis of 20 samples with a 95% confidence interval. The reference for these midspan blade pressure measurements is the static pressure at the exit of the rotor measured on the rotor drum. Thus, the blade surface and the reference static pressures are measured at different radii. Hence, a correction for the resulting difference in the radial acceleration is applied in calculating the blade surface static pressure coefficient defined in Equation 1.

$$\bar{C}_p = \frac{\bar{P}_s - \bar{P}_{exit}}{1/2\ \rho\ U_t^2} \qquad (1)$$

where U_t is the rotor blade tip speed.

Periodic Data

The periodic data of interest are the harmonic components of the aerodynamic forcing function to the first stage rotor blade row together with the resulting rotor blade surface unsteady pressures and unsteady pressure differences. These are determined by defining

a digitized ensemble averaged periodic unsteady aerodynamic data set consisting of the rotating cross hot-wire probe and blade surface dynamic pressure transducer signals at each steady operating point. In particular, these time-variant signals are digitized with a high speed A-D system at a rate of 100 kHz and then ensemble averaged.

The key to this averaging technique is the ability to sample data at a preset time, accomplished by an optical encoder mounted on the rotor shaft. The microsecond range step voltage signal from the encoder is the data initiation time reference and triggers the high speed A-D multiplexer system. To significantly reduce the random fluctuations superimposed on the periodic signals of interest, 200 averages are used. A Fast Fourier Transform (FFT) algorithm is then applied to these ensemble averaged signals to determine the harmonic components of the unsteady aerodynamic forcing function and the resulting rotor blade surface harmonic unsteady pressures and pressure differences.

The unsteady inlet flow field to the rotor row is measured with the rotating cross hot-wire probe which quantifies the relative velocity and flow angle. The velocity triangle relations depicted in Figure 1 are then used to determine the unsteady inlet flow field to the rotor, in particular, the streamwise and transverse velocity components, u^+ and v^+, respectively. These are then Fourier decomposed to determine the first harmonic of the streamwise and transverse velocity components, termed the streamwise and transverse gust components, $\hat{u}^+$ and $\hat{v}^+$.

The various unsteady aerodynamic gust mathematical models reference the gust generated airfoil aerodynamic response to a transverse gust at the leading edge of the airfoil. However, in the experiments described herein, the time-variant data are referenced to the initiation of the data acquisition shaft trigger pulse. Thus, for consistency with the models, the periodic data are further analyzed and referenced to a transverse gust at the leading edge of the first stage rotor blade. This is accomplished by assuming that: (1) the aerodynamic forcing function remains fixed in the stationary reference frame; and (2) the forcing function does not decay from the rotating hot-wire probe axial location to the rotor row leading edge plane.

The rotor blade surface unsteady pressure data, measured with the embedded high response pressure transducers, are analyzed to determine the harmonics of the chordwise distribution of the unsteady pressure coefficient, C_p, and the unsteady pressure difference coefficient, $C_{\Delta p}$. These are defined in Equation 2 and are specified from the Fourier coefficients of the digitized ensemble averaged dynamic pressure transducer signals.

$$C_p = \frac{\hat{p}}{\rho \bar{V}_x^2 \left(\frac{\hat{v}^+}{\bar{V}_x}\right) \bar{\beta}} \tag{2a}$$

$$C_{\Delta p} = C_{p,pressure} - C_{p,suction} \tag{2b}$$

where $\hat{v}^+$ is the first harmonic transverse gust component, $\bar{V}_x$ is the mean axial velocity, and $\bar{\beta}$ is the relative mean flow angle in radians.

The final form of the gust generated rotor blade row unsteady aerodynamic data define the chordwise distribution of the harmonic complex unsteady pressure and pressure difference coefficients. Also included as a reference where appropriate are predictions from the transverse gust analysis of Smith (1971). This model analyzes the unsteady aerodynamics generated on a flat plate airfoil cascade at zero incidence by a transverse gust convected with an inviscid, subsonic, compressible flow.

RESULTS

A series of experiments are performed to investigate and quantify the effects on the unsteady aerodynamic gust response of the first stage rotor blade row due to the detailed variation of the unsteady aerodynamic forcing function generated by the IGV wakes. Forcing function effects include both the transverse and chordwise gust components, defined by the ratio of the amplitudes of the first harmonic streamwise-to-transverse gust components, $|\hat{u}^+/\hat{v}^+|$, and the gust amplitude, defined by the ratio of the first harmonic transverse gust magnitude to mean axial velocity, $|\hat{v}^+/\bar{V}_x|$. The ratio of the streamwise-to-transverse gust amplitude, $|\hat{u}^+/\hat{v}^+|$, was varied by changing the IGV setting angle. The level of steady aerodynamic loading, characterized by the mean incidence angle, was varied as a parameter. The variation in the rotor blade steady loading was obtained by holding the rotor speed constant and varying the mass flow rate and, thus, the mean flow incidence angle to the rotor blade row.

Periodic Aerodynamic Forcing Function

Four distinct 36-per-revolution aerodynamic forcing functions to the first stage rotor blade row are generated, characterized by nominal first harmonic streamwise-to-transverse gust amplitude ratios of 0.29, 0.37, 0.45, and 0.55. The unsteady aerodynamic gusts generated from the IGV wake first harmonic have nominal reduced frequency values between 5 and 6. The Fourier decomposition of these IGV wake aerodynamic forcing functions to the first stage rotor row shows a dominant 36-per-rev excitation fundamental harmonic with smaller higher harmonics. As the gust amplitude ratio increases, the transverse

harmonic gust amplitudes become smaller while the streamwise harmonic gust amplitudes become larger with respect to the mean axial velocity.

Blade Surface Steady Pressures

The effect of steady aerodynamic loading as characterized by the mean incidence angle on the rotor blade surface steady pressure coefficient is shown in Figure 3. The level of steady loading only affects the steady pressure distribution on the pressure surface over the front 40% of the chord. On the suction surface, the steady loading variation has a large effect on the steady pressure distribution over the entire suction surface. Also, these data give no indication of suction surface flow separation. It should be noted that these surface steady pressure distributions are not affected by the characteristics of the periodic unsteady aerodynamic forcing function.

Rotor Row Periodic Aerodynamic Response

The periodic aerodynamic response of the first stage rotor blade row to the IGV wake first harmonic forcing function are presented in the format of the chordwise distribution of the complex unsteady pressure coefficient on the individual rotor blade surfaces as well as the corresponding complex unsteady pressure difference coefficient generated by the 36-per-rev IGV wake first harmonic forcing function, with the steady loading level as a parameter.

Pressure Surface Unsteady Pressure

The effect of steady aerodynamic loading level on the IGV wake generated first harmonic complex unsteady pressure distribution on the rotor blade pressure surface is shown in Figures 4, 5, 6 and 7 for nominal streamwise-to-transverse gust amplitude ratios of 0.29, 0.37, 0.45 and 0.55, respectively. The first harmonic gust amplitude, characterized by $|\hat{v}^+/\bar{V}_x|$ values of approximately 0.1 is small compared to the mean axial velocity.

For each gust amplitude ratio value, the form of the dimensionless unsteady pressure coefficient specified in Equation 2 results in a compression of the unsteady pressure magnitude data over the entire pressure surface for all gust amplitude ratios and all but the two lowest steady loading levels. For these two loading cases, large variations are found in the magnitude data in the neighborhood of the quarter chord, with these variations decreasing with increasing gust amplitude ratio. This corresponds to the previously noted effects of steady loading on the rotor blade surface steady pressure wherein loading primarily influences the front part of the pressure surface. Namely, the steady pressure coefficient value for the rotor drum hub steady pressure coefficient upstream of the rotor row is approximately 0.24, thereby indicating that the mean flow field accelerates around the pressure surface leading edge before decelerating (diffusing) for the two lowest mean incidence angles, i.e., the steady pressure coefficient decreases and then increases.

The level of steady loading has only a minimal effect on the pressure surface unsteady pressure phase, the exception being the two lowest steady loading levels in the front chord region. Also as $|\hat{u}^+/\hat{v}^+|$ increases, the decrease in phase in the 25% chord region becomes less for the two low steady loading levels, while the three highest steady loading levels in the front chord region and all steady loading levels in the aft chord region remain relatively unaffected by the gust amplitude ratio.

Suction Surface Unsteady Pressures

The effect of steady aerodynamic loading on the IGV wake generated first harmonic complex unsteady pressure on the rotor blade suction surface is shown in Figures 8, 9, 10 and 11 for the four nominal gust amplitude ratio values.

The unsteady pressure coefficient magnitude on the entire suction surface is a strong function of the level of steady aerodynamic loading. This corresponds to the previously presented suction surface steady pressure data variation with mean incidence angle. For all gust amplitude ratios, the front-to-mid chord region data show a decreasing-increasing magnitude trend with chord, with the minimum magnitude chordwise location moving forward with increasing steady loading. This minimum corresponds to the minimum in the steady pressure chordwise distribution, Figure 5, wherein the chordwise location of the change from accelerating to decelerating mean flow moves forward with increasing mean incidence. Thus, similar to the pressure surface unsteady response in the front chord region at negative mean incidence angle, the unsteady gust interacts with the accelerating mean flow field around the suction surface in the front chord region. In the mid-to-aft chord region, the gust amplitude ratio alters the effect of steady loading on the chordwise distributions of the unsteady pressure response. Namely, for the large gust amplitude ratios, a decreasing-increasing unsteady pressure magnitude trend with chord occurs, with the minimum moving forward with increasing steady loading. As $|\hat{u}^+/\hat{v}^+|$ decreases, this increasing-decreasing magnitude trend with chord becomes smoother and the data increase dramatically in magnitude in the aft half chord. Thus, for this higher camber suction surface, the mean flow field interacts with the unsteady gust over the entire blade surface, with the gust amplitude ratio affecting the response over the aft half of the surface.

Nearest to the leading edge, the magnitude data increase with increasing steady loading level. As noted

previously, this steady loading trend is attributed to the IGV wake first harmonic gust interacting with the mean accelerating flow field around the blade leading edge. Hathaway et. al. (1987) have experimentally demonstrated the interaction of a rotor wake with a downstream stator row. They found that from approximately -20% to 10% of the downstream stator chord, the rotor wake generated unsteady velocity magnitude increases, with the increase becoming larger as steady loading increases. This indicates that the wake generated gust magnitude increases due to the interaction with the accelerating mean flow field around the blade leading edge.

With regard to the phase of the unsteady pressure, the streamwise-to-transverse gust amplitude ratio has minimal effect, with steady loading primarily affecting the phase on the aft three quarters of the chord. As the mean incidence angle is increased from the low loading level, the chordwise variation of the phase data on the aft part of the surface becomes linear, with the extent of this linear distribution increasing with increasing mean incidence. This linear chordwise distribution indicates the existence of a wave phenomenon, with a convective velocity equal to the mean axial velocity through the blade row (20.5 m/sec). This mean axial velocity wave phenomenon has been experimentally detected by other authors, Fleeter, et al. (1980) and Hodson (1984) but is yet to be physically explained.

Summarizing these blade surface steady loading and gust amplitude ratio effects, for the low camber pressure surface in the chordwise region where the mean flow field does not accelerate, i.e., the mid-to-aft chord region for all steady loading levels and the front chord region for the three high steady loading levels, the data compress for all gust amplitude ratios, indicating that steady loading as characterized by the mean flow incidence is a key mechanism for the low camber unsteady aerodynamic wake response. However, in an accelerating mean flow field, i.e., the front chord region for the two low steady loading levels, mean flow field interactions with the unsteady gust are also important. As the gust amplitude ratio increases, this interaction lessens. On the higher camber suction surface, the interaction between the mean flow field and the unsteady gust affects the unsteady aerodynamic response over the entire blade surface for all steady loading levels and streamwise-to-transverse gust amplitude ratios. Also, the gust amplitude ratio has a large effect on these interactions over the aft half of the blade surface.

Unsteady Pressure Differences

The steady loading effect on the first harmonic of the complex unsteady pressure difference across the rotor blade camberline is shown in Figures 12, 13, 14 and 15 for the nominal streamwise-to-transverse gust amplitude ratios of 0.29, 0.37, 0.45 and 0.55, respectively. Also presented as a reference are the flat plate cascade, inviscid, transverse gust predictions of Smith (1971) and Whitehead (1987).

The effects of steady loading on the previously presented individual pressure and suction surface magnitude and phase data are still apparent, with the suction surface effects being dominant. For example, analogous to the high gust amplitude steady loading trends on the suction surface for the high gust amplitude ratio, the unsteady pressure difference magnitude data show two decreased magnitude regions, one in the front chord region and the other in the mid-to-aft chord region, with the chordwise location of the magnitude minima moving forward with increased steady loading. Also, the chordwise location where the rapid increase in value of the phase data begins to occur moves forward with increasing steady loading similar to the suction surface, whereas for the low steady loading level, the phase decreases sharply at 25% rotor chord per the pressure surface trends. Similar to the steady loading trends in the suction surface aft chord region, as the gust amplitude ratio decreases, the magnitude data increase.

These steady loading effects cause the chordwise distribution of the unsteady pressure difference magnitude and phase data to differ greatly from the flat plate cascade predictions, with the magnitude data not just decreasing with increasing chord and the phase data not remaining nearly constant with chord per the predictions. The lowest steady loading level, which most closely approximates the prediction model no loading condition, shows fair comparison with the magnitude data except in chord regions where strong gust interactions with the steady flow field occur, i.e., the pressure surface interaction at 25% chord and the suction surface interaction in the aft chord. The prediction differs from the phase data by approximately 90 degrees over the entire blade except, once again, in the 25% and aft chord region.

Effect of Gust Amplitude

The previous results considered the periodic aerodynamic response of the first stage rotor blade row to relatively small amplitude IGV wake first harmonic gusts, with the ratio of the transverse gust to mean axial velocity on the order of 0.1. The effect of larger amplitude gusts, $|\bar{v}^+/\bar{V}_x|$ on the order of 0.3, on the blade surface unsteady pressure response, including the effect of steady loading, are presented in Figures 16 and 17, where the effect of operation at the five nominal steady loading levels is also included. In particular, these figures present the chordwise distribution of the complex unsteady pressure coefficient on the pressure and suction surfaces generated by large amplitude 36-per-rev IGV wake first harmonic forcing functions.

The effect of the larger amplitude gusts on the pressure surface unsteady pressure response is

demonstrated by comparing the high amplitude gust generated response with that resulting from the low amplitude gust of the same nominal streamwise-to-transverse gust amplitude ratio value, Figures 5 and 16. Nearly identical unsteady pressure magnitude and phase responses are shown for both gust amplitudes except in the 25% chord region for the lowest two mean flow incidence angles. In this front chord region at negative mean flow incidence, the interaction between the accelerating mean flow field and the unsteady gust is weaker for the larger amplitude gust, as evidenced by the decrease in the magnitude and phase variation.

The effect of large amplitude gusts on the suction surface unsteady pressure response is seen by comparing the high and low amplitude gust generated response for equivalent gust amplitude ratio values, Figures 9 and 17. The phase data are unaffected by the gust amplitude, with the steady loading effect on the phase chordwise distributions being nearly equivalent. However, the magnitude data are greatly affected by the gust amplitude, particularly over the aft three quarters of the surface. The high amplitude gust magnitude data are greatly decreased compared to the low amplitude gust magnitude data, with the steady loading effect being greatly reduced. Thus, similar to the pressure surface front chord region at negative mean flow incidence, the interaction of high amplitude gusts with the mean flow is weaker than the interaction of low amplitude gusts with the mean flow.

SUMMARY AND CONCLUSIONS

The rotor blade row fundamental unsteady aerodynamic flow physics generated by periodic wakes were investigated at realistic values of the reduced frequency. In particular, the effects of the detailed unsteady aerodynamic forcing function, including both the transverse and chordwise first harmonic gust components and the gust amplitude, as well as steady aerodynamic loading on the unsteady aerodynamic gust response of the first stage rotor blade row were investigated and quantified. This was accomplished by means of a series of experiments performed in an extensively instrumented axial flow research compressor.

The rotor blade surface steady loading distributions were quantified with surface static pressure taps and a rotor-based Scanivalve system. The aerodynamic forcing function to the rotor blade row was determined with a rotating cross hot-wire probe, with the aerodynamic gust generated rotor blade surface unsteady pressure chordwise distributions measured with embedded ultra-miniature high response dynamic pressure transducers.

The detailed IGV wake generated unsteady aerodynamic results of these experiments are summarized in the following.

Forcing Function

* The IGV wake forcing function shows a dominant 36-per-rev, with smaller higher harmonic content.

Blade Surface Steady Pressures

* Steady loading affects the steady pressure distribution on the front portion of the blade pressure surface and over the entire suction surface.

* The unsteady gust amplitude ratio and magnitude have negligible effect on the steady pressur distribution.

Pressure Surface Response

* The unsteady pressure phase data are nearly independent of the steady loading level and the gust amplitude ratio except in the front chord region at negative mean flow incidence.

* The selected unsteady pressure nondimensionalization compresses the magnitude data with regard to mean flow incidence angle for each gust component amplitude ratio except in the front chord region for negative mean flow incidence.

* Increasing the gust amplitude ratio results in weaker interactions between the mean and unsteady flow fields in the front chord region at negative mean flow incidence.

* Large amplitude gusts reduce this interaction between the unsteady gust and the accelerating mean flow field.

* The magnitude of the unsteady pressure response on the blade pressure surface, i.e., the low camber surface, is thus primarily affected by the level of steady loading as characterized by the mean flow incidence angle except in the accelerating mean flow field of the front chord region at negative mean flow incidence.

Suction Surface Response

* The unsteady pressure phase data are nearly independent of the gust component amplitude ratio, with increased mean incidence resulting in a linear chordwise distribution which corresponds to a wave phenomenon convected at the mean axial velocity of the flow through the rotor blade row.

* The selected unsteady pressure nondimensionalization does not compress the magnitude data with regard to mean flow incidence angles.

* The mid-to-aft chord magnitude data are a strong function of the gust amplitude ratio, with the increase in magnitude with increasing steady loading becoming smaller with increasing gust amplitude ratio.

* Large amplitude gusts reduce these mean flow field interactions with the unsteady gust, similar to the pressure surface.

* The magnitude of the unsteady pressure response on the blade suction surface, i.e., the higher camber surface, is thus affected by both the steady flow field interactions and the gust amplitude ratio.

Unsteady Pressure Difference Response

* The unsteady pressure difference data reflect the effects of loading on the pressure and suction surface unsteady data, with the suction surface effects being dominant.

* These steady loading effects cause the chordwise distribution of the magnitude and phase data to differ greatly from the flat plate cascade predictions.

* The lowest steady loading level data was correlated with flat plate cascade predictions, with the unsteady aerodynamic response correlation being fair.

ACKNOWLEDGEMENTS

Research sponsored by the Air Force Office of Scientific Research (AFSC) under Contract F49620-88-C-0022. The United States Government is authorized to reproduce and distribute reprints for governmental purposes notwithstanding any copyright notation hereon.

REFERENCES

Capece, V.R. and Fleeter, S., "Unsteady Aerodynamic Interactions in a Multi-Stage Compressor," *ASME Paper No. 87-GT-171*, 1987.

Capece, V.R., Manwaring, S.R., and Fleeter, S. "Unsteady Blade Row Interactions in a Multi-Stage Compressor" *AIAA Journal of Propulsion*, Vol. 2, No. 2, March-April 1986, pp. 168-174.

Fleeter, S., Bennett, W.A., and Jay, R.L., "The Time-Variant Aerodynamic Response of a Stator Row Including the Effects of Airfoil Camber," *ASME Journal of Engineering for Power*, Vol. 102, April 1980, pp. 334-343.

Fleeter, S., Jay, R.L., and Bennett, W.A., "Rotor Wake Generated Unsteady Aerodynamic Response of a Compressor Stator," *ASME Journal of Engineering for Power*, Vol. 100, October, 1978, pp. 664-675.

Gallus, H.E. Lambertz, J., and Wallman, Th., "Blade-Row Interaction in an Axial-Flow Subsonic Compressor Stage," *ASME Journal of Engineering for Power*, Vol. 102, January 1980, pp. 169-177.

Hardin, L.W., Carta, F.O., and Verdon, J.M., "Unsteady Aerodynamic Measurements on a Rotating Compressor Blade Row at Low Mach Number," *ASME Journal of Turbomachinery*, Vol. 109, No. 4, October 1987, pp. 499-507.

Hathaway, M.D., Suder, K.L., Okiishi, T.H., Strazisar, A.J., and Adamczyzk, J., "Measurements of the Unsteady Flow Field Within the Stator Row of a Transonic Axial-Flow Fan II - Results and Discussion," *ASME Paper No. 87-GT-227*, June 1987.

Hodson, H.P., "Measurements of Wake-Generated Unsteadiness in the Rotor Passages of Axial Flow Turbines," *ASME Paper No. 84-GT-189*, June 1984.

Manwaring, S.R. and Fleeter, S., "Inlet Distortion Generated Periodic Aerodynamic Rotor Response," *ASME Journal of Turbomachinery*, Vol. 112, No. 2, April 1990, pp. 298-307.

Manwaring, S.R. and Fleeter, S., "Forcing Function Effects on Rotor Periodic Aerodynamic Response," ASME Paper 90-GT-109 *ASME International Gas Turbine Conference*, June 1990.

O'Brien, W.F., Cousins, W.R., and Sexton, M.R., "Unsteady Pressure Measurements and Data Analysis Techniques in Axial-Flow Compressors," *Measurement Methods in Rotating Components of Turbomachinery*, ASME, 1980, pp. 195-201.

Smith, S.N., "Discrete Frequency Sound Generation in Axial Flow Turbomachines," *ARC R&M 3709*, 1971.

Suder, K.L., Hathaway, M.D., Okiishi, T.H., Strazisar, A.J., and Adamcyzk, J., "Measurements of the Unsteady Flow Field Within the Stator Row of a Transonic Axial-Flow Fan I - Measurement and Analysis Technique," *ASME Paper No. 87-GT-226*, June 1987.

Whitehead, D.S., 1987, "Classical Two-Dimensional Methods," AGARD Manual on Aeroelasticity in Axial Flow Turbomachines, Volume 1: Unsteady Turbomachinery Aerodynamics, *AGARDograph No. 298*, pp. 3-1 - 3-30.

Table 1. Overall airfoil and compressor characteristics

	ROTOR	STATOR	IGV
Airfoil type	C4	C4	C4
Number of Airfoils	43	31	36
Chord, C (mm)	30	30	30
Solidity, C/S	1.14	1.09	0.96
Camber, θ	28.0	27.7	36.9
Stagger Angle, γ	36.0	-36.0	21.0
Inlet Metal Angle, β_1	50.0	30.0	0.0
Aspect Ratio	2.0	2.0	2.0
Thickness/Chord (%)	10.0	10.0	10.0
Flow Rate (kg/s)		2.03	
Design Axial Velocity (m/s)		24.4	
Design Rotational Speed (RPM)		2250	
Number of Stages		3	
Design Stage Pressure Ratio		1.0	
Inlet Tip Diameter (mm)		420	
Hub/Tip Radius Ratio		0.714	
Stage Efficiency (%)		85	

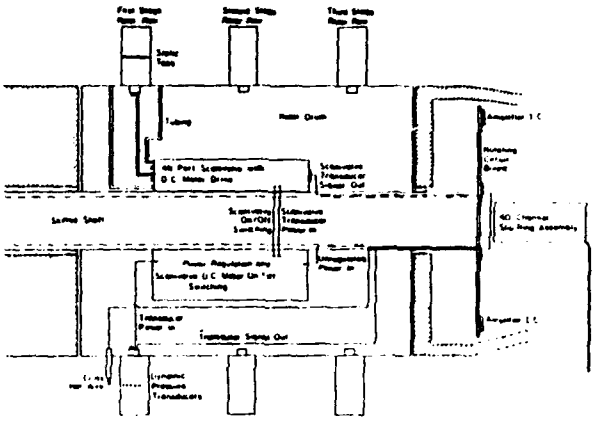

Figure 2. Rotor based instrumentation

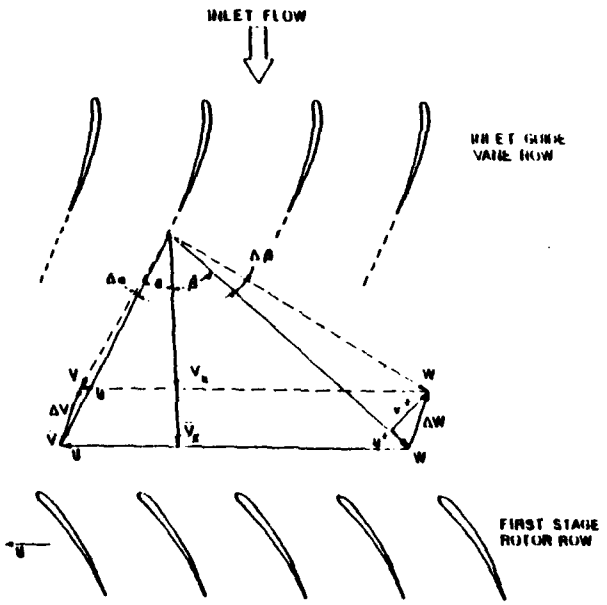

Figure 1. Schematic of IGV wake generated transverse and streamwise unsteady velocities, u^+ and v^+

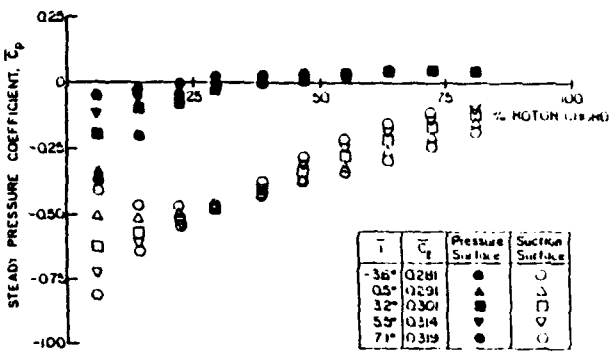

Figure 3. Steady pressure chordwise distributions for five steady loading levels

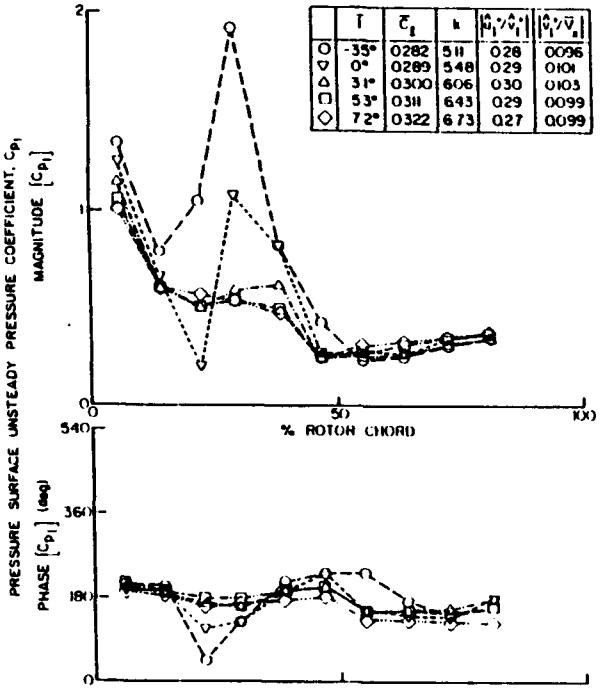

	$\bar{i}$	$\bar{C}_t$	k	$\lvert\hat{C}_1/\hat{C}_1\rvert$	$\lvert\hat{C}_1/\bar{V}_x\rvert$
○	-35°	0282	511	028	0096
▽	0°	0289	548	029	0101
△	31°	0300	606	030	0105
□	53°	0311	643	029	0099
◇	72°	0322	673	027	0099

Figure 4. Steady loading effect on blade pressure surface unsteady response for a nominal 1st harmonic $|\hat{u}^+/\hat{v}^+|$ of 0.29.

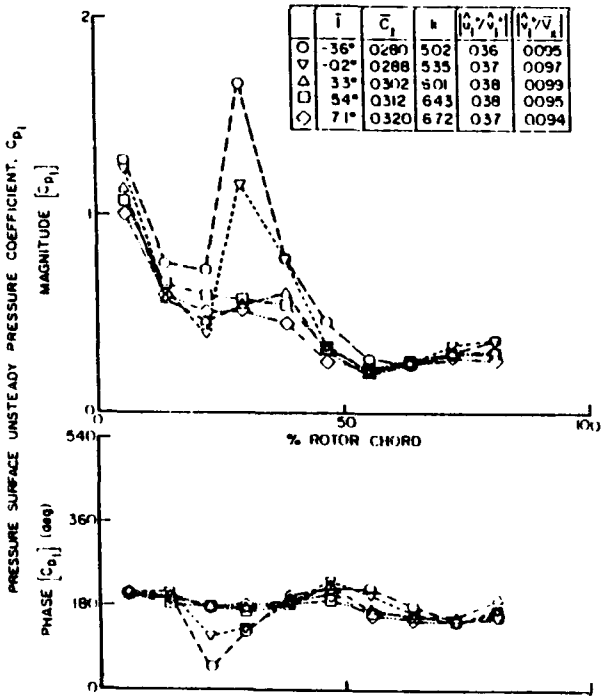

	$\bar{i}$	$\bar{C}_t$	k	$\lvert\hat{C}_1/\hat{C}_1\rvert$	$\lvert\hat{C}_1/\bar{V}_x\rvert$
○	-36°	0280	502	036	0095
▽	-02°	0288	535	037	0097
△	33°	0302	601	038	0099
□	54°	0312	643	038	0095
◇	71°	0320	672	037	0094

Figure 5. Steady loading effect on blade pressure surface unsteady response for a nominal 1st harmonic $|\hat{u}^+/\hat{v}^+|$ of 0.37.

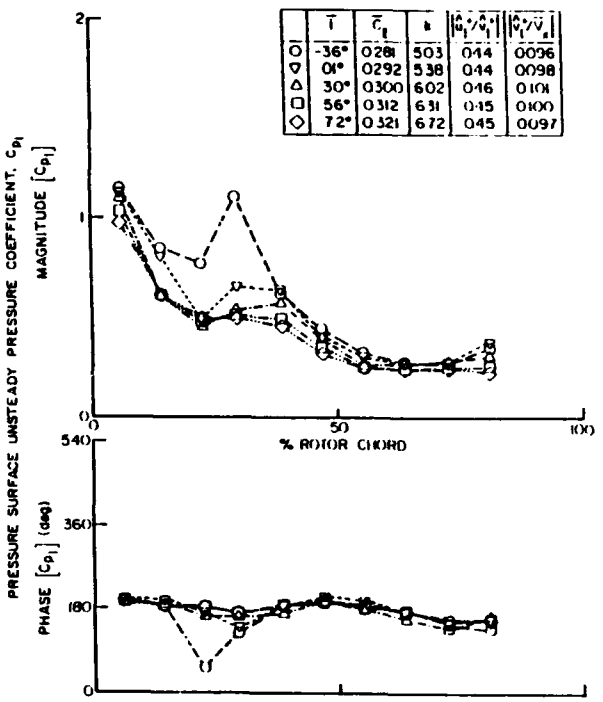

	$\bar{i}$	$\bar{C}_t$	k	$\lvert\hat{C}_1/\hat{C}_1\rvert$	$\lvert\hat{C}_1/\bar{V}_x\rvert$
○	-36°	0281	503	044	0096
▽	04°	0292	538	044	0098
△	30°	0300	602	046	0101
□	56°	0312	631	045	0100
◇	72°	0321	672	045	0097

Figure 6. Steady loading effect on blade pressure surface unsteady response for a nominal 1st harmonic $|\hat{u}^+/\hat{v}^+|$ of 0.45.

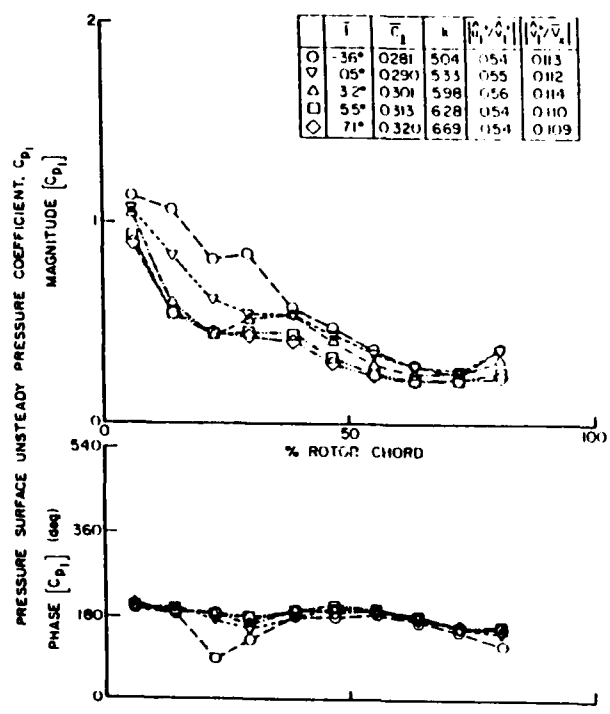

	$\bar{i}$	$\bar{C}_t$	k	$\lvert\hat{C}_1/\hat{C}_1\rvert$	$\lvert\hat{C}_1/\bar{V}_x\rvert$
○	-36°	0281	504	054	0113
▽	05°	0290	535	055	0112
△	32°	0301	598	056	0114
□	55°	0313	628	054	0110
◇	71°	0320	669	054	0109

Figure 7. Steady loading effect on blade pressure surface unsteady response for a nominal 1st harmonic $|\hat{u}^+/\hat{v}^+|$ of 0.55.

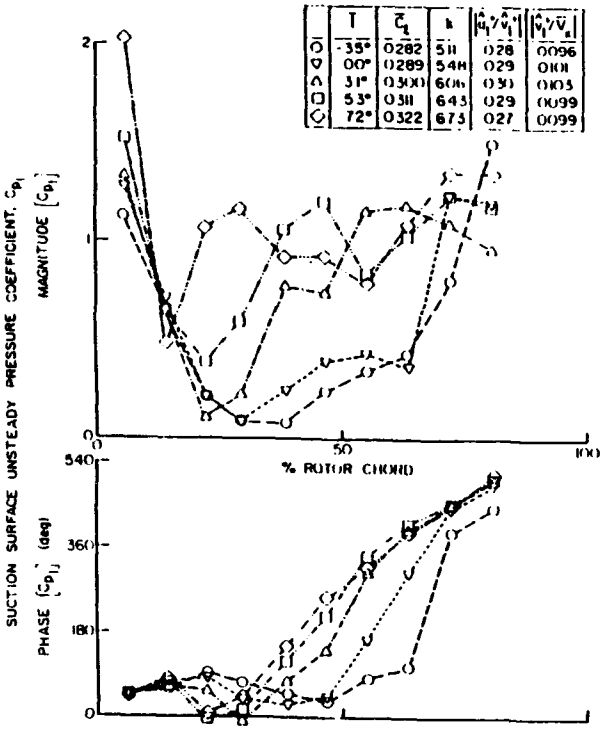

Figure 8. Steady loading effect on blade suction surface unsteady response for a nominal 1st harmonic $|\hat{u}^+/\hat{v}^+|$ of 0.29.

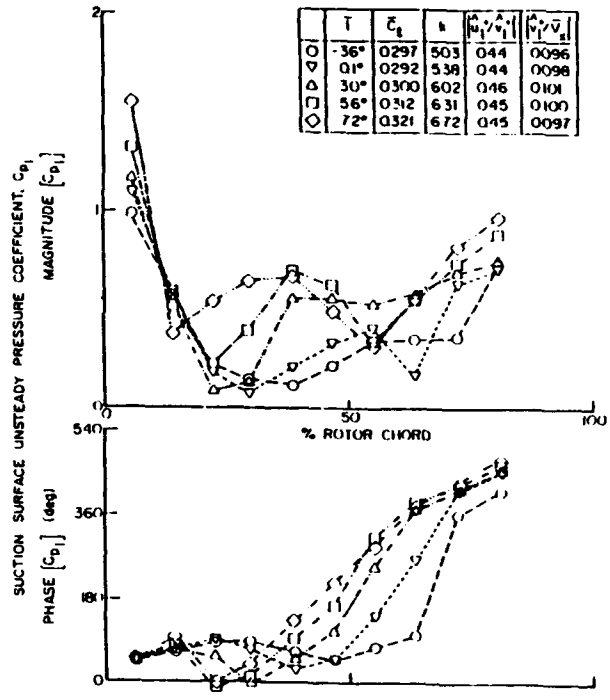

Figure 10. Steady loading effect on blade suction surface unsteady response for a nominal 1st harmonic $|\hat{u}^+/\hat{v}^+|$ of 0.45.

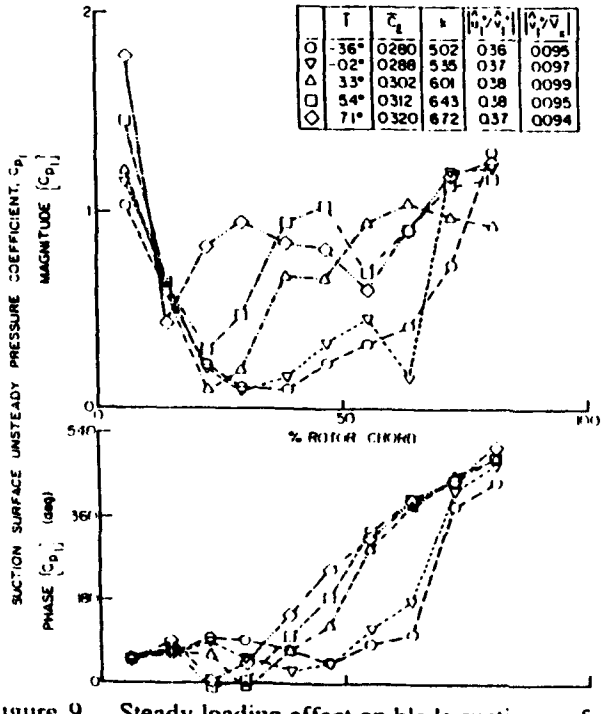

Figure 9. Steady loading effect on blade suction surface unsteady response for a nominal 1st harmonic $|\hat{u}^+/\hat{v}^+|$ of 0.37.

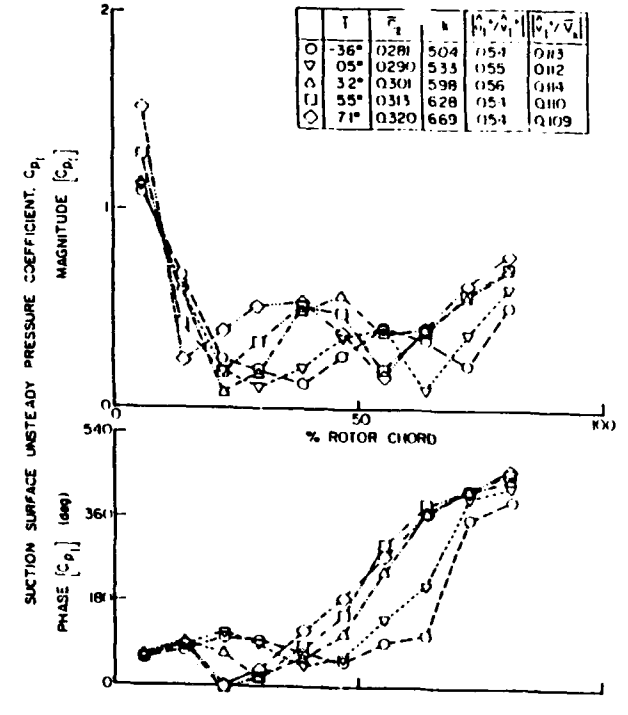

Figure 11. Steady loading effect on blade suction surface unsteady response for a nominal 1st harmonic $|\hat{u}^+/\hat{v}^+|$ of 0.55.

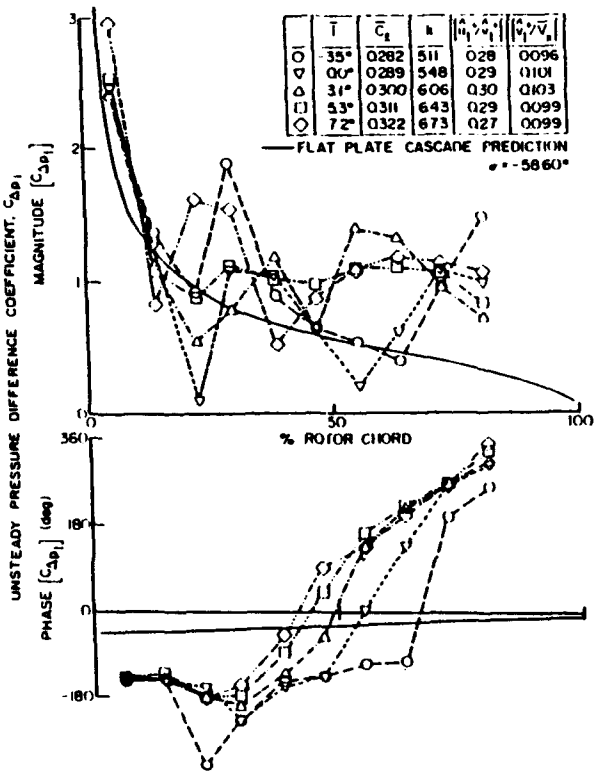

Figure 12. Steady loading effect on blade unsteady pressure difference response for a nominal 1st harmonic $|\hat{u}^+/\hat{v}^+|$ of 0.29.

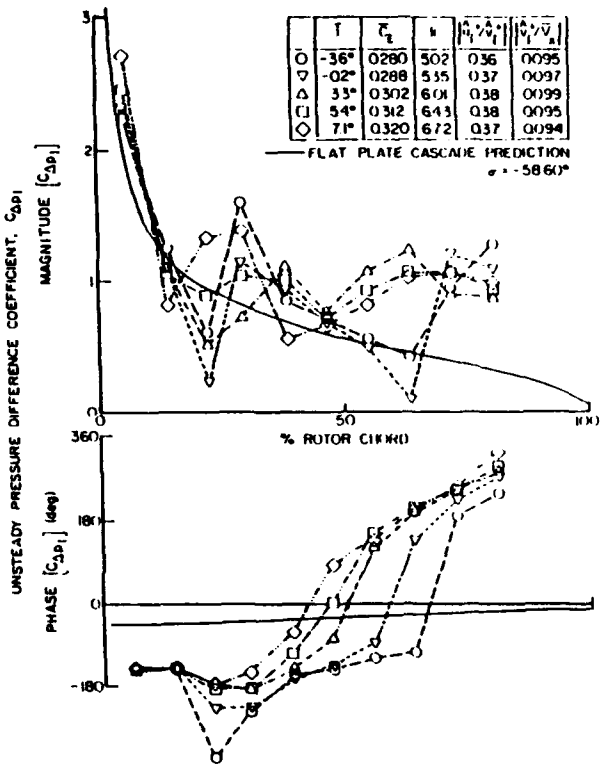

Figure 13. Steady loading effect on blade unsteady pressure difference response for a nominal 1st harmonic $|\hat{u}^+/\hat{v}^+|$ of 0.37.

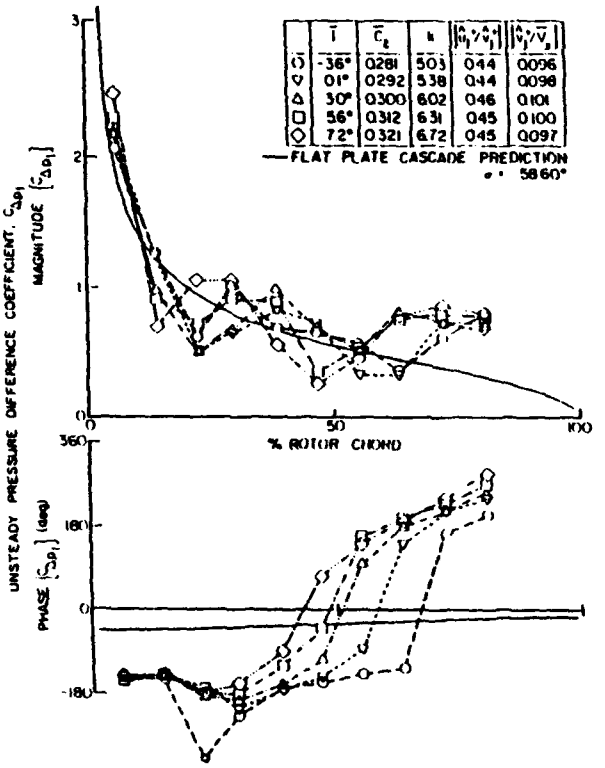

Figure 14. Steady loading effect on blade unsteady pressure difference response for a nominal 1st harmonic $|\hat{u}^+/\hat{v}^+|$ of 0.45.

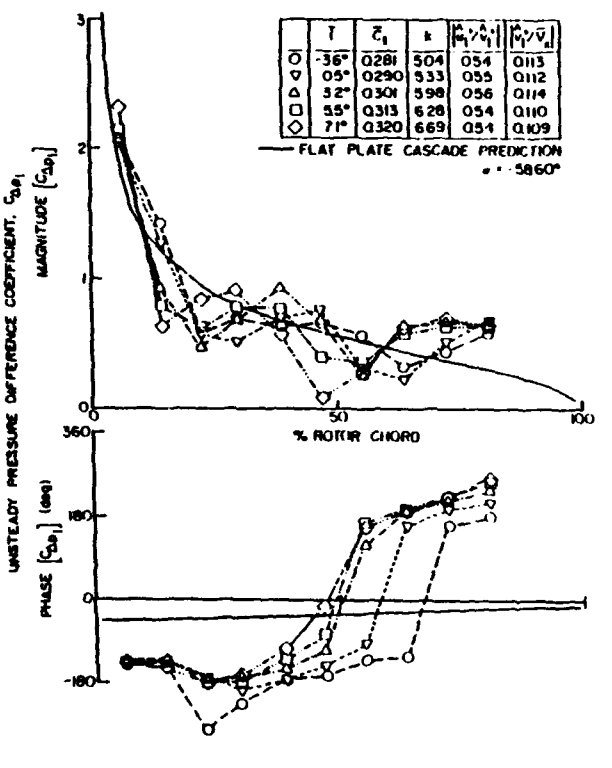

Figure 15. Steady loading effect on blade unsteady pressure difference response for a nominal 1st harmonic $|\hat{u}^+/\hat{v}^+|$ of 0.55.

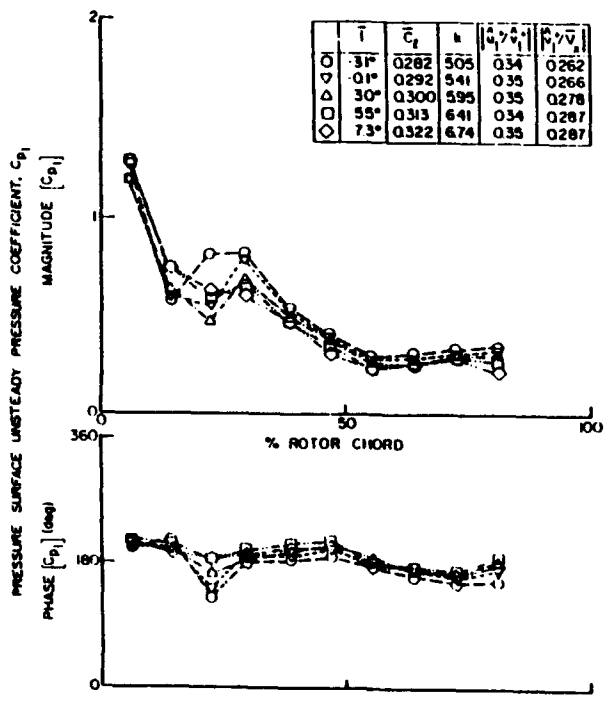

Figure 16. Steady loading effect on blade pressure surface response for large amplitude gusts

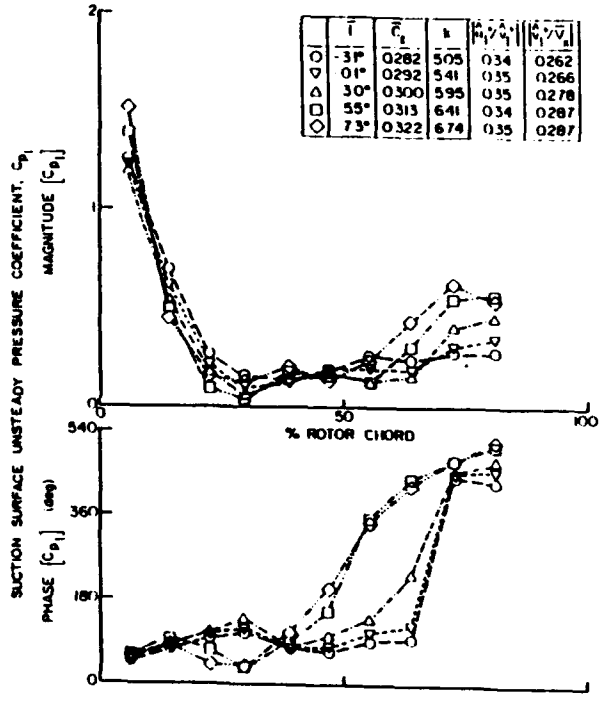

Figure 17. Steady loading effect on blade suction surface response for large amplitude gusts

APPENDIX VIII

Viscous Aerodynamic Analysis of an Oscillating Flat Plate Airfoil with a Locally Analytical Solution

AIAA Journal

Viscous Aerodynamic Analysis of an Oscillating Flat-Plate Airfoil

Linda M. Schroeder* and Sanford Fleeter†
Purdue University, West Lafayette, Indiana

Abstract

CONSIDERABLE progress has been made in the prediction of the unsteady aerodynamics of oscillating airfoils. These analyses are typically limited to inviscid potential flows, with the unsteady flow assumed to be a small perturbation to the mean flow and the Kutta condition imposed. By considering the airfoils to be zero-thickness flat plates at zero mean incidence, the steady and unsteady flowfields are uncoupled, with the steady flow being uniform and parallel.

In this paper, an analysis is developed that models the unsteady aerodynamics of an harmonically oscillating flat-plate airfoil, including the effects of mean flow incidence angle, in an incompressible laminar flow at moderate values of the Reynolds number. The unsteady viscous flow is assumed to be a small perturbation to the steady viscous flowfield. The nonuniform and nonlinear steady flowfield is described by the Navier-Stokes equations and is independent of the unsteady flow. The small-perturbation unsteady viscous flow is described by a system of linear partial differential equations that are coupled to the steady flowfield, thereby modeling the strong dependence of the unsteady aerodynamics on the steady flow. Solutions for both the steady and unsteady viscous flowfields are obtained by a locally analytical method in which the discrete algebraic equations representing the flowfield equations are obtained from analytical solutions in individual local grid elements.

The locally analytical method for steady two-dimensional fluid flow and heat-transfer problems was initially developed by Chen et al.[1,2] They have shown that it has several advantages over finite-difference and finite-element methods, including being less dependent on grid size, with the system of algebraic equations relatively stable. Also, since the solution is analytical, it is differentiable and is a continuous function.

Contents

For harmonic time dependence at a frequency ω, the nondimensional continuity and Navier-Stokes equations in terms of the vorticity $\tilde{\zeta}$ and the stream function $\tilde{\psi}$ are

$$\nabla^2\tilde{\zeta} = \tilde{\zeta}_{xx} + \tilde{\zeta}_{yy} = Re(k\tilde{\zeta}_t + \tilde{u}\tilde{\zeta}_x + \tilde{v}\tilde{\zeta}_y) \tag{1a}$$

$$\nabla^2\tilde{\psi} = -\tilde{\zeta} \tag{1b}$$

where $\tilde{\zeta} = \tilde{v}_x - \tilde{u}_y$, $\tilde{u} = \tilde{\psi}_y$, $\tilde{v} = -\tilde{\psi}_x$, $Re = U_\infty C/\nu$ denotes the Reynolds number based on the airfoil chord, and $k = \omega C/U_\infty$ is the reduced frequency.

The equations describing the steady and unsteady viscous flows are determined by decomposing the flowfield into steady and small-perturbation harmonic unsteady components. For the unsteady flow, the second-order terms are neglected as small compared to the first-order terms.

The coupled nonlinear partial differential equations describing the steady flowfield are independent of the unsteady flow as shown in Eq. (2). The vorticity equation is nonlinear, with the stream function described by a linear Poisson equation that is coupled to the vorticity equation through the vorticity source term. The pressure also is described by a linear Poisson equation, with the source term dependent on the steady flowfield,

$$\nabla^2\zeta = Re(U\zeta_x + V\zeta_y) \tag{2a}$$

$$\nabla^2\psi = -\zeta \tag{2b}$$

$$\nabla^2 P = -2(U_x V_y - V_x U_y) \tag{2c}$$

where U and V are the steady chordwise and normal velocity components.

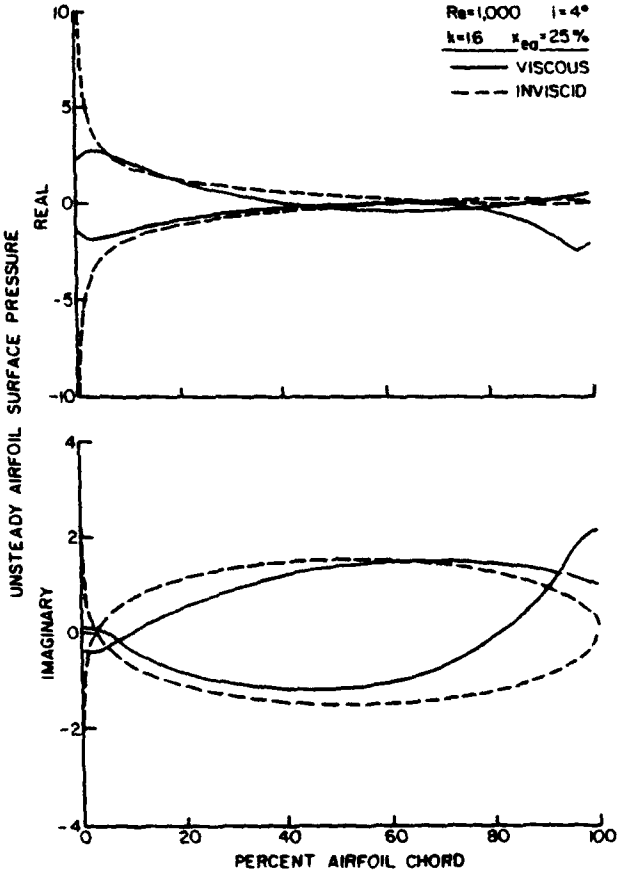

Fig. 1 Unsteady airfoil surface pressures for Re = 1000 and 4 deg incidence.

Presented as Paper 88-0130 at the AIAA 26th Aerospace Sciences Meeting, Reno, NV, Jan. 11-14, 1988; received Feb. 29, 1988; synoptic received Aug. 15, 1988. Full paper available at AIAA Library, 555 W. 57th St., New York, NY 10019. Price: microfiche, $4.00; hard copy, $9.00. **Remittance must accompany order.**

*AFRAPT Trainee, Thermal Sciences and Propulsion Center, School of Mechanical Engineering (currently Associated Aerodynamics Engineer, Sundstrand TurboMach). Member AIAA.

†Professor and Director, Thermal Sciences and Propulsion Center, School of Mechanical Engineering. Associate Fellow AIAA.

APPENDIX IX

Locally Analytical Prediction of the Viscous Aerodynamics of an Oscillating Flat Plate

International Journal of Mathematical and Computer Modeling

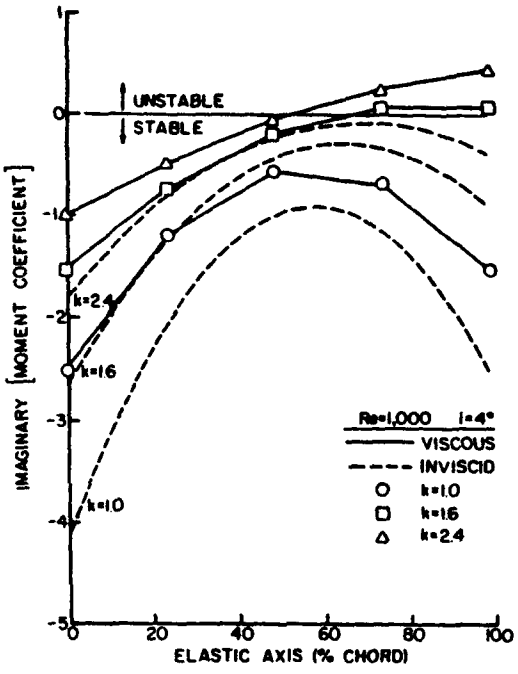

Fig. 2 Variation of the imaginary aerodynamic moment coefficient with elastic axis for $Re = 1000$ and 4 deg incidence.

The coupled linear partial differential equations describing the unsteady harmonic flowfield are given in Eq. (3). The unsteady flow is coupled to the steady flowfield. In particular, in both the unsteady vorticity transport and pressure equations, the coefficients are dependent on the steady flowfield with the unsteady stream function coupled to the solution for the unsteady vorticity.

$$\nabla^2\xi = Re(ki\xi + U\xi_x + V\xi_y + u\zeta_x + v\zeta_y) \tag{3a}$$

$$\nabla^2\psi = -\xi \tag{3b}$$

$$\nabla^2 p = -2[(u_x V_y + v_y U_x) - (v_x U_y + u_y V_x)] \tag{3c}$$

where $i = \sqrt{-1}$, and u and v denote the unsteady perturbation chordwise and normal velocity components.

The steady flow boundary conditions specify no slip between the fluid and the surface and that the velocity normal to the surface is zero. For the unsteady flow, the velocity of the fluid must be equal to that of the surfaces and the unsteady chordwise velocity component must satisfy a no-slip boundary condition. For a flat-plate airfoil, executing small-amplitude harmonic torsion mode oscillations about an elastic axis location at x_{ea} measured from the leading edge, the linearized normal velocity boundary condition in Eq. (4) is applied on the mean position of the oscillating airfoil,

$$v(x, 0) = \alpha[ik(x - x_{ea}) + U_o]e^{ikt} \tag{4}$$

where α is the amplitude of oscillation.

Locally analytical solutions for the unsteady and steady viscous flowfields then are developed. In this method, the discrete algebraic equations that represent the aerodynamic equations are obtained from analytical solutions in individual local grid elements. This is accomplished by dividing the flowfield into computational grid elements. In each element, the nonlinear convective terms of the steady Navier-Stokes equations are locally linearized. The nonlinear character of the steady flowfield is preserved as the flow is only locally linearized, that is, independently linearized in individual grid elements. Analytical solutions to the linear equations describing both the steady and unsteady flowfields in each element then are determined. The solution for the complete flowfield is obtained through the application of the global boundary conditions and the assembly of the locally analytic solutions.

This unsteady viscous flow model and locally analytical solution are used to investigate the effects of Reynolds number, mean flow incidence angle, and reduced frequency on the unsteady aerodynamics of an harmonically oscillating airfoil. Predictions are obtained on a 50×35 rectangular grid with $\Delta x = 0.025$ and $\Delta y = 0.025$ and 21 points located on the airfoil. The convergence criteria for the stream function iterations are both 10^{-4}, with the vorticity tolerance being 5×10^{-2}. The tolerances for the pressure iterations are 10^{-6} and 10^{-5} for the internal and external iterations, respectively. The computational time averaged 440 CPU on the Cyber 205, with an average of 160 iterations for the stream function and vorticity solutions and an additional 160 iterations for the pressure solution.

The chordwise distributions of the complex unsteady pressure on the individual surfaces of an oscillating airfoil at four degrees of incidence and a Reynolds number of 1000 is presented in Fig. 1. The corresponding classical inviscid Theodorsen prediction[3] is also shown. Viscosity has a large effect on the complex unsteady surface pressures, particularly the real part, over the front part of the airfoil. In particular, one difference between the two solutions is that the viscous solution is finite at the leading edge, whereas the inviscid solution is singular.

The torsion mode flutter stability of an airfoil is determined by the imaginary part of the unsteady aerodynamic moment in Eq. (5). Thus, Fig. 2 shows the airfoil stability as a function of the elastic axis location, with the reduced frequency as parameter at a Reynolds number of 1000 for an incidence angle of 4 deg, together with Theodorsen's inviscid zero incidence results. Viscous effects are seen to generally decrease the relative stability of the airfoil at all elastic axis locations, with the largest relative decrease in airfoil stability associated with the lower reduced frequency:

$$C_M = \frac{M}{\frac{1}{2}\rho C^2 U^2 k^2 \pi} = \frac{\int_0^1 (p_{\text{lower}} - p_{\text{upper}})(x - x_{ea})\, dx}{\frac{1}{4}\rho C^2 U^2 k^2 \pi} \tag{5}$$

Acknowledgment

This research was sponsored, in part, by the Air Force Office of Scientific Research.

References

[1]Chen, C. J., Naseri-Neshat, H., and Ho, K. S., "Finite Analytic Numerical Solution of Heat Transfer in Two-Dimensional Cavity Flow," *Journal of Numerical Heat Transfer*, Vol. 4, 1981, pp. 179–197.

[2]Chen, C. J. and Yoon, Y. H., "Finite Analytic Numerical Solution of Axisymmetric Navier-Stokes and Energy Equations," *Journal of Heat Transfer*, Vol. 5, Aug. 1983, pp. 639–645.

[3]Theodorsen, T., "General Theory of Aerodynamic Instability and the Mechanism of Flutter," NACA TR-496, 1935.

Mathl Comput. Modelling, Vol. 12, No. 6, pp. 707–719, 1989
Printed in Great Britain.

0895-7177/89 $3.00 + 0.00

LOCALLY ANALYTICAL PREDICTION OF THE VISCOUS AERODYNAMICS OF AN OSCILLATING FLAT PLATE AIRFOIL

L. M. SCHROEDER,† J. M. WOLFF‡ and S. FLEETER§
Thermal Sciences and Propulsion Center, School of Mechanical Engineering, Purdue University, West Lafayette, IN 47907, U.S.A.

(*Received August 1988; accepted for publication October 1988*)

Communicated by E. Y. Rodin

Abstract—A mathematical model is developed to predict the unsteady aerodynamics of a flat plate airfoil executing harmonic torsional motion in an incompressible laminar flow at moderate values of the Reynolds number. The unsteady viscous flow is assumed to be a small perturbation to the steady viscous flow described by the Navier–Stokes equations. Solutions for both the steady and the unsteady viscous flow fields are obtained by developing locally analytical solutions. This model is then utilized to demonstrate the effects of Reynolds number, mean flow incidence angle and reduced frequency on the complex unsteady airfoil surface pressure distributions as well as airfoil stability.

NOMENCLATURE

C_{Li} = Imaginary component of lift coefficient
C_{Lr} = Real component of lift coefficient
C_{Mi} = Imaginary component of moment coefficient
C_{Mr} = Real component of moment coefficient
k = Reduced frequency
p = Dimensionless unsteady pressure
P = Dimensionless steady pressure
Re = Reynolds number
u = Nondimensional unsteady velocity in the x direction
U = Nondimensional steady velocity in the x direction
U_∞ = Magnitude of free-stream velocity
v = Nondimensional unsteady velocity in the y direction
x_{ea} = Elastic axis location
x = Coordinate in the mean flow direction
y = Coordinate in the normal flow direction
Δx = Step size in the x direction
Δy = Step size in the y direction
α' = Amplitude of airfoil oscillation
ψ = Nondimensional unsteady stream function
Ψ = Nondimensional steady stream function
ξ = Nondimensional unsteady vorticity
ζ = Nondimensional steady vorticity
ω = Frequency of oscillation

INTRODUCTION

Considerable progress has been made in the prediction of the unsteady aerodynamics of oscillating airfoils. These analyses are typically limited to inviscid potential flows, with the unsteady flow assumed to be a small perturbation to a uniform mean flow and the Kutta condition imposed on the unsteady flow field. By considering the airfoils to be zero thickness flat plates at zero mean incidence, the steady and unsteady flow fields are uncoupled, with the steady flow being uniform and parallel.

Unsteady aerodynamic analyses have been developed which include the effects of viscosity, thereby removing the need for the Kutta conditions. Yates [1] formulated an incompressible viscous flat plate airfoil theory with a zero thickness boundary layer. Also, the low Reynolds number incompressible Oseen flow model has been used to calculate zero incidence oscillating flat plate aerodynamics [2, 4]. These analyses utilize classical aerodynamic solution techniques, resulting in integral equation solutions. Although such classical models and solution techniques are of value, advanced numerical techniques permit the flow physics modeling to be extended. In this regard,

†AFRAPT trainee, currently at Sundstrand Turbomach.
‡AFRAPT trainee.
§Professor and Director, Thermal Sciences and Propulsion Center.

unsteady viscous flow models are being developed which march in time, with one primary interest being the patterns of the unsteady flow [e.g. 4–6].

In this paper, an analysis is developed which models the unsteady aerodynamics of an harmonically oscillating flat plate airfoil, including the effects of mean flow incidence angle, in an incompressible laminar flow at moderate values of the Reynolds number. The unsteady viscous flow is assumed to be a small perturbation to the steady viscous flow field. Hence, the Kutta condition is not appropriate for either the steady or the unsteady flow fields. The steady flow field is described by the Navier–Stokes equations. It is thus nonuniform and nonlinear. Also, the steady flow field is independent of the unsteady flow field. The small perturbation unsteady viscous flow is described by a system of linear partial differential equations that are coupled to the steady flow field, thereby modeling the strong dependence of the unsteady aerodynamics on the steady flow. Solutions for both the steady and the unsteady viscous flow fields are obtained by developing a locally analytical method in which the discrete algebraic equations which represent the flow field equations are obtained from analytical solutions in individual local grid elements.

The concept of locally linearized solutions was applied to the problem of the steady inviscid transonic flow past thin airfoils by Spreiter and Alksne [7, 8] and subsequently extended to oscillating airfoils by Stahara and Spreiter [9]. The locally analytical method for steady two-dimensional fluid flow and heat transfer problems was initially developed by Chen *et al.* [10–12] and extended to unsteady inviscid airfoil and cascade flow fields by Chiang and Fleeter [13]. Chen has shown that this method has several advantages over the finite differences and finite element methods. For example, it is less dependent on grid size and the system of algebraic equations is relatively stable. Also, since the solution is analytical, it is differentiable and is a continuous function in the solution domain. The disadvantage is that a great deal of mathematical analysis is required before programming.

MATHEMATICAL MODEL

The two-dimensional flow past an isolated airfoil is schematically depicted in Fig. 1, which also defines the cartesian x–y coordinate system. For harmonic time dependence at a frequency ω, the nondimensional forms of the continuity and Navier–Stokes equations are given by

$$\bar{u}_x + \bar{v}_y = 0, \tag{1a}$$

$$k\bar{u}_t + \bar{u}\bar{u}_x + \bar{v}\bar{u}_y = -\bar{p}_x + (\bar{u}_{xx} + \bar{u}_{yy})/\mathrm{Re} \tag{1b}$$

and

$$k\bar{v}_t + \bar{u}\bar{v}_x + \bar{v}\bar{v}_y = -\bar{p}_y + (\bar{v}_{xx} + \bar{v}_{yy})/\mathrm{Re}, \tag{1c}$$

where $\mathrm{Re} = U_\infty C/\nu$ denotes the Reynolds number, and $k = \omega C/U_\infty$ is the reduced frequency.

There are three dependent variables, the two velocity components and the pressure. To reduce the number of dependent variables, a vorticity, $\bar{\zeta}$, stream function, $\bar{\psi}$, formulation is utilized:

$$\nabla^2\bar{\zeta} = \bar{\zeta}_{xx} + \bar{\zeta}_{yy} = \mathrm{Re}(k\bar{\zeta}_t + \bar{u}\bar{\zeta}_x + \bar{v}\bar{\zeta}_y) \tag{2a}$$

and

$$\nabla^2\bar{\psi} = -\bar{\zeta}, \tag{2b}$$

where

$$\bar{\zeta} = \bar{v}_x - \bar{u}_y \quad \text{and} \quad u = \bar{\psi}_y; \quad \bar{v} = -\bar{\psi}_x.$$

Unsteady small perturbation model

For a flat plate airfoil executing small-amplitude harmonic oscillations, the flow field is decomposed into steady and harmonic unsteady components, with the unsteady component assumed to be a small perturbation to the steady component:

$$\bar{\zeta}(x, y, t) = \zeta(x, y) + \mathrm{e}^{it}\xi(x, y), \tag{3a}$$

$$\bar{\psi}(x, y, t) = \Psi(x, y) + \epsilon'' \psi(x, y), \tag{3b}$$

$$\bar{u}(x, y, t) = U(x, y) + \epsilon'' u(x, y), \tag{3c}$$

$$\bar{v}(x, y, t) = V(x, y) + \epsilon'' v(x, y) \tag{3d}$$

and

$$\bar{p}(x, y, t) = P(x, y) + \epsilon'' p(x, y), \tag{3e}$$

where

$$\xi \ll \zeta, \quad \psi \ll \Psi, \quad u \ll U, \quad v \ll V, \quad p \ll P.$$

The equations describing the steady and unsteady viscous flow fields are determined by substituting equations 3(a–e) into equations 2(a, b), and grouping together the time-independent and the time-dependent terms. For the unsteady flow, the second-order terms are neglected as small compared to the first-order terms. Also, as the linearized unsteady flow is assumed to be harmonic, the $\exp(it)$ is dropped, for convenience.

The resulting coupled nonlinear partial differential equations describing the steady flow field, equations 4(a–c), are independent of the unsteady flow. The vorticity equation is nonlinear, with the stream function described by a linear Poisson equation which is coupled to the vorticity equation through the vorticity source term. The pressure is also described by a linear Poisson equation, with the source terms dependent on the steady flow field:

$$\nabla^2 \zeta = \mathrm{Re}(U\zeta_x + V\zeta_y), \tag{4a}$$

$$\nabla^2 \Psi = -\zeta \tag{4b}$$

$$\nabla^2 P = -2(U_x V_y - V_x U_y). \tag{4c}$$

The resulting coupled linear partial differential equations describing the unsteady harmonic flow field are given in equations 5(a–c). The unsteady flow is coupled to the steady flow field. In particular, in both the unsteady vorticity transport and pressure equations, the variable coefficients are dependent on the steady flow field with the unsteady stream function coupled to the solution for the unsteady vorticity:

$$\nabla^2 \xi = \mathrm{Re}(ki\xi + U\xi_x + V\xi_y + u\zeta_x + v\zeta_y), \tag{5a}$$

$$\nabla^2 \psi = -\xi \tag{5b}$$

and

$$\nabla^2 p = -2[(u_x V_y + v_y U_x) - (v_x U_y + u_y V_x)]. \tag{5c}$$

Steady flow boundary conditions

The steady flow boundary conditions specify no slip between the fluid and the surface and that the velocity normal to the surface is zero. In terms of the stream function and vorticity, these boundary conditions are specified by

$$\Psi = \text{const} \qquad \text{on solid surfaces} \tag{6a}$$

and

$$\zeta = -U_y = -\Psi_{yy} \qquad \text{on solid surfaces.} \tag{6b}$$

Unsteady flow boundary conditions

The unsteady boundary conditions require that the velocity of the fluid is equal to that of the surfaces. For a flat plate airfoil executing small-amplitude harmonic torsion mode oscillations about an elastic axis located at x_{ea} measured from the leading edge, the linearized normal velocity boundary condition is applied on the mean position of the oscillating airfoil, and is given by

$$v(x, 0) = \alpha'[ik(x - x_{ea}) + U_0]e^{it}, \tag{7}$$

where α' is the amplitude of oscillation.

The fluid is viscous. Thus the unsteady chordwise velocity component must satisfy the nonslip boundary condition,

$$u(x, 0) = 0. \tag{8}$$

LOCALLY ANALYTICAL SOLUTIONS

The locally analytical solutions for the unsteady and steady viscous flow fields are now developed. In this method, the discrete algebraic equations which represent the aerodynamic equations are obtained from analytical solutions in individual local grid elements. This is accomplished by dividing the flow field into computational grid elements. In each individual element the nonlinear convective terms of the Navier–Stokes equations which describe the steady flow are locally linearized. The nonlinear character of the steady flow field is preserved as the flow is only locally linearized, that is, independently linearized in individual grid elements. Analytical solutions to the linear equations describing both the steady and the unsteady flow fields in each element are then determined. The solution for the complete flow field is obtained through the application of the global boundary conditions and the assembly of the locally analytic solutions in the individual grid elements.

Steady Flow Field

Steady vorticity

The steady vorticity transport is described by equation (4a) which is nonlinear because of the convective terms $U\zeta_x + V\zeta_y$. These terms are locally linearized by assuming that the velocity components U and V, which are the coefficients of the vorticity, are constant in each individual grid element, i.e. locally linearized:

$$U = \frac{2A}{Re}, \qquad V = \frac{2B}{Re}, \tag{9}$$

where A and B are constants in an individual grid element, taking on different values *in* each grid element. The resulting locally linearized vorticity equation is

$$2A\zeta_x + 2B\zeta_y = \zeta_{xx} + \zeta_{yy}. \tag{10}$$

This locally linearized equation can be solved analytically to determine the vorticity, ζ, in a grid element, thereby providing the functional relationships between the vorticity, ζ, in an individual grid element and the boundary values specified on that grid element. This vorticity transport equation is elliptic. Therefore, to obtain a unique solution for the typical uniform grid element with center (x_0, y_0), Fig. 2, boundary conditions must be specified on all four boundaries. These boundary conditions are expressed in an implicit formulation in terms of the nodal values of the

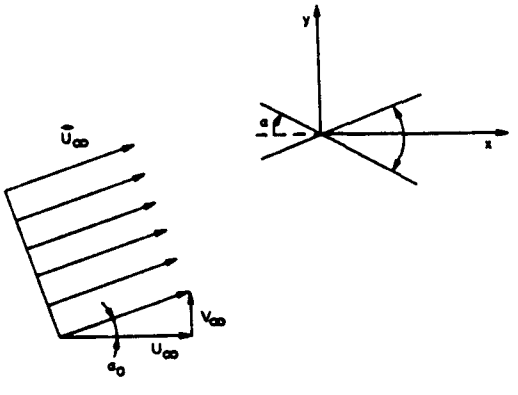

Fig. 1. Flow field schematic.

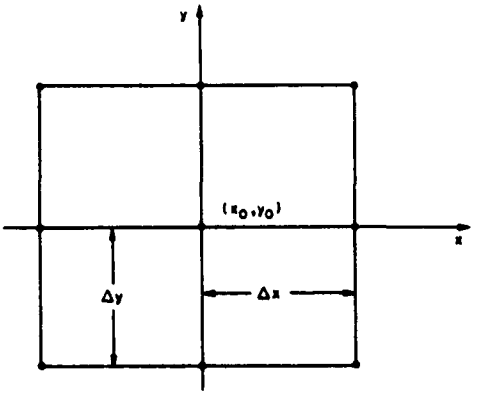

Fig. 2. Typical computational grid element.

vorticity along the boundaries of the element. A second-order polynomial is used to approximate the vorticity on each of the boundaries:

$$\zeta(x, y_0 + \Delta y) = a_1^i + a_2^i x + a_3^i x^2, \tag{11a}$$

$$\zeta(x_0 + \Delta x, y) = b_1^i + b_2^i y + b_3^i y^2, \tag{11b}$$

$$\zeta(x, y_0 - \Delta y) = c_1^i + c_2^i x + c_3^i x^2, \tag{11c}$$

and

$$\zeta(x_0 - \Delta x, y) = d_1^i + d_2^i y + d_3^i y^2, \tag{11d}$$

where a_1^i, b_1^i, c_1^i and d_1^i are constants determined from the three nodal points on each boundary side and the x and y distances are all measured from the center of the element (x_0, y_0).

The analytical solution to equation (10) subject to the boundary conditions (11a–d) is determined by separation of variables:

$$\zeta(x, y) = e^{(Ax + By)} \sum_{n=1}^{n=\infty} \{[B_{1_n}^i \sinh(E_{1_n} x) + B_{2_n}^i \cosh(E_{1_n} x)]\sin(\lambda_{1_n}^i (y + \Delta y)) + [B_{1_n}^i \sinh(E_{2_n} y) + B_{2_n}^i \cosh(E_{2_n} y)]\sin(\lambda_{2_n}^i (x + \Delta x))\}. \tag{12}$$

Steady stream function

The locally analytical solution for the stream function is obtained by a procedure analogous to that used for the vorticity. First, the flow region is subdivided into computational grid elements.

The stream function is described by a linear Poisson equation which is coupled to the vorticity, equation (4b). This stream function Poisson equation is also elliptic. Therefore, to obtain a unique analytical solution for the typical grid element, continuous conditions must be specified on all four boundaries. As for the vorticity transport equation, continuous boundary conditions are represented in an implicit formulation in terms of the nodal values of the stream function by second-order polynomials in x or y as measured from the element center (x_0, y_0):

$$\Psi(x, y_0 + \Delta y) = a_1^\psi + a_2^\psi x + a_3^\psi x^2, \tag{13a}$$

$$\Psi(x_0 + \Delta x, y) = b_1^\psi + b_2^\psi y + b_3^\psi y^2, \tag{13b}$$

$$\Psi(x, y_0 - \Delta y) = c_1^\psi + c_2^\psi x + c_3^\psi x^2 \tag{13c}$$

and

$$\Psi(x_0 - \Delta x, y) = d_1^\psi + d_2^\psi y + d_3^\psi y^2, \tag{13d}$$

where a_1^ψ, b_1^ψ, c_1^ψ and d_1^ψ are constants determined from the three nodal points on each boundary side.

The stream function equation is linear and possesses a nonhomogeneous term, $-\zeta(x, y)$, which couples the stream function to the vorticity. To solve equation (4b) subject to the boundary conditions (13a–d), it is divided into two component problems. One problem has a homogeneous equation with nonhomogeneous boundary conditions, whereas the second problem has a nonhomogeneous equation with homogeneous boundary conditions:

$$\Psi = \Psi^a + \Psi^b. \tag{14}$$

Problem 1:

$$\nabla^2 \Psi^a = 0$$

$$\Psi^a(x, y_0 + \Delta y) = a_1^\psi + a_2^\psi x + a_3^\psi x^2$$

$$\Psi^a(x_0 + \Delta x, y) = b_1^\psi + b_2^\psi y + b_3^\psi x^2$$

$$\Psi^a(x, y_0 - \Delta y) = c_1^\psi + c_2^\psi x + c_3^\psi x^2$$

$$\Psi^a(x - \Delta x, y_0) = d_1^\psi + d_2^\psi y + d_3^\psi y^2. \tag{15}$$

Problem 2:

$$\nabla^2 \Psi^b = -\zeta(x, y)$$
$$\Psi^b(x_0 + \Delta x, y) = 0$$
$$\Psi^b(x_0 - \Delta x, y) = 0$$
$$\Psi^b(x, y_0 + \Delta y) = 0$$
$$\Psi^b(x, y_0 - \Delta y) = 0. \tag{16}$$

The solutions for Ψ^a and Ψ^b are then determined by separation of variables:

$$\begin{aligned}\Psi(x, y) = \sum_{n=1}^{n=\infty} \{&[B^{\dagger}_{\dagger n} \sinh(\lambda^{\dagger}_{\dagger n} x) + B^{\dagger}_{\ddagger n} \cosh(\lambda^{\dagger}_{\dagger n} x)]\sin(\lambda^{\dagger}_{\dagger n}(y + \Delta y)) \\ &+ [B^{\dagger}_{\ddagger n} \sinh(\lambda^{\dagger}_{\ddagger n} y) + B^{\dagger}_{\ddagger n} \cosh(\lambda^{\dagger}_{\ddagger n} y)]\sin(\lambda^{\dagger}_{\ddagger n}(x + \Delta x)) \\ &+ [G^{\dagger}_{\ddagger n} \sinh(\lambda^{\dagger}_{\ddagger n} y) + G^{\dagger}_{\ddagger n} \cosh(\lambda^{\dagger}_{\ddagger n} y) + G^{\dagger}_{\dagger n} + G^{\dagger}_{\ddagger n} y + G^{\dagger}_{\ddagger n} y^2] \\ &\times \sin(\lambda^{\dagger}_{\ddagger n}(x + \Delta x))\}. \end{aligned} \tag{17}$$

Steady velocity and pressure

The stream function is continuously differentiable across the grid element. Hence the U and V velocity components can be obtained analytically by differentiating the stream function solution. The solutions for Ψ, ζ, U and V are then used to determine the pressure in the flow field and on the boundaries. Thus, the locally analytical solutions for the velocity components and the pressure are performed as post processes.

Unsteady Flow Field

Unsteady vorticity

The unsteady vorticity is described by a linear partial differential equation with nonconstant coefficients, equation (5a). In particular, the unsteady perturbation velocity coefficients u and v vary across the typical computational grid element. However, the steady velocity coefficients U and V are known from the previously determined steady-state solution and are constant in the typical grid element, as specified in equations 4(a–c).

To determine the locally analytical solution to the unsteady perturbation vorticity equation, it is approximated as a constant coefficient partial differential equation in individual grid elements. This is accomplished by assuming that the perturbation velocities u and v are constant in each element:

$$u = \frac{2A'}{\mathrm{Re}}, \qquad v = \frac{2B'}{\mathrm{Re}}, \tag{18}$$

where A′ and B′ are constant in each individual grid element, taking on different values in different grid elements.

Thus, the following linear constant coefficient partial differential equation defines the unsteady perturbation vorticity in an individual computational grid element:

$$k \cdot i \cdot \mathrm{Re}\xi + 2A\xi_x + 2B\xi_y + (2A'\zeta_x + 2B'\zeta_y) = \xi_{xx} + \xi_{yy}. \tag{19}$$

To determine the analytical solution in the typical grid element, equation (19) is rewritten as follows:

$$-(2A\xi_x + 2B\xi_y) + \xi_{xx} + \xi_{yy} = S(x, y), \tag{20}$$

where

$$S(x, y) = (2A'\zeta_x + 2B'\zeta_y + k \cdot \mathrm{Re} \cdot i\xi).$$

It is then transformed to an homogeneous equation by the following change in the dependent variable:

$$\zeta(x, y) = \xi(x, y) + \frac{S\left(Ax + \frac{B}{A}y\right)}{2\left(A^2 + \frac{B^2}{A}\right)}.$$

The resulting homogeneous equation is

$$\nabla^2\zeta = 2A\zeta_x + 2B\zeta_y. \tag{21}$$

This equation is of the same form as that for the steady linearized vorticity, equation (10). Thus, the solution for ζ is obtained in a manner exactly analogous to that for the steady vorticity, ζ, and is given by

$$\begin{aligned}\zeta(x_0, y_0) = {} & z_1(x_0 + \Delta x, y_0 + \Delta y)\zeta(x_0 + \Delta x, y_0 + \Delta y) \\ & + z_2(x_0 + \Delta x, y_0)\zeta(x_0 + \Delta x, y_0) \\ & + z_3(x_0 + \Delta x, y_0 - \Delta y)\zeta(x_0 + \Delta x, y_0 - \Delta y) \\ & + z_4(x_0, y_0 - \Delta y)\zeta(x_0, y_0 - \Delta y) \\ & + z_5(x_0 - \Delta x, y_0 - \Delta y)\zeta(x_0 - \Delta x, y_0 - \Delta y) \\ & + z_6(x_0 - \Delta x, y_0)\zeta(x_0 - \Delta x, y_0) \\ & + z_7(x_0 - \Delta x, y_0 + \Delta y)\zeta(x_0 - \Delta x, y_0 + \Delta y) \\ & + z_8(x_0, y_0 + \Delta y)\zeta(0, \Delta y),\end{aligned} \tag{22}$$

where the coefficients z_i are dependent on the steady-state velocity components, U and V.

Unsteady stream function

The unsteady stream function is described by equation (5b). This equation is identical to that for the steady stream function, equation (4b). Hence, the solution procedure is identical to that for the steady stream function. As the coefficients for the stream function are only a function of their position in the grid element, i.e. Δx and Δy, the unsteady coefficients remain the same as those found previously for the steady stream function $\Psi(x_0, y_0)$. Thus, the solution for the unsteady stream function is determined from the steady stream function solution, equation (17), by replacing Ψ by ψ and the steady vorticity ζ by the unsteady vorticity ξ. The algebraic equation for the value of the unsteady stream function at the center of the typical element in terms of the values of the unsteady stream function and vorticity at its eight neighboring values is given by

$$\begin{aligned}\psi(x_0, y_0) = {} & p_1^1\psi(x_0 + \Delta x, y_0 + \Delta y) + p_2^1\psi(x_0 + \Delta x, y_0) \\ & + p_3^1\psi(x_0 + \Delta x, y_0 - \Delta y) + p_4^1\psi(x_0, y_0 - \Delta y) \\ & + p_5^1\psi(x_0 - \Delta x, y_0 - \Delta y) + p_6^1\psi(x_0 - \Delta x, y_0) \\ & + p_7^1\psi(x_0 - \Delta x, y_0 + \Delta y) + p_8^1\psi(x_0, y_0 + \Delta y) \\ & + q_1^1\xi(x_0 + \Delta x, y_0 + \Delta y) + q_2^1\xi(x_0 + \Delta x, y_0) \\ & + q_3^1\xi(x_0 + \Delta x, y_0 - \Delta y) + q_4^1\xi(x_0, y_0 - \Delta y) \\ & + q_5^1\xi(x_0 - \Delta x, y_0 - \Delta y) + q_6^1\xi(x_0 - \Delta x, y_0) \\ & + q_7^1\xi(x_0 - \Delta x, y_0 + \Delta y) + q_8^1\xi(x_0, y_0 + \Delta y) \\ & + q_9^1\xi(x_0, y_0).\end{aligned} \tag{23}$$

Unsteady velocity and pressure

The unsteady velocity components u and v are determined by differentiating the unsteady stream function, with the locally analytical solution for the unsteady pressure determined by a post process.

RESULTS

The small perturbation unsteady viscous flow model and locally analytical solution are utilized to investigate the effects of Reynolds number, mean flow incidence angle and reduced frequency on the unsteady aerodynamics of a harmonically oscillating airfoil. These results are presented in the form of the unsteady pressure distributions on the surfaces of the oscillating airfoil and the complex unsteady aerodynamic lift and moment coefficients, defined below:

$$C_L = \frac{L}{\frac{1}{2}\rho c U^2 k^2 \pi} = \frac{\int_{c=0}^{c=1} (p_{\text{lower}} - p_{\text{upper}})\,dx}{\frac{1}{2}\rho c U^2 K^2 \pi} \tag{24a}$$

and

$$C_M = \frac{M}{\frac{1}{2}\rho c^2 U^2 k^2 \pi} = \frac{\int_{c=0}^{c=1} (p_{\text{lower}} - p_{\text{upper}})(x - x_{ea})\,dx}{\frac{1}{4}\rho c^2 U^2 k^2 \pi}. \tag{24b}$$

Predictions are obtained on a 50×35 rectangular grid with $\Delta x = 0.025$ and $\Delta y = 0.025$. Twenty-one points are located on the flat plate airfoil. The convergence criteria for the internal and external iterations for the stream function are both 10^{-4}, with the vorticity tolerance being $5 \cdot 10^{-2}$. The tolerances for the pressure iterations are 10^{-6} and 10^{-5} for the internal and external iterations, respectively. The computational time averaged 440 CPU on a Cyber 205, with an average of 160 iterations for the solutions of the stream function and vorticity and an additional 160 iterations for the pressure solution.

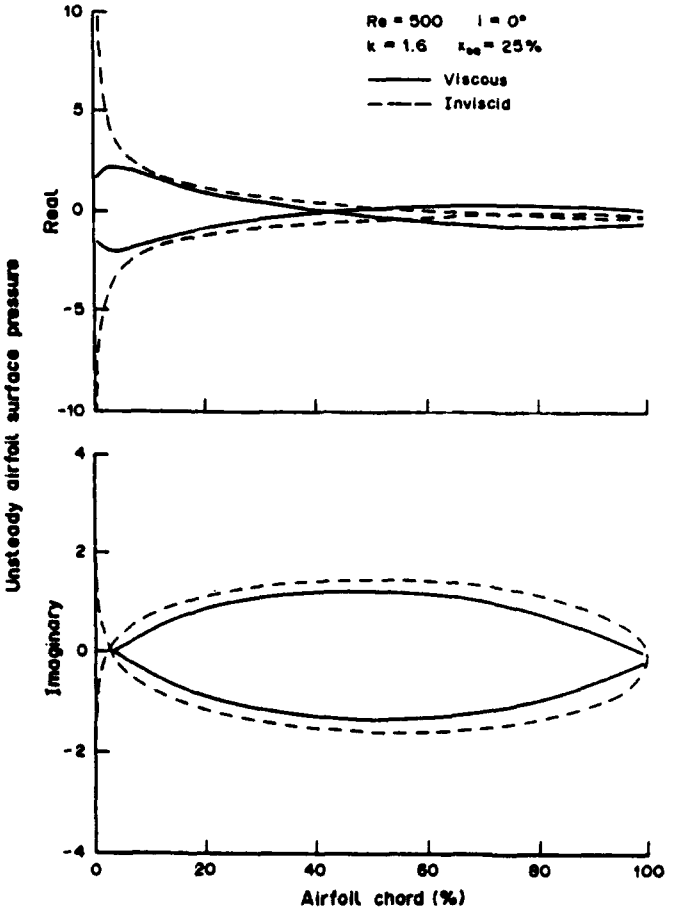

Fig. 3. Unsteady airfoil surface pressure for Re = 500 and 0° incidence.

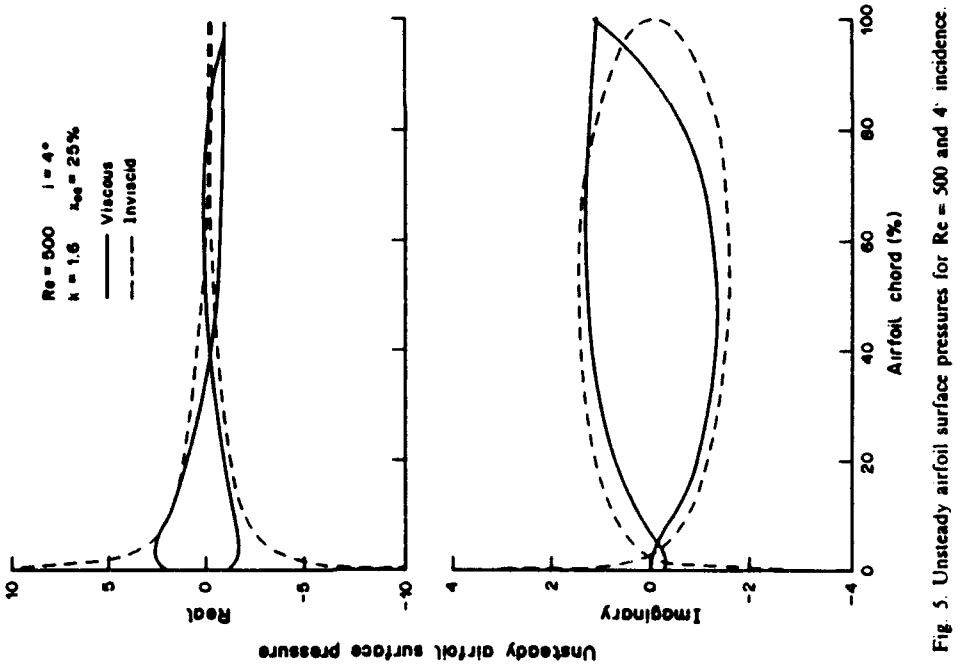

Fig. 5. Unsteady airfoil surface pressures for Re = 500 and 4° incidence.

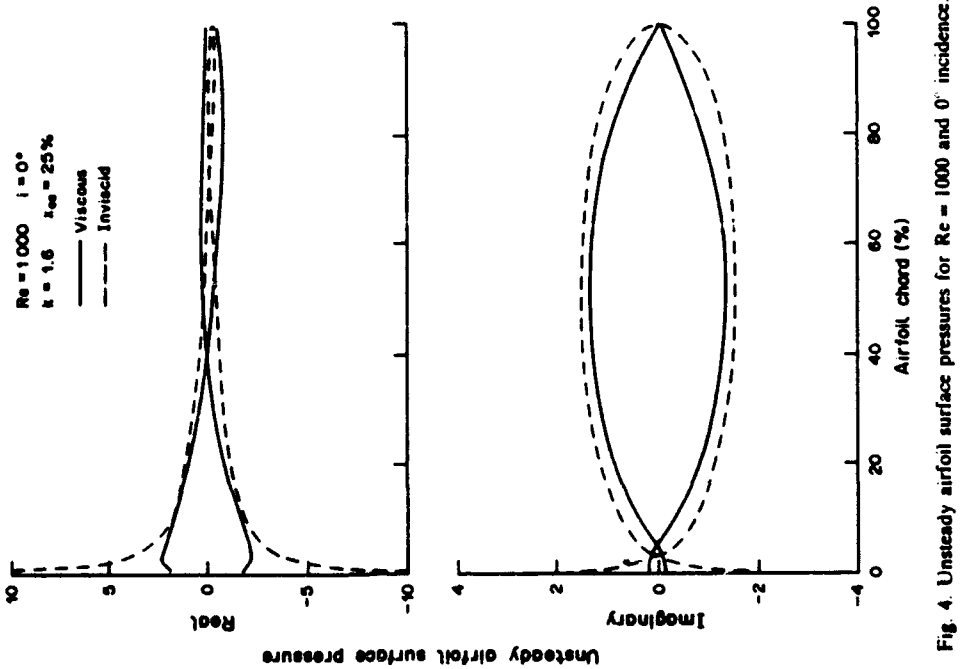

Fig. 4. Unsteady airfoil surface pressures for Re = 1000 and 0° incidence.

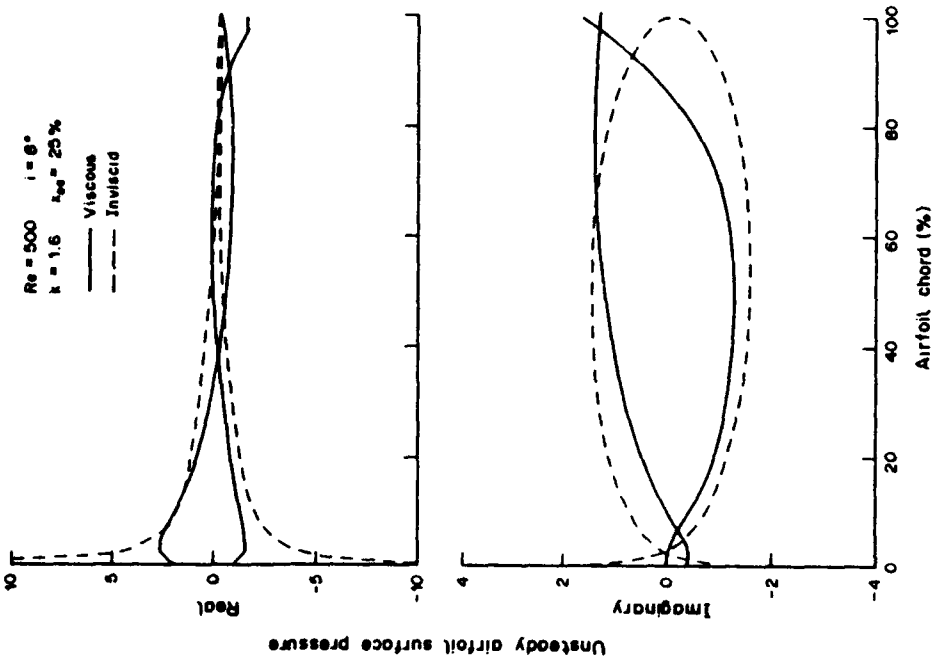

Fig. 7. Unsteady airfoil surface pressures for Re = 500 and 8 incidence.

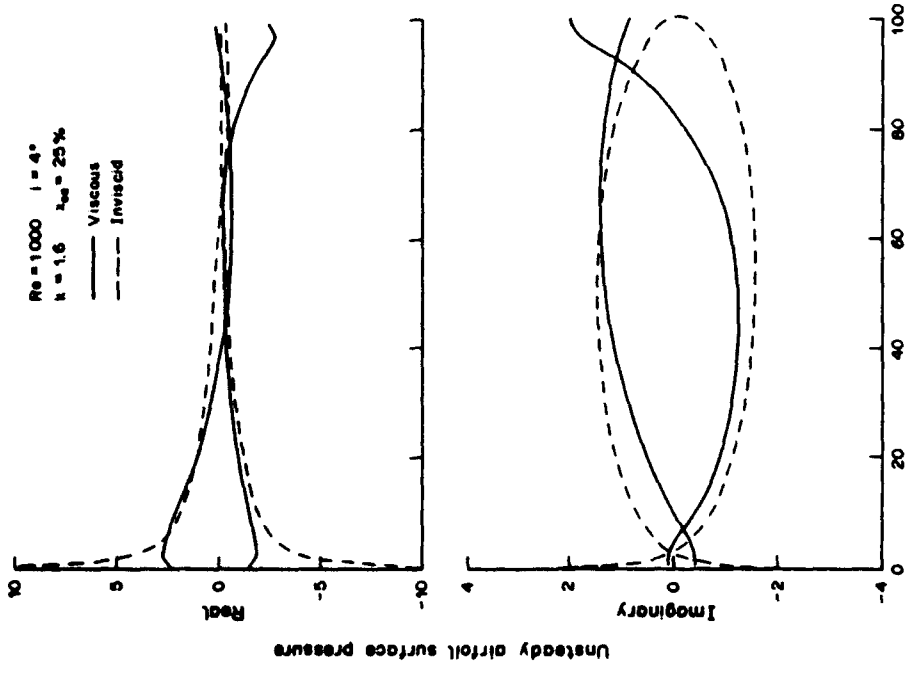

Fig. 6. Unsteady airfoil surface pressures for Re = 1000 and 4 incidence.

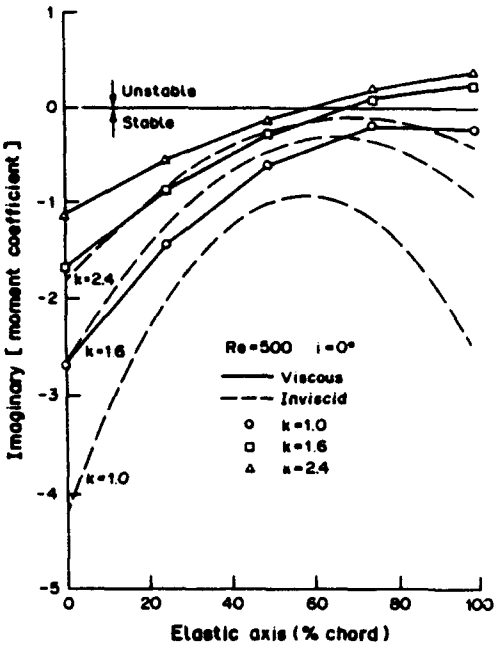

Fig. 8. Variation of the imaginary aerodynamic moment coefficient with the elastic axis for Re = 500 and 0° incidence.

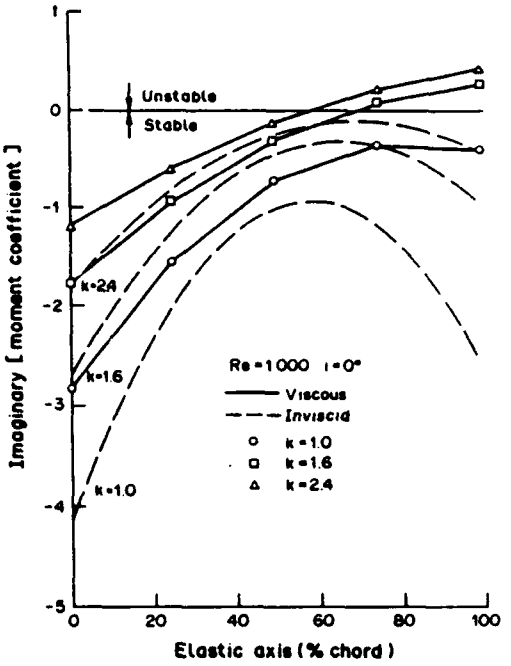

Fig. 9. Variation of the imaginary aerodynamic moment coefficient with the elastic axis for Re = 1000 and 0 incidence.

The chordwise distributions of the complex unsteady pressure on the individual surfaces of an oscillating airfoil at 0°, 4° and 8° of incidence and Reynolds numbers of 500 and 1000 are presented in Fig. 3–7. The corresponding classical inviscid Theodorsen predictions [14] are also shown.

Viscosity is seen to primarily affect the complex unsteady surface pressures over the front and rear portions of the airfoil. It should be noted that one essential difference between the two solutions is that the viscous one is finite at the leading edge, whereas the inviscid solution is singular.

Increasing the Reynolds number from 500 to 1000 results in a small increase in the absolute magnitude of the complex unsteady pressures on the front part of the airfoil surface. For nonzero incidence angle values, neither the real nor the imaginary components of the chordwise unsteady pressure distributions are symmetric, with this nonsymmetry increasing with increasing incidence angle. Also, as the incidence angle is increased, the pressure difference between the two airfoil surfaces at the trailing edge is increased.

The torsion mode flutter stability of an airfoil is determined by the imaginary part of the unsteady aerodynamic moment if there is no mechanical damping. Thus, the effects of incidence angle, Reynolds number and reduced frequency on the imaginary part of the moment coefficients are considered in Figs 8–11 together with Theodorsen's inviscid zero incidence results. In particular, these figures present the imaginary part of the unsteady aerodynamic moment coefficient as a function of the elastic axis location, with the reduced frequency as parameter at Reynolds numbers of 500 and 1000 for incidence angles of 0° and 4°. Also, the effects of Reynolds number and incidence angle on the complex unsteady aerodynamic lift and moment on an airfoil with a quarter-chord elastic axis location are presented in Table 1.

In this inviscid, incompressible flow field, the minimum relative stability is found when the elastic axis is located in the mid to aft chord region of the airfoil. As the reduced frequency is increased from 1.0 to 2.4, the relative stability of the airfoil is decreased, with the location of the elastic axis for minimum relative stability moving aft with increasing values of the reduced frequency.

Viscous effects are seen to generally decrease the relative stability of the airfoil at all elastic axis locations at both 0° and 4° of incidence. The largest relative decrease in airfoil stability is associated with the lower reduced frequency value. Also, increasing the Reynolds number from 500 to 1000 results in a decrease in the relative airfoil stability. In fact, at zero incidence, the airfoil becomes

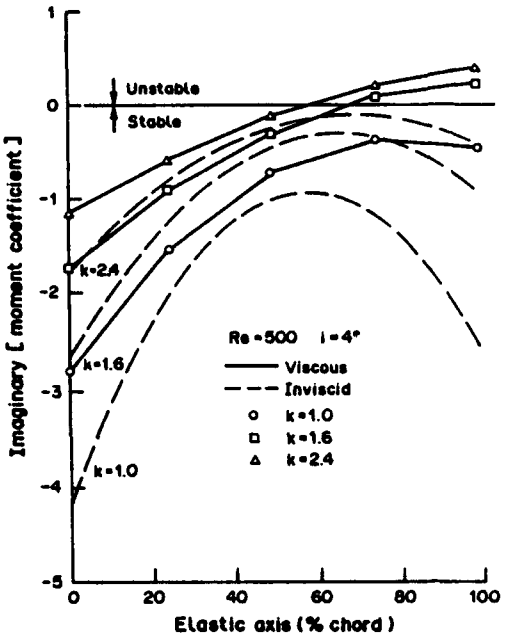

Fig. 10. Variation of the imaginary aerodynamic moment coefficient with the elastic axis for Re = 500 and 4° incidence.

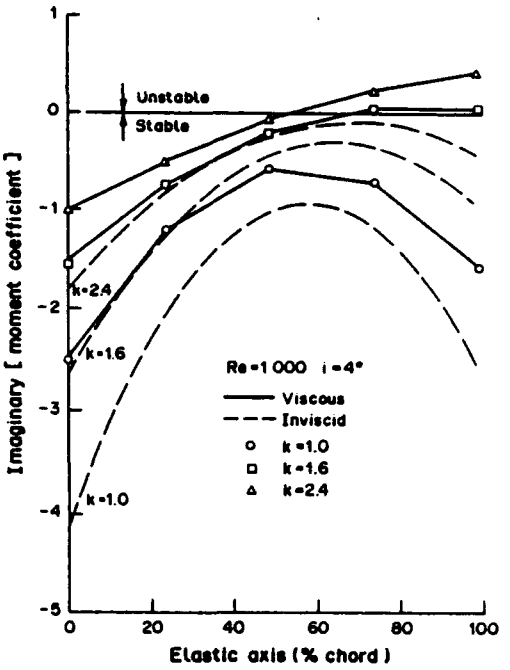

Fig. 11. Variation of the imaginary aerodynamic moment coefficient with the elastic axis for Re = 1000 and 4° incidence.

Table 1. Unsteady aerodynamic lift and moment coefficients for $x_{ea} = 25\%$ and $k = 1.6$

	Lift		Moment	
	C_{L_r}	C_{L_i}	C_{M_r}	C_{M_i}
Theodorsen	−1.523	−2.271	+0.375	−1.25
Viscous solver, $\alpha = 0°$				
Re = 500	−0.375	−1.680	0.602	−0.868
Re = 1000	−0.433	−1.735	0.593	−0.929
Viscous solver, $\alpha = 4°$				
Re = 500	−0.419	−1.687	0.517	−0.913
Re = 1000	−1.002	−1.462	−0.024	−0.741
Viscous solver, $\alpha = 8°$				
Re = 500	−0.438	−1.568	0.400	−0.908

unstable for all reduced frequency values with an elastic axis located at 75% chord at a Reynolds number of 1000. Increasing the value of the incidence angle results in an increase in the relative stability of the airfoil. However, at a Reynolds number of 1000 with an elastic axis at 75% chord, the airfoil is still unstable at a reduced frequency value of 1.0, the lowest value considered.

SUMMARY AND CONCLUSIONS

A mathematical model has been developed to predict the unsteady aerodynamics of a flat plate airfoil executing harmonic torsional motions in an incompressible laminar flow at moderate values of the Reynolds number. The unsteady viscous flow is assumed to be a small perturbation to the steady viscous flow which is described by the Navier–Stokes equations. Thus, the steady flow is nonuniform and nonlinear and is also independent of the unsteady flow field. The small perturbation unsteady viscous flow field is described by a system of linear partial differential equations that are coupled to the steady flow field, thereby modeling the strong dependence of the unsteady aerodynamics on the steady flow.

Solutions for both the steady and the unsteady viscous flow fields are obtained by developing a locally analytical solution. In this approach, the discrete algebraic equations which represent the

flow field equations are obtained from analytical solutions in individual local grid elements. The complete flow field solutions are then obtained through the application of the global boundary conditions and the assembly of the local grid element solutions. This model and locally analytical solution were then utilized to demonstrate the effects of Reynolds number, mean flow incidence angle, reduced frequency value and elastic axis location on the complex unsteady airfoil surface pressure distributions and also on the torsional stability of the airfoil.

Viscosity was shown to have a large effect on the complex unsteady surface pressures, particularly the real part, over the front part of the airfoil. Also, the real part of the inviscid unsteady pressure is greatly increased in magnitude as compared to the viscous predictions over the front half of the airfoil, with the imaginary part of the viscous and inviscid solutions of approximately the same magnitude aft of the airfoil leading edge inviscid singularity. In terms of airfoil stability, viscous effects were shown to generally decrease the relative stability of the airfoil, with the largest decrease associated with the low reduced frequency value. Increasing the Reynolds number caused a decrease in the relative stability of the airfoil stability, whereas increasing the incidence angle results in increased airfoil stability.

Acknowledgement—This research was sponsored, in part, by the Air Force Office of Scientific Research.

REFERENCES

1. J. E. Yates, Unsteady viscous thin airfoil theory. AGARD Report No. 671 (1978).
2. W. H. Chu, An aerodynamic analysis for flutter in Oseen type viscous flow. *J. Aerospace Sci.* **29**, 781–789 (1962).
3. S. F. Shen and P. Crimi, The theory for an oscillating thin airfoil as derived from the Oseen equation. *J. Fluid Mech.* **23**, 585–609 (1985).
4. U. B. Mehta and Z. Lavan, Starting vortex separation bubbles and stall: A numerical study of laminar unsteady flow around an airfoil. *J. Fluid Mech.* **67**, 227–256 (1975).
5. J. F. Thompson, F. C. Thames, R. L. Walker and S. P. Shanka, Numerical solution of the unsteady Navier-Stokes equations for arbitrary bodies using boundary fitted curvilinear coordinates. In *Proc. Symp. on Unsteady Aerodynamics*, Univ. of Arizona, Tucson (Edited by R. B. Kinney), pp. 453–465 (1975).
6. J. C. Wu and S. Sampath, A numerical study of viscous flow around an airfoil. AIAA Paper 76–337 (1976).
7. J. R. Spreiter and A. Y. Alksne, Thin airfoil theory based an approximate solution of the transonic flow equation Report NACA-TR-1359 (1958).
8. J. R. Spreiter, Aerodynamics of wings and bodies at transonic speeds. *J. Aerospace Sci.* **26**, 465–487 (1959).
9. S. S. Stahara and J. R. Spreiter, Development of a nonlinear unsteady transonic flow theory. Report NASA TR-2285 (1973).
10. C. J. Chen, H. Naseri-Neshat and K. S. Ho, Finite analytic numerical solution of heat transfer in two-dimensional cavity flow. *J. numer. Heat Transfer* **4**, 179–197 (1981).
11. C. J. Chen and Y. H. Yoon, Finite analytic numerical solution of axisymmetric Navier–Stokes and energy equations. *J. Heat Transfer* **5**, 639–645 (1983).
12. C. J. Chen and P. Li, The finite analytic method for steady and unsteady heat transfer problems. ASME Paper 80-HT-86 (1980).
13. H. D. Chiang and S. Fleeter, Prediction of the oscillating aerodynamics of a loaded airfoil cascade by a locally analytical method. AIAA Paper 88-0331 (1988).
14. T. Theodorsen, General theory of aerodynamic instability and the mechanism of flutter. Report NACA TR-496 (1935).

APPENDIX X

Prediction of Turbulence Generated Random Vibrational Response of Turbomachinery Blading

International Journal of Turbo and Jet Engines

International Journal of Turbo and Jet Engines. 6. 247-255 (1989)

Prediction of Turbulence Generated Random Vibrational Response of Turbomachinery Blading

Thomas E. Booth and Sanford Fleeter
Thermal Sciences and Propulsion Center, School of Mechanical Engineering, Purdue University, West Lafayette, Indiana 47907, U.S.A.

Abstract

An analysis is developed to predict the turbulence generated single-degree-of-freedom bending and torsion mode vibrational response of a turbomachine blade row operating in a subsonic compressible flow field. The turbulence is assumed to be random in the neighborhood of the blade natural frequency of interest and to generate a large number of constant amplitude, harmonic, unsteady aerodynamic lift forces and moments on the blading with equally distributed frequencies. The resulting random airfoil vibrations thus occur at the blade natural frequency. The unsteady aerodynamics generated by the blade response, i.e., the aerodynamic damping, as well as the effect of blade aerodynamic coupling are also considered.

Nomenclature

C	airfoil chord
C_{Lh}	unsteady aerodynamic translation lift coefficient
$C_{M\alpha}$	unsteady aerodynamic torsional moment coefficient
I	mass moment of inertia
k	reduced frequency
L	unsteady lift
M	unsteady moment
q	airfoil translational velocity
U	freestream velocity
x_o	elastic axis location
β	interblade phase angle
δ_A	log dec due to aerodynamic damping
δ_m	log dec due to mechanical damping
$\bar{\omega}$	excitation frequency
ω_α	airfoil torsional natural frequency
ω_h	airfoil translational natural frequency

Subscripts

h	translation
α	torsion

Introduction

The vibrational response of turbomachinery blading to aerodynamic excitations is one of the most troublesome problems in the development of advanced gas turbine engines. When the excitation source is periodic, for example due to a fixed obstruction in the flow field, Campbell diagrams /1/ are utilized to predict the operating conditions at which aerodynamically forced, constant amplitude, blade vibrations will occur. However, flow induced vibrational response problems are also generated by nonperiodic random aerodynamic excitation sources. In particular, turbulence can generate random amplitude vibrations at the blade

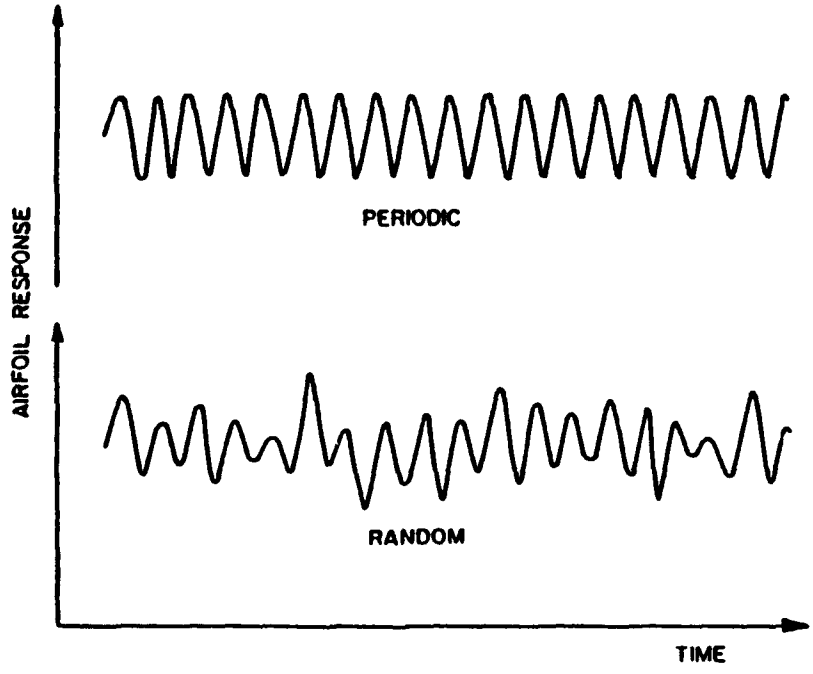

Fig. 1. Periodic and random blade vibrational response.

natural frequency, as depicted schematically in Figure 1. This problem was initially considered by Whitehead /2/ from the point of view of determining the bending mode aerodynamic damping of an isolated airfoil in an incompressible flow field.

In this paper, an analysis is developed and utilized to predict the turbulence generated bending and torsion mode vibrational response of a turbomachine blade row operating in a subsonic compressible flow field. Thus, the modeling of reference /3/ is extended herein to the more realistic and important cases of torsional response modes, subsonic compressible flow fields, and to cascaded airfoils. A strip theory representation of the blade row is utilized, with the vibrational characteristics of the typical two-dimensional blade section modeled as a damped translation or torsion mode single-degree-of-freedom system. The turbulence is the aerodynamic forcing function and is assumed to be random over the range of frequencies near the airfoil natural frequency of interest. The basis of this model is to then consider the turbulence to generate a large number of constant amplitude, harmonic, unsteady aerodynamic lift forces and moments on the airfoils with uniformly distributed frequencies. The resulting random airfoil vibrations thus occur at the airfoil natural frequency, with the power spectra of the turbulence generated airfoil unsteady aerodynamic excitation, S_E, and the resulting blade displacement, S_R, having the form depicted schematically in Figure 2.

Airfoil Response Model

The representative two-dimensional airfoil section is modeled as a mass-spring-damper system, Figure 3, with the single-degree-of-freedom translation and torsion mode equations of motion given in Equation 1.

$$m\frac{d^2h}{dt^2} + \frac{m\omega_h\delta_m}{\pi}\frac{dh}{dt} + m\omega_h^2 h = L(t) \tag{1a}$$

$$I_\alpha\frac{d^2\alpha}{dt^2} + \frac{I_\alpha\omega_\alpha\delta_m}{\pi}\frac{d\alpha}{dt} + I_\alpha\omega_\alpha^2\alpha = M(t) \tag{1b}$$

where m denotes the airfoil mass, I_α is the mass moment of inertia, δ_m is the log decrement of the airfoil vibration due to mechanical damping, ω_h and ω_α are the translation and torsion mode airfoil natural frequencies, respectively, and L(t) and M(t) represent the unsteady aerodynamic lift forces and moments.

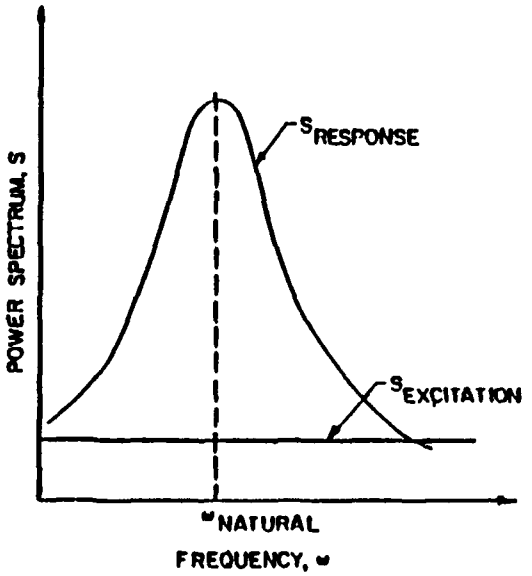

Fig. 2. Schematic power spectra of turbulence excitation and airfoil response.

The turbulence generates harmonic unsteady aerodynamic lift forces and moments which excite the airfoil, thereby driving the random airfoil response at the harmonic excitation frequency, ω_h or ω_α. Thus, the unsteady aerodynamic forces and moments acting on the airfoil, L(t) and M(t), are each modeled as comprised of two components: (1) those due to the unsteady aerodynamic forcing function, i.e. the turbulence; (2) those induced by the resulting airfoil random response, i.e., the aerodynamic damping. These are specified in Equation (2):

$$L(t) = (L_{response} + L_{turbulence})e^{i\omega t} \quad (2a)$$

$$M(t) = (M_{response} + M_{turbulence})e^{i\omega t} \quad (2b)$$

where L and M are complex constants and ω denotes the airfoil natural frequency of interest, either ω_h or ω_α.

The response induced unsteady aerodynamic forces and moments are expressed in conventional nondimensional form.

$$L_{response} = \pi\rho UCqC_{Lh} \quad (3a)$$

$$M_{response} = \pi\rho U^2C^2\alpha C_{M\alpha} \quad (3b)$$

where C_{Lh} and $C_{M\alpha}$ are the nondimensional complex coefficients defining the lift due to translation and the moment due to torsion, respectively, acting on the airfoil.

The airfoil equations of motion specified in Equation (4) are obtained by assuming the airfoil translational and torsional responses to be harmonic at the excitation frequency $\bar{\omega}$ and substituting Equations (2) and (3) into Equation (1).

$$mh\langle -\bar{\omega}^2 + \omega_h^2 + \frac{\bar{\omega}^2 \mathrm{Im}(C_{Lh})}{2k\chi} + \frac{i\bar{\omega}\omega_h}{\pi}\left[\delta_m + \frac{\pi\bar{\omega}\mathrm{Re}(C_{Lh})}{2\omega_h k\chi}\right]\rangle = L_{turbulence} \quad (4a)$$

$$\alpha I_\alpha\langle -\bar{\omega}^2 + \omega_\alpha^2 - \frac{\pi\rho U^2C^2\mathrm{Re}(C_{M\alpha})}{I_\alpha} + i\left[\frac{\bar{\omega}\omega_\alpha}{\pi}\delta_m - \pi\rho U^2C^2\mathrm{Im}(C_{M\alpha})\right]\rangle = M_{turbulence} \quad (4b)$$

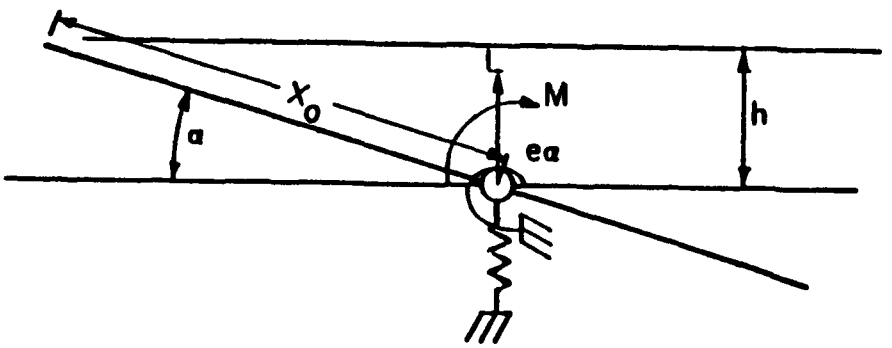

Fig. 3. Airfoil section vibrational model.

where $k = \bar{\omega}C/2U$ is the reduced frequency and $\chi = m/\pi\rho C^2$ is the mass ratio.

The following translation and torsion airfoil displacements are then determined by considering the system to be lightly damped.

$$h = \frac{L_{turbulence}/m}{(\omega_h'^2 - \bar{\omega}^2) + \frac{i\omega_h^2}{\pi}(\delta_m + \delta_{Ah})} \quad (5a)$$

$$\alpha = \frac{M_{turbulence}/I_\alpha}{(\omega_\alpha'^2 - \bar{\omega}^2) + \frac{i\omega_\alpha^2}{\pi}(\delta_m + \delta_{A\alpha})} \quad (5b)$$

where:

$$\omega_h'^2 = \omega_h^2\left[1 + \frac{Im(C_{Lh})}{2k\chi}\right] ;$$

$$\omega_\alpha'^2 = \omega_\alpha^2\left[1 - \frac{Re(C_{M\alpha})}{4k^2\chi}\right]$$

$$\delta_{Ah} = \frac{-\pi R_e(C_{Lh})}{2k\chi} ;$$

$$\delta_{A\alpha} = \frac{\pi I_m(C_{M\alpha})}{4k^2\chi}$$

and δ_{Ah} and $\delta_{A\alpha}$ are the log decrement of the airfoil motion in translation and torsion due to aerodynamic damping.

Random Response Power Spectra

For the case being considered herein, the forcing function is completely random in the neighborhood of the airfoil natural frequency of interest. Thus, the excitation power spectrum, S_E, is constant, per Figure 2.

The power spectrum of the response is a function of the excitation power spectrum. For a random excitation with power spectrum S_E, the following response power spectra are determined from Equations (5) /3, 4/. These are also of the form depicted in Figure 2.

$$S_{Rh} = \frac{S_E/m^2}{(\omega_h'^2 - \bar{\omega}^2)^2 + \frac{\omega_h^4}{\pi^2}(\delta_m + \delta_{Ah})^2} \quad (6a)$$

$$S_{R\alpha} = \frac{S_E/I_\alpha^2}{(\omega_\alpha'^2 - \bar{\omega}^2)^2 + \frac{\omega_\alpha^4}{\pi^2}(\delta_m + \delta_{A\alpha})^2} \quad (6b)$$

The response autocorrelation functions given in Equation (7) are determined from the Fourier transforms of the response power spectra. These have the form of a decaying vibration.

$$\phi_{Rh}(\tau) = \frac{\pi^2 S_E}{2m^2\omega_h^2(\delta_m + \delta_{Ah})} \times$$

$$\times \exp\left[\frac{-\omega_h\tau(\delta_m + \delta_{Ah})}{2\pi}\right]\cos(\omega_h\tau) \quad (7a)$$

$$\phi_{R\alpha}(\tau) = \frac{\pi^2 S_E}{2I_\alpha^2\omega_\alpha^3(\delta_m + \delta_{A\alpha})} \times$$

$$\times \exp\left[\frac{-\omega_\alpha\tau(\delta_m + \delta_{A\alpha})}{2\pi}\right]\cos(\omega_\alpha\tau) \quad (7b)$$

The mean square of the responses are then determined by setting $\tau = 0$ in Equation (7).

$$\phi_{Rh}(0) = \bar{h}^2 = \frac{\pi^2 S_E}{2m^2\omega_h^3(\delta_m + \delta_{Ah})} \quad (8a)$$

$$\phi_{R\alpha}(0) = \bar{\alpha}^2 = \frac{\pi^2 S_E}{2I_\alpha^2\omega_\alpha^3(\delta_m + \delta_{A\alpha})} \quad (8b)$$

To this point in the analysis, it has been assumed that only one airfoil in the blade row is responding to the turbulence. However, for the case of identical blades, all of the blades will be excited. In particular, all of the blades will respond at a constant amplitude but with a blade-to-blade phase difference, β. Values for this interblade phase angle are determined by the number of blades in the row: $\beta = 2\pi n/N$ where $1 \leq n \leq N$ and N is the number of blades in a given row.

Because the random forces and moments acting on each airfoil are uncorrelated, the power spectra on each blade are constant and equal: $S_{E\beta} = S_E/N$. Thus, for each interblade phase angle value, the power spectra can be written per Equation (9).

$$S_{Rh_\beta} = \frac{4S_E k^2 \chi^2}{m^2 \omega_h^4 N} \times$$

$$\times \frac{1}{(\mathrm{Im}[C_{Lh_\beta}] - Y_h)^2 + (\mathrm{Re}[C_{Lh_\beta}])^2} \quad (9a)$$

$$S_{R\alpha_\beta} = \frac{16 S_E k^4 \chi^2}{I_\alpha^2 \omega_\alpha^4 N} \times$$

$$\times \frac{1}{(\mathrm{Re}[C_{M\alpha_\beta}] - Y_\alpha)^2 + (\mathrm{Im}[C_{M\alpha_\beta}])^2} \quad (9b)$$

where

$$Y_h = 2k\chi[(\frac{\bar{\omega}}{\omega_h})^2 - 1];$$

$$Y_\alpha = 4k^2\chi[(\frac{\bar{\omega}}{\omega_\alpha})^2 - 1]$$

Since the vibration at each interblade phase angle is uncorrelated, the power spectrum of the motion of any one airfoil is the sum of the power spectra of the motion in each possible interblade phase angle.

$$S_{Rh} = \frac{4S_E k^2 \chi^2}{m^2 \omega_h^4} S_h(Y_h) \quad (10a)$$

$$S_{R\alpha} = \frac{16 S_E k^4 \chi^2}{I_\alpha^2 \omega_\alpha^4} S_\alpha(Y_\alpha) \quad (10b)$$

where:

$$S_h(Y_h) = \frac{1}{N} \sum_{n=1}^{N} \times$$

$$\times \frac{1}{(\mathrm{Im}[(C_{Lh\beta}) - Y_h]^2 + [\mathrm{Re}(C_{Lh\beta})]^2}$$

$$S_\alpha(Y_\alpha) = \frac{1}{N} \sum_{n=1}^{N} \times$$

$$\times \frac{1}{(\mathrm{Re}[C_{M\alpha_\beta}] - Y_\alpha)^2 + (\mathrm{Im}[C_{M\alpha_\beta}])^2}$$

$$Y_h = 2k\chi[(\frac{\bar{\omega}}{\omega_h})^2 - 1];$$

$$Y_\alpha = 4k^2\chi[(\frac{\bar{\omega}}{\omega_\alpha})^2 - 1]$$

In general, there are a large number of blades in the row. Therefore the sums appearing in Equation (10) can be replaced by an integral.

$$S_h(Y_h) = \frac{1}{2\pi} \times$$

$$\times \int_0^{2\pi} \frac{d\beta}{(\mathrm{Im}[C_{Lh_\beta}] - Y_h)^2 + (\mathrm{Re}[C_{Lh_\beta}])^2} \quad (11a)$$

$$S_\alpha(Y_\alpha) = \frac{1}{2\pi} \times$$

$$\times \int_0^{2\pi} \frac{d\beta}{(\mathrm{Re}[C_{M\alpha_\beta}] - Y_\alpha)^2 + (\mathrm{Im}[C_{M\alpha_\beta}])^2} \quad (11b)$$

For the special case wherein only one airfoil responds to the turbulence, the unsteady aerodynamics are independent of the interblade phase angle /5/. The values of $S_h(Y_h)$ and $S_\alpha(Y_\alpha)$ then reduce to the following:

$$S_h(Y_h) = \frac{1}{(\mathrm{Im}[C_{Lh}] - Y_h)^2 + (\mathrm{Re}[C_{Lh}])^2} \quad (12a)$$

$$S_\alpha(Y_\alpha) = \frac{1}{(\mathrm{Re}[C_{M\alpha}] - Y_\alpha)^2 + (\mathrm{Im}[C_{M\alpha}])^2} \quad (12b)$$

where:

$$C_{Lh} = \frac{1}{2\pi} \int_0^{2\pi} C_{Lh_\beta} d\beta \; ;$$

$$C_{M\alpha} = \frac{1}{2\pi} \int_0^{2\pi} C_{M\alpha_\beta} d\beta$$

Results

The mathematical model developed herein is utilized to demonstrate the turbulence excited vibrational response of a turbomachine blade row operating in a subsonic compressible flow field. For this study, the motion induced unsteady aerodynamics are based on a flat plate airfoil cascade executing harmonic translation or torsion mode oscillations in an inviscid, compressible, flow field /6/. The parameters modeled include the cascade solidity and stagger angle, the torsion mode elastic axis location, the Mach number, the reduced frequency, and the interblade phase angle.

The turbulence excited translation and torsion mode responses of the blade row are demonstrated in Figures 4 and 5, respectively. For these particular operating conditions, the torsion mode response amplitude is larger than the bending one. Also, aerodynamic coupling of the blades increases the amplitude of response for both modes of vibration, but particularly the torsion mode. This larger effect on the torsion mode response is related to the fact that torsion mode flutter is possible in this flow regime and, therefore, the relative aerodynamic damping in torsion may be less than that in translation. This is considered in the following.

The torsion mode flutter boundary for the case of no structural damping can be calculated from the motion induced unsteady aerodynamics. In particular, when the imaginary part of the moment coefficient is zero, the cascade has no aerodynamic damping and flutter is predicted. Figure 6 shows the flutter boundary determined from the unsteady aerodynamic analysis of reference /6/ in the format of the reduced frequency versus the torsional elastic axis location.

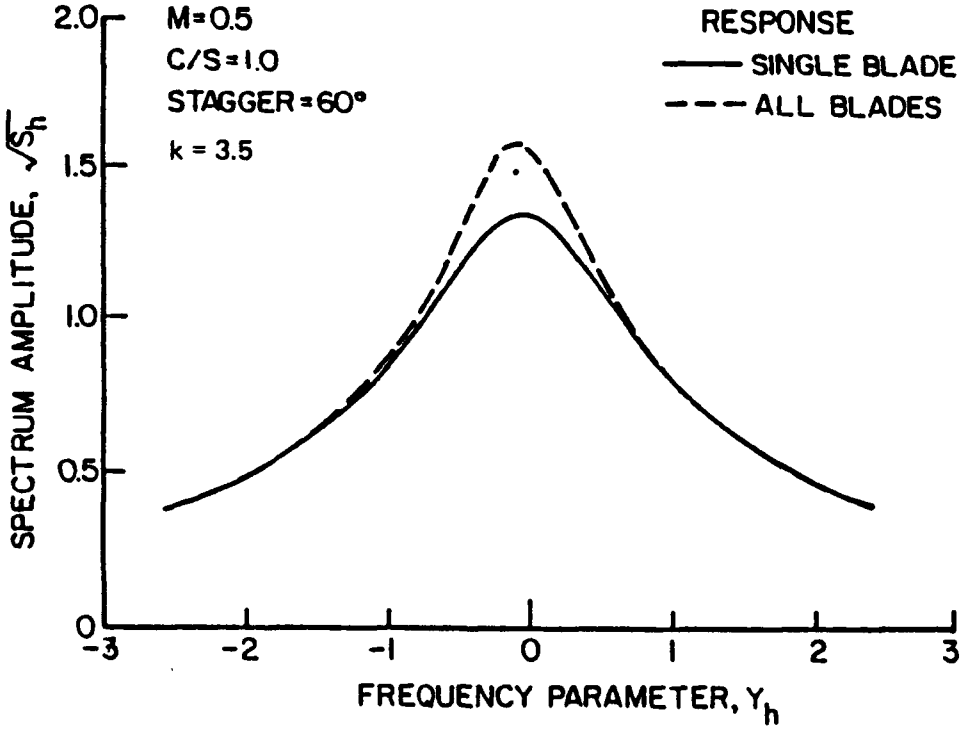

Fig. 4. Turbulence excited translational airfoil response.

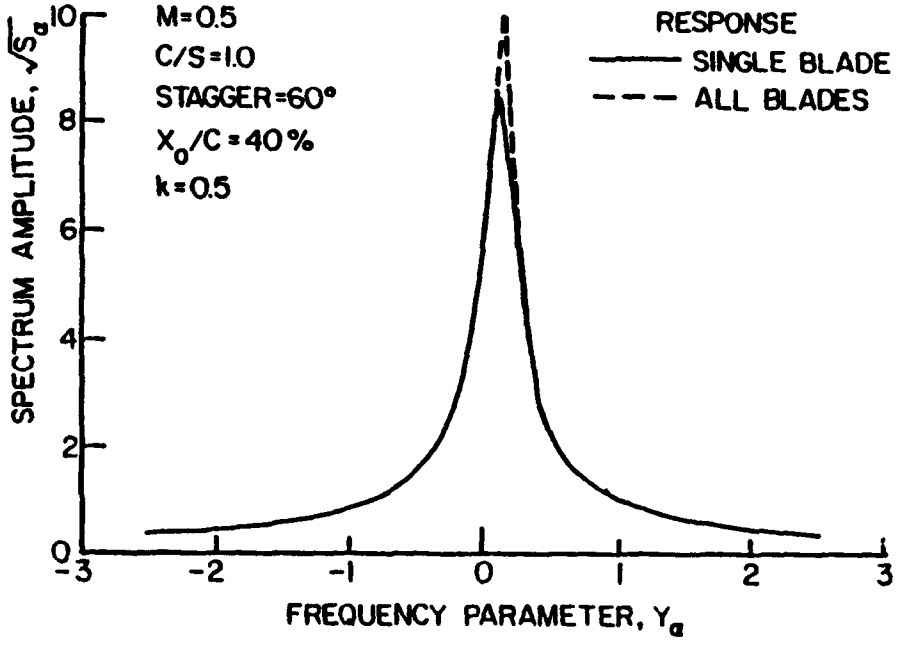

Fig. 5. Turbulence excited torsional airfoil response.

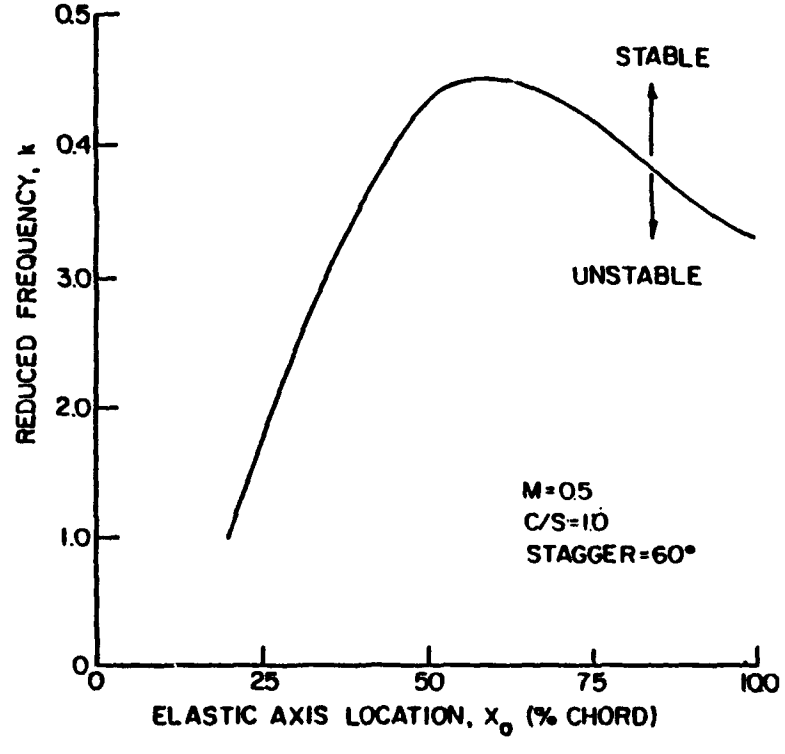

Fig. 6. Torsion mode flutter boundary.

The significant effect of flutter margin and aerodynamic damping, i.e., blade row operation near to the flutter boundary, is now demonstrated. This is accomplished by considering the turbulence induced torsion mode airfoil response near to and far from the flutter boundary, Figure 7. As the elastic axis location is moved aft from the airfoil leading edge and, thus, the torsional flutter boundary is approached, the amplitude of the response increases, with a factor of two difference between the 10% and the 40% chord elastic axis positions. This is due to the decreased aerodynamic damping as the flutter boundary is approached.

The significance of aerodynamic coupling of the blading is also apparent in Figure 7. In particular, for the 10%, 20% and 30% chord elastic axis positions, there is no difference in the predicted amplitudes of response for (1) the case with no aerodynamic coupling and a single blade responding and (2) aerodynamic coupling with all blades responding. However, very near to the flutter boundary with the elastic axis located at 40% chord, the blading response to the turbulence is significantly greater for the case of aerodynamic coupling and all blades vibrating than the corresponding single blade, no aerodynamic coupling, situation.

Summary and Conclusions

An analysis has been developed and utilized to predict the turbulence generated bending and torsion mode vibrational responses of a turbomachine blade row operating in a subsonic compressible flow field. The basis of this model is considering the turbulence to generate a large number of constant amplitude, harmonic, unsteady aerodynamic forces and moments with uniformly distributed frequencies on the blading. This model also includes the unsteady aerodynamics generated by the blade response, i.e., the aerodynamic damping, as well as the effects of blade aerodynamic coupling.

This model was then utilized to investigate turbulence generated translation and torsion mode forced vibratory response of a blade row operating in a subsonic compressible flow field. Aerodynamic coupling of the blades increased the amplitude of response for both the torsion and translation modes of vibration, but particularly the torsion mode. This larger effect on the torsion mode response was shown to be due to the decreased level of aerodynamic damping as the flutter margin of the blade row is decreased. In particular, for the

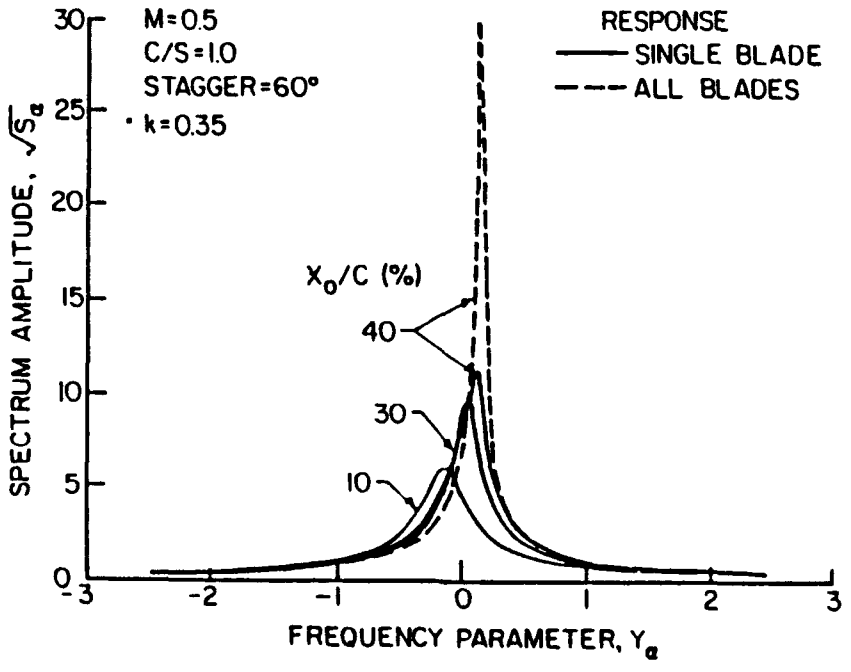

Fig. 7. Effect of flutter margin on torsional airfoil response.

case of turbulence excited torsion mode response, as the flutter margin is decreased: (1) the amplitude of the forced response is increased; (2) the aerodynamic coupling of the airfoils significantly increased the amplitude of response in the neighborhood of the flutter boundary.

Acknowledgement

This research was sponsored in part by the Air Force Office of Scientific Research.

References

1. OATES, G.C. (editor), *"The Aero-Thermodynamics of Aircraft Gas Turbine Engines"*, AFAPL-TR-78-52, July 1978.
2. WHITEHEAD, D.C., "The Analysis of Blade Vibration Due to Random Excitation", Aeronautical Research Council R&M 3252, 1962.
3. MEIROVITCH, L., *Elements of Vibration Analysis*, McGraw-Hill, 1986.
4. NIGAM, N.C., *Introduction to Random Vibrations*, MIT Press, 1983.
5. CRAWLEY, E.F. and HALL, K.C., "Optimization and Mechanism of Mistuning in Cascades", ASME Journal of Engineering for Gas Turbines and Power, Vol. 107, No. 2, April 1985.
6. FLEETER, S., "The Fluctuating Lift and Moment Coefficients for Cascaded Airfoils in a Nonuniform Compressible Flow", AIAA Journal of Aircraft, Vol. 10, No. 2, March 1973.

APPENDIX XI

Viscous Oscillating Cascade Aerodynamics and Flutter by a Locally Analytical Method

AIAA Paper 90-0579

AIAA-90-0579

VISCOUS OSCILLATING CASCADE AERODYNAMICS AND FLUTTER BY A LOCALLY ANALYTICAL METHOD

James M. Wolff+ and Sanford Fleeter*
Thermal Sciences and Propulsion Center
School of Mechanical Engineering
Purdue University
West Lafayette, Indiana 47907

Abstract

A mathematical model is developed to analyze the viscous aerodynamics of an harmonically oscillating flat plate airfoil cascade in an incompressible laminar flow. The steady flow field is described by the Navier-Stokes equations, with the unsteady viscous flow modeled as a small perturbation to this steady flow. Solutions for both the steady and the unsteady viscous flow fields are then obtained by developing locally analytical solutions. The significant effects of Reynolds number, elastic axis, interblade phase angle and incidence angle on the oscillating cascade unsteady aerodynamics and torsional flutter characteristics are then demonstrated.

Nomenclature

C	airfoil chord
C_M	unsteady moment coefficient
k	reduced frequency, $\omega C / U_\infty$
Re	Reynolds number, $U_\infty C / \nu$
S	cascade spacing
U_∞	free-stream velocity magnitude
x_{ea}	elastic axis location
x	mean flow direction coordinate
y	normal flow direction coordinate
y_m	mean airfoil position
Δx	x direction step size
Δy	y direction step size
$(\Delta x_0, \Delta y_0)$	center of grid element
α_0	mean flow incidence angle
α'	amplitude of airfoil oscillation
β	interblade phase angle
ψ	nondimensional unsteady stream fuction
Ψ	nondimensional steady stream fuction
ζ	nondimensional unsteady vorticity
ξ	nondimensional steady vorticity
ς	cascade stagger angle

Introduction

Airfoil and airfoil cascade unsteady aerodynamics are fundamental research areas of interest to a variety of applications, with turbomachinery design being of particular interest herein. As a result, considerable progress has been made in predicting the unsteady aerodynamic response of an airfoil cascade. Initially such unsteady aerodynamic analyses were restricted to thin airfoil potential flow theory, with the unsteady flow assumed to be small as compared to the mean steady potential flow field. In addition, the airfoils were considered to be flat plates at zero mean incidence. Thus, the unsteady aerodynamics become uncoupled from the steady flow, leading to a model wherein the flow is linearized about a uniform parallel flow. Solutions were obtained with classical airfoil techniques, resulting in analytical solutions in the form of integral equations. A model of this type which has found widespread application to turbomachines is that developed by Whitehead [1]. This model analyzes the incompressible inviscid unsteady aerodynamics of a cascade of flat plate airfoils at zero incidence.

Although such classical models and integral techniques are important, the development of numerical methods is enabling the mathematical modeling to be extended and enhanced. The various numerical methods utilized to solve partial differential equations are distinguished from one another by the means used to derive the corresponding algebraic representation of the differential equations. In finite difference methods, Taylor series expansion and control volume formulations are most often used. For finite element methods, variational formulations and the method of weighted residuals are employed. In the locally analytical method, the discrete algebraic equations are obtained from the analytical solution in each individual local grid element.

The various numerical techniques have enabled the inviscid unsteady potential flow through an airfoil cascade to be analyzed, for example References 2 through 5, with these techniques beginning to be utilized to predict unsteady viscous flows, References 6 through 9. In this regard, Schroeder and Fleeter [10] developed a model and locally analytical solution to predict the unsteady viscous aerodynamics of an isolated flat plate airfoil executing harmonic torsional motions in an incompressible laminar flow at low Reynolds number values.

In this paper, the effects of Reynolds number, mean incidence angle, elastic axis and interblade phase angle on the incompressible viscous unsteady aerodynamics and the resulting effect on the cascade torsional flutter characteristics are generated by the harmonic torsional motions of a flat plate airfoil cascade analyzed. This is accomplished by developing a mathematical model which significantly extends the modeling and locally analytical solution initially proposed in Reference 10. In particular, the model developed herein analyzes the steady viscous flow at moderate values of the Reynolds number past a flat plate airfoil cascade and the unsteady viscous aerodynamic interaction of this steady flow field to harmonic torsional motion. The unsteady viscous flow is assumed to be a small perturbation to the steady viscous flow. The steady flow field, described by the Navier-Stokes equations, is nonuniform and nonlinear and is also independent of the unsteady flow. The small perturbation unsteady viscous flow field is described by a system of linear partial differential equations that are coupled to the steady flow field, thereby modeling the strong dependence of the unsteady aerodynamics on the steady flow.

Locally analytical solutions for both the steady and the unsteady viscous flow fields are developed. In this method, the discrete algebraic equations which represent the steady and unsteady flow field equations are obtained from analytical

+ AFRAPT Trainee
* Professor

solutions in individual grid elements. Locally analytical solutions are then developed by applying these solutions to individual grid elements, with the integration and separation constants determined from the boundary conditions in each grid element. The complete flow field solutions are obtained through the application of the global boundary conditions. It should be noted that the nonlinear character of the complete steady flow field is preserved as the flow is only locally linearized, i.e., independently linearized solutions are obtained in individual grid elements.

Mathematical Model

The two-dimensional flow field together with the cartesian coordinate system are schematically depicted in Figure 1. For harmonic time dependence at frequency ω, the flow field is described by the nondimensional continuity and Navier-Stokes equations, written in terms of the vorticity, $\bar{\zeta}$, and the stream function, $\bar{\psi}$, in Equation 1.

$$\nabla^2 \bar{\zeta} = \bar{\zeta}_{xx} + \bar{\zeta}_{yy} = Re\left(k\,\bar{\zeta}_t + \bar{u}\,\bar{\zeta}_x + \bar{v}\,\bar{\zeta}_y\right) \tag{1a}$$

$$\nabla^2 \bar{\psi} = -\bar{\zeta} \tag{1b}$$

where $\bar{\zeta} = \bar{v}_x - \bar{u}_y$ and $\bar{u} = \bar{\psi}_y$; $\bar{v} = -\bar{\psi}_x$.

The flow field is decomposed into steady and harmonic unsteady components, with the unsteady component assumed to be a small perturbation to the steady component.

$$\bar{\zeta}(x,y,t) = \xi(x,y) + e^{it}\zeta(x,y) \tag{2a}$$

$$\bar{\psi}(x,y,t) = \Psi(x,y) + e^{it}\psi(x,y) \tag{2b}$$

$$\bar{u}(x,y,t) = U(x,y) + e^{it}u(x,y) \tag{2c}$$

$$\bar{v}(x,y,t) = V(x,y) + e^{it}v(x,y) \tag{2d}$$

$$\bar{p}(x,y,t) = P(x,y) + e^{it}p(x,y) \tag{2e}$$

where

$$\zeta \ll \xi,\ \psi \ll \Psi,\ u \ll U,\ v \ll V,\ p \ll P$$

The equations describing the steady and unsteady viscous flow fields are determined by substituting Equation 2 into Equation 1, and grouping together the time independent and the time dependent terms. For the unsteady flow, the second order terms are neglected as small compared to the first order terms. Also, as the linearized unsteady flow is assumed to be harmonic, the exp(it) is dropped, for convenience.

The resulting coupled nonlinear partial differential equations describing the steady flow field, Equation 3, are independent of the unsteady flow. The vorticity equation is nonlinear, with the stream function described by a linear Poisson equation which is coupled to the vorticity equation through the vorticity source term. The pressure is also described by a linear Poisson equation with the source terms dependent on the steady flow field.

$$\nabla^2 \xi = Re\left(U\xi_x + V\xi_y\right) \tag{3a}$$

$$\nabla^2 \Psi = -\xi \tag{3b}$$

$$\nabla^2 P = 2\left(U_x V_y - V_x U_y\right) \tag{3c}$$

The resulting coupled linear partial differential equations describing the unsteady harmonic flow field are given in Equation 4. The unsteady flow is coupled to the steady flow field. In particular, in both the unsteady vorticity transport and pressure equations, the variable coefficients are dependent on the steady flow field with the unsteady stream function coupled to the solution for the unsteady vorticity.

$$\nabla^2 \zeta = Re\left(k\,i\,\zeta + u\,\xi_x + U\,\zeta_x + v\,\xi_y + V\,\zeta_y\right) \tag{4a}$$

$$\nabla^2 \psi = -\zeta \tag{4b}$$

$$\nabla^2 p = 2\left|\left(u_x V_y + v_y U_x\right) - \left(v_x U_y + u_y V_x\right)\right| \tag{4c}$$

Boundary Conditions

The steady flow boundary conditions specify that: (1) there is no slip between the fluid and the airfoil, and (2) the fluid velocity normal to the stationary airfoils is zero on the airfoil surfaces.

$$U = V = 0 \qquad \text{on airfoil surfaces} \tag{5}$$

A stream function and vorticity formulation is being utilized. Thus corresponding stream function and vorticity boundary conditions must be specified. These are determined from the definitions of the stream function and the vorticity in conjunction with Equation 5. The steady stream function is defined by $\Psi_y = U$ and $\Psi_x = -V$. Since U and V are both zero on the airfoil, Ψ must be a constant on the airfoil surfaces. The vorticity is defined as $\xi = V_x - U_y$. Since V is constant, namely zero, on the airfoil, V_x is zero, and therefore $\xi = -U_y$ on the airfoil surfaces.

$$\Psi = \text{constant} \qquad \text{on airfoil surfaces} \tag{6}$$

$$\xi = -U_y = -\Psi_{yy} \qquad \text{on airfoil surfaces} \tag{7}$$

The passage-to-passage periodicity of the cascade is achieved by extending the computational flow field of a typical single passage one grid element in the normal direction at the top and bottom of the passage and then applying the calculated values at the upper and lower boundaries. The passage-to-passage stream function values differ by a constant while the passage-to-passage vorticity values are the same. The periodicity boundary conditions are given in Equation 8.

$$\Psi(x, -\Delta y) = \Psi(x, S - \Delta y) - \text{constant} \tag{8a}$$

$$\Psi(x, S + \Delta y) = \Psi(x, \Delta y) + \text{constant} \tag{8b}$$

$$\xi(x, -\Delta y) = \xi(x, S - \Delta y) \tag{8c}$$

$$\xi(x, S + \Delta y) = \xi(x, \Delta y) \tag{8d}$$

where $\Psi(-\infty, S) - \Psi(-\infty, 0)$ is a constant and Δy is the grid increment in the y direction.

The periodic boundary conditions are shifted by the cosine of the stagger angle (ς) in the x-direction for the staggered cascade, Figure 2. The flow field is extended in both the upstream and downstream directions to allow the nonoverlapping grid section to be treated as far field boundary conditions.

The inlet and exit far field boundary conditions for the cascade steady flow are developed below. The far field inlet flow is uniform for both the zero and nonzero mean flow incidence flows, as specified in the following boundary conditions.

$$\xi (x \rightarrow -\infty , y) = 0 \qquad (9a)$$

$$\Psi (x \rightarrow -\infty , y) = y \qquad (9b)$$

When the mean flow incidence angle is zero, U = 1, V = $-\Psi_x = 0$, and $\xi_x = 0$ define the cascade exit far field flow field. Thus the cascade exit far field boundary conditions are given in Equation 10.

$$\Psi (x \rightarrow \infty , y) = \Psi (\infty - \Delta x, y) \qquad (10a)$$

$$\xi (x \rightarrow \infty , y) = \xi (\infty - \Delta x, y) \qquad (10b)$$

where Δx is the grid increment in the x direction.

With a nonzero mean flow incidence angle, neither U nor V is zero in the exit far field. The far field exit flow is assumed to be uniform, defined by $\xi_x = 0$. For the stream function far field exit boundary condition a Taylor series expansion is used in both the normal and streamwise directions. These far field exit boundary conditions are given in Equation 11.

$$\Psi (x \rightarrow \infty, y) = (\Psi (\infty - \Delta x, y) - V\, dx + \Psi (\infty, y + \Delta y) - U\, dy) / 2 \qquad (11a)$$

$$\xi (x \rightarrow \infty , y) = \xi (\infty - \Delta x, y) \qquad (11b)$$

The flow is steady in the upstream and downstream far field. Hence the unsteady far field boundary conditions require the far field perturbation velocity to be zero. Neumann boundary conditions, analogous to the steady boundary conditions, are thus applied to the stream function, Equation 12a. Also, the far field unsteady velocity components and vorticity are zero, Equation 12b.

$$\psi = \text{constant} \qquad \text{Far Field} \qquad (12a)$$

$$u = v = \zeta = 0 \qquad \text{Far Field} \qquad (12b)$$

The unsteady boundary conditions on the airfoil surfaces specify that the velocity of the fluid is equal to that of the surfaces. For a flat plate airfoil cascade executing small amplitude harmonic torsion mode oscillations about an elastic axis located at x_{ea} as measured from the leading edge, the linearized normal velocity boundary condition is given in Equation 13. This boundary condition is applied on the mean position of the oscillating airfoils, y_m.

$$v (x, y_m) = \alpha' k U_\infty + \alpha' [i k (x - x_{ea})] \qquad (13)$$

where α' is the amplitude of oscillation, and $k = \dfrac{\omega C}{U_\infty}$ is the reduced frequency.

The fluid is viscous. Thus the unsteady chordwise velocity component must satisfy the no - slip boundary condition applied on the mean position of the oscillating airfoil, Equation 14.

$$u (x, y_m) = 0 \qquad (14)$$

The unsteady stream function and vorticity airfoil surface boundary conditions corresponding to these unsteady velocity boundary conditions are as follows.

$$\psi (x, y_m) = -\alpha' k \left| U_\infty x + i \left(\frac{x}{2} - x_{ea} \right) x \right| \qquad (15a)$$

$$\zeta (x, y_m) = \alpha' i k - u_y (x, y_m) \qquad (15b)$$

The unsteady periodic cascade boundary conditions are developed analogous to the steady ones and take into account the constant specified interblade phase angle, β. The model is extended one grid element in the normal direction at the top and bottom of a typical single blade-to-blade passage. This allows the computational grid to overlap at the top and bottom of the single passage. Calculated values are then used at the upper and lower boundaries, Figure 2. The passage-to-passage stream function values differ by a constant while the passage-to-passage vorticity values are the same, Equation 16. The constant interblade phase angle, β, defines the airfoil-to-airfoil differences in the unsteady aerodynamics, with the unsteady aerodynamics on adjacent airfoils differing by β. The interblade phase angle is defined by the number of blades on the rotor. Thus, the periodic unsteady cascade boundary conditions are specified by changing the upper and lower boundary conditions to reflect the interblade phase angle.

$$\psi (x , -\Delta y) = (\psi (x , S - \Delta y) - \text{constant}) / (\cos \beta + i \sin \beta) \qquad (16a)$$

$$\psi (x , S + \Delta y) = (\psi (x , \Delta y) + \text{constant}) * (\cos \beta + i \sin \beta) \qquad (16b)$$

$$u (x , -\Delta y) = u (x , S - \Delta y) / (\cos \beta + i \sin \beta) \qquad (16c)$$

$$u (x , S + \Delta y) = u (x , \Delta y) * (\cos \beta + i \sin \beta) \qquad (16d)$$

$$v (x , -\Delta y) = v (x , S - \Delta y) / (\cos \beta + i \sin \beta) \qquad (16e)$$

$$v (x , S + \Delta y) = v (x , \Delta y) * (\cos \beta + i \sin \beta) \qquad (16f)$$

$$\zeta (x , -\Delta y) = \zeta (x , S - \Delta y) / (\cos \beta + i \sin \beta) \qquad (16g)$$

$$\zeta (x , S + \Delta y) = \zeta (x , \Delta y) * (\cos \beta + i \sin \beta) \qquad (16h)$$

where $\psi (-\infty, S) - \psi (-\infty, 0)$ is a constant.

Locally Analytical Solutions

Locally analytical solutions are obtained for the unsteady and steady viscous flow fields. In this method, the discrete algebraic equations which represent the aerodynamic equations are obtained from analytical solutions in individual local grid elements. This is accomplished by dividing the flow field into computational grid elements. In each individual element the nonlinear convective terms of the Navier-Stokes equations which describe the steady flow are locally linearized. The nonlinear character of the steady flow is preserved as the flow is only locally linearized, that is, independently linearized in individual grid elements. Analytical solutions to the linear equations describing both the steady and the unsteady flow fields in each element are then determined. The solution for the complete flow field is obtained through the application of the global boundary conditions and the assembly of the locally analytic solutions in the individual grid elements.

Steady Flow Field

The steady vorticity transport is described by Equation 3 which is nonlinear because of the convective terms $U \xi_x + V$

ξ_y. These terms are locally linearized by assuming that the velocity components U and V, which are the coefficients of the vorticity, are constant in each individual grid element, that is, locally linearized.

$$U = \frac{2A}{Re} \qquad V = \frac{2B}{Re} \tag{17}$$

where A and B are constants in an individual grid element, taking on different values in each grid element.

The resulting locally linearized vorticity equation is given in Equation 18. This locally linearized equation is solved analytically to determine the steady vorticity, ξ, in a grid element, thereby providing the functional relationships between the vorticity in an individual grid element and the boundary values specified on that grid element.

$$2A\,\xi_x + 2B\,\xi_y = \xi_{xx} + \xi_{yy} \tag{18}$$

This vorticity transport equation is elliptic. Therefore, to obtain a unique solution for the typical uniform grid element with center (x_o,y_o), Figure 3, boundary conditions must be specified on all four boundaries. These boundary conditions are expressed in an implicit formulation in terms of the nodal values of the vorticity along the boundaries of the element. A second-order polynomial is used to approximate the vorticity on each of the boundaries.

$$\begin{aligned}
&\xi\,(x,y_o+\Delta y) = a_1\xi + a_2\xi\, x + a_3\xi\, x^2 \\
&\xi\,(x_o+\Delta x,y) = b_1\xi + b_2\xi\, y + b_3\xi\, y^2 \\
&\xi\,(x,y_o-\Delta y) = c_1\xi + c_2\xi\, x + c_3\xi\, x^2 \\
&\xi\,(x_o-\Delta x,y) = d_1\xi + d_2\xi\, y + d_3\xi\, y^2
\end{aligned} \tag{19}$$

where $a_i\xi$, $b_i\xi$, $c_i\xi$, $d_i\xi$ are constants determined from the three nodal points on each boundary side and the x and y distances are all measures from the center of the element (x_o,y_o).

The analytical solution to Equation 18 subject to the boundary conditions specified in Equation 19 is determined by separation of variables.

$$\begin{aligned}
\xi\,(x,y) = e^{(Ax+By)} \sum_{n=1}^{n=\infty} \Big\{ &\left[B^{\xi}_{1n}\sinh\left(E_{1n}x\right)\right. \\
&\left. + B^{\xi}_{2n}\cosh\left(E_{1n}x\right)\right] \sin\left(\lambda^{\xi}_{1n}(y+\Delta y)\right) \\
+ \left[B^{\xi}_{3n}\sinh\left(E_{2n}y\right) + B^{\xi}_{4n}\cosh\left(E_{2n}y\right)\right] &\sin\left(\lambda^{\xi}_{2n}(x+\Delta x)\right) \Big\}
\end{aligned} \tag{20}$$

The locally analytical solution for the stream function is obtained by a procedure analogous to that used for the vorticity after subdividing the flow region into computational grid elements.

The steam function is described by a linear Poisson equation which is coupled to the vorticity and also is elliptic, Equation 3b. Therefore, to obtain a unique analytical solution for the typical grid element, continuous conditions must be specified on all four boundaries. As for the vorticity transport equation, continuous boundary conditions are represented in an implicit formulation in terms of the nodal values of the stream function by second-order polynomials in x or y as measured from the center of the element (x_o,y_o).

$$\begin{aligned}
&\Psi\,(x,y_o+\Delta y) = a_1\Psi + a_2\Psi\, x + a_3\Psi\, x^2 \\
&\Psi\,(x_o+\Delta x,y) = b_1\Psi + b_2\Psi\, y + b_3\Psi\, y^2 \\
&\Psi\,(x,y_o-\Delta y) = c_1\Psi + c_2\Psi\, x + c_{3y}\Psi\, x^2 \\
&\Psi\,(x_o-\Delta x,y) = d_1\Psi + d_2\Psi\, y + d_3\Psi\, y^2
\end{aligned} \tag{21}$$

where $a_i\Psi$, $b_i\Psi$, $c_i\Psi$, $d_i\Psi$, are constants determined from the three nodal points on each boundary side.

The stream function equation is linear and possesses a nonhomogeneous term, $-\xi\,(x,y)$, which couples the stream function to the vorticity. To solve Equation 3b subject to the boundary conditions specified in Equation 21, it is divided into two component problems. One problem has a homogeneous equation with nonhomogeneous boundary conditions, whereas the second problem has a nonhomogeneous equation with homogeneous boundary conditions.

$$\Psi = \Psi a + \Psi b \tag{22}$$

Problem 1:

$$\begin{aligned}
&\nabla^2\,\Psi a = 0 \\
&\Psi a\,(x,y_o+\Delta y) = a_1\Psi + a_2\Psi\, x + a_3\Psi\, x^2 \\
&\Psi a\,(x_o+\Delta x,y) = b_1\Psi + b_2\Psi\, y + b_3\Psi\, y^2 \\
&\Psi a\,(x,y_o-\Delta y) = c_1\Psi + c_2\Psi\, x + c_{3y}\Psi\, x^2 \\
&\Psi a\,(x_o-\Delta x,y) = d_1\Psi + d_2\Psi\, y + d_3\Psi\, y^2
\end{aligned} \tag{23}$$

Problem 2:

$$\begin{aligned}
&\nabla^2\,\Psi b = -\,\xi\,(x,y) \\
&\Psi b\,(x,y_o+\Delta y) = 0 \\
&\Psi b\,(x_o+\Delta x,y) = 0 \\
&\Psi b\,(x,y_o-\Delta y) = 0 \\
&\Psi b\,(x_o-\Delta x,y) = 0
\end{aligned} \tag{24}$$

The solutions for Ψa and Ψb are then determined by separation of variables.

$$\begin{aligned}
\Psi\,(x,y) = \sum_{n=1}^{n=\infty} \Big\{ &\left[\left[B^{\Psi}_{1n}\sinh\left(\lambda^{\Psi}_{1n}x\right)\right.\right. \\
&\left.\left. + B^{\Psi}_{2n}\cosh\left(\lambda^{\Psi}_{1n}x\right)\right] \sin\left(\lambda^{\Psi}_{1n}(y+\Delta y)\right)\right. \\
&+ \left[B^{\Psi}_{3n}\sinh\left(\lambda^{\Psi}_{2n}y\right) + B^{\Psi}_{4n}\cosh\left(\lambda^{\Psi}_{2n}y\right)\right] \sin\left(\lambda^{\Psi}_{2n}(x+\Delta x)\right) \\
&+ \left[G^{\Psi}_{1n}\sinh\left(\lambda^{\Psi}_{2n}y\right) + G^{\Psi}_{2n}\cosh\left(\lambda^{\Psi}_{2n}y\right) + \right. \\
&\left.\left. G^{\Psi}_{1n} + G^{\Psi}_{2n}y + G^{\Psi}_{3n}y^2\right] \sin\left(\lambda^{\Psi}_{2n}(x+\Delta x)\right) \Big\}
\end{aligned} \tag{25}$$

The stream function is continuously differentiable across the grid element. Hence the U and V velocity components can be obtained analytically by differentiating the stream function solution. The solution for Ψ, ξ, U and V are then used to determine the pressure in the flow field and on the boundaries. Thus, the locally analytical solutions for the velocity components and the pressure are determined as post processes.

Unsteady Flow Field

The unsteady vorticity is described by a linear partial differential equation with nonconstant coefficients u and v vary across the typical computational grid element. However, the steady velocity coefficients U and V are known from the previously determined steady state solution and are constant in the typical grid element, as specified in Equation 17.

To determine the locally analytical solution to the unsteady perturbation vorticity equation, it is approximated as a constant coefficient partial differential equation in individual grid elements. This is accomplished by assuming that the perturbation velocities u and v are constant in each element.

$$u = \frac{2A'}{Re} \qquad v = \frac{2B'}{Re} \tag{26}$$

where A' and B' are constant in each individual grid element, taking on different values in different grid elements.

The resulting linear constant coefficient partial differential equation defines the unsteady perturbation vorticity in an individual computational grid element.

$$k\cdot i\cdot Re\,\zeta + 2A\,\zeta_x + 2B\,\zeta_y + (2A'\,\xi_x + 2B'\,\xi_y) = \zeta_{xx} + \zeta_{yy} \tag{27}$$

To determine the analytical solution in the typical grid element, Equation 27 is rewritten as a homogeneous equation.

$$\nabla^2\bar{\zeta} = 2A\,\bar{\zeta}_x + 2B\,\bar{\zeta}_y \tag{28}$$

where:

$$\bar{\zeta}(x,y) = \zeta(x,y) + \frac{S\left(Ax + \frac{B}{A}y\right)}{2\left(A^2 + \frac{B^2}{A}\right)};$$

$$\text{and } S(x,y) = \left(2A'\xi_x + 2B'\xi_y + k\cdot Re\cdot i\,\zeta\right)$$

This equation is of the same form as that for the steady linearized vorticity, Equation 18. Thus, the solution for $\bar{\zeta}$ is obtained in a manner exactly analogous to that for the steady vorticity, ξ, and is given in Equation 29.

$$\begin{aligned}\bar{\zeta}(x,y) = {} & z_1(x+\Delta x,y+\Delta y)\,\bar{\zeta}(x+\Delta x,y+\Delta y) \\ & + z_2(x+\Delta x,y)\,\bar{\zeta}(x+\Delta x,y) \\ & + z_3(x+\Delta x,y-\Delta y)\,\bar{\zeta}(x+\Delta x,y-\Delta y) \\ & + z_4(x,y-\Delta y)\,\bar{\zeta}(x,y-\Delta y) \\ & + z_5(x-\Delta x,y-\Delta y)\,\bar{\zeta}(x-\Delta x,y-\Delta y) \\ & + z_6(x-\Delta x,y)\,\bar{\zeta}(x-\Delta x,y) \\ & + z_7(x-\Delta x,y+\Delta y)\,\bar{\zeta}(x-\Delta x,y+\Delta y) \\ & + z_8(x,y+\Delta y)\,\bar{\zeta}(x,y+\Delta y)\end{aligned} \tag{29}$$

where the coefficients z_i are dependent on the steady state velocity components, U and V.

The unsteady stream function is described by Equation 4b. This equation is identical to that for the steady stream function, Equation 3b. Hence, an identical solution procedure is utilized. As the coefficients for the stream function are only a function of their position in the grid element, that is, Δx and Δy, the unsteady coefficients remain the same as those found previously for the steady stream function $\Psi(x_0,y_0)$. Thus, the solution for the unsteady stream function is determined from the steady stream function solution, Equation 25, by replacing Ψ by ψ and the steady vorticity ξ by the vorticity ζ. The algebraic equation for the value of the unsteady stream function at the center of the typical element in terms of the values of the unsteady stream function and vorticity at its eight neighboring values is given in Equation 30.

$$\begin{aligned}\psi(x_0,y_0) = {} & p_1^{\psi}\,\psi(x_0+\Delta x,y_0+\Delta y) + p_2^{\psi}\,\psi(x_0+\Delta x,y_0) \\ & + p_3^{\psi}\,\psi(x_0+\Delta x,y_0-\Delta y) + p_4^{\psi}\,\psi(x_0,y_0-\Delta y) \\ & + p_5^{\psi}\,\psi(x_0-\Delta x,y_0-\Delta y) + p_6^{\psi}\,\psi(x_0-\Delta x,y_0) \\ & + p_7^{\psi}\,\psi(x_0-\Delta x,y_0+\Delta y) + p_8^{\psi}\,\psi(x_0,y_0+\Delta y) \\ & + q_1^{\psi}\,\zeta(x_0+\Delta x,y_0+\Delta y) + q_2^{\psi}\,\zeta(x_0+\Delta x,y_0) \\ & + q_3^{\psi}\,\zeta(x_0+\Delta x,y_0-\Delta y) + q_4^{\psi}\,\zeta(x_0,y_0-\Delta y) \\ & + q_5^{\psi}\,\zeta(x_0-\Delta x,y_0-\Delta y) + q_6^{\psi}\,\zeta(x_0-\Delta x,y_0) \\ & + q_7^{\psi}\,\zeta(x_0-\Delta x,y_0+\Delta y) + q_8^{\psi}\,\zeta(x_0,y_0+\Delta y) \\ & + q_9^{\psi}\,\zeta(x_0,y_0)\end{aligned} \tag{30}$$

The unsteady velocity components u and v are determined by differentiating the unsteady stream function, with the locally analytical solution for the unsteady pressure determined by a post process.

Results

The unsteady viscous flow model and the locally analytical solutions developed herein are utilized to demonstrate the effects of moderate Reynolds number, interblade phase angle, elastic axis and mean flow incidence on the unsteady aerodynamics and flutter characteristics of a flat plate airfoil cascade.

The unsteady aerodynamic results are presented in the format of the real and imaginary components of the unsteady airfoil surface pressure difference across the chordline of a cascaded airfoil, and the corresponding complex unsteady moment, as defined in Equation 31.

$$C_M = \frac{M}{\rho c^2 U^2 \pi} = \frac{\int_{c=0}^{c=1} (p_{lower} - p_{upper})(x - x_{c_4})\,dx}{\rho c^2 U^2 \pi} \tag{31}$$

The cascade predictions are obtained on a 126 x 37 rectangular grid, Figure 4, with $\Delta x = \Delta y = 0.025$ and 41 points on the airfoil surfaces, thereby limiting results to moderate values of the Reynolds numbers. The convergence criteria for the internal and external steady stream function iterations are 10^{-4}, with a steady vorticity tolerance of $5\cdot10^{-2}$. The computational time ranged from 825 CPU seconds on the Cyber 205. The convergence criteria for the internal and

external unsteady stream function iterations are 10^{-4}, with a unsteady vorticity tolerance of $5 \cdot 10^{-4}$. The tolerances for the unsteady pressure iterations are 10^{-6} and 10^{-5} for the internal and external iterations, respectively. The computational time averaged 2200 seconds CPU time on the Cyber 205, with an average of 300 iterations for the solutions of the stream function and vorticity and an additional 200 iterations for the pressure solution.

The steady flow model and its locally analytical solution are first utilized to predict the steady viscous flow past the cascade. For example, Figure 5 shows the predicted stream function contours for two passages, with the steady vorticity on the airfoil surface for Reynolds number of 1,000 and zero incidence with 30 degrees stagger. Figure 6 shows the predicted stream function contours for two passages, with the steady vorticity on the airfoil surface for Reynolds number of 1,000 with 8 degrees of incidence and 30 degrees stagger.

The effects of viscosity on both the unsteady viscous aerodynamics generated by the oscillating flat plate cascade which are coupled to the steady viscous flow and the cascade flutter characteristics are then analyzed with the unsteady flow model and its locally analytical solution. In particular, the effects of Reynolds number, elastic axis location, interblade phase angle, and incidence angle on the oscillating airfoil unsteady pressure difference across the chordline of a referenced airfoil and the corresponding complex unsteady aerodynamic moment are demonstrated. Also presented as a reference are the corresponding inviscid predictions obtained from the classical incompressible flow cascade model of Whitehead[1].

The effects of Reynolds number and interblade phase angle on the complex unsteady pressure difference are presented in Figures 7 through 9. The viscous predictions are nonsingular at the airfoil leading edge whereas the inviscid results are singular. There is general trendwise agreement in the viscous and inviscid predictions of the chordwise unsteady pressure distribution, with only the real part at 0 degrees interblade phase angle exhibiting relatively good correlation. As will be seen, differences between the viscous and inviscid predictions result in large differences in the corresponding unsteady moment predictions.

Mean flow incidence angle has only a small effect on the viscous predictions of the complex unsteady pressure difference, Figure 10. To gain some insight into this result, the predicted steady airfoil surface pressure difference for mean flow incidence angles of 0 and 8 degrees are presented in Figure 11. There are only small differences between the two pressure distributions, with no indication of flow separation.

The torsion mode flutter stability of a cascade of airfoils is determined by the imaginary part of the unsteady aerodynamic moment if there is no mechanical damping. Thus, the effects of Reynolds number, mean flow incidence angle, and interblade phase angle on the imaginary part of the moment coefficient are considered in Figures 12 and 13. In particular, these figures present the viscous predictions of the imaginary part of the moment coefficients as a function of elastic axis location, with interblade phase angle as a parameter for incidence angles of 0 and 8 degrees. Also shown are the corresponding inviscid predictions.

Viscosity has a destabilizing effect on the cascade for elastic axis locations forward of approximately midchord. Namely the inviscid predictions indicate that the cascade is stable for all elastic axis locations, with the interblade phase angle value having minimal effect. In contrast, the viscous predictions show that viscosity is either stabilizing or destabilizing depending on the location of the elastic axis, with the interblade phase angle having a large effect on the increased cascade stability for elastic axis locations aft of approximately midchord. Also, a comparison of the 0 and 8 degree mean flow incidence angle viscous results shows that this increased incidence is slightly destabilizing.

Summary and Conclusions

A mathematical model has been developed to analyze the two-dimensional steady and unsteady aerodynamics of a cascade of flat plate airfoils in an incompressible laminar flow with the unsteady aerodynamics generated by harmonic torsion mode oscillations of the airfoil cascade. The unsteady viscous flow is assumed to be a small perturbation to the steady viscous flow which is described by the Navier-Stokes equations. The small perturbation unsteady viscous flow field is described by a system of linear partial differential equations that are coupled to the steady flow field.

Solutions for both the steady and the unsteady viscous flow fields were obtained by developing locally analytical solutions. In this approach, the discrete algebraic equations which represent the flow field equations are obtained from analytical solutions in individual grid elements. For the steady viscous flow, this was accomplished by first locally linearizing the convective terms in the Navier-Stokes equations. The complete flow field solutions are then obtained through the application of the global boundary conditions and the assembly of the local grid element solutions.

This model and locally analytical solutions were then utilized to demonstrate the effects of viscosity on both the oscillating cascade unsteady aerodynamics and the cascade flutter characteristics. In particular, the complex unsteady chordwise pressure differences and resulting unsteady aerodynamic moment on a referenced airfoil of the cascade in a viscous flow characterized by Reynolds numbers of 500 and 1,000 were analyzed and correlated with classical inviscid results for a stagger angle of 30 degrees, reduced frequency of 2.0, elastic axis of 0.5, incidence angles of 0 and 8 degrees, and interblade phase angles from 0 to 180 degrees.

Acknowledgements

Research sponsored by the Air Force Office of Scientific Research (AFSC) under Contract F49620-88-C-0022. The United States Government is authorized to reproduce and distribute reprints for governmental purposes notwithstanding any copyright notation hereon.

References

1. Whitehead, D. S., "Force and Moment Coefficients for Vibrating Aerofoils in Cascade", *Aeronautical Research Council Reports and Memoranda*, R & M No. 3254, 1962.

2. Sisto, F., "Linearized Theory of Nonstationary Cascades at Fully Staled or Supercavitated Conditions", *ZAMM*, Volume 47, Number 8, 1967, pp. 531-542.

3. Ives, D. C., and Liutermoza, J. F., "Second - Order Accurate Calculation of Transonic Flow over Turbomachinery Cascades", *AIAA Journal*, Vol. 17, 1978, pp. 870 - 876.

4. Ives, D. C., and Liutermoza, J. F., "Analysis of Transonic Cascade Flow Using Conformal Mapping and Relaxation Techniques", *AIAA Paper 76-370*, AIAA Ninth Fluid and Plasma Dynamics Conference, San Diego, 1976.

5 Rae, W. J., and Homicz, G. F., "A Rectangular - Coordinate Method for Calculating Nonlinear Transonic Potential Flow Fields in Compressor Cascades", *AIAA Paper 78-248*, AIAA Sixteenth Aerospace Sciences Meeting, Huntsville, Ala., 1978.

6. Yates, J. E., "Unsteady Viscous Thin Airfoil Theory", *AGARD Report Number 671*, September, 1978.

7. Dodge, P. R., "Numerical Method for 2D and 3D Viscous Flows", *AIAA Jounal*, Vol. 15, No. 7, 1977, pp. 961 - 965.

8. Ghia, U., Ghia, K. N., Rubin, S. G., and Khosla, P. K., "Study of Incompressible Flow Separation Using Primitive Variables", *Computers and Fluids*, Vol. 9, 1981, pp. 123 - 142.

9. Harlow, F. H., and Welch, J. E., "Numerical Calculation of Time - Dependent Viscous Incompressible Flow of Fluid with Free Surface", *Physics of Fluids*, Vol. 8, 1965, pp. 2182 - 2189.

10. Schroeder, L.M. and Fleeter, S., "Viscous Aerodynamic Analysis of an Oscillating Flat Plate Airfoil with a Locally Analytical Solution", *AIAA Paper 88-0130*, January 1988.

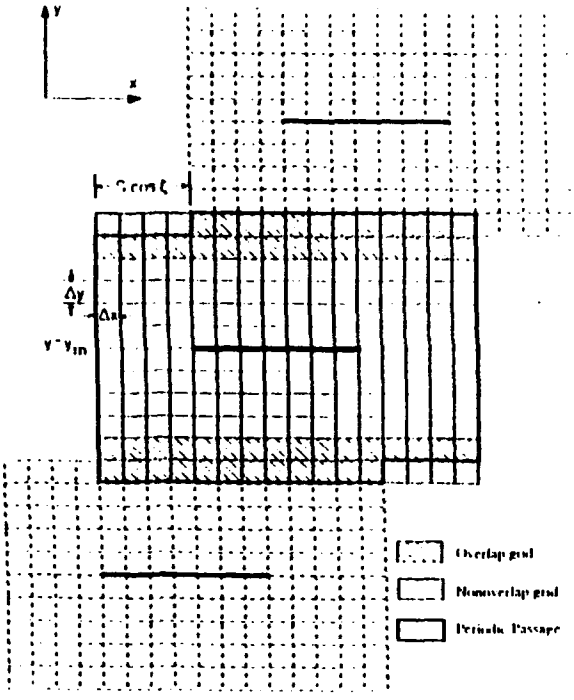

Figure 2. Computational cascade geometry

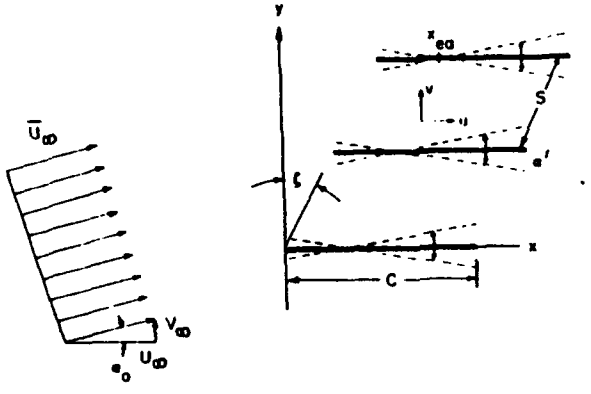

Figure 1. Flow field schematic

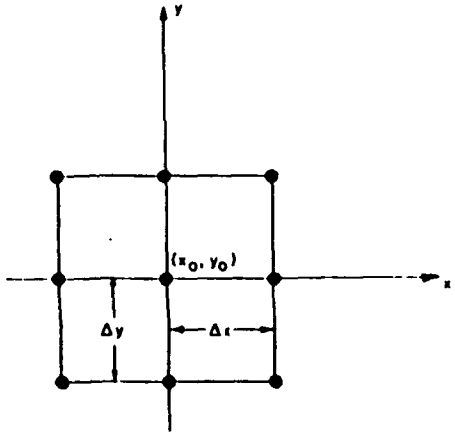

Figure 3. Computational grid element

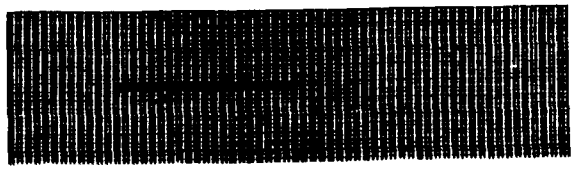

Figure 4. Computational grid

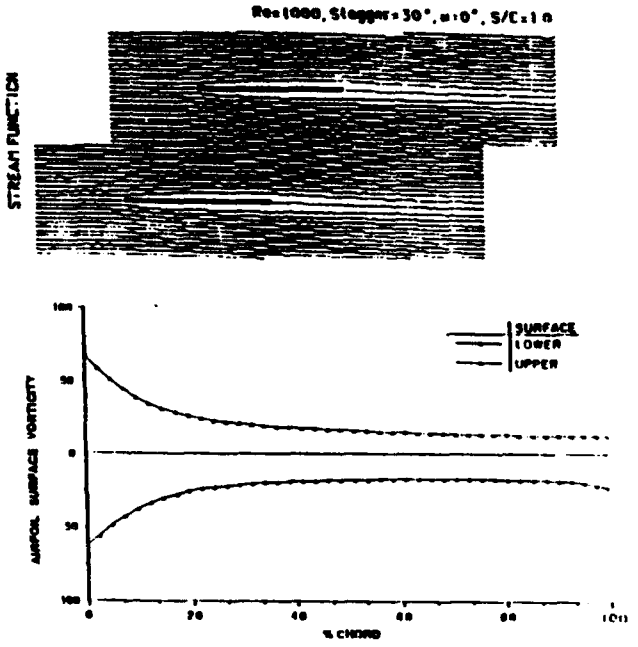

Figure 5. Cascade stream function and airfoil surface vorticity
$\zeta = 30°$, $\alpha_o = 0°$, $R_e = 1{,}000$, C/S = 1.0

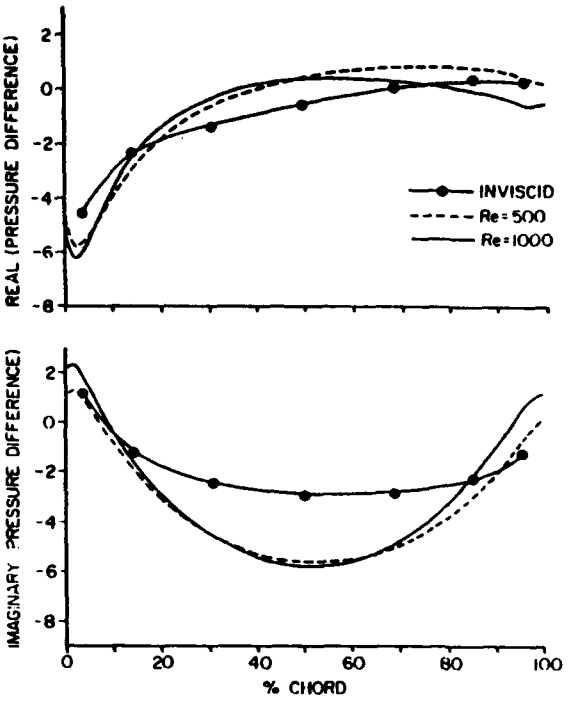

Figure 7. Unsteady pressure difference:
$k = 2.0$, $x_{ea} = 0.5$, $\alpha_o = 8°$, $\zeta = 30°$, $\beta = 0°$

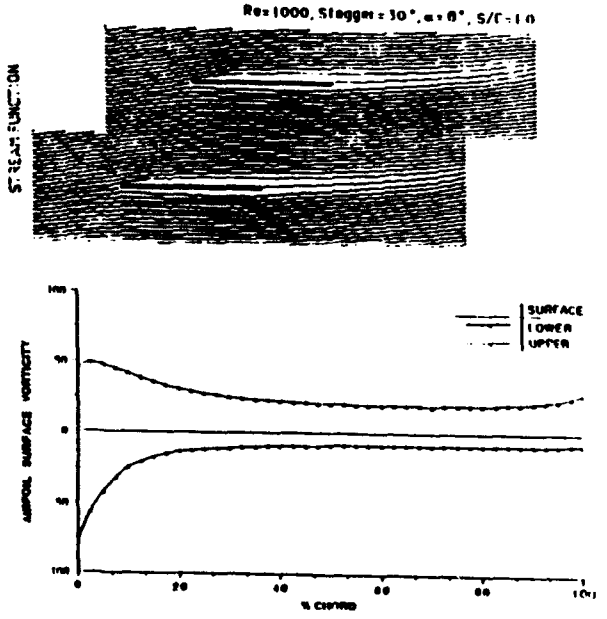

Figure 6. Cascade stream function and airfoil surface vorticity
$\zeta = 30°$, $\alpha_o = 8°$, $R_e = 1{,}000$, C/S = 1.0

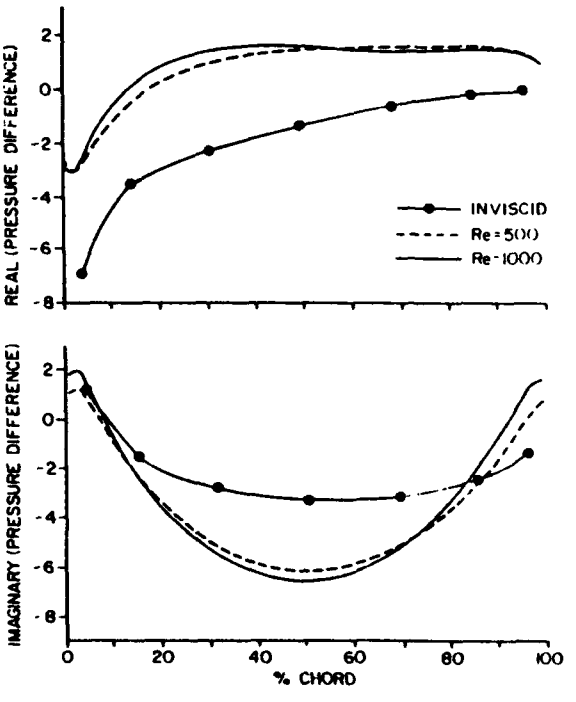

Figure 8. Unsteady pressure difference:
$k = 2.0$, $x_{ea} = 0.5$, $\alpha_o = 8°$, $\zeta = 30°$, $\beta = 90°$

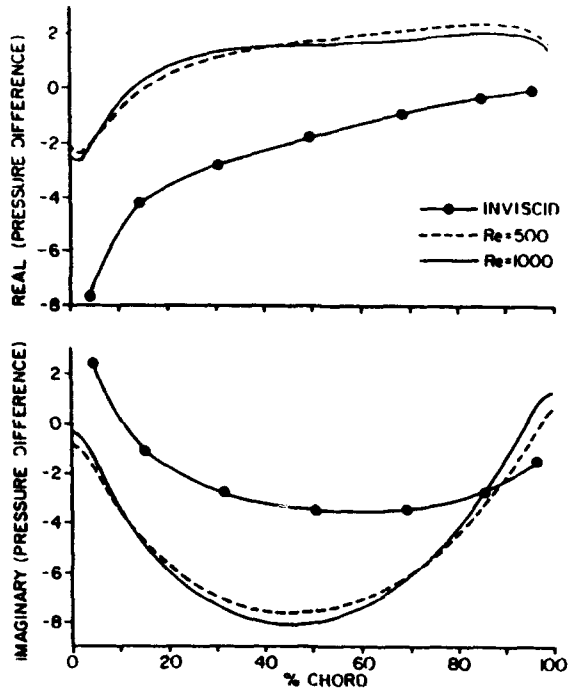

Figure 9. Unsteady pressure difference:
$k = 2.0$, $x_{ea} = 0.5$, $\alpha_o = 8°$, $\zeta = 30°$, $\beta = 180°$

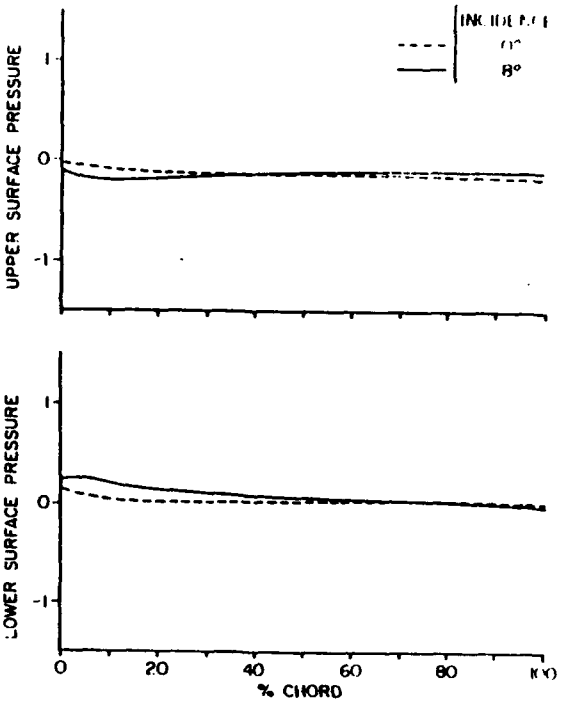

Figure 11. Steady pressure difference variation with incidence angle:
$R_e = 1{,}000$, $\zeta = 30°$

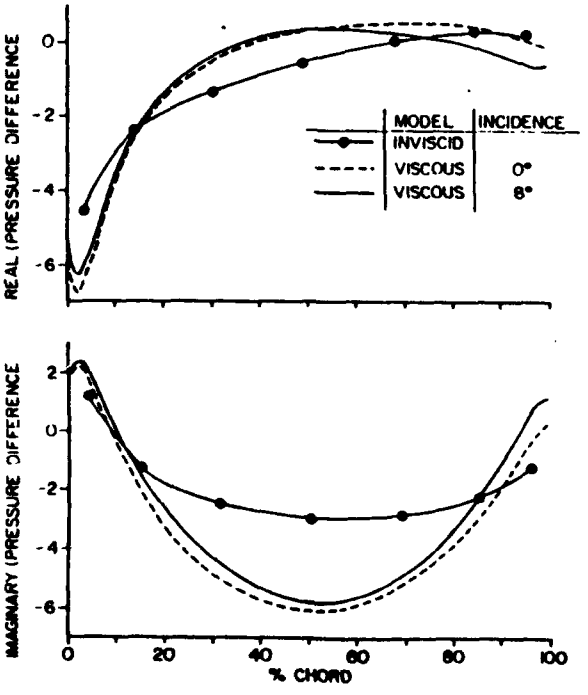

Figure 10. Unsteady pressure difference:
$R_e = 1{,}000$, $x_{ea} = 0.5$, $k = 2.0$, $\zeta = 30°$, $\beta = 0°$

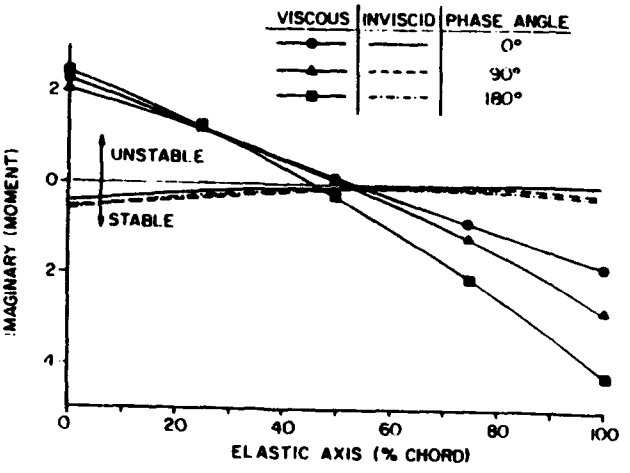

Figure 12. Imaginary moment as a function of elastic axis and interblade phase angle:
$R_e = 1{,}000$, $k = 2.0$, $\alpha_o = 0°$, $\zeta = 30°$

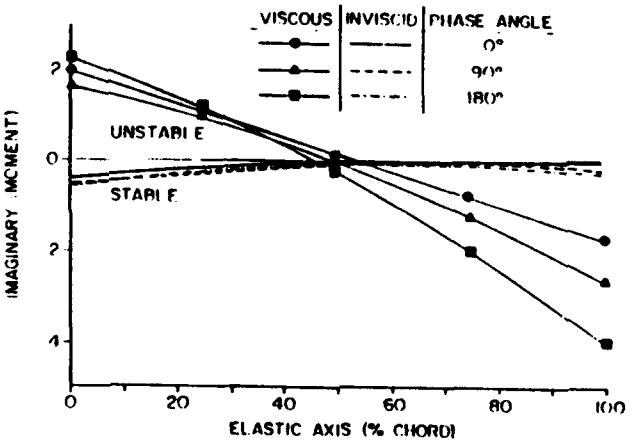

Figure 13. Imaginary moment as a function of elastic axis and interblade phase angle:
$R_c = 1{,}000$, $k = 2.0$, $\alpha_o = 8°$, $\zeta = 30°$

APPENDIX XII

Oscillating Cascade Unsteady Aerodynamics Including Separated Flow Effects

Computational Mechanics

Computational Mechanics (1991) 8, 383-398

Computational Mechanics

Oscillating cascade unsteady aerodynamics including separated flow effects

J. A. Eley and S. Fleeter
School of Mechanical Engineering, Purdue University, West Lafayette, Indiana 47907, USA

Abstract. A mathematical model is developed to predict the effect of flow separation on the unsteady aerodynamic lift and moment acting on a two-dimensional flat plate cascade which is harmonically oscillating in a subsonic flow field. The unsteady flow is considered to be a small perturbation to the uniform steady flow, with the steady flow assumed to separate at a specified fixed position on the airfoil suction surface. This formulation does not require the difference in the upwash velocity across the airfoil in the separated flow region to be determined before calculating the unsteady pressure difference across the chordline of the airfoils, thereby eliminating the assumption that the upwash difference is zero at the trailing edge when the steady flow is separated. Results obtained demonstrate that although flow separation decreases bending mode stability, it does not result in bending mode flutter. However, flow separation can result in torsion mode flutter, with this instability being a function of the location of both the separation point and the elastic axis.

List of symbols

d	nondimensional distance D/C
h	nondimensional distance H/C
k	reduced frequency, $\omega C/U_\infty$
p	perturbation pressure
u	perturbation velocity in the x direction
v	perturbation velocity in the y direction
x	nondimensional chordwise Caretesian coordinate, X/C
x_s	nondimensional separation point location measured from the leading edge
y	nondimensional normal Cartesian coordinate, Y/C
y_b	bending mode nondimensional displacement
C	airfoil chord
C_l	unsteady lift coefficient
C_M	unsteady moment coefficient
C_p	pressure difference coefficient, $\Delta p/\rho_\infty U_\infty^2$
D	distance between leading edges of adjacent airfoils as measured in the x direction
H	distance between mean positions of adjacent airfoils as measured in the Y direction
M_∞	Mach number at $x = \pm\infty$
P	fluid static pressure
P_∞	fluid static pressure at $x = \pm\infty$
S	spacing between adjacent airfoils
α	airfoil angular displacement for torsional oscillations
β	$(1 - M_\infty^2)^{1/2}$
γ	cavitation number
θ	cascade stagger angle
ν	Fourier transform variable
σ	cascade interblade phase angle
ϕ	velocity potential
ω	circular frequency

Subscripts

h	bending mode oscillation
α	torsional mode oscillation
$+$	upper surface
$-$	lower surface

Superscripts
ATT attached flow
COR correction
SEP separated flow
* Fourier transform
(¯) complex amplitude

1 Introduction

The continuing demand for more efficient axial flow compressors for gas turbine engines is being achieved by higher rotational speeds, thinner airfoils, higher pressure ratios per stage, and increased operating temperatures. As a result, the possibility of an aerodynamic blade row instability is an important design consideration. Namely, under certain conditions, a blade row operating in a completely uniform flow field can enter into a self-excited oscillation known as flutter. The motion is sustained by the extraction of energy from the uniform flow during each vibratory cycle, with the flutter frequency generally corresponding to one of the lower blade or coupled blade-disk natural frequencies.

To predict the aerodynamic stability of a rotor, a typical airfoil section approach is utilized. The three-dimensional flow field through the rotor is approximated by two-dimensional strips along the blade span. For each strip, the structural dynamic properties and the unsteady aerodynamic loading due to harmonic airfoil oscillations must be determined. Finite element techniques enable the structural and vibrational characteristics to be accurately predicted. However, accurate predictions of the flutter characteristics of the blade row cannot be made due to inadequacies in current state-of-the-art oscillating cascade models.

Unsteady aerodynamic models are typically restricted to thin airfoil theory, with the unsteady disturbances generated by the oscillating airfoils assumed to be small compared to the mean steady potential flow field. In addition, the airfoils are considered to be flat plates at zero incidence. Thus, the unsteady aerodynamics become uncoupled from the steady flow, leading to a model wherein the flow is linearized about a uniform and parallel flow. Kernel function methods can then often be utilized to determine analytical solutions for the unsteady aerodynamic lift and moment acting on the oscillating airfoils.

When the mean flow does not separate from the airfoil, i.e., unstalled flutter, a number of such unsteady aerodynamic models have been developed. For example, Whitehead (1960) developed a model for incompressible flow through an infinite cascade of oscillating flow plate airfoils by constructing a vorticity distribution on each airfoil which satisfied the boundary conditions. Fleeter (1973) extended this model to include compressible flow by using Fourier transform theory and the linearized small perturbation potential flow equation. Smith (1972) developed an analogous subsonic model by replacing the airfoils by a series of continuous singularity distributions. For both subsonic and supersonic inlet flow Mach numbers, Ni (1979) developed a corresponding kernel function analysis.

The particular problem of interest herein is subsonic stall flutter. It is the oldest, most common type of flutter and is generally attributed to separated flow on the suction surface of the airfoils caused by operating beyond some critical mean flow incidence angle at subsonic Mach numbers. Bending, torsion, and coupled vibrational modes have been documented when this type of flutter is encountered at part speed in a high speed fan and at or near the design speed in a low or high pressure compressor.

Only a very few unsteady aerodynamic models appropriate for stall flutter prediction have been developed. In these, the flow is considered to separate at a specified position on the airfoil suction surface, with this separation point fixed throughout the airfoil oscillation cycle. Also, the pressure in the separated flow region and the wake is assumed to be constant. Woods (1957) developed a model for incompressible potential flow past an isolated airfoil. An incompressible flow oscillating cascade unsteady aerodynamic model for turbomachine applications was formulated by Sisto (1967). Perumal and Sisto (1975) developed a model for incompressible flow through an infinite cascade of oscillating airfoils using conformal mapping and the acceleration potential.

More recently, Chi (1980, 1985) used Fourier transform theory and the linearized small perturbation potential flow equation to develop an oscillating airfoil and airfoil cascade model for subsonic compressible flow. This solution consists of an attached flow unsteady aerodynamic solution and a correction to account for the effects of the flow separation. This correction is determined by solving two integral equations: one for the difference in the upwash velocity across the airfoil in the separated flow region, and a second for the correction of the unsteady pressure difference across the airfoil chordline due to the separated flow. However, Chi assumes that the Kutta condition applies to the separated flow region, i.e., the upwash difference becomes zero at the airfoil trailing edge even though the flow is separated.

In this paper, an unsteady aerodynamic cascade analysis which is appropriate for the design prediction of subsonic stall flutter in turbomachines is developed. In particular, this model will predict the effect of flow separation on the unsteady lift and moment acting on a two-dimensional flat plate airfoil cascade which is harmonically oscillating in a subsonic flow field. The unsteady flow field is considered to be a small perturbation to the uniform steady flow, with the steady flow assumed to separate at a specified fixed position on the suction surface of the airfoils. In this formulation, the difference in the upwash velocity across the airfoil in the separated flow region is not required to be determined before calculating the correction of the unsteady pressure difference across the chordline of the airfoils, thereby eliminating the assumption that the upwash difference is zero at the trailing edge when the steady flow is separated.

2 Unsteady aerodynamic model

This model considers the inviscid flow past an oscillating airfoil cascade. The fluid is assumed to be a thermally and calorically perfect gas, with the subsonic flow inviscid and irrotational. The far upstream flow is uniform with velocity U_∞ and approaches the cascade at zero mean incidence angle. The steady flow is assumed to separate from a specified fixed position on the suction surfaces of the airfoils, with the constant pressure separated flow region confined to a thin slit extending to downstream infinity, Fig. 1. The unsteady aerodynamics of interest are generated by small amplitude translational or torsional oscillations of the airfoil cascade, with a constant interblade phase angle.

The linearized partial differential equation for the unsteady velocity potential, ϕ, is given in Eq. (1), with the linearized unsteady Bernoulci equation specified in Eq. (2).

$$\frac{\partial^2\phi}{\partial X^2}+\frac{\partial^2\phi}{\partial Y^2}-\frac{1}{a_\infty^2}\left(\frac{\partial^2\phi}{\partial t^2}+2U_\infty\frac{\partial^2\phi}{\partial X\,\partial t}+U_\infty^2\frac{\partial^2\phi}{\partial X^2}\right)=0, \qquad p=-\rho_\infty\left(\frac{\partial\phi}{\partial t}+U_\infty\frac{\partial\phi}{\partial X}\right). \tag{1,2}$$

Equations (1) and (2) are first used to derive the unsteady pressure difference across the airfoil for attached flow, and then to derive a correction for the flow separation using the condition that the pressure is constant in the separated flow region. As this is a linear analysis, the unsteady pressure

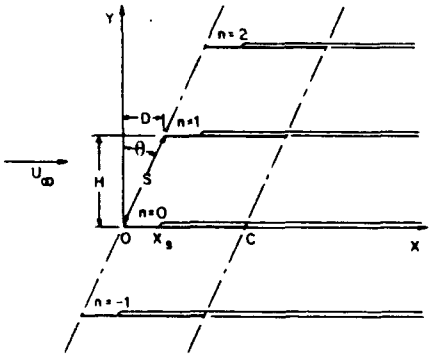

Fig. 1. Cascade and flow field configuration

and the resulting unsteady aerodynamic lift and moment acting on the airfoils are expressed as a sum of the fully attached flow solution and a correction due to the flow separation.

For the portion of the airfoil where the flow is attached, the velocity component normal to the airfoil surface, the upwash velocity, must be equal to the airfoil surface velocity. This boundary condition, Eq (3a), is satisfied at the airfoil mean position. However, in the separated flow region, the velocity component normal to the airfoil surface is not equal to the surface velocity, and therefore is unknown. This perturbation velocity must be determined using the condition that the pressure is constant in the separated flow region, with the cavitation number defined in Eq. (3b) and the separated flow region boundary condition given in Eq. (4).

$$v = \frac{dY_b}{dt} + U_\infty (X - X_{ea})\frac{d\alpha}{dt} + U_\infty \alpha \quad \text{at} \quad Y = 0^{\pm}, \quad 0 \leqq X \leqq X_s, \qquad \gamma(t) = -\frac{p}{\frac{1}{2}\rho_\infty U_\infty^2} X > X_s \tag{3a, b}$$

$$p = -\tfrac{1}{2}\rho_\infty U_\infty^2 \gamma(t) \quad \text{at} \quad Y = 0^{+}, \quad X > X_s, \tag{4}$$

where X_s specifies the separation chordwise position.

Nondimensionalizing the spatial dimensions with respect to the airfoil chord, C, assuming harmonic time dependence for the airfoil motion and the flow variables at a frequency ω and substituting these quantities into Eqs. (1, 2) and (3), results in the following for the perturbation velocity potential, the perturbation pressure, and the attached and separated flow unsteady boundary conditions.

$$\beta^2 \frac{\partial^2 \bar{\phi}}{\partial x^2} + \frac{\partial^2 \bar{\phi}}{\partial y^2} - 2ikM_\infty^2 \frac{\partial \bar{\phi}}{\partial x} + k^2 M_\infty^2 \bar{\phi} = 0, \qquad \bar{p} = -\frac{\rho_\infty U_\infty}{C}\left(ik + \frac{\partial}{\partial x}\right)\bar{\phi} \tag{5, 6}$$

$$\bar{v} = U_\infty\{\bar{q} + \bar{\alpha}(1 + ik(x - x_{ea}))\} \quad \text{at} \quad y = 0^{\pm}, \quad 0 \leqq x \leqq x_s, \quad \bar{p} = -\tfrac{1}{2}\rho_\infty U_\infty^2 \bar{\gamma} \quad \text{at} \quad y = 0^{+}, \quad x > x_s \tag{7, 8}$$

where

$$M_\infty = \frac{U_\infty}{a_\infty}; \quad \beta^2 = 1 - M_\infty^2; \quad k = \frac{\omega C}{U_\infty} \quad \text{and} \quad \bar{q} = ik\bar{y}_b.$$

Once Eq. (5) is solved, Eq. (6) is used to compute the unsteady pressure difference across the airfoil. This is then integrated to obtain the unsteady aerodynamic lift and moment acting on the airfoil.

3 Fourier transforms

Equation (5) for the perturbation velocity potential is reduced to an ordinary differential equation by use of Fourier transforms, with the Fourier transform pair defined in Eq. (9).

$$FT[g(x)] = g^*(v) = \int_{-\infty}^{+\infty} g(x)\exp(-ivx)dx \quad \text{and} \quad g(x) = \frac{1}{2\pi}\int_{-\infty}^{+\infty} g^*(v)\exp(ivx)dv. \tag{9}$$

Applying the Fourier transform technique and assuming that all flow perturbations remain bounded in the far field leads to the following ordinary differential equations for the transformed perturbation velocity potential and pressure.

$$\frac{d^2\bar{\phi}^*}{dy^2} + \mu^2 \bar{\phi}^* = 0, \qquad \bar{p}^*(v, y) = -\frac{i\rho_\infty U_\infty}{C}\{k + v\}\bar{\phi}^*(v, y) \tag{10, 11}$$

where $\mu^2 = -\beta^2 v^2 + 2kM_\infty^2 v + k^2 M_\infty^2$.

The general solution to Eq. (10) for the perturbation velocity potential is given in Eq. (12).

$$\bar{\phi}^* = A_1 \sin(\mu y) + A_2 \cos(\mu y) \tag{12}$$

The constants A_1 and A_2 are evaluated from the normal velocity boundary conditions on two adjacent airfoils. The time dependent perturbations at $(x+d, y+h)$ are taken to lead the same perturbations at (x, y) by the constant interblade phase angle σ.

The transformed boundary conditions on the upper surface of the zeroth airfoil and the lower surface of the first airfoil of Fig. 1 are given in Eqs. (13).

$$\left.\frac{\partial\bar{\phi}^*}{\partial y}\right|_{y=0^+} = C\bar{v}^*(\nu)|_{y=0^+} = C\bar{v}^*_+, \qquad \left.\frac{\partial\bar{\phi}^*}{\partial y}\right|_{y=h^-} = C\exp(i(\sigma-\nu d))\bar{v}^*(\nu)|_{y=0^-} = C\exp(i(\sigma-\nu d))\bar{v}^*_- . \tag{13a, b}$$

Equations (13) are used to solve for the constants A_1 and A_2 in Eq. (12) in terms of $\bar{v}^*_+$ and $\bar{v}^*_-$. Recall that for attached flow, both $\bar{v}^*_-$ and $\bar{v}^*_+$ are known. However, in the separated flow region, $\bar{v}^*_+$ is unknown. The resulting solution for $\bar{\phi}^*$ is given in Eq. (14),

$$\bar{\phi}^*(\nu, y) = \frac{C\bar{v}^*_+\sin(\mu y)}{\mu} + \frac{C(\bar{v}^*_+\cos(\mu h) - \bar{v}^*_-\exp(-i(\nu d-\sigma))\cos(\mu y)}{\mu\sin(\mu h)}. \tag{14}$$

This expression for $\bar{\phi}^*$ is used in the unsteady pressure equation, Eq. (11), with the following definitions useful

$$\bar{p}^*_+ \equiv \bar{p}^*|_{y=0^+}, \quad \bar{p}^*_- \equiv \bar{p}^*|_{y=0^-}, \qquad \bar{\phi}^*_+ \equiv \bar{\phi}^*|_{y=0^+}, \quad \bar{\phi}^*_- \equiv \bar{\phi}^*|_{y=0^-}. \tag{15a, b}$$

Evaluating Eq. (11) at $y = 0^+$ and 0^- and then using Eq. (14), the unsteady pressure on the upper and lower surfaces of the zeroth airfoil is determined

$$\frac{\bar{p}^*_+}{\rho_\infty U_\infty^2} = A^*\frac{\bar{v}^*_+}{U_\infty} - B^*\frac{\bar{v}^*_-}{U_\infty}, \qquad \frac{\bar{p}^*_-}{\rho_\infty U_\infty^2} = C^*\frac{\bar{v}^*_+}{U_\infty} - A^*\frac{\bar{v}^*_-}{U_\infty}, \tag{16a, b}$$

where

$$A^* = \frac{(k+\nu)\cos(\mu h)}{i\mu\sin(\mu h)} = \frac{(k+\nu)\cot(\mu h)}{i\mu};$$

$$B^* = \frac{(k+\nu)\exp(-i(\nu d-\sigma))}{i\mu\sin(\mu h)} \quad \text{and} \quad C^* = \frac{(k+\nu)\exp(i(\nu d-\sigma))}{i\mu\sin(\mu h)}.$$

Equation (16) is used to obtain independent equations for the upwash difference coefficient and the unsteady pressure difference correction coefficient. First Eq. (20) is rewritten as follows:

$$\frac{\bar{p}^{*AVE}}{\rho_\infty U_\infty^2} + \frac{1}{2}\frac{\Delta\bar{p}^*}{\rho_\infty U_\infty^2} = (A^*-B^*)\frac{\bar{v}^{*AVE}}{U_\infty} + \frac{1}{2}(A^*+B^*)\frac{\Delta\bar{v}^*}{U_\infty},$$

$$\frac{\bar{p}^{*AVE}}{\rho_\infty U_\infty^2} - \frac{1}{2}\frac{\Delta\bar{p}^*}{\rho_\infty U_\infty^2} = (A^*-C^*)\frac{\bar{v}^{*AVE}}{U_\infty} + \frac{1}{2}(A^*+C^*)\frac{\Delta\bar{v}^*}{U_\infty}. \tag{17a, b}$$

Subtracting Eq. (17b) from Eq. (17a) and manipulating the results leads to Eq. (18)

$$\frac{\bar{v}^{*AVE}}{U_\infty} = K^*\frac{\Delta\bar{p}^*}{\rho_\infty U_\infty^2} + L^*\frac{\Delta\bar{v}^*}{U_\infty}, \tag{18}$$

where

$$K^* = \frac{1}{2A^*-B^*-C^*} \quad \text{and} \quad L^* = \frac{(C^*-B^*)}{2(2A^*-B^*-C^*)}.$$

Equation (17a) is then multiplied by (A^*-C^*) and Eq. (17b) by (A^*-B^*), with the resulting equations added. This gives the following

$$\frac{\bar{p}^{*AVE}}{\rho_\infty U_\infty^2} = L^*\frac{\Delta\bar{p}^*}{\rho_\infty U_\infty^2} + M^*\frac{\Delta\bar{v}^*}{U_\infty}, \quad \text{where} \quad M^* = \frac{A^{*2}-B^*C^*}{2A^*-B^*-C^*}. \tag{19}$$

Chi (1980, 1985) performs the Fourier inversion of Eqs. (18) and (19) and further manipulates the result to obtain integral equations for $\frac{\Delta\bar{v}(x)}{U_\infty}$ and $\frac{\Delta\bar{p}^{COR}(x)}{\rho_\infty U_\infty^2}$.

However, by further manipulating Eqs. (18) and (19), independent equations may be derived for the upwash difference coefficient and the unsteady pressure difference correction coefficient. First, substitute

$$\frac{\bar{v}^{*AVE}}{U_\infty} = \frac{\bar{v}^*_-}{U_\infty} + \frac{1}{2}\frac{\Delta\bar{v}^*}{U_\infty} \quad \text{and} \quad \frac{\Delta\bar{p}^*}{\rho_\infty U_\infty^2} = \frac{\Delta\bar{p}^{*ATT}}{\rho_\infty U_\infty^2} + \frac{\Delta\bar{p}^{*COR}}{\rho_\infty U_\infty^2}$$

into Eq. (18). The result is:

$$\frac{\bar{v}^*_-}{U_\infty} + \frac{1}{2}\frac{\Delta\bar{v}^*}{U_\infty} = K^*\frac{\Delta\bar{p}^{*ATT}}{\rho_\infty U_\infty^2} + K^*\frac{\Delta\bar{p}^{*COR}}{\rho_\infty U_\infty^2} + L^*\frac{\Delta\bar{v}^*}{U_\infty}. \tag{20}$$

In the attached flow region of the airfoil, Eq. (21) is valid, with the only unknown being the attached flow unsteady pressure difference

$$\frac{\bar{v}^*_-}{U_\infty} = K^*\frac{\Delta\bar{p}^{*ATT}}{\rho_\infty U_\infty^2}. \tag{21}$$

An equation for the separated flow unsteady pressure difference correction coefficient is obtained by subtracting Eq. (21) from Eq. (20)

$$\frac{\Delta\bar{p}^{*COR}}{\rho_\infty U_\infty^2} = (A^* - C^*)\frac{\Delta\bar{v}^*}{U_\infty}. \tag{22}$$

In this equation, both the unsteady pressure difference correction coefficient and the upwash difference coefficient are unknown. Therefore, another equation is needed.

Rewriting Eq. (19) yields the following

$$\frac{\bar{p}^*_+}{\rho_\infty U_\infty^2} - \left(L^* + \frac{1}{2}\right)\frac{\Delta\bar{p}^{*ATT}}{\rho_\infty U_\infty^2} = \left(L^* + \frac{1}{2}\right)\frac{\Delta\bar{p}^{*COR}}{\rho_\infty U_\infty^2} + M^*\frac{\Delta\bar{v}^*}{U_\infty}. \tag{23}$$

Equation (22) is solved for $\Delta\bar{v}^*/U_\infty$ which is then substituted into Eq. (23). The resulting equation leads to the following independent equation for the unsteady pressure difference correction coefficient

$$K^*\frac{\Delta\bar{p}^{*COR}}{\rho_\infty U_\infty^2} = \left(T^* - \frac{1}{2}\hat{K}^*_c\right)\frac{\Delta\bar{p}^{*ATT}}{\rho_\infty U_\infty^2} + (\hat{K}^*_c - Q^*)\frac{\bar{p}^*_+}{\rho_\infty U_\infty^2}, \tag{24}$$

where

$$T^* = \frac{L^{*2}}{A^*}; \quad Q^* = \frac{L^*}{A^*}; \quad \text{and} \quad K^*_c = \frac{1}{2A^*}.$$

An equation for $\Delta\bar{v}^*/U_\infty$ is obtained by substituting Eq. (22) into Eq. (19)

$$\frac{\Delta\bar{v}^*}{U_\infty} = -(Q^* + \hat{K}^*_c)\frac{\Delta\bar{p}^{*ATT}}{\rho_\infty U_\infty^2} + 2\hat{K}^*_c\frac{\bar{p}^*_+}{\rho_\infty U_\infty^2}. \tag{25}$$

The Fourier inversion may now be performed for both the attached flow solution, Eq. (21), and the separated flow correction, Eqs. (24) and (25).

The Fourier inversion for the attached flow, Eq. (21), noting that $\frac{\Delta\bar{p}^{ATT}(\zeta)}{\rho_\infty U_\infty^2} = 0$ off of the airfoil, is given in Eq. (26),

$$\frac{\bar{v}_-(x)}{U_\infty} = \int_0^1 K(x-\zeta)\frac{\Delta\bar{p}^{ATT}(\zeta)}{\rho_\infty U_\infty^2}d\zeta; \quad \text{where} \quad K(\eta) = \frac{1}{2\pi}\int_{-\infty}^{+\infty} K^*\exp(iv\eta)dv. \tag{26}$$

Note that this is the same attached flow equation as obtained by Smith (1972) when differences in notation are taken into account.

The Fourier inversion of the separated flow equation is:

$$\int_{LL}^{+\infty} K(x-\zeta)\frac{\Delta\bar{p}^{COR}(\zeta)}{\rho_\infty U_\infty^2}d\zeta = \int_{LL}^{+\infty}\left\{T(x-\zeta)-\frac{1}{2}\hat{K}_c(x-\zeta)\right\}\frac{\Delta\bar{p}^{ATT}(\zeta)}{\rho_\infty U_\infty^2}d\zeta + \int_{LL}^{+\infty}\left\{\hat{K}_c(x-\zeta)-Q(x-\zeta)\right\}\frac{\bar{p}_+(\zeta)}{\rho_\infty U_\infty^2}d\zeta, \tag{27}$$

where

$$T(\eta)=\frac{1}{2\pi}\int_{-\infty}^{+\infty} T^*\exp(iv\eta)dv, \quad Q(\eta)=\frac{1}{2\pi}\int_{-\infty}^{+\infty} Q^*\exp(iv\eta)dv, \quad \hat{K}_c(\eta)=\frac{1}{2\pi}\int_{-\infty}^{+\infty}\hat{K}_c^*\exp(iv\eta)dv.$$

LL = Lower Limit (to be determined) and $T(\eta)$, $Q(\eta)$ and $\hat{K}_c(\eta)$ are evaluated in the Appendices.

The inverse transform of the upwash differences, Eq. (25), is

$$\frac{\Delta\bar{v}(x)}{U_\infty} = -\int_{x_s}^{1}\{Q(x-\zeta)+\hat{K}_c(x-\zeta)\}\frac{\Delta\bar{p}^{ATT}(\zeta)}{\rho_\infty U_\infty^2}d\zeta - R(x), \tag{28}$$

where $R(x)=\int_{x_s}^{+\infty}\hat{K}_c(x-\zeta)\bar{\gamma}\,d\zeta$ and is presented in the appendix.

The cascade unsteady pressure difference correction equation becomes

$$\int_{x_s}^{+\infty} K(x-\zeta)\frac{\Delta\bar{p}^{COR}(\zeta)}{\rho_\infty U_\infty^2}d\zeta = \int_{x_s}^{1}\left\{T(x-\zeta)-\frac{1}{2}\hat{K}_c(x-\zeta)\right\}\frac{\Delta\bar{p}^{ATT}(\zeta)}{\rho_\infty U_\infty^2}d\zeta - \frac{1}{2}\int_{x_s}^{\infty}\{\hat{K}_c(x-\zeta)-Q(x-\zeta)\}\bar{\gamma}\,d\zeta. \tag{29}$$

The upper limits of $+\infty$ are undesirable since $\Delta\bar{p}^{COR}(\zeta)/\rho_\infty U_\infty^2$ will be obtained by collocation. To eliminate this problem, this equation is rewritten by breaking the first and third integrals into integrals from $\zeta = x_s$ to $\zeta = 1$ and from $\zeta = 1$ to $\zeta = +\infty$

$$\begin{aligned}&\int_{x_s}^{1} K(x-\zeta)\frac{\Delta\bar{p}^{COR}(\zeta)}{\rho_\infty U_\infty^2}d\zeta + \int_{1}^{+\infty} K(x-\zeta)\frac{\Delta\bar{p}^{COR}(\zeta)}{\rho_\infty U_\infty^2}d\zeta\\ &= \int_{x_s}^{1}\left\{T(x-\zeta)-\frac{1}{2}\hat{K}_c(x-\zeta)\right\}\frac{\Delta\bar{p}^{ATT}(\zeta)}{\rho_\infty U_\infty^2}d\zeta - \frac{1}{2}\int_{x_s}^{1}\{\hat{K}_c(x-\zeta)-Q(x-\zeta)\}\bar{\gamma}d\zeta\\ &\quad -\frac{1}{2}\int_{x_s}^{\infty}\{\hat{K}_c(x-\zeta)-Q(x-\zeta)\}\bar{\gamma}\,d\zeta.\end{aligned} \tag{30}$$

As $x_s \to 1$, the integrals with upper limit of 1 become zero. Then

$$\int_{1}^{+\infty} K(x-\zeta)\frac{\Delta\bar{p}^{COR}(\zeta)}{\rho_\infty U_\infty^2}d\zeta = -\frac{1}{2}\int_{1}^{+\infty}\{\hat{K}_c(x-\zeta)-Q(x-\zeta)\}\bar{\gamma}\,d\zeta.$$

Since both of these integrals are independent of x_s, they must be equal for all x_s. Subtracting these from Eq. (30), the final cascade separated flow unsteady pressure difference correction equation is obtained

$$W(x)=\int_{x_s}^{1} K(x-\zeta)\frac{\Delta\bar{p}^{COR}(\zeta)}{\rho_\infty U_\infty^2}d\zeta, \tag{31}$$

where

$$W(x)=\int_{x_s}^{1}\left\{T(x-\zeta)-\frac{1}{2}\hat{K}_c(x-\zeta)\right\}\frac{\Delta\bar{p}^{ATT}(\zeta)}{\rho_\infty U_\infty^2}d\zeta - \frac{1}{2}\int_{x_s}^{1}\{\hat{K}_c(x-\zeta)-Q(x-\zeta)\}\bar{\gamma}\,d\zeta.$$

Once the attached flow solution is determined from Eq. (26) and the cavitation number specified, Eq. (31) is solved by collocation to obtain the separated flow unsteady pressure difference correction coefficient.

4 Unsteady aerodynamic lift and moment coefficients

The unsteady lift coefficient, positive in the $+y$ direction, is defined as

$$\bar{C}_L = \frac{\bar{L}}{\rho_\infty U_\infty^2 C} = -\int_0^1 \frac{\Delta\bar{p}(\zeta)}{\rho_\infty U_\infty^2} d\zeta. \tag{35}$$

Substituting Eq. (36) into Eq. (35) and noting that the unsteady pressure difference correction is zero upstream of the separation point, leads to Eq. (37):

$$\frac{\Delta\bar{p}(\zeta)}{\rho_\infty U_\infty^2} = \frac{\Delta\bar{p}^{ATT}(\zeta)}{\rho_\infty U_\infty^2} + \frac{\Delta\bar{p}^{COR}(\zeta)}{\rho_\infty U_\infty^2} \tag{36}$$

$$\bar{C}_L^{SEP} = \bar{C}_L^{ATT} + \bar{C}_L^{COR}, \quad \text{where} \quad \bar{C}_L^{ATT} = -\int_0^1 \frac{\Delta\bar{p}^{ATT}(\zeta)}{\rho_\infty U_\infty^2} d\zeta \quad \text{and} \quad \bar{C}_L^{COR} = -\int_{x_s}^1 \frac{\Delta\bar{p}^{COR}(\zeta)}{\rho_\infty U_\infty^2} d\zeta. \tag{37}$$

The unsteady moment coefficient, positive counterclockwise about an elastic axis at the leading edge, is defined as

$$\bar{C}_M = \frac{\bar{M}}{\rho_\infty U_\infty^2 C^2} = -\int_0^1 \zeta \frac{\Delta\bar{p}(\zeta)}{\rho_\infty U_\infty^2} d\zeta. \tag{38}$$

Substituting Eq. (36) into Eq. (38) yields:

$$\bar{C}_M^{SEP} = \bar{C}_M^{ATT} + \bar{C}_M^{COR}, \quad \text{where} \quad \bar{C}_M^{ATT} = -\int_0^1 \zeta \frac{\Delta\bar{p}^{ATT}(\zeta)}{\rho_\infty U_\infty^2} d\zeta \quad \text{and} \quad \bar{C}_M^{COR} = -\int_{x_s}^1 \zeta \frac{\Delta\bar{p}^{COR}(\zeta)}{\rho_\infty U_\infty^2} d\zeta. \tag{39}$$

5 Results

The mathematical model developed herein is utilized to demonstrate the effects of flow separation on the unsteady aerodynamics of an harmonically oscillating flat plate cascade in a subsonic flow field. The attached flow part of the model predictions are obtained from the Smith code (1987). It predicts the unsteady pressure difference coefficient and the cascade translation and torsion mode unsteady aerodynamic lift and moment coefficients. The separated flow part of the model uses the attached flow results to analyze the separated flow unsteady pressure difference correction coefficient, the unsteady aerodynamic lift and moment correction coefficients, and the upwash difference coefficient for a specified separation point location and cavitation number. Note that for the results presented herein, a zero cavitation number is considered. The separated flow unsteady aerodynamic lift and moment coefficients are then added to the attached flow values to obtain the separated flow coefficients.

The effect of flow separation on the magnitude and phase of the cascade bending mode unsteady pressure difference coefficient is shown in Figs. 2 and 3. A leading edge flow separation point decreases the magnitude of C_{pb} by a factor of approximately two. Also, the attached and separated flow phase angles of C_{pb} are not equal.

Figure 4 shows the magnitude of the bending mode upwash difference coefficient with leading edge flow separation for an isolated airfoil and an airfoil cascade. Recall that the upwash difference coefficient is zero for attached flow. Note that the upwash difference coefficient is not zero downstream of the trailing edge for either the isolated airfoil or the cascade, as was assumed by Chi (1980, 1985). The fact that a nonzero constant value is approached downstream of the trailing

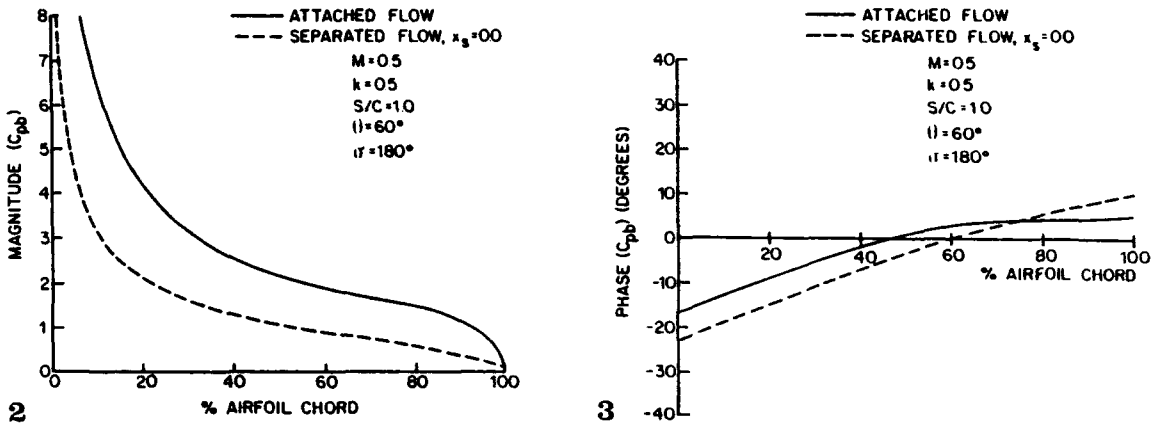

Figs. 2 and 3. 2 Magnitude of bending mode unsteady pressure difference coefficient for attached flow and leading edge separation. 3 Phase angle of bending mode unsteady pressure difference coefficient for attached flow and leading edge separation

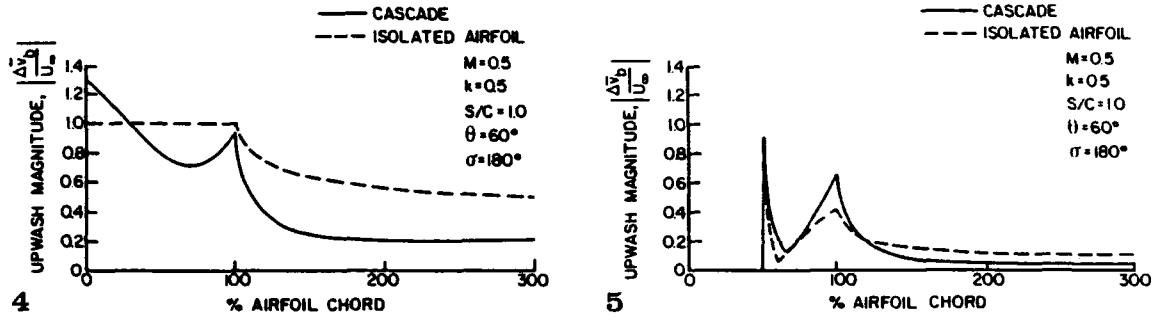

Figs. 4 and 5. Magnitude of bending mode upwash difference coefficient 4 for leading edge flow separation; 5 for midchord flow separation

edge is consistent with the assumption that the separation wake extends to downstream infinity. Midchord flow separation, Fig. 5, tends to produce a more rapidly changing upwash difference coefficient magnitude than does leading edge separation. Again, the upwash difference coefficient does not become zero downstream of the trailing edge. Also, the separated flow upwash difference magnitude for both the isolated airfoil and the cascade exhibit a sharp dip near 60% chord. Both the real and imaginary parts of the upwash difference coefficient are smooth in the region of 60% airfoil chord, with this dip being caused by the real part of the coefficient passing through zero at this point.

The effects of leading edge flow separation on the bending mode suction surface upwash velocity distribution are shown in Figs. 6 and 7 for an isolated airfoil and an airfoil cascade. The attached flow results are the same for both the isolated airfoil and the cascade since both upwash velocities are equal to the airfoil surface velocity. The cascading effects are shown by the differences between the isolated airfoil and cascade separated flow upwash distributions. In Fig. 7 the separated flow curve for the isolated airfoil is identical to the attached flow curve.

To demonstrate the effects of flow separation on bending mode stability, the complex unsteady lift coefficients are calculated using ten collocation points for a cascade with solidity of one and a stagger angle of 60 degrees. In particular, Figs. 8 through 13 show the attached flow, midchord flow separation, and leading edge flow separation complex bending mode lift coefficients for inlet Mach numbers of 0.0 and 0.5, with interblade phase angle and reduced frequency as parameters. It should be noted that the Mach 0.5 unsteady lift coefficients change rapidly near the acoustic resonance conditions. Thus a smaller range of interblade phase angle values is considered for Mach

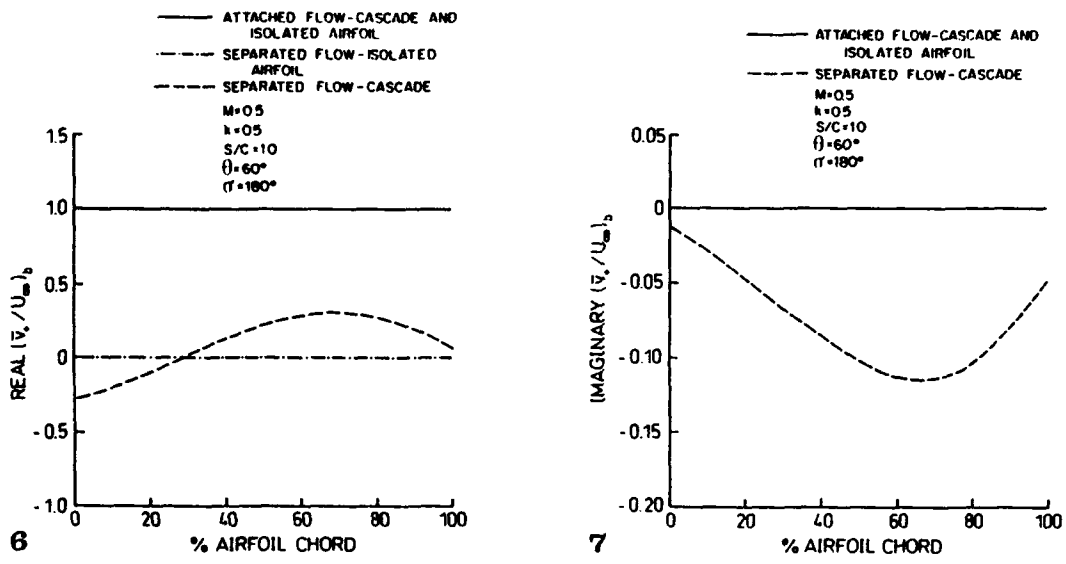

Figs. 6 and 7. 6 Real part of bending mode suction surface upwash velocity for attached flow and leading edge separation. 7 Imaginary part of bending mode suction surface upwash velocity for attached flow and leading edge separation

0.5 than for Mach 0.0 to avoid these resonances. Also, a positive value of the real part of $\bar{C}_{Lb}$ indicates a bending mode instability when there is no mechanical damping.

With attached flow, the cascade is stable for all interblade phase angles and reduced frequencies for both values of the inlet Mach number. As the region of flow separation increases, i.e., as the separation point moves from the midchord to the leading edge, the unsteady lift coefficient reduced frequency contours decrease in size and shift to the right, although remaining in the stable range. Thus, flow separation, although not resulting in bending mode flutter, does decrease the bending mode stability of the cascade.

For the case of torsional flutter, stability is determined from the imaginary part of the unsteady moment coefficient. In particular, for zero mechanical damping, a torsion mode instability exists whenever Imaginary $(\bar{C}_{M\alpha}) \geqq 0.0$, with the flutter reduced frequency defined as the value at which Imaginary $(\bar{C}_{M\alpha}) = 0.0$. To demonstrate the effects of flow separation on torsion mode stability, a baseline cascade with a solidity of one and a stagger angle of 60 degrees is considered.

The baseline cascade with attached flow is unstable for certain interblade phase angle values and elastic axis locations. The flutter boundary interblade phase angle, i.e., the interblade phase angle which yields the largest range of reduced frequencies for which flutter is possible is shown as a function of elastic axis location in Fig. 14 for inlet Mach numbers of 0.0, 0.3, and 0.8. Utilizing these interblade phase angle values, Fig. 15 shows the attached flow flutter boundaries of the baseline cascade in the form of reduced frequency for flutter as a function of elastic axis location, with Mach number as a parameter. Each curve represents the neutral stability boundary, with the airfoils being unstable at reduced frequencies below the curve and stable for reduced frequencies above the curve. Note that a decreasing flutter reduced frequency corresponds to an increasing value of U_∞ for which flutter is just possible. Increasing the Mach number is seen to enhance the cascade stability, indicated by the decreased unstable reduced frequency range.

The effects of flow separation on torsional flutter are demonstrated by determining the flutter boundaries of the baseline cascade with attached flow and with flow separation at midchord, 10% chord, and at the leading edge. These results, generated by varying the reduced frequency and utilizing the previously determined attached flow flutter boundary interblade phase angle values, are presented in the form of torsional flutter boundary versus elastic axis location for inlet Mach numbers of 0.0, 0.3, and 0.8, with separation point location as a parameter, Figs. 16 through 18.

Torsion mode stability is seen to be a function of the location of both the separation point and the elastic axis. Midchord flow separation produces a larger range of frequencies for which flutter

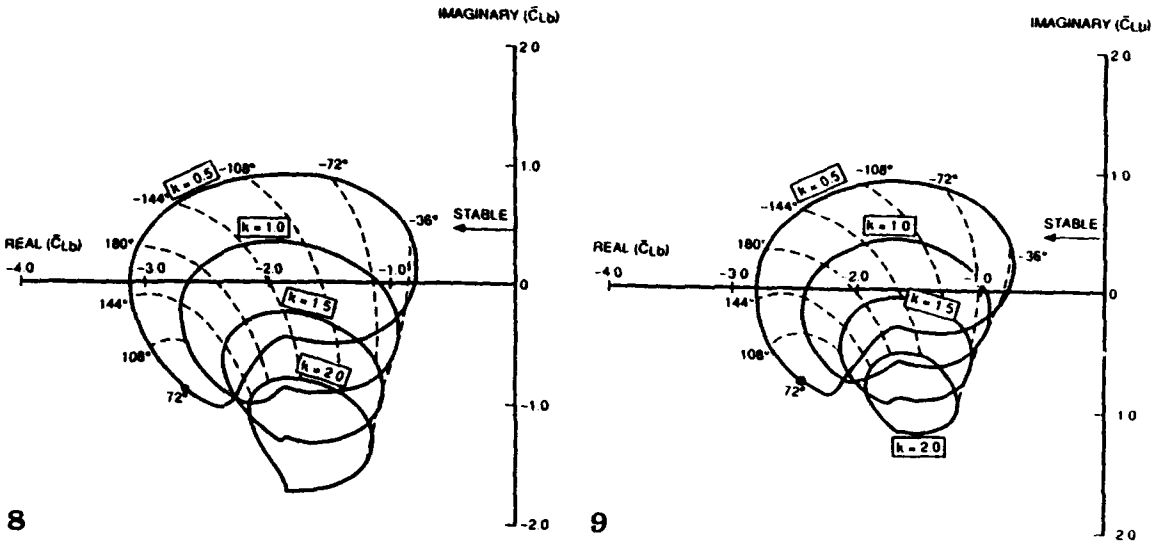

Figs. 8 and 9. Bending mode unsteady lift coefficient **8** for attached flow; **9** for midchord flow separation. ($S/C = 1.0$, $\theta = 60$ degrees, and $M = 0.0$)

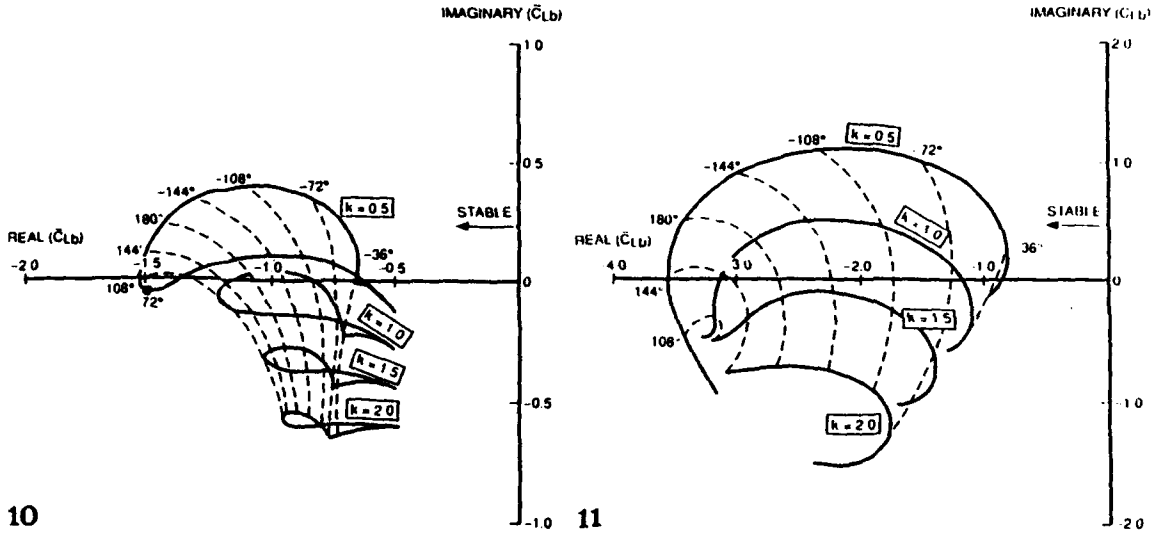

Figs. 10 and 11. Bending mode unsteady lift coefficient **10** for leading edge flow separation ($S/C = 1.0$, $\theta = 60$ degrees, and $M = 0.0$); **11** for attached flow ($S/C = 1.0$, $\theta = 60$ degrees, and $M = 0.5$)

may occur than does attached flow for elastic axis locations in the range of 20% to about 65% chord for all Mach numbers. This indicates decreased cascade stability for these elastic axis locations. For elastic axis locations aft of about 65% chord, midchord flow separation tends to have a stabilizing effect for all Mach numbers.

Flow separation at 10% airfoil chord has a destabilizing effect for elastic axis locations from 20% to about 40% chord, and a stabilizing effect for elastic axis locations greater than about 40% chord.

Leading edge flow separation has a stabilizing effect for all elastic axis locations. It should be noted that a considerable part of the torsional unsteady moment coefficient value is derived from the singular nature of the unsteady pressure distribution in the airfoil leading edge region. For the cases of flow separation of 10% and 50% chord, the unsteady pressure distribution is unaffected

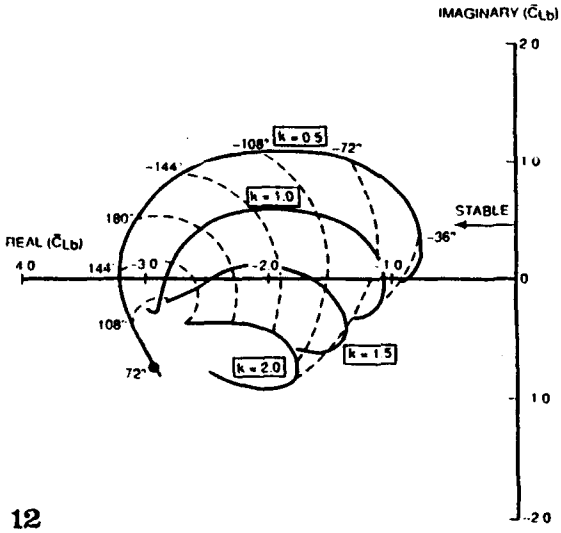

12

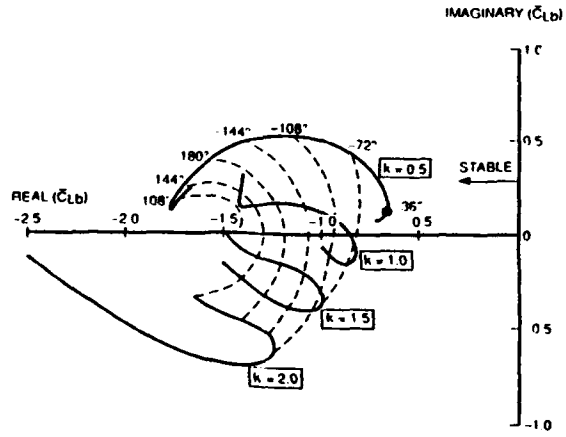

13

Figs. 12 and 13. Bending mode unsteady lift coefficient 12 for midchord flow separation, 13 for leading edge separation. ($S/C = 1.0$, $\theta = 60$ degrees, and $M = 0.5$)

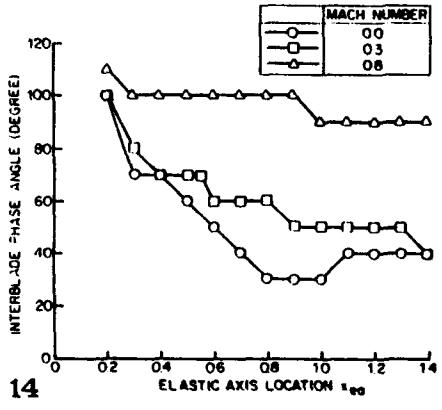

14

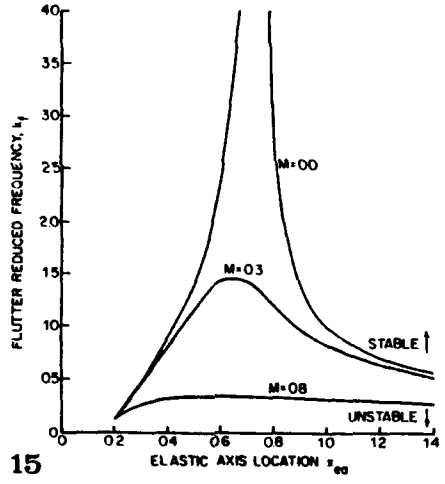

15

Figs. 14 and 15. 14 Interblade phase angles for torsional flutter boundary, 15 torsional flutter boundary for attached flow. ($S/C = 1.0$ and $\theta = 60$ degrees)

by the flow separation in the region near the leading edge, whereas for leading edge flow separation the entire unsteady pressure distribution is affected.

As for the attached flow flutter boundaries, increasing the Mach number enhances the separated flow cascade stability, indicated by the decreased unstable reduced frequency range.

It is generally expected that flow separation would decrease the torsion mode cascade stability. As previously stated, the results obtained from the separated flow analysis developed herein indicate that the stability is a function of the location of both the separation point and the elastic axis. However, it should be noted that this analysis is based on quite restrictive assumptions. A zero mean incidence angle is considered, thereby eliminating the nonlinear features of the attached and separated flow fields. Also, the separation point location is fixed throughout the cycle of airfoil oscillation. In reality, the flow may separate and reattach during each cycle of airfoil motion

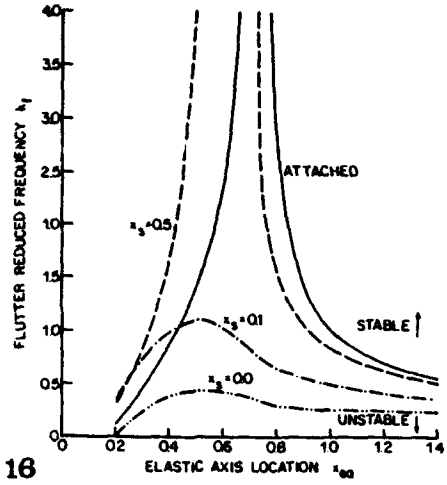

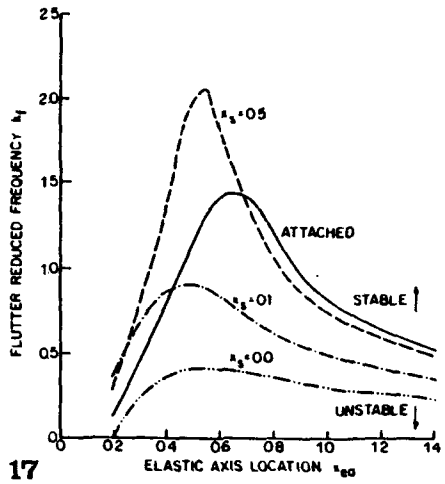

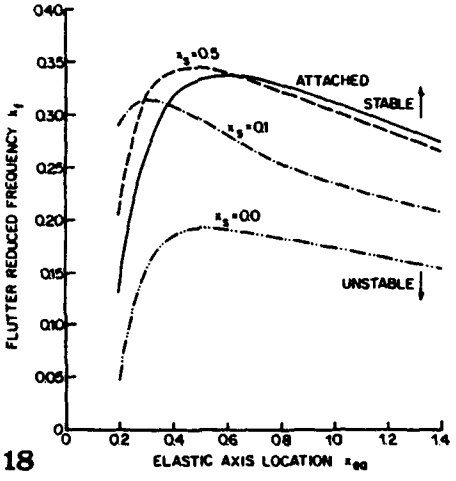

Figs. 16–18. Torsional flutter boundary for separated flow. ($S/C = 1.0$, $\theta = 60$ degrees, and **16** $M = 0.0$; **17** $M = 0.3$; **18** $M = 0.8$

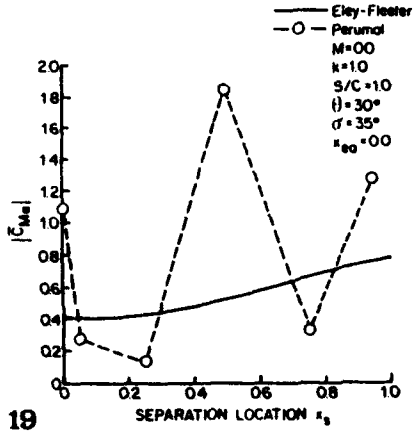

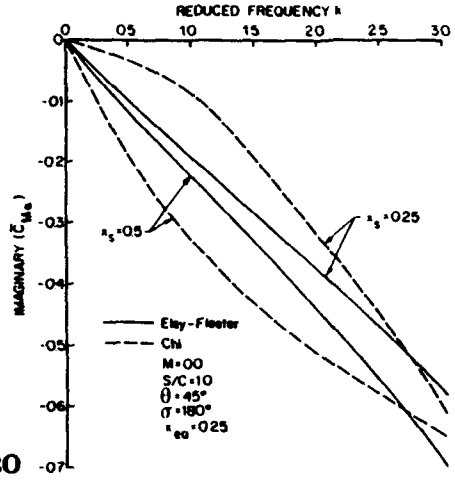

Figs. 19 and 20. **19** Torsion mode unsteady moment coefficient magnitude, comparison to Perumal. **20** Imaginary torsional mode unsteady moment coefficient, comparison to Chi

creating hysteresis effects in the torsional unsteady moment coefficient. Finally, the separation region may be large and partially block the flow passage, thereby affecting the flow field upstream of the separation point. If these restrictions were removed from the model, it might be found that flow separation tends to always decrease cascade stability.

Finally, comparisons of the results obtained with the model developed herein and those developed by Perumal (1975) and Chi (1980, 1985) are considered for an airfoil cascade executing harmonic torsion mode oscillations in an incompressible flow. The comparison with the Perumal model predictions of the magnitude of the unsteady moment coefficient versus separation point location are shown in Fig. 19. The analysis developed herein predicts a smoothly varying moment coefficient with separation point location, as expected based on the model assumptions. In contrast, the Perumal model yields widely varying and probably unrealistic results. Fig.20 shows a comparison of the results obtained with the model developed herein and that of Chi with flow separation at 25% and 50% airfoil chord. The Chi model predicts larger changes in the imaginary part of the moment coefficient as the separation point location is moved from 25% to 50% airfoil chord than does the present anlysis.

6 Summary and conclusions

A mathematical model was developed to predict the effect of flow separation on the unsteady aerodynamic lift and moment acting on two-dimensional flat plate airfoils and cascades which are harmonically oscillating in a subsonic flow field. The unsteady flow was considered to be a small perturbation to the uniform steady flow, with the steady flow assumed to separate at a specified fixed position on the suction surface of the airfoils. In this formulation, the difference in the upwash velocity across the airfoil in the separated flow region was not required to be determined before calculating the unsteady pressure difference across the chordline of the airfoils, thereby eliminating the assumption that the upwash difference is zero at the trailing edge when the steady flow is separated.

This model was then used to investigate the effect of flow separation on bending and torsion mode cascade stability. In the bending mode, the effects of airfoil leading edge and midchord flow separation on the unsteady aerodynamic lift coefficient for several reduced frequency and interblade phase angle values were considered for inlet Mach numbers of 0.0 and 0.5. In the torsion mode, the effects of airfoil leading edge, 10% and 50% chord flow separation on the cascade flutter boundary as a function of the elastic axis location were considered for inlet Mach numbers of 0.0, 0.3, and 0.8. These results demonstrated that although flow separation does decrease the bending mode stability, it does not result in flutter. In the torsion mode, however, flow separation can lead to flutter, with the cascade torsional stability being a function of both the location of the separation point and the elastic axis.

Acknowledgements

This research was sponsored, in part, by the Air Force Office of Scientific Research.

Appendix A

The functions $T(x)$, $Q(x)$ and $\hat{K}_c(x)$ are evaluated by the residue theorem of complex variables. These functions are given in Eqs. (A1) through (A3).

$$T(x) = \frac{\exp\left\{\dfrac{ikM_\infty^2 x}{\beta^2}\right\}}{4h}\left\{\frac{(1+\operatorname{sgn}(x))}{2}\Omega(x) + \operatorname{sgn}(x)\sum_{m=1}^{\infty}\Psi_m(x) + \operatorname{sgn}(x)\sum_{n=0,\pm1,\pm2,\ldots}\Gamma_n(x)\right\} \quad \text{(A1)}$$

$$Q(x) = -\frac{i\exp\left\{\frac{ikM_\infty^2 x}{\beta^2}\right\}}{2h}\left\{\frac{(1+\mathrm{sgn}(x))}{2}\Omega(x) + \mathrm{sgn}(x)\sum_{m=1}^{\infty}\Psi_m(x) + \mathrm{sgn}(x)\sum_{n=0,\pm1,\pm2,\ldots}\Gamma_n(x)\right\} \tag{A2}$$

$$\hat{K}_c(x) = -\frac{\exp\left\{\frac{ikM_\infty^2 x}{\beta^2}\right\}}{2h}\left\{\frac{1+\mathrm{sgn}(x)}{2}\Omega(x) + \mathrm{sgn}(x)\sum_{m=1}^{\infty}\Psi_m(x)\right\} \tag{A3}$$

where

$$\Omega(x) = -\frac{hk\tanh(hk)\sin^2(\hat{z}_0 d-\hat{\sigma})e^{i\hat{z}_0 x}}{\{\cosh(hk)-\cos(\hat{z}_0 d-\hat{\sigma})\}^2}, \quad \Psi_m(x) = \frac{(\mu_m h)^2\tan^2(z_m d-\hat{\sigma})e^{iz_m x}}{h^2\beta^2 z_m\left(z_m+\frac{k}{\beta^2}\right)}$$

$$\Gamma_n(x) = \frac{\{(i\bar{\mu}_n hx+\Theta_n)\tan(\bar{\mu}_n h)+(2d+\Theta_n)\bar{\mu}_n h\}e^{i\bar{z}_n x}}{(d-\Theta_n)^2\left(\bar{z}_n+\frac{k}{\beta^2}\right)} - \frac{\bar{\mu}_n h g(\bar{z}_n)e^{i\bar{z}_n x}}{(d-\Theta_n)^3\left(\bar{z}_n+\frac{k}{\beta^2}\right)^2}$$

$$g(\bar{z}_n) = \left\{\left(\bar{z}_n+\frac{k}{\beta^2}\right)((d^2-\Theta_n^2)-\Lambda_n\tan(\bar{\mu}_n h)-\Theta_n(d-\Theta_n)\tan^2(\bar{\mu}_n h))+(d-\Theta_n)\tan(\bar{\mu}_n h)\right\}$$

$$\hat{z}_0 = -\frac{k}{\beta^2}, \quad \hat{\sigma} = \sigma - \frac{kM_\infty^2 d}{\beta^2}, \quad \mu_m h = \frac{(2m-1)\pi}{2}, \quad m=1,2,3,\ldots, \quad z_m = \frac{i\,\mathrm{sgn}(x)P_m}{\beta h}, \quad m=1,2,3,\ldots$$

$$P_m = \left\{\left(\frac{(2m-1)\pi}{2}\right)^2 - \left(\frac{kM_\infty h}{\beta}\right)^2\right\}^{1/2}, \quad \Theta_n = \left.\frac{d\mu h}{dz}\right|_{z=\bar{z}_n} \quad \Lambda_n = \left.\frac{d^2\mu h}{dz^2}\right|_{z=\bar{z}_n} \quad \bar{\mu}_n h = \bar{z}_n d + (2n\pi-\sigma),$$
$$n=0,\pm1,+2,\ldots$$

Note that:

$$\hat{K}_c^* = \frac{1}{2A^*} \quad \text{and} \quad K^* = \frac{1}{2A^*-B^*-C^*} = \frac{1}{2A^*-(B^*+C^*)}.$$

For zero stagger angle and ninety degree interblade phase angle $(B^*+C^*)=0$ so that $K^*=\hat{K}_c^*$. The function $\hat{K}_c(x)$ is found to give identical values, to six digits right of the decimal point, to Smith's function $K(x)$ evaluated at the special case just described.

Appendix B

The function $R(x)$ is obtained by evaluating Eq. (B1) by analytical integration, Eq. (B2).

$$R(x) = \int_{x_s}^{+\infty}\hat{K}_c(x-\zeta)\bar{\gamma}\,d\zeta. \tag{B1}$$

$$R(x) = \bar{\gamma}\left[\sum_{m=1}^{\infty}\left\{\frac{f_m}{a_m}+\frac{g_m}{b_m}(e^{b_m(x-x_s)}-1)\right\}+\frac{i\tanh(hk)}{2}\{e^{-ik(x-x_s)}-1\}\right], \tag{B2}$$

where

$$f_m = -\frac{(\mu_m h)^2}{2hP_m\left(P_m+\frac{ihk}{\beta}\right)},$$

$$a_m = \left(\frac{P_m}{\beta h} + \frac{ikM_\infty^2}{\beta^2}\right), \quad g_m = -\frac{(\mu_m h)^2}{2hP_m\left(P_m - \frac{ihk}{\beta}\right)}, \quad b_m = \left(-\frac{P_m}{\beta h} + \frac{ikM_\infty^2}{\beta^2}\right),$$

$$P_m = \left\{\left(\frac{(2m-1)\pi}{2}\right)^2 - \left(\frac{kM_\infty h}{\beta}\right)^2\right\}^{1/2}; \quad \mu_m h = \frac{(2m-1)\pi}{2}, \quad m = 1, 2, 3, \ldots$$

References

Chi, M. R. (1980): Unsteady Aerodynamics in Stalled Cascade and Stall Flutter Prediction. ASME Paper 80-C2/Aero-1

Chi, M. R. (1985): Separated Flow Unsteady Aerodynamic Theory. J. Aircraft 22/11, 956–964

Fleeter, S. (1973): Fluctuating Lift and Moment Coefficients for Cascaded Airfoils in a Nonuniform Compressible Flow. J. Aircraft 10/2, 93–98

Ni, R. H. (1979): A Rational Analysis of Periodic Flow Perturbation in Supersonic Two-Dimensional Cascade. ASME J. Eng. for Power. 101/3, 431–439

Perumal, P. V. K. (1975): Thin Airfoil in Eddy-Array and Part-Stalled Oscillating Cascade. Ph.D. Thesis, Stevens Inst. of Technol.

Sisto, F. (1967): Linearized Theory of Nonstationary Cascades at Fully Stalled or Supercavitated Conditions. ZAMM, 47, 531–541

Smith, S. N. (1972): Discrete Frequency Sound Generation in Axial Flow Turbomachines. ARCR & M 3709

Whitehead, D. S. (1960): Force and Moment Coefficients for Vibrating Airfoils in Cascade. ARCR & M 3254

Whitehead, D. S. (1987): Classical Two-Dimensional Methods. AGARD Manual in Aeroelasticity in Axial Flow Turbomachines. AGARD AG 298

Woods, L. C. (1957): Aerodynamic Forces on an Oscillating Airfoil Fitted With a Spoiler. Proc. Roy. Soc. London, Series A, 239, 328–337

Communicated by S. N. Atluri, May 15, 1991

GENERAL INSTRUCTIONS FOR COMPLETING SF 298

The Report Documentation Page (RDP) is used in announcing and cataloging reports. It is important that this information be consistent with the rest of the report, particularly the cover and title page. Instructions for filling in each block of the form follow. It is important to ***stay within the lines*** to meet ***optical scanning requirements***.

Block 1. Agency Use Only *(Leave blank)*.

Block 2. Report Date. Full publication date including day, month, and year, if available (e.g. 1 Jan 88). Must cite at least the year.

Block 3. Type of Report and Dates Covered. State whether report is interim, final, etc. If applicable, enter inclusive report dates (e.g. 10 Jun 87 - 30 Jun 88).

Block 4. Title and Subtitle. A title is taken from the part of the report that provides the most meaningful and complete information. When a report is prepared in more than one volume, repeat the primary title, add volume number, and include subtitle for the specific volume. On classified documents enter the title classification in parentheses.

Block 5. Funding Numbers. To include contract and grant numbers; may include program element number(s), project number(s), task number(s), and work unit number(s). Use the following labels:

C	- Contract	**PR**	- Project
G	- Grant	**TA**	- Task
PE	- Program Element	**WU**	- Work Unit Accession No.

Block 6. Author(s). Name(s) of person(s) responsible for writing the report, performing the research, or credited with the content of the report. If editor or compiler, this should follow the name(s).

Block 7. Performing Organization Name(s) and Address(es). Self-explanatory.

Block 8. Performing Organization Report Number. Enter the unique alphanumeric report number(s) assigned by the organization performing the report.

Block 9. Sponsoring/Monitoring Agency Name(s) and Address(es). Self-explanatory.

Block 10. Sponsoring/Monitoring Agency Report Number. *(If known)*

Block 11. Supplementary Notes. Enter information not included elsewhere such as: Prepared in cooperation with...; Trans. of...; To be published in.... When a report is revised, include a statement whether the new report supersedes or supplements the older report.

Block 12a. Distribution/Availability Statement. Denotes public availability or limitations. Cite any availability to the public. Enter additional limitations or special markings in all capitals (e.g. NOFORN, REL, ITAR).

- **DOD** - See DoDD 5230.24, "Distribution Statements on Technical Documents."
- **DOE** - See authorities.
- **NASA** - See Handbook NHB 2200.2.
- **NTIS** - Leave blank.

Block 12b. Distribution Code.

- **DOD** - Leave blank.
- **DOE** - Enter DOE distribution categories from the Standard Distribution for Unclassified Scientific and Technical Reports.
- **NASA** - Leave blank.
- **NTIS** - Leave blank.

Block 13. Abstract. Include a brief *(Maximum 200 words)* factual summary of the most significant information contained in the report.

Block 14. Subject Terms. Keywords or phrases identifying major subjects in the report.

Block 15. Number of Pages. Enter the total number of pages.

Block 16. Price Code. Enter appropriate price code *(NTIS only)*.

Blocks 17. - 19. Security Classifications. Self-explanatory. Enter U.S. Security Classification in accordance with U.S. Security Regulations (i.e., UNCLASSIFIED). If form contains classified information, stamp classification on the top and bottom of the page.

Block 20. Limitation of Abstract. This block must be completed to assign a limitation to the abstract. Enter either UL (unlimited) or SAR (same as report). An entry in this block is necessary if the abstract is to be limited. If blank, the abstract is assumed to be unlimited.